Influence of the Thermo Mechanical Control Processing Finishing Condition on Microstructure and Properties of High Strength Low Alloy Pipeline Steels

Victor Carretero Olalla

Promotoren: prof. dr. ir. R. Petrov, prof. dr. ir. L. Kestens
Proefschrift ingediend tot het behalen van de graad van
Doctor in de Ingenieurswetenschappen: Materiaalkunde

Vakgroep Toegepaste Materiaalwetenschappen
Voorzitter: prof. dr. ir. J. Degrieck
Faculteit Ingenieurswetenschappen en Architectuur
Academiejaar 2014 - 2015

UNIVERSITEIT
GENT

ISBN 978-90-8578-813-3
NUR 971
Wettelijk depot: D/2015/10.500/57

"Gratus animus est una virtus non solum maxima, sed etiam mater virtutum omnium reliquarum"

"A thankful heart is not only the greatest virtue, but the parent of all the other virtues"

Marcus Tullius Cicero, (103 BC-43 BC)

Acknowledgments

I am deeply grateful to my supervisors Professor Roumen Petrov and Professor Leo Kestens, for their guidance and support throughout the course of my thesis. I deeply appreciate their belief in me. I am indebted to Roumen and Leo for the many learning experiences that they provide me with. Roumen and Leo, I appreciate the multicultural environment within your group. I consider myself very fortunate for being able to work together with all the great researchers in the Department of Materials Science and Engineering at Ghent University.

A sincere note of gratitude is extended to OCAS. Particularly to dr. Philippe Thibaux, and dr. Martin Liebeherr for giving me the opportunity of working in the present project. I would like to express my special appreciation and gratitude to my daily industrial advisor dr. Nuria Sanchez Mouriño. I can only say that, one could not wish for a better professional and friendlier mentor. Thanks a lot Nuria!

I would like to give special thanks to Professor Yvan Houbaert for giving me the first opportunity of joining the department of Materials Science and Engineering at Ghent University as Erasmus master thesis student. I am also grateful to dr. D. Ruiz Romera for the traineeship opportunity at OCAS.

I appreciate the efforts of the PhD committee members. Thank you all for your availability and contribution to the examination of my PhD.

I wish to thank the staff of the department of Materials Science and Engineering of Ghent University as well as the technical staff of OCAS for their various forms of assistance. I owe my gratitude to all those people who have made this dissertation possible.

I would like to thank all my colleagues from the Department of Material Science and Engineering, who contributed to make the PhD time a unique period in my life. It has been my pleasure to share the PhD experience with all of you. I would like to express my appreciation to my officemates An Verdiere and Aleksandar Davidkov. They always help in creating a pleasant working environment. I am grateful for having a chance to meet many inspiring people from different parts of the world.

I consider myself very fortunate to have made a lot of friends during these years in Ghent. Thanks to all my friends of "if yu ar jiar tunait", 'if u r liandola tunait" "peña los trasgos"

“steaua mineral”, “chucrut/karaoke nights”, “cipolinas” “kot mates” “latinos F.C.” “salsa classes”, “Manolo’s BBQs”…… . Special mention to those of you who have been all these years around: Amparo, Conchi, Nuria, Trompi, Miguelito, Yiyus, Eduardo, Imagine, Fernando, Benedicto, Joana, Laura, Alfonso, Ivonne, Yara, Maria, Ana, Diego, Pepe, Paco, Gleen, Kenny, Josima, Jarinda, David, Arveloa, Lobo, Principe, Adri, Cf7, Arturo, Illo, Luis, Alicia, Guillermo, Alexey, Edgar, Hadi, Elisabete, Diana, Jurij, Vitaliy, Sugus, Jai, Felipe, … (and many more I might forget). They made my life in Ghent a truly memorable experience.

I owe many thanks to my girlfriend’s family. Thank you all for make me feeling always at home.

My deepest thanks and gratitude go to my family; they worked hard and scarified much to give me, one of the best gifts you can give to your child- education. This work is dedicated to my grandfather who recently passed away.

Finally, I would like to thank my girlfriend, Celine, for her unconditional support and love. I could not have completed this thesis without Celine by my side. Thanks to the beautiful blue eyes I see before falling sleep, thanks to the beautiful blue eyes I see when a new day starts.

Thank you all.

Victor

Ghent, May 2015

Summary

Pipelines are infrastructures to transport large quantities of gas and crude oil from natural reserves to the storage places for post-processing and distribution. High Strength Low Alloy (HSLA) steels offer the appropriate strength-toughness-weldability combinations, required for this type of structures. Many properties of HSLA steels, such as the strength, toughness, and crack arrestability, are determined by the microstructure, which is effectively controlled through the chemical composition of the steel and the thermo-mechanical processing parameters. This dissertation focuses on the process that takes place in the pipeline steel during the stage known as Thermo Mechanical Control Process (TMCP). TMCP is a technique designed to impart the final shape and mechanical properties of steels by controlling the interactions among deformation, recrystallization and phase transformation during hot deformation. TMCP is aimed at producing strong and tough steel by increasing the density of ferrite nucleation sites in the parent austenite phase. This increased density of nucleation sites results, in turn, in a refined ferrite microstructure during cooling. The development of TMCP practices stems from the need for increased strength and toughness of large diameter pipelines, which are installed in arctic regions. Significant knowledge has been gained in the last 90 years with regards to TMCP and many improvements have been made in the processing of steels. However, despite the significant strides made in the last decades, much remains unresolved as it relates to the prediction of microstructures and, by extension, the resulting mechanical properties of pipeline steels.

Consequently, this thesis is aimed at elucidating the correlation between the composition, processing, microstructure, mechanical properties, and performance of pipeline steels. This was done by determining the effect of the deformation path and subsequent cooling route on the microstructural evolution of the hot deformed material. Particularly, the thesis is intended at contributing toward a better understanding of the influence of the chemical composition and processing parameters during final rolling on the microstructure of the pipeline steel sheets.

HSLA pipeline steels are polycrystalline materials. Each individual crystal in the plates has certain crystal properties which differ with the directions of atomic arrangement and hence the

the individual crystals are anisotropic. This anisotropy of the plates depends on whether regions with the same atomic arrangement (grains), are randomly oriented, or have some preferred crystallographic orientation (crystallographic texture). Specific crystallographic orientations are developed during rolling. This work describes and discusses the microstructure and texture evolution which occur during the studied TMCP. In the current study, textures develop both during deformation and recrystallization of austenite. At the end of the TMCP, the final texture is inherited (with specific orientation relationships) by the austenitic products. The effects of variations in the TMCP parameters on mechanical properties were investigated and an analysis of the process parameters (i.e. finishing rolling reduction draught, cooling condition) is also described. In addition, the mechanical behavior was analyzed as a function of the chemical composition; the effects of varying Nb and C content on the final properties of the pipeline steels were examined.

The determination of the strengthening mechanism under different rolling parameters provides a comprehensive assessment of the correlations between processing parameters, microstructure, and properties. A number of explanations are given to clarify the variations of the mechanical properties including the particular implications of recrystallization-precipitation interactions on the TMCP schedules used in the thesis.

Additionally, this thesis focuses on the investigations of microstructure on the fracture toughness. A description of the proposed variables governing fracture resistance in HSLA pipeline steels is also included.

The results obtained in this study, provide a complete understanding of the dependence of strength and toughness on the chemical composition and microstructure. For example: The Medium C - High Nb steel exhibits the largest sensitivity to variations in the thermo-mechanical processing parameters. This steel should, therefore, benefit from tuning of the thermo-mechanical processing parameters but may suffer from a scatter in properties if certain parameters (at FRT or cooling rate) are not perfectly controlled.

It has been observed that various chemical compositions differ not only in absolute values of microstructural features (i.e. average grain size) but also in the way (microstructure heterogeneity) in which they display sensitivity to changes in the TMCP schedule. The results of this study indicate that the finish rolling temperature influences the texture development in the plates whereas, the reduction draught has, in general, no impact on the austenite

transformation textures. One consequence of the processing temperature is that well-defined patterns of particular texture gradients can be identified.

Aforementioned Medium C - High Nb steel exhibits a good balance between the strength and toughness when the appropriate TMCP is followed, owing to the ability to develop a relatively homogeneous microstructure in all the studied TMCP scenarios, which (in the author's opinion) represents the first step in controlling the fracture toughness (assuming that the inclusion content has been previously strictly controlled). A relatively homogeneous microstructure develops, at least in part, owing to the larger fraction of Nb precipitates present in this steel compared to those of the other steels. Some of these precipitates prevent the growth of austenite grains prior to the austenite to ferrite transformation. Additionally the high yield strengths obtained at low finish rolling temperature are correlated with the enhanced precipitation hardening achieved in the low finish rolling temperature followed by accelerated cooling condition and low finish rolling temperature followed by air cooling TMCP routes.

An important finding that emerged from the presented results is that, the attribution of toughness behavior to a single factor/microstructural feature, fails to resolve the correlation between the crack propagation and the microstructure. The foundations for the analysis of the correlation between splitting and the Cleavage Morphology Clustering parameter have also been established.

The PhD thesis is organized in eight chapters; Chapter I introduces the subject and describes the importance of the pipeline steel with regards to societal needs; prognoses for the future are also considered. Chapter II includes an overview of the most relevant advances in the field of TMCP (with special emphasis on HSLA pipeline steels). Chapter III states the objectives and the general methodology of the work. Chapter IV briefly describes the experimental procedures. Chapter V describes and discusses the microstructure and texture evolution which occur during the studied TMCP. The effects of variations in the TMCP parameters on mechanical properties were also investigated. In addition, the mechanical behavior was analyzed as a function of the chemical composition. The third section of Chapter V focuses on the investigations into microstructural control of the fracture toughness. Furthermore, the determination of the strengthening mechanism under different rolling parameters is described in the last part of Chapter V. Chapter VI provides a comprehensive assessment of the correlations among processing parameters, microstructure, and properties. A series of tables

are presented in order to easily assess the improvement of the yield strength and the corresponding impact on the ductile to brittle transition temperature. In this general discussion chapter, a number of explanations are given to clarify the variability of the mechanical properties presented in Chapter V. The aforementioned discussion includes particular implications of recrystallization-precipitation interactions during the TMCP schedules used in the thesis. An interpretation of the synergies between different strengthening mechanisms is also included. To finalize, Chapter VI incorporates a description of the proposed variables governing fracture resistance in HSLA pipeline steels. Chapter VII summarizes the main conclusions of the thesis, and Chapter VIII enumerates the suggestions for further studies.

Samenvatting

Pijpleidingen zijn constructies om grote hoeveelheden gas en ruwe olie te transporteren van de natuurlijke winningsgebieden tot aan de opslagplaatsen voor nabehandeling en distributie. Laag-gelegeerde hoog-sterkte stalen (High Strength Low Alloy – HSLA steels) voorzien in de juiste balans van sterkte, taaiheid en lasbaarheid die vereist is voor dergelijke constructies. Veel eigenschappen van HSLA stalen zoals sterkte, taaiheid en crack arrestability, worden bepaald door de microstructuur die efficiënt gecontroleerd wordt door de chemische samenstelling van het staal en de thermo-mechanische procesparameters. Dit proefschrift richt zich op het proces dat plaatsvindt in het pijplijnstaal tijdens de stap gekend als Thermo Mechanical Controlled Processing (TMCP). TMCP is een techniek die beoogt het walsproces dusdanig te sturen dat een finaal plaatproduct bekomen wordt met gewenste dimensies en mechanische eigenschappen als resultaat van een nauwgezette controle van de interacties tussen vervorming, rekristallisatie en fasentransformaties tijdens de warmvervorming. Het doel van TMCP is het produceren van sterk en taai staal door de dichtheid van ferriet nucleatieplaatsen te verhogen in de ouderlijke austenietfase, zodat een verfijnde ferrietmicrostructuur gevormd wordt tijdens het afkoelen. De ontwikkeling en toepassing van TMCP vloeit voort uit de noodzaak van verhoogde sterkte en taaiheid van pijpleidingen met een grote diameter, die in arctische gebieden worden geïnstalleerd. Belangrijke kennis is opgedaan in de afgelopen 90 jaar met betrekking tot TMCP en veel verbeteringen zijn aangebracht in de verwerking van staal. Echter, ondanks de aanzienlijke vooruitgang die geboekt is gedurende de afgelopen decennia blijven veel problemen onopgelost. Deze zijn voornamelijk gerelateerd aan de voorspelling van microstructuren en bij uitbreiding de resulterende mechanische eigenschappen van de pijplijnstalen.

Het doel van deze thesis is daarom het toelichten van het verband tussen samenstelling, maakproces, microstructuur, mechanische eigenschappen en prestatie van pijplijnstalen. Dit werd gedaan door het bepalen van het effect van de vervormingsstappen en de daaropvolgende afkoeling op de microstructurele evolutie van het warmvervormd materiaal. In het bijzonder wordt de thesis bedoeld om bij te dragen tot een beter begrip van de invloed van de chemische samenstelling en de procesparameters tijdens het eindwalsen op de microstructuur van de pijplijnstaalplaten.

Samenvatting

HSLA pijplijnstalen zijn polykristallijne materialen. Elk individueel kristal in een plaat heeft bepaalde kristaleigenschappen die variëren naargelang de richtingen van de atoomordening, waardoor de individuele kristallen anisotroop zijn. Deze anisotropie van de platen is afhankelijk van of gebieden met dezelfde atoomordening (korrels) willekeurig georiënteerd zijn, of deze een preferentiële kristallografische oriëntatie (kristalstructuur) hebben. Specifieke kristallografische oriëntaties worden ontwikkeld tijdens het walsen. Dit werk beschrijft en bespreekt de microstructuur- en textuurevolutie die zich voordoet tijdens de bestudeerde TMCP. In de huidige studie ontwikkelen de texturen zich zowel tijdens de vervorming als tijdens de rekristallisatie van austeniet. Aan het einde van de TMCP wordt de uiteindelijke textuur geërfd (met bepaalde oriëntatieverbanden) van de austenitische producten. De effecten van wijzigingen in de TMCP parameters op de mechanische eigenschappen werden onderzocht en de procesparameters (d.w.z. het ontwerp van de eindwalsreductie, de conditie van het afkoelen) werden ook geanalyseerd.. Bovendien werd het mechanisch gedrag geanalyseerd als een functie van de chemische samenstelling; de effecten van variërende Nb- en C-gehaltes op de uiteindelijke eigenschappen van de pijplijnstalen werden onderzocht.

De bepaling van het verstevigingsmechanisme met verschillende walsparameters biedt een uitgebreide beoordeling van de correlaties tussen de procesparameters, microstructuur en eigenschappen. Een aantal verklaringen worden gegeven om de variaties van de mechanische eigenschappen zoals de specifieke gevolgen van rekristallisatie-precipitatie interacties op de TMCP schema’s gebruikt in de thesis te verduidelijken.

Bovendien richt dit onderzoek zich ook op de microstructurele afhankelijkheid van de breuktaaiheid. Er wordt een gedetailleerde beschrijving gegeven van de microstructurele toestandsvariabelen die van belang zijn voor het breuk-gedrag van HSLA pijplijnstalen.

De in deze studie verkregen resultaten geven een volledig begrip van de invloed van chemische samenstelling en microstructuur op de sterkte en taaiheid. Als voorbeeld toont het medium C - hoog Nb staal de grootste gevoeligheid voor variaties in de thermo-mechanische procesparameters. Dit staal zou daarom baat moeten hebben bij het afstemmen van de thermo-mechanische procesparameters, maar kan last hebben van een spreiding in eigenschappen als bepaalde parameters (bij FRT of afkoelsnelheid) niet perfect gecontroleerd zijn.

Er werd waargenomen dat een variatie in chemische samenstelling niet alleen leidt tot verschillen in absolute waarden van microstructurele eigenschappen (zoals gemiddelde

korrelgrootte), maar ook in de manier waarop deze eigenschappen gevoeligheid tonen voor veranderingen in het TMCP schema (microstructurele heterogeniteit). De resultaten van deze studie geven aan dat de eindwalstemperatuur de textuurontwikkeling in de platen beïnvloedt, in tegenstelling tot de walsreductie die in het algemeen geen invloed heeft op de austeniet-transformatie texturen. Een gevolg van de procestemperatuur is dat goed gedefinieerde patronen van bepaalde textuurgradiënten geïdentificeerd kunnen worden.

Het eerdergenoemd medium C - hoog Nb staal vertoont een goed evenwicht tussen de sterkte en taaiheid als de geschikte TMCP gevolgd wordt, wegens de mogelijkheid om een relatief homogene microstructuur te ontwikkelen in alle bestudeerde TMCP schema's, wat (naar de mening van de auteur) de eerste stap in de controle van de breuktaaiheid vertegenwoordigt (ervan uitgaande dat de hoeveelheid insluitsels strikt gecontroleerd is). Een relatief homogene microstructuur ontstaat, ten minste gedeeltelijk, door de grotere fractie van Nb precipitaten aanwezig in dit staal vergeleken met andere staalsoorten. Sommige van deze precipitaten hinderen de groei van austenietkorrels alvorens de transformatie van austeniet naar ferriet plaatsvindt. Daarnaast worden de hoge vloeigrenzen, verkregen bij lage eindwalstemperatuur, gecorreleerd met de verbeterde precipitatieharding bereikt in de lage eindwalstemperatuur gevolgd door versnelde afkoeling en in de lage eindwalstemperatuur gevolgd door luchtkoeling in de TMCP routes.

Een belangrijke bevinding die voortgekomen is uit de gepresenteerde resultaten, is dat het toeschrijven van taaiheidsgedrag aan één enkele factor/microstructurele eigenschap er niet in slaagt om een correlatie tussen scheurgroei en microstructuur te vinden. De fundamenten voor de analyse van de correlatie tussen splitsing en de Cleavage Morfology Clustering parameter zijn ook gevestigd.

De thesis is georganiseerd in acht hoofdstukken; Hoofdstuk I introduceert het onderwerp en beschrijft het belang van de pijplijnstalen met betrekking tot maatschappelijke behoeften; prognoses voor de toekomst worden ook beschouwd. Hoofdstuk II bevat een overzicht van de meest relevante ontwikkelingen op het gebied van TMCP (met speciale nadruk op HSLA pijplijnstalen). Hoofdstuk III geeft de doelstellingen en de algemene methodologie van het werk. Hoofdstuk IV beschrijft bondig de experimentele procedures. Hoofdstuk V beschrijft en bespreekt de microstructuur- en de textuurevolutie die zich voordoet tijdens de bestudeerde TMCP schema's, waarbij de effecten van gewijzigde TMCP parameters op de mechanische eigenschappen uitgebreid werden onderzocht. Bovendien werd het mechanisch gedrag

geanalyseerd als een functie van de chemische samenstelling. Het derde deel van hoofdstuk V richt zich op de microstructurele afhankelijkheid van de breuktaaiheid. De bepaling van het verstevigingsmechanisme onder verschillende walsparameters wordt beschreven in het laatste deel van hoofdstuk V. Hoofdstuk VI biedt een uitgebreide evaluatie van de correlaties tussen de procesparameters, microstructuur en eigenschappen. Een reeks tabellen worden weergegeven om de verbetering van de vloeigrens en de bijbehorende gevolgen voor de overgangstemperatuur van ductiel naar bros gedrag gemakkelijk te beoordelen. In dit algemene discussie-hoofdstuk worden een aantal verklaringen gegeven om de variatie van de mechanische eigenschappen gepresenteerd in hoofdstuk V te verklaren. De bovengenoemde discussie omvat bijzondere gevolgen van rekristallisatie-precipitatie interacties tijdens de TMCP schema's gebruikt in het proefschrift. Een interpretatie van de synergie tussen de verschillende verstevigingsmechanismen is ook inbegrepen. Om af te ronden, bevat hoofdstuk VI een beschrijving van de voorgestelde variabelen die van belang zijn voor het breukgedrag in HSLA pijplijnstalen. Hoofdstuk VII geeft een overzicht van de belangrijkste conclusies van het proefschrift, en hoofdstuk VIII geeft een opsomming van suggesties voor verdere studies.

Table of contents

Table of contents

List of Symbols and abbreviations

A_{c1}	Temperature at which, during heating, austenite starts to form
A_{c3}	Temperature at which, during heating, transformation of the ferrite into austenite ends
ACC	Accelerated Cooling Condition
ALAMEL	Advance LAMEL model
ANOVA	Analysis of variance
API	American Petroleum Institute
Ar_1	Temperature at which, during cooling, transformation of the austenite into ferrite + cementite ends
Ar_3	Temperature at which, during cooling, transformation of the austenite into ferrite starts
ARB	Accumulative Roll Bonding
ASTM	American Society for Testing and Materials
b	Burgers vector
BCC	Body Centre Cubic
BF	Bright Field
BDWTT	Battelle Drop Weight Tear Test
B_L	Lower bainite
BOF	Basic oxygen furnace
BTC	Battelle Two Curve
B_U	Upper bainite
CBED	Convergent beam electron diffraction
CAT	Crack Arrest Temperature
CC	Controlled Cooling
CCT	Continuous Cooling Temperature diagram
CE	Carbon Equivalent
CNI	Critical National Infrastructures
CMC	Cleavage Morphology Clustering
C_p	The apparent specific heat capacity
CR	Controlled Rolling
C_R	Cooling rate
CRLP	Composite Reinforced Line Pipe
CTOD	Crack Tip Opening Angle
CVN	Charpy V-notch impact
D and D_γ	Austenite grain size prior to deformation
DBTT	Ductile to Brittle Transition Temperature
DRX	Dynamic Recrystallization
DT	Dynamic Transformation
DVR	Dynamic Recovery
D_α	Ferrite grain size
DWTT	Drop-Weight Tear Test
EBSD	Electron backscatter diffraction
EAF	Electric Arc Furnace
ECAP	Equal-Channel Angular Pressing
E_f	Fracture energy
E_i	Energy absorbed during initiation of the crack
E_p	Energy absorbed during propagation
FATT	Fracture Propagation transition Temperature

FCC	Face Centre Cubic
FRT	Finish Rolling Temperature
G	Shear modulus
GB	Grain boundary
GCM	Grain Clustering Maps
GS	Grain size
hkl	Miller indices
HSLA	High Strength Low Alloy
HAGB	High angle grain boundariy
ICP-MS	Inductively- Coupled Plasma Mass Spectrometry
IEA	International Energy Agency
IF Steel	Interstitial Free steel
IIW	International institute for welding
IPQ	Inverse pole figures
IQ	Image quality
J_{IC}	Rice J integral
k	Avrami exponent
KAM	Kernel Average Misorientation
K_{IC}	Fracture toughness critical stress intensity factor
K-S	Kurdjumov-Sachs
K_Y	Grain boundary unlocking term
LAGB	Low Angle Grain Boundary
LNG	Liquefied Natural Gas
LSE	Low self energy region
M	Average Taylor factor
M/A	Martensite/ Austenite constituents
MC	Morphology Clustering
M_S	Temperature at which, during cooling, transformation of the austenite into martensite starts
Mtoe	Million tons of oil equivalent,
n	Work hardening
N_L	Number of intersections per length with a random line
N-W	Nishiyama-Wassermann
ODF	Orientation Distribution Function
OM	Optical microscope
P_{cm}	Critical metal parameter (low carbon and limited alloying elements)
P_D	Degenerate pearlite
P_L	Lamellar pearlite
P_s	Precipitation start
$P_{s'}$	Precipitation start deform austenite
PSN	Particle Stimulating Nucleation
Q	Activation energy
R	Universal gas constant
R_S	Recrystallization start
RD	Rolling direction
r.m.s	Root mean square
r.m.s	Root mean squares
RCR	Recrystallization Controlled Rolling
RPMP	Reinforced Polymer Mortar Pipe
RTRP	Reinforced-Thermosetting-Resin-Pipe

List of Symbols and abbreviations

SAED	Selected area electron diffraction
S_{eff}	Effective surface boundary area/unit of volume in austenite
SEM	Scanning electron microscope
$S_{g.b.}$	Sum of the area of grain boundaries
SIP	Strain Induce Precipitation
SMYS	Specified Minimum Yield Strength
SRX	Static Recrystallization
STEM	Scanning Transmission Electron Microscope
T	Temperature
t	Time
TD	Transversal direction
TEM	Transmission Electron Microscopy
TMCP	Thermo Mechanical Control Process
Tnr	Temperature no recrystallization
UPS	Upper self energy region
UOE	U-ing, O-ing Expansion
UTS	Ultimate tensile Strength
X	Recrystallized fraction
XRD	X-Ray diffraction
Y/T	Yield to tensile strength ratio
YS	Yield strength
Z	Zener-Hollomon parameter
ZA	Zone Axis
α	Ferrite
α'_M	Martensite
α_A	Acicular ferrite
α_B	Bainitic ferrite
$\alpha_{B(G)}$	Granular bainitic ferrite
α_p	Polygonal ferrite
α_{qp}	Quasi polygonal ferrite
α_W	Widmanstatten ferrite
γ	Austenite
Q_{RX}	Apparent activation energy for recrystallization
$t_{0.5x}$	Time necessary for 50% recrystallization
$\dot{\varepsilon}$	Strain rate
ε_p	Peak strain
ε_r	Accumulated strain
ε_s	Steady state strain
ξ_g	Extinction distance
λ	Wavelength
σ_0	Intrinsic lattice friction stress
σ_d	Dislocation strengthening
σ_h	Hoop stress
σ_p	Precipitation strengthening
σ_p	Peak stress
σ_{ss}	Solid solution strengthening
σ_Y	Yield stress
ρ	Dislocation density

List of figures

Chapter I

Chapter II

List of tables

Chapter I

Chapter II

"Todo pasa y todo queda,
pero lo nuestro es pasar,
pasar haciendo caminos,
caminos sobre el mar.
Nunca perseguí la gloria,
ni dejar en la memoria
de los hombres mi canción;
yo amo los mundos sutiles,
ingrávidos y gentiles,
como pompas de jabón.
Me gusta verlos pintarse
de sol y grana, volar
bajo el cielo azul, temblar
súbitamente y quebrarse...
Nunca perseguí la gloria.
Caminante, son tus huellas
el camino y nada más;
caminante, no hay camino,
se hace camino al andar.
Al andar se hace camino
y al volver la vista atrás
se ve la senda que nunca
se ha de volver a pisar.
Caminante no hay camino
sino estelas en la mar..."

"Everything passes and everything stays,
but our fate is to pass,
to pass making paths,
paths on the sea.
I never looked for glory,
nor to leave in the memory
of mankind my song;
I love subtle worlds,
lightness and gentile,
like soap bubbles.
I like to watch them painting
of sun and garnet, to fly
under the blue sky, tremble
suddenly and break...
I never looked for glory.
Walker, your treads are
the path and nothing more;
walker, there is no path,
the path is made when walking.
When walking the path is made
and when looking back
you see the path that never
has to be walked again.
Walker, there is no path,
but trails in the sea..."

Antonio Machado (1875-1939) Cantares

CHAPTER I

General introduction

I.1 Overview of the world energy context

In its broadest sense, energy, particularly a source of energy, is one of the basic conditions required for life. Besides, in our civilization, energy represents the main tool to fulfill basic human needs. The modern energy services are one of the most important assistances that any country can provide to its citizens in order to ensure their well being. Energy (see Figure I.1) is the core of the interdependencies between the Critical National Infrastructures (CNI). The CNI are the pillars of the security and economy of any country.[1]

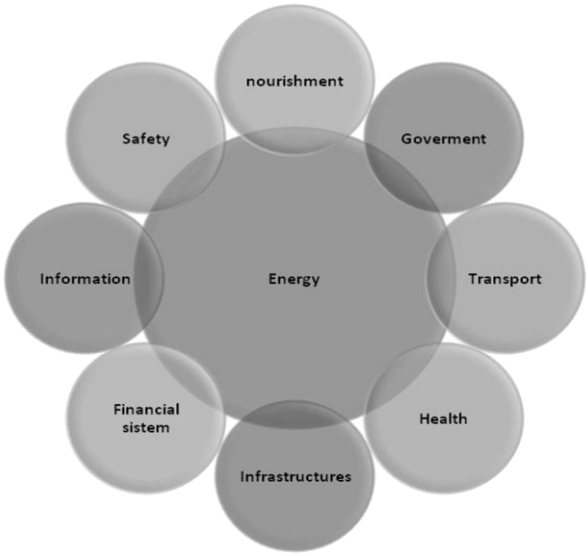

Figure I.1 *Interdependencies between energy and the CNI, pillars of an advance society.*

The International Energy Agency (IEA) estimates an average annual investment of $48 billion in order to provide universal modern energy access by 2030 [2]. Recent world energy outlook [3], presents projections of energy trends through to 2035. Taking into account the new developments in economic and politic situations, it is suggested that the global energy demand will grow by more than one-third until 2035. The prognoses account China, India

and the Middle East to contribute 60% of this increase (cf. Figure I.2). The later predictions go in agreement with those proposed by the organization of the Petroleum Exporting Countries [4] or the forecast of one of the largest energy dealing multinationals (cf. Figure I.3)[5].

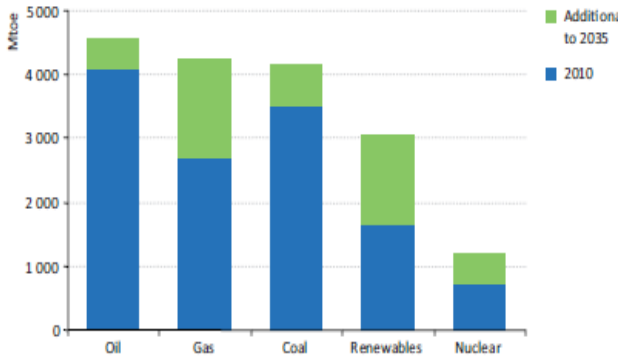

Figure I.2 *World primary energy demand by fuel (Million tons of oil equivalent, Mtoe) considering the general case scenario "Golden rules case scenario" IEA [6].*

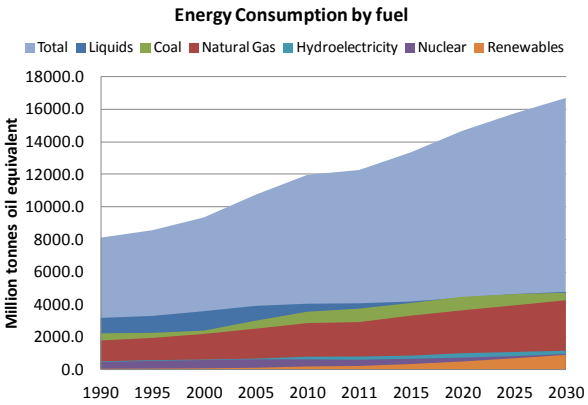

Figure I.3 *World energy consumption historic data and forecast (up to 2030) by fuel [5].*

Notwithstanding the policies to reduce our CO_2 footprint and to leave an environmental friendly lasting legacy for the coming generations, fossil fuels remain dominant in the global energy mix. Between the trends identified in the above study is worth mentioning those forecasting that driven by new upstream technologies will unlock tight oil and gas resources, by the end of present decade. According to these forecasts the United States is expected to develop into the largest oil producer, overtaking Saudi Arabia, becoming a net oil exporter around 2030 and switching the direction of international oil trade towards Europe and Asia. Moreover, it is remarkable that natural gas is the only fossil fuel for which the global demand grows in all scenarios. A special attention should be paid to China's consumption which grows up to four times with respect to the current use [3].

The main conclusion that can be drawn from the mentioned outlooks indicates the inevitable necessity of transportation networks linking the resources and the consumption. The pipelines are infrastructures to transport large quantities of gas and crude oil from natural reserves to the storage places for post-processing and distribution. The majority of oil and gas is, and will be transported via pipelines. Without line pipes it would be impossible to satisfy the huge oil and gas needs of the current society. Moreover, in terms of safety pipelines are much safer and cost effective than rail or road tanks as a way of transportation [7]. As an example of such efficiency, the Canadian energy pipeline association network transports three million barrels of oil every day, which is equivalent to fill 15000 tanker truck loads or 4200 rail cars [8].

Energy efficiency policies are implemented (i.e. European Union has committed to cut of 20% of its energy demand by 2020) not only to reduce emissions and control global warming or climate change but also to easily overcome worldwide fluctuations in price and supply. In this direction Europe, as other countries, is committed to reach a scenario where oil and gas are potentially available from various streams and sources, and therefore avoiding cuts in supply [9]. In the recent years, there has been an increasing interest in creating a well-developed import-export infrastructure, leading to execution of huge oil and gas transportation projects. Several studies [10, 11] reported estimates of gas demand in Europe coupled with the existing supply sources in Russia, Middle East and Northern Africa, even analyzing the possible bottlenecks in gas transportation infrastructure, with the final purpose of developing cost-minimization models within the European gas supply system.

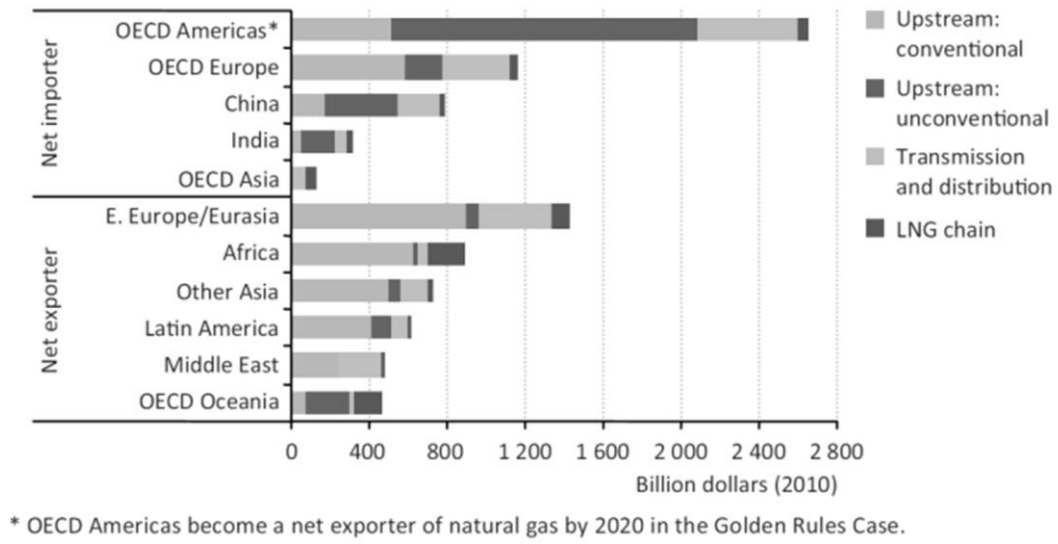

Figure I.4 *Cumulative investment in natural gas-supply infrastructure by major region and type in the "Golden rules case scenario" 2012-2035 IEA.[6]**;** Liquefied Natural Gas (LNG)*

According to the prognosis of the international energy agency IEA published in 2010 [6], the cumulative investment in conventional and unconventional gas supply infrastructure in the period 2012–2035 (in year 2010 dollars) would be of $9.7 trillion (see Figure I.4). This highlights the importance of gas and also oil transport infrastructure in the global economy and by extension justifies the efforts that should be made to ensure safety during the long distance transportation of these fuels.

Table I-1 includes the most strategically and remarkable worldwide pipeline projects which are currently under construction or in a planning phase.

I.2.Materials for pipeline

According to *Ashby* [12], the choice of the proper material for a given application underlies in meeting the technical requirements of the design safely and economically. High Strength Low Alloy (HSLA) steels offer the appropriate strength-toughness-weldability combinations, required for this type of structures. HSLA steels are and will remain in the future the main material for pipelines for gas and oil transportation.

PIPELINE	FROM	DELIVERY	FUEL	OPERATIONAL	LENGTH (Km)	STRATEGIC IMPACT
IGI Poseidon	Greece	Italy	Gas	2015	807	It will complete the natural gas corridor through Turkey, Greece and Italy
South Stream	Russia	Italy Slovenia Croatia Bosnia Serbia Hungary Bulgaria	Gas	2015	2380	Strengthening the European energy security
Nord Stream	Russia	Germany	Gas	2012	1222	Direct connection between the vast gas reserves in Russia and energy markets in the EU
Trans-Caspian	Turkmenistan	Azerbaijan	Gas	Final decision regarding route under discussion		European markets are serviced from more sources than Russian's network
White Stream	Georgia	Romania	Gas	2016	1238	E.U. connectivity to Georgia, bypassing Russia
Trans Adriatic TAP	Turkey	Italy	Gas	Implementation phase Construction planed to begin in 2016	3500	Along its route, TAP will connect with a number of existing and proposed pipelines, ensuring that the Southern Gas Corridor opens up to many different energy markets.

ESPO	Russia	China Pacific Ocean	oil	2013	4857	Increase Russian importance as Asian oil supplier
Altai	Russia	China	Gas	2015	2800	Cover Chinese gas demand
Alaska Denali	Alaska North Slope	U.S. Midwest	Gas	Unknown	2760	Serve North American markets
Keystone XL	Alberta	Oklahoma Illinois	Oil	2015	3456	Reduce imports from Venezuela and middle east
Tapi	Turkmenistan	India	Gas	2017	1735	export route avoiding both Iran and Russia
IP (Iran – Pakistan	Iran	Pakistan	Gas	2013	2775	A crucial key on the path to peace

Table I-1 *Remarkable worldwide pipeline projects currently under construction or in a planning phase [8, 13-23].*

Although steel pipes are widely used in gathering, transmission and distribution of natural gas, there are other materials under consideration for future transport of gas. Reinforced-thermosetting-resin-pipe (RTRP) and glass-fiber-reinforced polymer mortar pipe (RPMP) are two examples of alternative materials for pipelines. Composite Reinforced Line Pipe (CRLP) is a type of pipe which consists of steel pipe coated or wrapped in a continuous composite shell material that adds strength and protection to the steel [24]. There are few reasons to consider composites as pipeline materials: *(i)* Composites are highly resistant to many corrosive chemicals and compounds, including H_2S. *(ii)* Composites are significantly lighter than steel [24]. However, when comparing the physical properties (strength) of steel with other potential materials for pipeline applications as fiberglass or plastic based pipe materials, steel has the advantage when the pressure is the critical factor. In addition, from the economical and sustainable (recycling) points of view the use of steel is more advantageous.

The mechanical and functional properties of the steel pipe depend strongly on the microstructure. The production of steel with required chemical composition, microstructure and properties is carried out in steel plants through many interconnected processes that can be laid out in various combinations depending of several factors as: available raw materials, technical constrains of each production plant (available energy, equipment), products portfolio…

Figure I.5 illustrates a generic flow scheme of the two main steel making routes: (I) integrated route whose distinguishing elements are the blast furnace and the basic oxygen furnace (BOF), and (II) electric arc furnace (EAF) route. The BOF utilizes pig iron (produced in the blast furnace from ore, limestone, coke) and scrap as raw materials while the EAF uses mainly scrap to produce new steel. Once the molten steel has the desired composition continuous casting is accomplished. Subsequently hot rolling and cold rolling are implemented before executing the shaping, forming, and surface treatment of the final product.

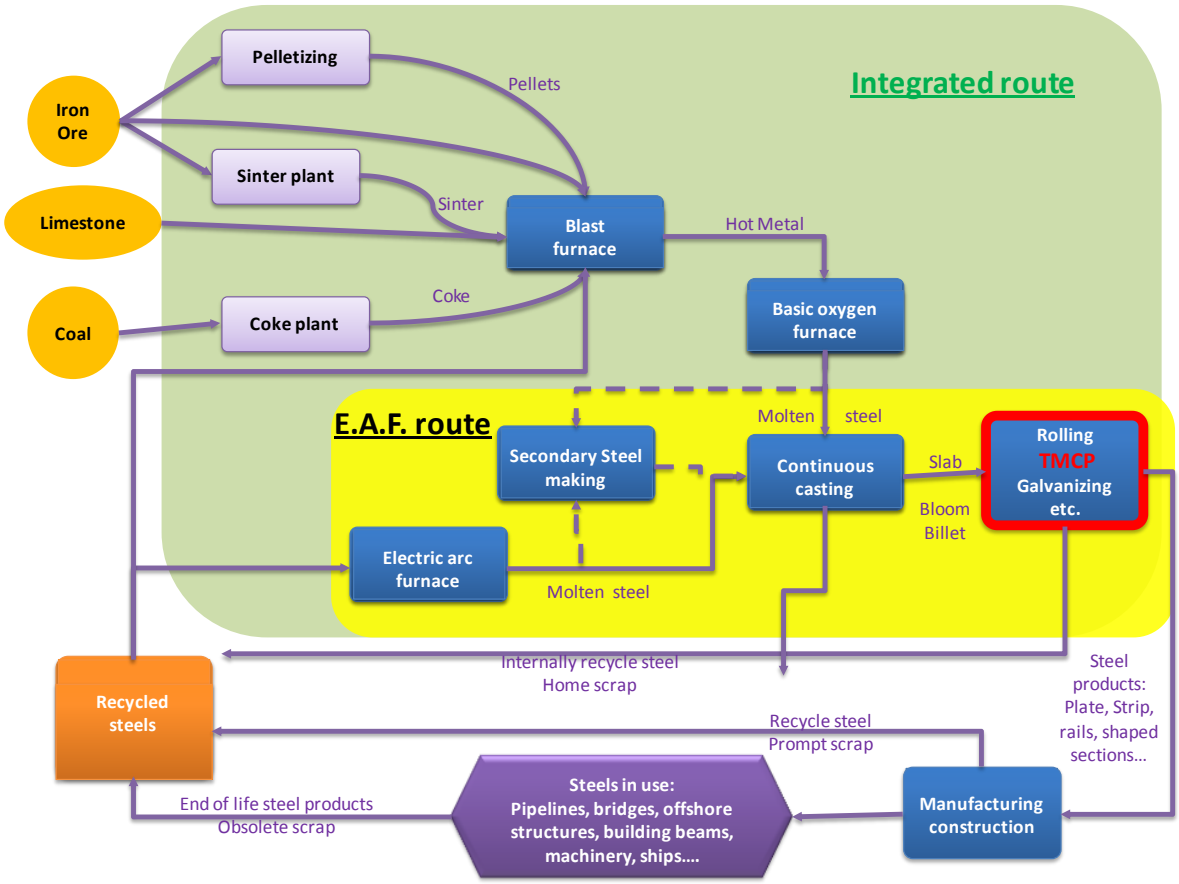

Figure I.5 *Routes to steel making. TMCP stage highlighted in red. (adapted from International iron and steel institute [25]).*

This dissertation focuses on the process that takes place in the pipeline steel during hot rolling stage, particularly the stage known as Thermo Mechanical Control Process (TMCP), with intention to understand of the physical metallurgy and the ability to control the microstructure and properties of the pipeline steel at this stage.

References

[1] H. Group, "The financial Aspects of the Security of Assets and Infrastructure in the Energy sector," European Commision2012.

[2] I.E.A, "Energy for all. Financing access for the poor," International Energy Agency 2011.

[3] I.E.A, "World Energy Outlook 2012," International Energy Agency 2012.

[4] "World Oil Outlook 2012," Organization of the Petroleum Exporting Countries 2012.

[5] BP, "BP Energy Outlook 2030: January 2013," BP, Ed. 2013.

[6] I.E.A, "Golden Rules for a Golden age of Gas," International Energy Agency 2012.

[7] P. Hopkins, "Oil and Gas pipelines: yesterday and today," 2007.

[8] CEPA. Available: http://www.cepa.com/about-pipelines/why-pipelines

[9] "Energy infrastructure priorities for 2020 and beyond — A Blueprint for an integrated European energy network," E. Commission, Ed. European Commission, 2011.

[10] U. Remme, M. Blesl, and U. Fahl, "Future European gas supply in the resource triangle of the Former Soviet Union, the Middle East and Northern Africa," *Energy Policy,* vol. 36, pp. 1622-1641, 2008.

[11] N. I. Voropai, S. M. Senderov, and A. V. Edelev, "Detection of “bottlenecks” and ways to overcome emergency situations in gas transportation networks on the example of the European gas pipeline network," *Energy,* vol. 42, pp. 3-9, 2012.

[12] M. Ashby and K. Johnson, "The art of materials selection," *materialstoday,* vol. 6, pp. 24-35, 2003.

[13] *Trans Adriatic Pipeline* Available: http://www.tap-ag.com/the-pipeline

[14] C. E. E. Partners. Available: http://www.ceep.be/southern-gas-corridor-eu-co-operation-chinese-dominance/

[15] *Gas pipeline Pakistan-Iran*. Available: http://rt.com/op-edge/gas-pipeline-pakistan-iran-068/

[16] *Alaska-Denali*. Available: http://www.arcticgas.gov/Alaska-Natural-Gas-Pipeline-Project-History

[17] *Tapi pipeline*. Available: http://www.ogj.com/articles/print/volume-111/issue-3/transportation/roadblocks-remain-to-tapi-pipeline.html

[18] *Gazprom*. Available: http://www.gazprom.com/about/production/projects/pipelines/altai/

[19] *Epso oil pipeline*. Available: http://www.osw.waw.pl/en/publikacje/eastweek/2013-01-09/completion-espo-oil-pipeline-connects-siberia-to-pacific-ocean

[20] *Nord-stream*. Available: http://www.nord-stream.com/

[21] *White-stream*. Available: http://www.white-stream.com/#

[22] *South-stream*. Available: http://www.south-stream.info/en/

[23] *igi-poseidon*. Available: http://www.igi-poseidon.com/english/index.asp

[24] P. Laney, "Use of composite pipe materials in the transportation of natural gas," Idaho national engineering and environmental laboratory 2002.

[25] Available: http://www.worldsteel.org/

Mais je ne craindrai pas de dire que je pense avoir eu beaucoup d'heur de m'être rencontré dès ma jeunesse en certains chemins qui m'ont conduit à des considérations et des maximes dont j'ai formé une méthode, par laquelle il me semble que j'ai moyen d'augmenter par degrés ma connaissance, et de l'élever peu à peu au plus haut point auquel la médiocrité de mon esprit et la courte durée de ma vie lui pourront permettre d'atteindre. Car j'en ai déjà recueilli de tels fruits, qu'encore qu'au jugement que je fais de moi-même je tâche toujours de pencher vers le côté de la défiance plutôt que vers celui de la présomption, et que, regardant d'un œil de philosophe les diverses actions et entreprises de tous les hommes, il n'y en ait quasi aucune qui ne me semble vaine et inutile, je ne laisse pas de recevoir une extrême satisfaction du progrès que je pense avoir déjà fait en

I will not hesitate, however, to avow my belief that it has been my singular good fortune to have very early in life fallen in with certain tracks which have conducted me to considerations and maxims, of which I have formed a method that gives me the means, as I think, of gradually augmenting my knowledge, and of raising it by little and little to the highest point which the mediocrity of my talents and the brief duration of my life will permit me to reach. For I have already reaped from it such fruits that, although I have been accustomed to think lowly enough of myself, and although when I look with the eye of a philosopher at the varied courses and pursuits of mankind at large, I find scarcely one which does not appear in vain and useless , I never the less derive the highest satisfaction from the progress I conceive

la recherche de la vérité, et de concevoir de telles espérances pour l'avenir, que si, entre les occupations des hommes, purement hommes, il y en a quelqu'une qui soit solidement bonne et importante, j'ose croire que c'est celle que j'ai choisie.

René Descartes (1596 – 1650)

Discurse de la methode

myself to have already made in the search after truth, and cannot help entertaining such expectations of the future as to believe that if, among the occupations of men as men, there is any one really excellent and important, it is that which I have chosen

CHAPTER II

Background

II.1 Historical survey

In general terms, thermo-mechanical control processing (TMCP) is a technique designed to impart the final shape and mechanical properties of steels by controlling the interactions among deformation, recrystallization and phase transformation during hot deformation. Hot rolling was originally designed to produce desirable external shapes (i.e. thickness, length) of the finished or semi-finished products [1]. Years later, the control of the thermal and deformation paths resulted in steels with better properties without use of special heat treatments or highly alloyed grades. In the current work, TMCP will be defined as the combination of controlled rolling (CR) and controlled cooling (CC). TMCP is therefore a sophisticated recipe that combines well-defined thermal and deformation paths [2]. In depth, thermo-mechanical processing is aimed at producing strong and tough steel by increasing the density of ferrite (α) nucleation sites in the parent

austenite (γ) phase. This increased density of nucleation sites results in a refined α microstructure during cooling [1].

It is well established that grain refinement results in simultaneous increase of the strength and toughness of the steel [3-5]. As such, various methods (see Table II.1-1 [6]) have been studied with the aim of producing ultra-fine α microstructures. However, until now, TMCP practices (which combine some of the listed strategies in Table II.1-1) on HSLA pipeline steels are the only ones which have been successfully implemented into large industrial scale production.

Techniques	**Ferrite grain size achieved (μm)**	**Log strain imposed**	**Deformation temperature K**	**Steels/ composition (wt%)**	**References**
ECAP	0.3	4	623	0.15C-1.1Mn-0.25Si	[7]
ARB	0.4	5.6	773	IF steel	[8]
Multiple compression	0.3	6.4	873	Austenitic stainless steel	[9]
Strain-induced ferrite transformation	1.0 (strip surface)	0.36	1053	0.06C-0.59Mn	[10]
DRX during hot deformation	2-5	Final rolling 2.2-3.6	1153-1033	0.11C-1.45Mn-0.34Si-0.068Nb	[11]
Deformation in the inter-critical region	2.1	2.3	973	0.17C-1.32Mn-0.44Si-0.15Nb	[12]
Warm rolling in the ferrite region	1-3	~0.55 X 5	Below A_1	IF steel	[13]

Table II.1-1 *Overview of the different techniques used to produce fine, and ultra-fine grains in steels [6].*

Thermo-mechanical treatments have existed since ancient times [14, 15]. Despite this, the first commercial steel produced under controlled rolling was, however, introduced in only the 1950s [16].

Significant knowledge has been gained in the last 90 years with regards to TMCP and many improvements have been made in the processing of steels. Table II.1-2 summarizes the main events which advanced the development of TMCP particularly for HSLA-Nb steels.

Year	Event	Reference
1801	Discover of Columbium (Niobium)	Hatchett [17]
1924	Described the advantages of grain refinement	Arrowsmith [18]
1925	Grain refinement by hot-rolling (increasing reduction or decreasing temperature)	Hanemman [19]
1939	Patent: effect of Nb on increasing the strength of hot rolled C-Mn steels	Becket [20]
1947	Relationship between ductile to brittle transition temperature and ferrite grain size	Barr-Tipper [21]
1958	Controlled low-temperature during last rolling passes	Vanderbeck [16]
1958	Production of the first high strength plate containing Nb	Great Lakes Steel [22]
1959	Addition of Nb increases strength but reduces toughness	Beiser [23]
1961	Patent: first TMCP pipeline steel containing Nb	Altenburger [24]
1963	Discovery of the precipitation hardening effect of Nb(CN) in the α matrix	Morrison [25]
1964	Influence of grain size on the upper yield stress	Petch [26]
1964	Relationships: Austenite G.S prior deformation–recrystallization rate –Austenite recrystallize G.S. Deformation T^{a} –rate recrystallization- Austenite recrystallize G.S	Grange [27]

1967	Large scale introduction of controlled rolling	Irvine [28]
1964	Nb retards recrystallization of austenite	Phillips [29]
1967		Irani [30]
1982	First on line accelerated cooling	Tsukada [31]
1994	Determination of T_{nr} in rolling mill and laboratory torsion test	Maccagno [32]
2013	Dynamic transformation of deformed austenite at temperatures above the Ae_3	Ghosh, Jonas [33]

Table II.1-2 *Summary of the significant milestones in the development of TMCP of HSLA Nb steels.*

The development of TMCP practices stems from the need for increased strength and toughness of large diameter pipelines, which are installed in artic regions. Tanaka [4], Morrison [5], Gray et al. [34], McQueen [35], and Ouchi [36] provided detailed literature reviews regarding the controlled rolling of high-strength low-alloyed steels. Nowadays, TMCP is governed by the need for a suitable selection of chemical composition combined with a meticulous thermal-deformation path, as well as the delicate balance of the metallurgical requirements, targeted material' properties, and capacity constraints of the production plant.

II.1.1 Requirements to the HSLA pipeline steels

Transmission pipelines usually have large diameters and operate at high pressures in order to achieve high transportation rates. Energy distribution companies typically maintain high operating pressures in gas (oil) transportation systems in order to reduce costs. This translates into a demand for higher strength steels. Figure II.1-1 compares the material weight of different steel grades for a given distance and pipe diameter. The use of higher grades has led to a reduction of wall thickness, which has an impact on the total project cost [37] since lower amounts of steel mean lower material transportation and pipe laying cost.

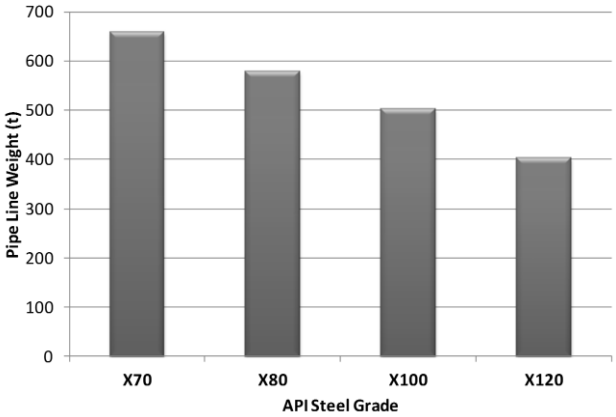

Figure II.1-1 *Pipe weight per 100km and122mm pipe diameter at fixed operating pressure. adapted from [38].*

Pipeline steel grades are typically classified according to the specifications proposed by the American Petroleum Institute (API). This specification denominates grades according to their minimum yield strength. For example grades X52 and X120 have yield strengths of approximately 52ksi or 360Mpa and 120ksi or 830Mpa respectively.

Steels are needed for exploiting artic and deep water hydrocarbon resources. Most research has, therefore, been focused on obtaining high strength and toughness without compromising the integrity and weldability of the pipeline. HSLA steels must satisfy stringent requirements in order to fulfill actual oil and gas pipeline specifications, for either onshore (API Spec 5L Line Pipe, 44th Edition), or offshore (DNV-OS-F101) [39] infrastructures. High operating pressures (i.e. 15MPa) require either thicker walls or higher strength. In addition, extraordinary fracture toughness is required, specially in cold environments. This requirement necessitates an appropriate application of physical metallurgical engineering through the combination of alloying condition and TMCP. The current thesis, does not consider seamless pipes. The pipes of interest should either be longitudinally welded during the conformation (such as UOE process) or spiral welded (spiral welded process). Steels used to make these pipes must, therefore, have good weldability without compromising the base material properties. This is attained through low carbon equivalence (C.E.) and/or low critical metal parameter P_{cm} values (low carbon and limited alloying elements) [40]. Table II.1-3 lists the various carbon equivalents formulae adopted by different institutions. CE formulae [41] were originally developed to calculate the C content which would contribute to hardenability. They were later, extended to determine the contribution

of the chemical composition to the hydrogen cracking susceptibility of steels. Many works have been published on the topic in order to establish safe welding criteria. For example *Yurioka and Suzuki* [42] discussed the effects of chemical composition on the factors which influence hydrogen cracking in steels.

Organization/Author	*Carbon equivalents (wt%)*	*Ref.*
International Institute for welding (IIW)	$CE_{IIW} = C + \frac{Mn}{6} + \frac{(Cu+Ni)}{15} + \frac{(Cr+Mo+V)}{5}$	[41]
Duren	$CE_q = C + \frac{Si}{30} + \frac{Mn+Cu}{16} + \frac{Ni}{40} + \frac{Cr}{10} + \frac{Mo}{15} + \frac{V}{10}$	[43]
Japanese Welding Engineering Society	$Pcm = C + \frac{Si}{30} + \frac{Mn}{20} + \frac{Cu}{20} + \frac{Ni}{60} + \frac{Cr}{20} + \frac{Mo}{15} + \frac{V}{10} + 5B$	[44]
Yurioka	$CEN = C + A(C) + \left(\frac{Si}{24} + \frac{Mn}{6} + \frac{Cu}{15} + \frac{Ni}{60} + \frac{Cr+Mo+Nb+V}{5} + 5B\right)$ where $A(C) = 0.75 + 0.25tanh\{20\,(C - 1.12)\}$	[45]

Table II.1-3 *Summary of the carbon equivalence formulae adopted by different institutions*

Specification	*C%*	*Nb%*	*Nb+V+Ti*
API PSL2/ISO 3183/GB/T 9711	0.12	-	≤0.15
API PSL2 Annex G (pipe resistant to ductile fracture)	0.10	-	≤0.15
API PSL2 Annex H (pipe for sour service)	0.10	0.08	≤0.15
API PSL2 Annex J (pipe for offshore service)	0.12	0.08	≤0.15
DNV-OS-F101 (pipe for offshore service)	0.12	0.08	≤0.15
CSA Z 245	0.26	0.11	-
CNPC	0.09	0.11	≤0.15

Table II.1-4 *C and Nb restrictions for TMCP X70 steel grade. Adapted from [46]*

Figure II.1-2 and Table II.1-4 show the historical changes in the requirements for pipeline steels, and the current C-Nb restrictions (different specifications) for TMCP welded X70 pipes, respectively. CE decreases with the development of new steel grades Figure II.1-2. The absorbed energy from the Charpy impact test (traditionally used as a standard to evaluate the resistance to unstable ductile fracture), on the other hand, increases with the years and the steel grades. The shear appearance transition temperature or fracture propagation transition temperature (FATT) obtained from the Battelle Drop-Weight tear test (BDWTT) also decreases as well over the years [36].

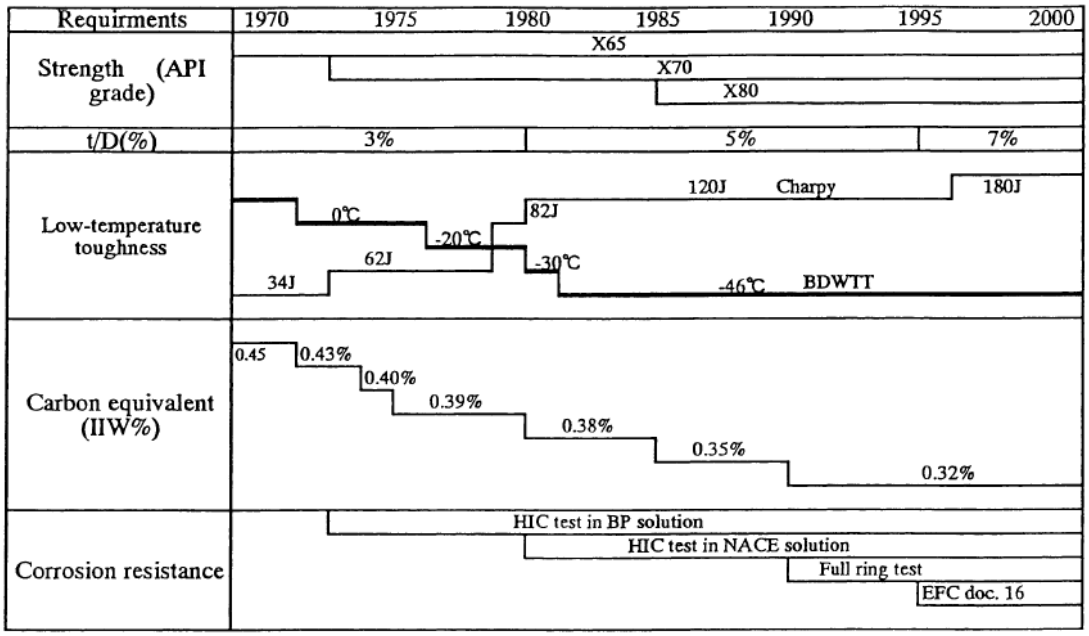

Figure II.1-2 *Historical changes in the properties of pipeline steel [36].*

Furthermore, hydrocarbon pipelines regularly transport sour gas H_2S, and consequently, must be constructed from steels which resist both stress corrosion and hydrogen induced cracking. Low yield to tensile strength Y/T ratios combined with high uniform elongation are also required. Lately, stress-based designs have been complemented by strain-based design methods [46-48], particularly for projects located in regions with high probability for landslides or earthquakes. The main philosophy of strain-based design is that the pipeline strain is allowed to exceed the specified yield strain, provided that the uniform plastic deformation does not affect the safety. Additionally, control of the ductile fracture propagation is one of the major concerns which

pipeline industry is facing. Particularly with the increasing demand of new control rolled steel grades (X100, X120) required to maintain integrity at high operational pressures.

Cold deformations may also adversely affect the plate properties during pipe forming (i.e. U.O.E. process). The measured yield strength of steel plate differs from that measured in the pipe [49-51]. This difference is attributed to the different strain history of the material, and is known as the Bauschinger effect [49, 50, 52]. The Bauschinger effect refers to the phenomenon in which resistance to plastic deformation is lowered when a material already deformed in one direction is strained in the opposite sense. The phenomenon, at the microstructural level, is related to dislocation pile up in the vicinity of obstacles and the un-relaxed internal stresses developed in the particle-matrix interface during cold working [52]. Flattening of the specimen for tensile testing introduces additional deformation, and it has been shown [50] that sample type: ((i) flattened full-section; (ii) round bar and (iii) ring and sampling place (full thickness or sub-size specimen) have an influence on yield stress measurements.

The oil/gas distributor must find a suitable compromise among economic considerations, safety and technological constraints. At the end, the transportation system must deliver the oil/gas at an attractive price, which satisfies international standards, and with low risk to the environment and population.

II.1.2 Microstructure – properties control in HSLA pipeline steels

Nowadays there are numerous possible process routes by which HSLA pipeline steels can be manufactured. Each steel producer (and even each production plant within a steel group) has its own schedule, which correspond, in essence, to different interpretations of a common philosophy. The thermo-mechanical control processing (TMCP), which can be divided into several technological steps:

- A suitable chemical composition is selected (alloying combined with processing leads to optimum cost-properties ratios).
- A proper slab reheating temperature is determined (chemical composition influences the determination of reheating temperature owing to the solutionizing temperature of the

alloying elements). The reheating temperature controls the growth of austenite (γ) grains

- Austenite grains are refined by way of γ recrystallization after each deformation pass of rough rolling (first stages of rolling). Roughing passes are typically done at temperatures above the so called "austenite non-recrystallization temperature" (Tnr) where γ statically recrystallizes after each deformation pass. Detailed studies on Tnr and how it can be determined, can be found elsewhere [53].
- Finish rolling in the non-recrystallization region is then used to obtain the final geometry of the strip (or plate). This rolling can be completely executed in the austenite region, or in some cases in the inter-critical γ-α region.
- Controlled cooling is subsequently applied to the material. Accelerated water cooling condition (ACC) is the generic term used to describe rapid cooling of the material, ACC will be discussed in more detail in section II.3.
- The last processing step entails coiling of the strips or leaving the plates on stock for final air cooling.

Pipeline steels are produced either in the form of plate or sheet. Plates and sheets are distinguished by the final thickness of the product. According to Dieter [54], plates generally have thicknesses greater than 6mm, whereas sheet and strip are thinner than 6mm. However in pipeline steel production, the above thickness limits are not rigid and the terms "sheet" and plate are used for coiled and non-coiled final products, respectively. Nowadays, coilers are so powerful that they can coil flat products with thicknesses of up to 25 or even 30 mm and so plates and sheets are distinguished by coiling, or the absence thereof, in the final processing stage. The final plates typically have dimensions (length × width) of 18 to 24m × 4 to 6m. Examples of a typical plate and coil rolling mill and ancillary equipment are shown in Figure II.1-3 and Figure II.1-4 respectively.

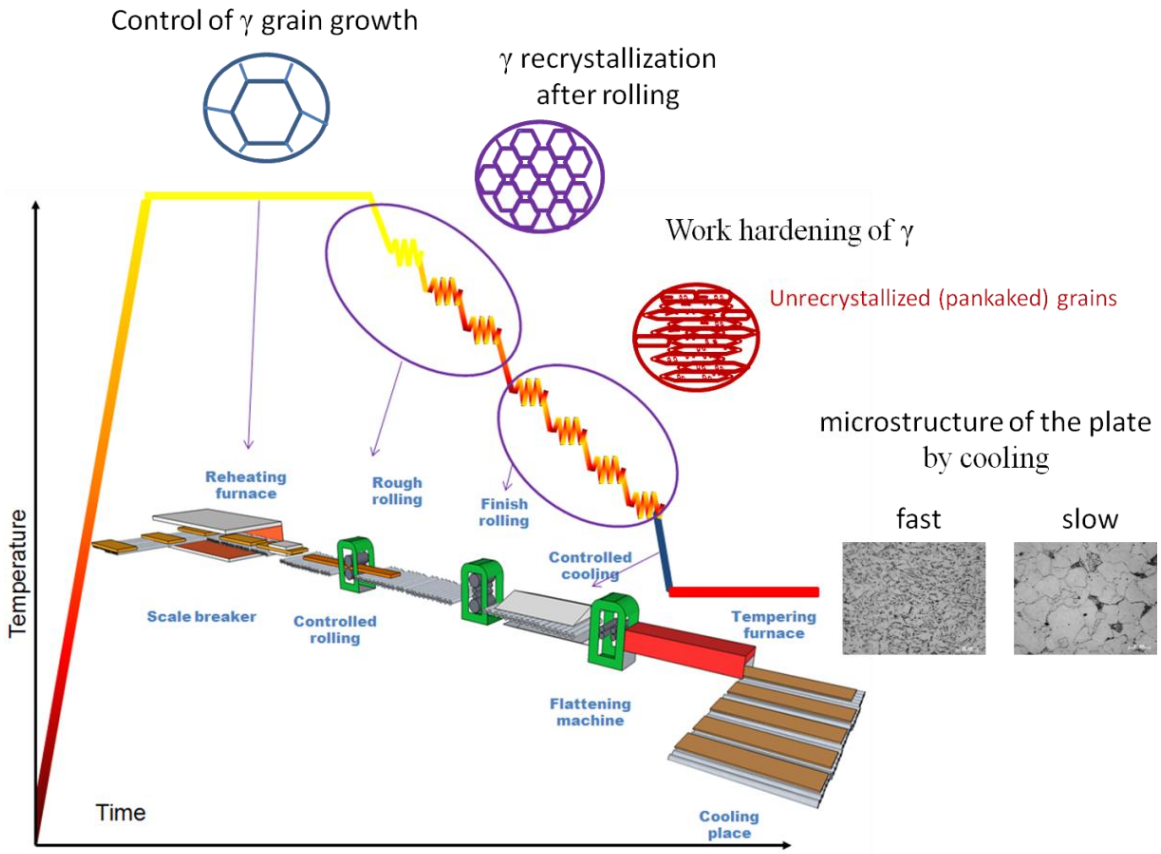

Figure II.1-3 *Schematic description of the rolling line, rolling schedule and corresponding microstructural evolution during TMCP of HSLA pipeline steel plates.*

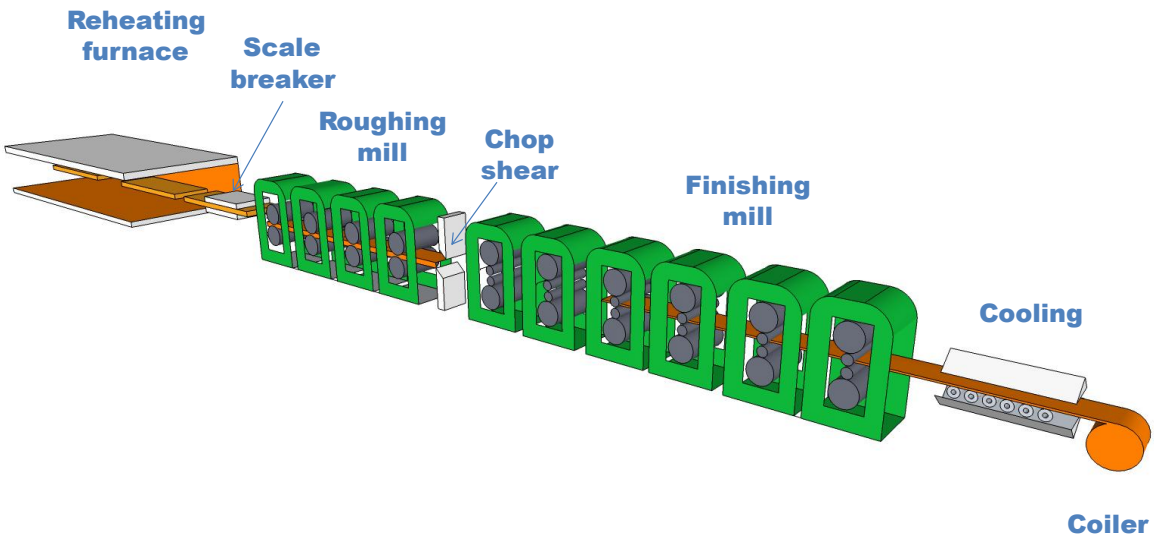

Figure II.1-4: *Schematic view of the rolling line for TMCP of coils.*

Slab reheating. The first stage in TMCP after casting is slab reheating. Pusher type furnaces or walking beam furnaces are the two technologies most widely used for this processing stage. The slabs can be transferred into the reheat furnace in three different ways: direct charging (straight from the caster), hot charging or cold charging. The primary function of the soaking furnace is to provide enough plasticity to the metal before hot rolling. However, the correct reheating temperature must be chosen in order to control the dissolution of the micro-alloying elements (Ti, Nb, V, Mo). Micro-alloying elements are needed for the suppression of austenite recrystallization below Tnr, precipitation hardening of the α phase... The reheating temperature and soaking time must be low enough to prevent the abnormal growth of austenite grains. In addition, pipeline steels are alloyed with Ti and the corresponding TiN particles controls γ grain growth. Although complete micro-alloying dissolution is only achieved at temperatures well above 1300°C (cf. Figure II.1-5), industrial reheating furnaces operate in the range 1150-1250°C where TiN remain undissolved. The temperature required for dissolution of Nb carbonitrides in austenite depends on the actual combination of alloying elements [55]. A variety of reheating approaches has been investigated in [56] where the slab reheating temperature was varied in order to prevent austenite grain growth.

Rough rolling. Once the slab leaves the reheating furnace it passes through a set of scale breakers where the oxide layer formed during reheating is removed by the combination of high pressure water and light rolling loads. After descaling, the slabs are directly introduced into the rolling mill. The cast microstructure is destroyed by rolling and replaced by a recrystallized austenite microstructure, since the deformation passes are done above the previously defined Tnr. Appropriate rolling schedules are important during the first passes in order to avoid early precipitation of Nb. Nb precipitates can also pin some austenite grain boundaries and partially retard recrystallization which, in turn, gives rise to a heterogeneous microstructure [55].

Industrial mills typically impart 20-35% reduction per pass for a total accumulated reduction of 60% in the rough rolling stage of processing. [57].

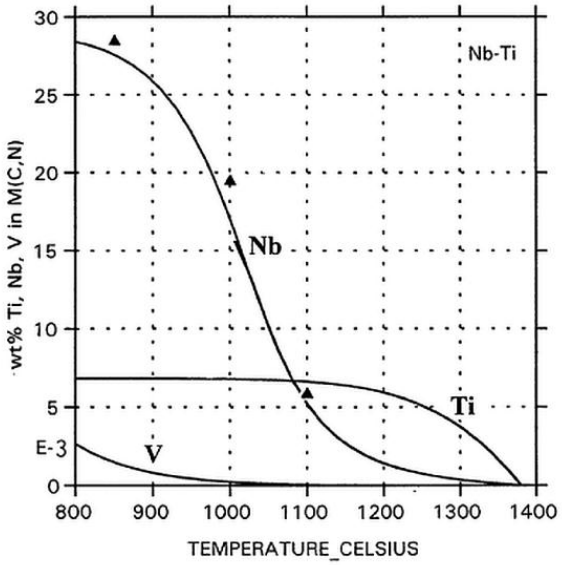

Figure II.1-5 *Calculated curves for precipitation of TiN, Nb(C,N), and V(C,N) and experimental data for Nb(C,N) in a 0.013wt% Nb, 0.007wt% Ti-steel (black triangles) [55].*

Transfer table. After rough rolling the steel plates are transferred to the finishing rolling mills. The temperature of the plate decreases during the transfer. Grain growth may occur if the delay time is too long giving rise to a mixed austenite microstructure [4, 30]. Alternatively, a continuous rolling schedule without specific delay between roughing and finishing can be applied.

Finish rolling. Before the steel enters the finishing rolling mill set, a secondary scale breaker is used to remove the oxide layer formed during the transfer. During finishing a series of usually 5 to 7 stands are used to decrease the thickness of the material in the case of strip layout (see Figure II.1-4). A reversible rolling mill is used in the case of plate rolling (see Figure II.1-3). Finish rolling passes are generally executed with decreasing reduction per pass in order to reduce the rolling loads since steels become harder at low temperatures. Rolling forces can be predicted only if the resistance of the material to deformation is sufficiently understood. Dislocation populations and their interaction with the precipitates formed at each step of TMCP, influence the resistance of the material to deformation. However, the finally formed microstructure depends crucially on the control of the temperature, reductions per pass and inter-pass times. The aforementioned parameters influence the occurrence of hardening, recovery and recrystallization processes, which determine, in general the dislocation density of the material. Moreover, parameters such as

the plate/strip velocity or strain rate of each stand are somewhat interconnected owing to the sequential character of rolling.

The pre-transformation state of the austenite must be taken into account if the finishing rolling of HSLA pipeline steels is done below Tnr. For example, heavily deformed austenite typically develops a homogeneous pancaked microstructure. The type of microstructure developed can influence the numbers of potential ferrite nucleation sites. The term austenite conditioning is used to describe the deformation generated defects such as high angle grain boundaries, in-grain shear bands, sub-grains and, dislocation clusters which provide large numbers of these potential ferrite nucleation sites. Fine-grained ferrite microstructures are formed upon cooling of the austenite-conditioned materials. The final rolling pas is done at the "finish rolling temperature" (or FRT). FRT is, maintained above the Ar_3, in most cases, despite the fact that the yield strength can be increased by final rolling in the inter-critical temperature range (between Ar_3 and Ar_1). Consistency of through-thickness properties such as the impact toughness, is, however, not guaranteed when rolling is done in this temperature range [58].

Cooling. Controlled cooling after rolling determines the final γ transformation product, and therefore plays an important role in the formation of final steel properties. Run-out tables and coilers were originally designed to reduce the length of the production line. However, metallurgical functionality has become essential in modern TMCP. Since the choice of one cooling process (characterized by the cooling rate) over another will determine the management (to make them active) of potential α nucleation sites [1]. The vast array of cooling and subsequent coiling practices leads to a wide range of final microstructures. These microstructures range from air-cooled polygonal ferrite-pearlite to ACC and coiled bainite/ acicular ferrite, with an amalgam of mixed microstructures (i.e. quasi-polygonal ferrite, degenerate pearlite, granular bainite…) lying in between see section II.3.3 for further details.

At least five types of cooling schedules are employed in industrial plate and strip pipeline steels TMCP cycles [59, 60]: air cooling, continuous accelerated cooling, early interrupted accelerated cooling, late interrupted accelerated cooling and combinations of at least any two of the aforementioned. Accelerated cooling techniques have been reviewed in [60], and *Figure II.1-6* summarizes the history of development of corresponding equipment. Techniques such as laminar cooling, pressured cooling and water curtains, cool the steel from above and below using water

nozzles which are located within independent, flow-controlled zones along the travelling direction of the material. Special measures are taken to maintain the flatness of the strips during high rate cooling. These measures include capturing the head end of and applying front tension to the strip. The key issue in cooling technologies is the attainment of a homogeneous distribution of properties not only through the thickness but also along the coil or plate. This is important since inaccuracies in cooling can lead to variations in mechanical properties such as those presented in Figure II.1-7.

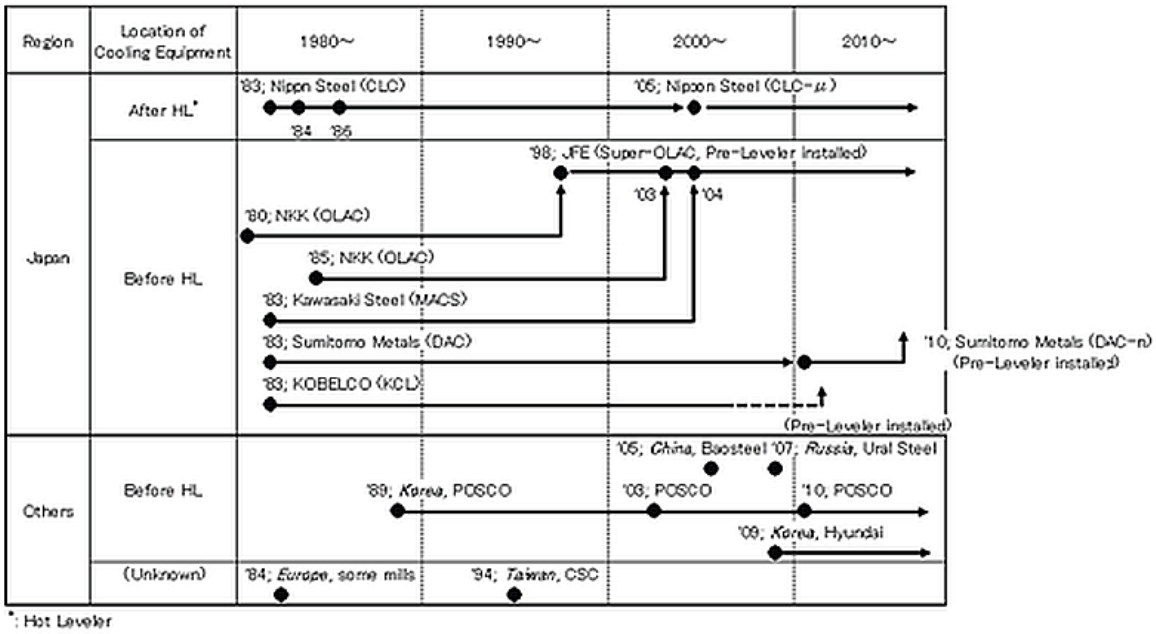

Figure II.1-6 *Evolution of cooling technologies during the last three decades in Japan [60]*

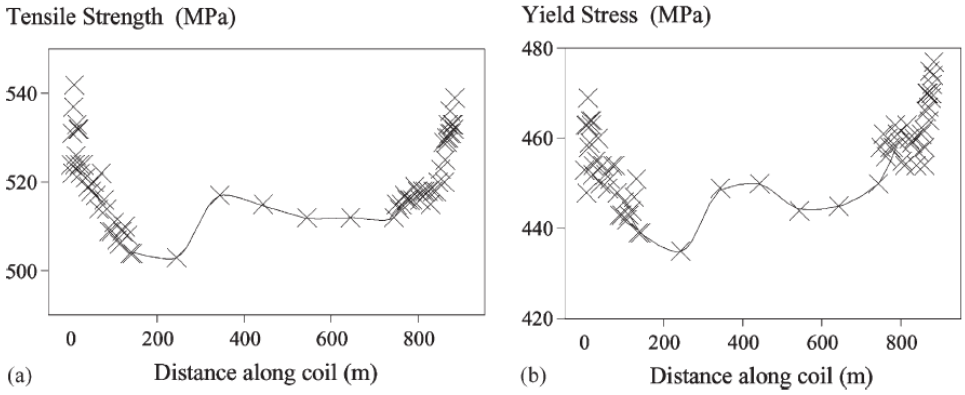

Figure II.1-7 *Tensile strength distribution along the coil length; (b) Yield stress distribution along the coil length in a 0.06wt% C, 0.047wt% Nb commercially hot-rolled steel; finish temperature of 865ºC; coiled at 650 ºC [61].*

II.2 Deformation of austenite

II.2.1 Recrystallization region

Deformation above the austenite recrystallization temperature is classically referred to as recrystallization controlled rolling RCR (see Figure II.2-5). RCR is done in order to obtain refined and equiaxed austenite grain microstructures. This refinement is achieved through the metallurgical changes which the steel undergo during RCR. These changes occur if the dislocation density increases to a certain value during rolling at high temperatures. The changes which occur depend on deformation conditions such as the temperature, strain, and strain rate. The austenite may work harden, dynamically recover and dynamically recrystallize during the deformation itself, or simply work harden during rolling, and recrystallize statically after some incubation period. In order to understand the γ microstructure after rolling, strain (ε) strain rate ($\dot{\varepsilon}$) , initial grain size, flow stress, and the Zener-Hollomon parameter (Z), must be considered. Z is temperature and strain-rate dependent and is defined as:

$$Z = \dot{\varepsilon}\ \exp(Q/RT) \qquad \textbf{\textit{II.2-1}}$$

Where $\dot{\varepsilon}$ is the strain rate, Q the activation energy for plastic deformation, R is the universal gas constant and T the temperature.

Hardening-softening behavior, associated with recovery and recrystallization can be divided into different regimes [62, 63] when plotted as a function of the applied strain (Figure II.2-1). Several papers have also described the kinetics of austenite softening and recrystallization in each region [63, 64]. If the material is processed with a strain that lies within hardening stage region I (Figure II.2-1), then the thermodynamically unstable γ is subsequently softened during inter-pass by means of static recrystallization. If the strain is too low then only recovery takes place. Dynamic recrystallization starts at a strain of about $0.7\varepsilon_p$ [1] (region II in Figure II.2-1). At this stage, meta-dynamic and dynamic recrystallization mechanisms operate simultaneously. Factors such as the initial γ grain size influence the occurrence of dynamic recrystallization [65]. After dynamic recrystallization, additional meta-dynamic recrystallization and grain growth may occur in region III for strains exceeding ε_s Figure II.2-1).

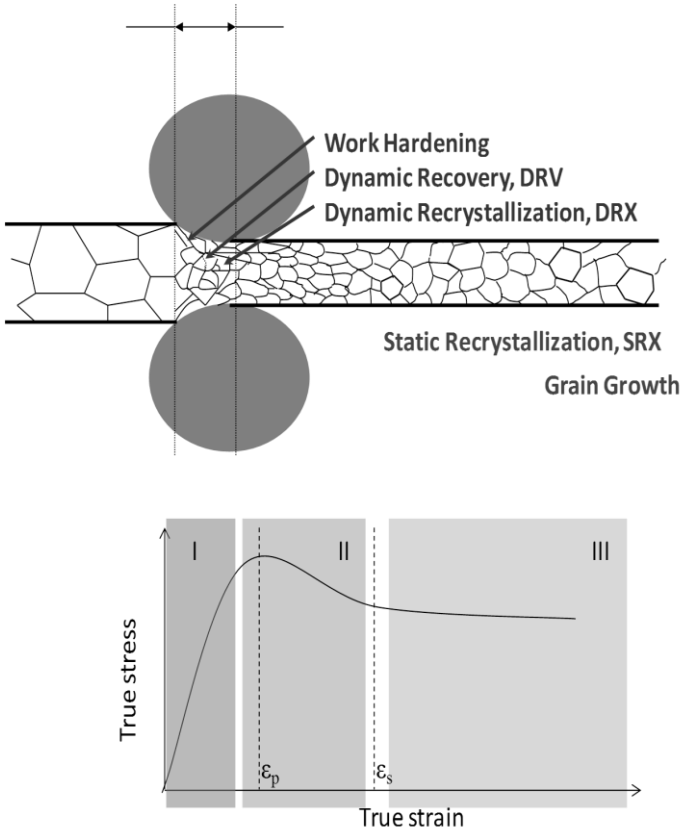

Figure II.2-1 *Evolution of γ microstructure during hot rolling (above); and schematic flow curve regions during rolling of γ (below).*

Static recrystallization is the dominant softening process which occurs during rough rolling of HSLA steels with large inter-pass times. Addition of small quantities of metallic alloying elements, such as Nb for solute hardening, increases ε_p and σ_p and therefore delays nucleation of DRX [66]. The grain size decreases gradually after successive reductions in the static recrystallization region. In such cases, the fraction of softening after each pass and the time required for recrystallization, can be described by a series of equations proposed by *Roberts et al.*[67], *Sellars* [62], *Choquet et al.*[68], *Hodgson* [69], *Laasraoui & Jonas* [70] and *Uranga et al*. [64]. In those studies the kinetics of static recrystallization was generally based on the *Johnson-Mehl-Avrami-Kolmogorov* equation (II.2-2), where the recrystallized volume fraction X is expressed as function of holding time after deformation; that is:

$$X = 1 - exp\left[A\left(\frac{t}{t_x}\right)^k\right] \qquad \textbf{II.2-2}$$

Where t is the holding time, t_x is the time for a given volume fraction X to recrystallize and k is the Avrami exponent.

Several empirical equations have been published for describing the time necessary for 50% recrystallization $t_{0.5x}$. II.2-3 is one such example.

$$t_{0.5x} = B\varepsilon^p D^q Z^r \dot{\varepsilon}^s exp\left(\frac{Q_{Rx}}{RT}\right) \qquad \textbf{II.2-3}$$

Where ε is the strain, D is the grain size prior to deformation, Z is the Zener-Hollomon parameter, $\dot{\varepsilon}$ is the strain rate, Q_{RX} is the apparent activation energy for recrystallization, R is the gas constant, and T the absolute temperature.

Softening behavior is therefore influenced by several variables including the composition, temperature, inter-pass time, or initial grain size. Figure II.2-2 [1] plots the softening as a function of inter-pass times for two material compositions with similar initial γ grain size. As expected, softening is enhanced with increasing inter-pass time and temperature. The change in slope of the lines is related to the transition from recovery to recrystallization.

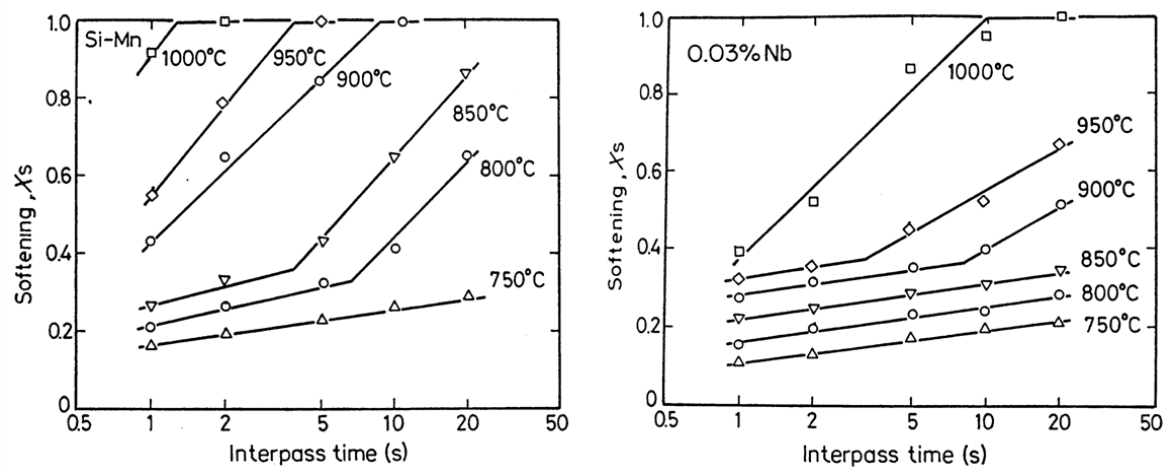

Figure II.2-2 *(a) Effect of inter-pass time and deformation temperature on the softening ratio for a Si-Mn steel, (pre-strain 0.2); (b) Effect of the interpass time and deformation temperature on the softening ratio for a 0.03wt% Nb steel, (pre-strain 0.2) [1].*

Industrial TMCP, however, yields non-equilibrium microstructures, which are more difficult to model than those obtained under isothermal conditions. Furthermore, alloying elements, especially those with very different atomic sizes from iron, have an influence on the hot strength

of austenite since they obstruct the motion of dislocations [1]. Several equations (i.e *Siciliano et al* [63]) are available in the literature for calculation of the hot strength of austenite.

II.2.2 Non- recrystallization region

Austenite grain refinement in the recrystallization region saturates when α nucleate only at boundaries of unstrained γ grain [71]. Further refinement is, therefore, achieved by promoting α nucleation in the interior of γ grains. Deformation in the non-recrystallization region (see Figure II.2-5) results in pancaked austenite grains which have internal deformation bands. These deformation bands are somewhat equivalent to γ grain boundaries, phenomena known as grain fragmentation. Grain boundary and deformation band areas comprise the total interfacial area $S_{v,}$ and nucleation in these regions leads to refinement of the α grain sizes (see section I.3). Retardation of recrystallization is, on the other hand, controlled by the temperature and the alloying elements, (especially Nb) present in the material [72].

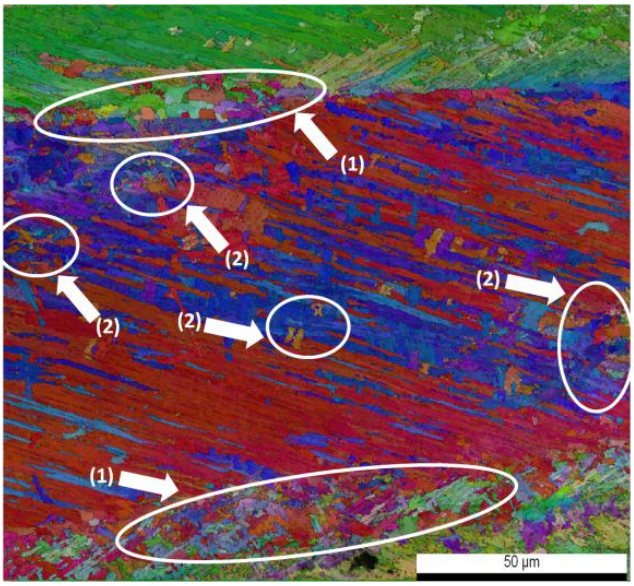

Figure II.2-3 *Inverse pole figure map showing the α nucleation of grains on the γ pancaked grain boundary (1), and on the γ deformation bands (2).*

α nucleates at both the boundaries of the pancaked γ grains (1) and the intra-granular deformation bands (2) (Figure II.2-3). Deformation bands divide the γ grains into zones with different crystal orientations, known as grain fragmentation, and thereby increase the number of

potential α nucleation sites compared to conventional hot rolling. This mechanism was confirmed by experimental observation (Figure II.2-3) and is schematically depicted in Figure II.2-4.

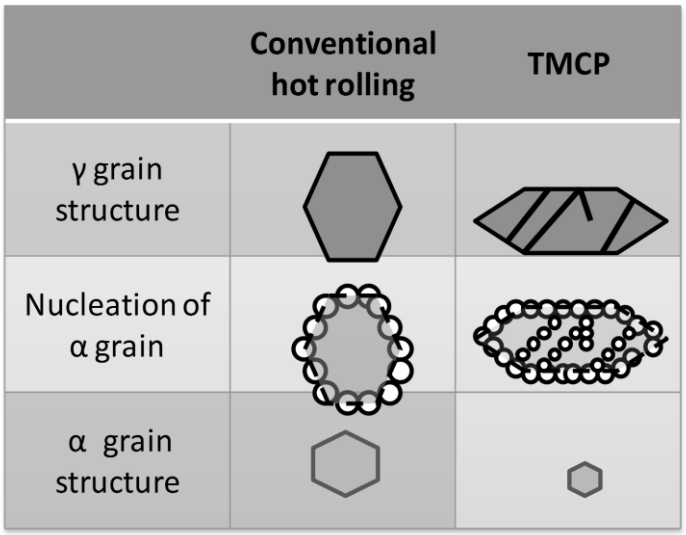

Figure II.2-4 *Differences between α nucleation sites when for conventional rolling and TMCP; adapted from [1].*

II.2.3 Two phase austenite-ferrite region.

Deformation in the two phase region (known as inter-critical rolling) produces microstructures which consist of deformed polygonal α grains and transformed α grains. The deformed α grains are comprised of sub-grains and cells, and undergo only recovery owing to the strain-induced precipitation of Nb (C N) which occurs therein [4] (see Figure II.2-5). This type of microstructure leads to different mechanical properties compared to those resulting from γ in the non-recrystallization region. These gains are, however, contrasted by through-thickness heterogeneity of properties (such as the toughness), and increased delamination or anisotropy owing to the development of certain texture components [4, 73]. The aforementioned problems may be attributed to a bimodal size distribution of recrystallized or recovered ferrite and the transformed product resulting in the development of unfavorable textures [74, 75].

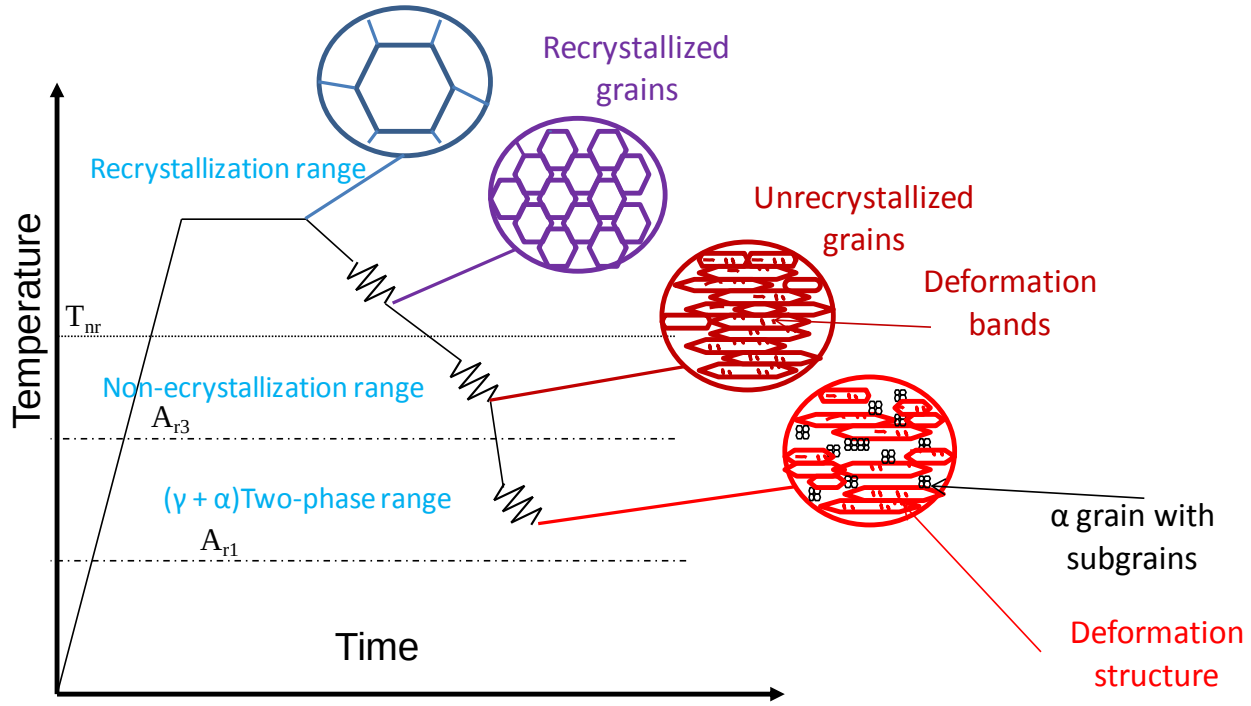

Figure II.2-5 *Schematic illustration of four stages of TMCP and the corresponding change in microstructure with deformation in each stage; adapted from [4].*

II.3 Austenite transformation

The cooling rates which are typically used in the processing of HSLA pipeline steels are high enough to suppress the formation of equilibrium microstructures (ferrite and pearlite) and to promote various non-equilibrium structures (degenerated pearlite, different types of bainite, martensite and/or martensitic-austenite conglomerates). More details about the mechanism of formation of these structures can be found elsewhere [76]. The cooling rate, austenite grain boundary area/unit of volume, and the presence of additional ferrite nucleation sites (for example deformation bands in pancaked austenite) constitute the set of parameters which control the austenite-ferrite transformation [77, 78] in Nb-containing HSLA steels. Some elements retard, while others promote, the decomposition of austenite. Ni, Mn, Cu, C and N stabilize and retard the decomposition of austenite by lowering Ar_3. In contrast, elements such as Si, Al, P, V, Mo, Ti, and Nb increase the Ar_3 temperature. The deformation imparted and the corresponding temperature during finish rolling (see Figure II.2 5), affect the phase transformation mainly by means of changing the nucleation sites and (nucleation) rate.

II.3.1 Transformation from recrystallized austenite

Ferrite nucleates on the grain boundaries of recrystallized austenite if the rolling is done completely within the recrystallized austenite region. Ferrite nucleation is governed by the effective surface boundary area/unit of volume in austenite, S_{eff}. For the case of recrystallized grains, S_{eff} is expressed as the sum of the area of grain boundaries $S_{g.b.}$. $S_{g.b}$ can be determined in various ways, for example, from equation (1) [79], where N_L is the number of intersections per length with a random line. $S_{g.b}$ may also by expressed as a function of the austenite grain diameter D_γ, as shown in equation II.3-2 [1].

$$S_{g.b.} = 2N_L \qquad \textbf{II.3-1}$$

$$S_{g.b.} = \frac{4}{\left(\sqrt{\pi\, D_\gamma}\right)} \qquad \textbf{II.3-2}$$

In other equations (i.e. equation II.3-3)[1], the ferrite grain size D_α is given as a function of $S_{g.b}$ for isothermal and continuous cooling transformations conditions.

$$D_\alpha = \left(\frac{2}{3n_s S_{g.b.}}\right)^{\frac{1}{3}} \qquad \textbf{II.3-3}$$

Where n_s is the number of grains nucleated per unit of area. Nucleation rate determination

after deformation is further discussed in [80]. In his overview of processing of HSLA plate and strip steels, *Panigrahi* [81] expressed the grain size of transformed ferrite, D_α as:

$$D_\alpha = 3.75 + 0.18D_\gamma + 1.4C_R^{-0.5} \qquad \textbf{II.3-4}$$

where C_R is the average cooling rate between 750-550°C in °C/s, and D_γ is the austenite grain size prior to transformation. Other equations for the ferrite grain size have been suggested in the literature, some of which are listed in Table II.3-1. Here, the ferrite grain size, $D_{\alpha,}$ is expressed as a function of the accumulated strain ε_r and the previously defined variables, $D_{,}$ D_γ and C_R.

Steel	*Equation*	*Reference*
C-Mn	$D_\alpha = (1 - 0.45{\varepsilon_r}^{0.5})\{1.4 + 5C_r^{-0.5} + 22[1 - \exp(-1.5 \cdot 10^{-2}D]\}$	[82]
Nb	$D_\alpha = (1 - 0.45{\varepsilon_r}^{0.5})\{2.5 + 3C_r^{-0.5} + 20[1 - \exp(-1.5 \cdot 10^{-2}D]\}$	[82]
V-Ti	$D_\alpha = (1 - 0.45{\varepsilon_r}^{0.5})\{3 + 1.4C_r^{-0.5} + 17[1 - \exp(-1.5 \cdot 10^{-2}D]\}$	[82]
V-Ti	$D_\alpha = 3.75 + 0.18D + 1.4C_r^{-0.5}$	[67]
C-Mn/ C_{eq}>0.35	$D_\alpha = (1 - 0.45{\varepsilon_r}^{0.5})d_{\alpha 0}$ $d_{\alpha 0} = (\beta_0 + \beta_1 C_{eq}) + \left((\beta_2 + \beta_3 C_{eq})\dot{C_r}^{-0.5} + \beta_4(1 - \exp(\beta_5)D\right.$ $\beta_0 = -0.4, \beta_1 = 6.37, \beta_2 = 24.2, \beta_3 = -59, \beta_4 = 22, \beta_5 = 0.015,$	[83]
C-Mn/ C_{eq}>0.35	$D_\alpha = (1 - 0.45{\varepsilon_r}^{0.5})d_{\alpha 0}$ $d_{\alpha 0} = (\beta_0 + \beta_1 C_{eq}) + \left((\beta_2 + \beta_3 C_{eq})\dot{C_r}^{-0.5} + \beta_4(1 - \exp(\beta_5)D\right.$ $\beta_0 = 22.6, \beta_1 = -57, \beta_2 = 3, \beta_3 = 0, \beta_4 = 22, \beta_5 = 0.015,$	[83]

Table II.3-1 *Equations describing the ferrite grain size transformed from recrystallized austenite.*

II.3.2 Transformation from non-recrystallized austenite

The increase of ferrite nucleation sites by deformation of austenite is due to: (I) the increase of the $S_{g.b}$, (II) to the formation of extra nucleation sites such as deformation structures. In other words, when deformed austenite transforms to ferrite the deformation bands and the grain boundaries provide nucleation sites for ferrite [80]. *Bae et al* [84] investigated, by way of Gleeble simulations, the effects of different austenite deformation conditions on the total surface of grain boundary ($S_{g.b}$) in HSLA steels. Figure II.3-1 shows that $S_{g.b}$ increases with increasing strain. The total surface area of the deformation bands should also be taken into account when S_{eff} is determined.

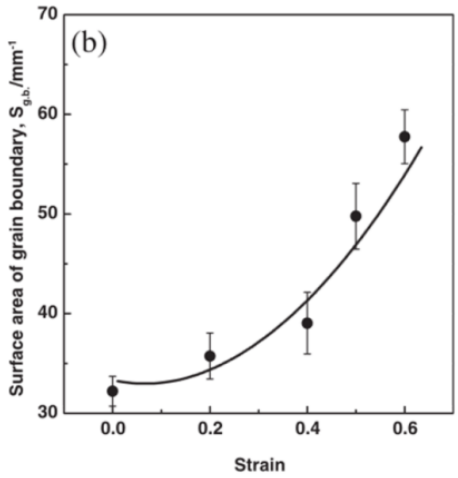

Figure II.3-1 *Variation of surface grain boundary area with strain for unrecrystallized austenite [84].*

Deformation structures, generally referred as deformation bands, consist of regions which have high densities of blocked dislocations located on adjacent slip lines. The motion of these dislocations results in lateral growth of the bands [81] (see Figure II.2-3). Deformations in excess of 20-30% lead to a significant increase in the density of deformation bands [84] in the material (see Figure II.3-2).

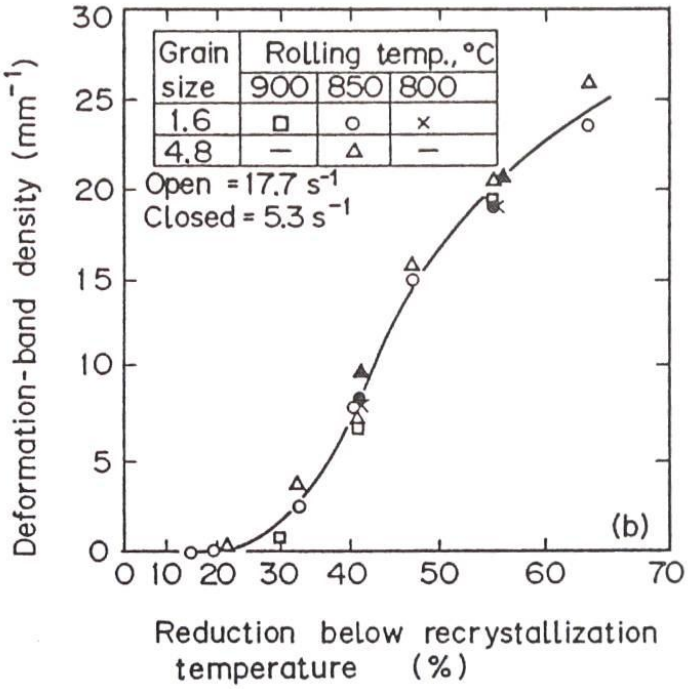

Figure II.3-2 *Effect of reduction below Tnr on deformation band density in a HSLA steel with 0.03Nb wt% [1].*

Figure II.3-3 [1] summarizes the impact of prior-transformation conditions on the final ferrite grain size of HSLA niobium steels. The graph reveals four distinct trends: (1) the ferrite grain size is inversely correlated to the S_{eff} interface area. (2) grain refinement is more effectively achieved by rolling in the austenite non-recrystallization region compared to deformation in the recrystallization region. (3) grain refinement is enhanced when heavy reductions are applied in the non-recrystallization region, compared to lower rolling reductions below T_{nr}. (4) smaller recrystallized grain size (prior to deformation in the non-recrystallization region) results in finer ferrite grain sizes. Further details regarding the estimation of ferrite grain sizes after hot deformation can be found in [1, 67, 82, 83].

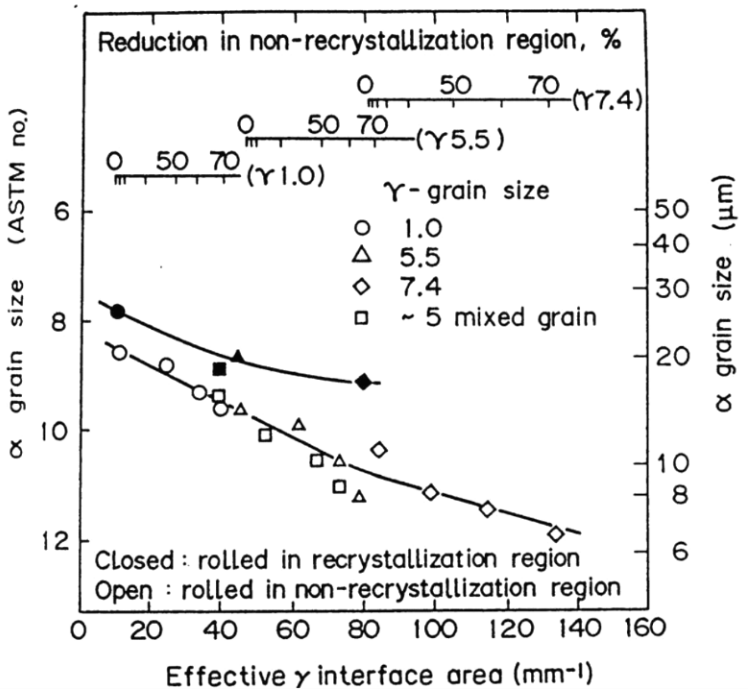

Figure II.3-3 *Influence of S_{eff}, reduction region and recrystallized austenite grain size on the final ferrite grain size. [1].*

II.3.3 Classification of the transformation products

The products of austenite transformation during cooling at different cooling rates can be predicted from a continuous cooling temperature (CCT) diagram. As mentioned in section II.3, ferrite, pearlite, bainite, Widmanstätten ferrite and martensite are the most common products of austenite. The vast number of microstructures resulting from TMCP of modern pipeline steels

exhibit makes metallographic identification of the phases increasingly difficult. In addition, the literature contains a wide variety of terms or nomenclatures which describe the aforementioned microstructures. This variety leads to confusions when different studies are compared. Reviews of ferritic microstructures in the continuously cooled, low carbon steels [85, 86], were done in order to establish a common classification scheme for austenite products, and also to standardize the techniques used to characterize the microstructures. Table II.3-2 lists the nomenclature used in *Microquant* [86] and the *Atlas for bainitic microstructures* [87] of the iron and steel institute of Japan.

Name	Symbol	Description	O.M.	EBSD	T.E.M
Polygonal ferrite	α_{p}	Equiaxed-polyhedral recrystallized shaped grains, crossing over former γ grain boundaries. No sub structure low dislocation density	annexe	annexe	annexe
Quasi polygonal ferrite	α_{qp}	Irregular, varying shape, crossing over former γ grain boundaries mostly recovered	annexe	annexe	annexe
Granular bainitic ferrite	$\alpha_{B(G)}$	Lathless bainitic ferritic structure, partially dislocated-recovered	annexe	annexe	annexe
Bainitic ferrite	α_{B}	Sheaf-like, lath-like dislocated structure preserves prior γ grain boundaries	annexe	annexe	annexe
Widmanstatten ferrite	α_{W}	Lath/plate shape, no internal substructure, nucleates at γ grain boundaries	annexe	annexe	annexe

Acicular ferrite	α_A	Small elongated feathery needles	annexe	annexe	annexe
Lamellar pearlite	P_L	Lamellar growth of ferrite and Fe_3C	annexe	annexe	annexe
Degenerate pearlite	P_D	Incomplete lamellar growth of ferrite and Fe_3C	annexe	annexe	annexe
Upper bainite	B_U	Structure with intra-lath cementite	annexe	annexe	annexe
Lower bainite	B_L	Structure with intra and inter lath cementite	annexe	annexe	annexe
Martensite	α'_M	Lath/plate like highly dislocated structure preserves prior γ grain boundaries	annexe	annexe	annexe
Martensite/ Austenite constituents	M/A	Minor, secondary constituent, highly dislocated, M and A phases coexist in a crystallographic relationship	annexe	annexe	annexe

Table II.3-2 *Description, nomenclature and representative micrographs of the γ transformation products.*

II.4 Texture evolution during hot rolling

HSLA pipeline steels are polycrystalline, have certain crystal properties which differ with the directions of atomic arrangement and are, therefore, anisotropic materials. This anisotropy depends on whether regions with the same atomic arrangement (grains), are randomly oriented, or have some preferred crystallographic orientation. Specific crystallographic orientations are developed during rolling [73, 74, 88-90] based on their relation to the favorable slip or twin systems. In the current study, textures develop both during deformation and recrystallization of austenite. At the end of the TMCP, the final texture is inherited (with specific orientation

relationships) by the austenitic products. Kurdjumov-Sachs (K-S) [91], Nishiyama-Wassermann (N-W) [92], and Bain [93] are the most frequently cited orientation relationships (Ors) for low carbon, low-alloyed steels Figure II.4-1. The crystallographic texture is generally determined by measuring individual pole figures with low index planes. This measured data is then used to calculate the orientation distribution function (ODF) (please see Chapter IV for further details about texture measurements).

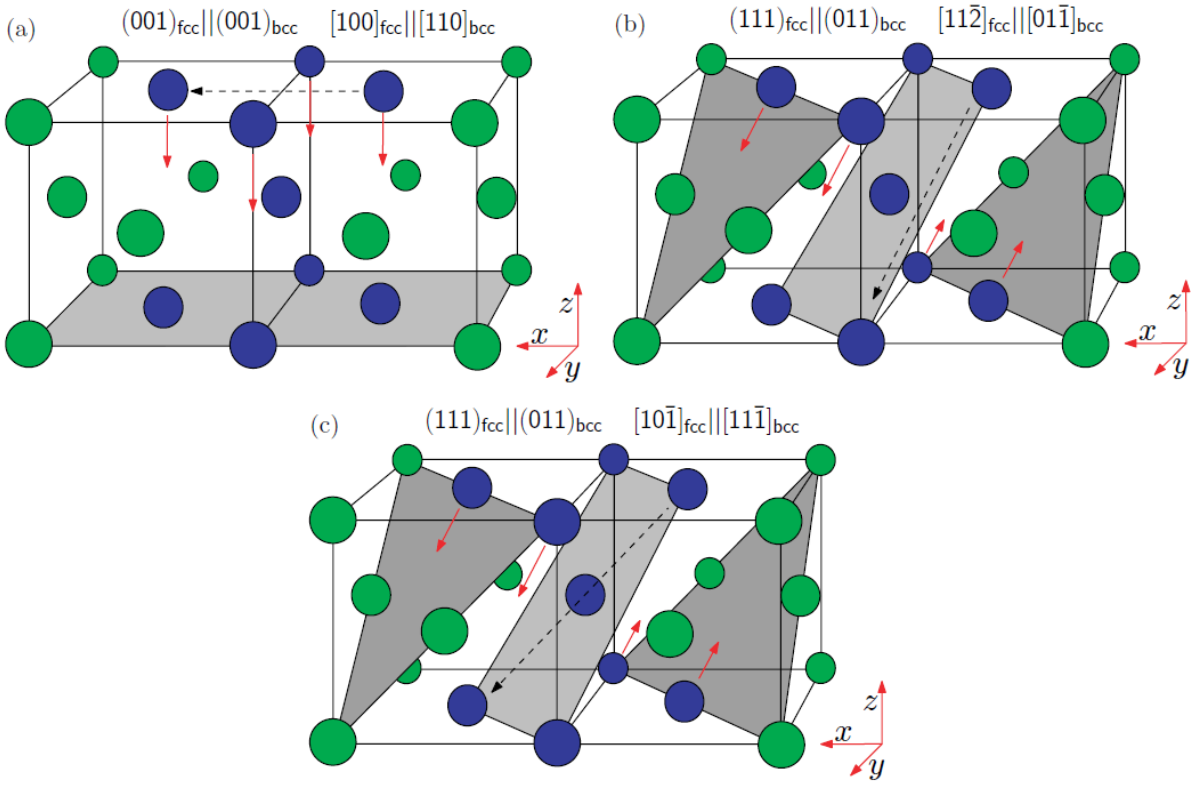

Figure II.4-1 *Orientation relationships between the parent (fcc) and (bcc) phases for the (a) Bain; (b) Nishiyama-Wassermann; and (c) Kurdjumov-Sachs paths. The blue atoms comprise a bcc unit cell. The red arrows indicate part of the motion which initiates the transformation. The dashed arrows indicate the invariant direction which is shared by parent and product phases [94].*

II.4.1 Transformation textures

The φ_2=45° ODF section (Figure II.4-2) contains most of the relevant BCC texture components observed in rolled and recrystallized steels [73, 95].

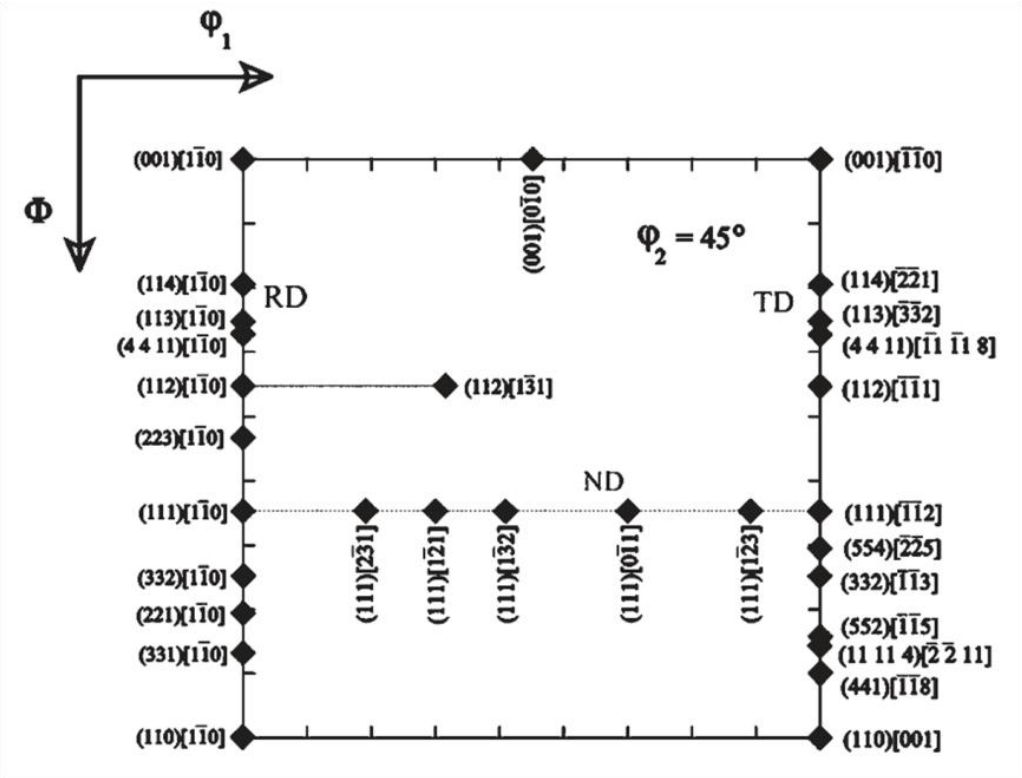

Figure II.4-2 *Plan view of φ_2=45° section showing selected orientations (Bunge notation).*

II.4.1.1 BCC texture products of recrystallized austenite

The texture developed during hot rolling at temperatures above T_{nr} is the {001} <010> cube also known as FCC recrystallization texture (Figure II.4-2) (red component in Figure II.4-3). *Vandermeer and Jensen* [96] attributed the dominance of the cube orientation after recrystallization to faster nucleation and growth of said grains compared to other orientations. The transformation texture products predicted to appear by K-S or N-W after austenite recrystallization, cooling, and phase transformation are highlighted in green (red outline) in Figure II.4-3 [95].

II.4.1.2 BCC texture products of unrecrystallized (deformed) austenite

As described by Jonas, Petrov and Kestens in [97] "when austenite is rolled below T_{nr} the dominant texture components are copper Cu {112}<111>, brass Br {110}<112>, S {123}<634>, and Goss {110}<001>. The effect of phase transformation on these components is depicted in Figure II.4-4 [95].

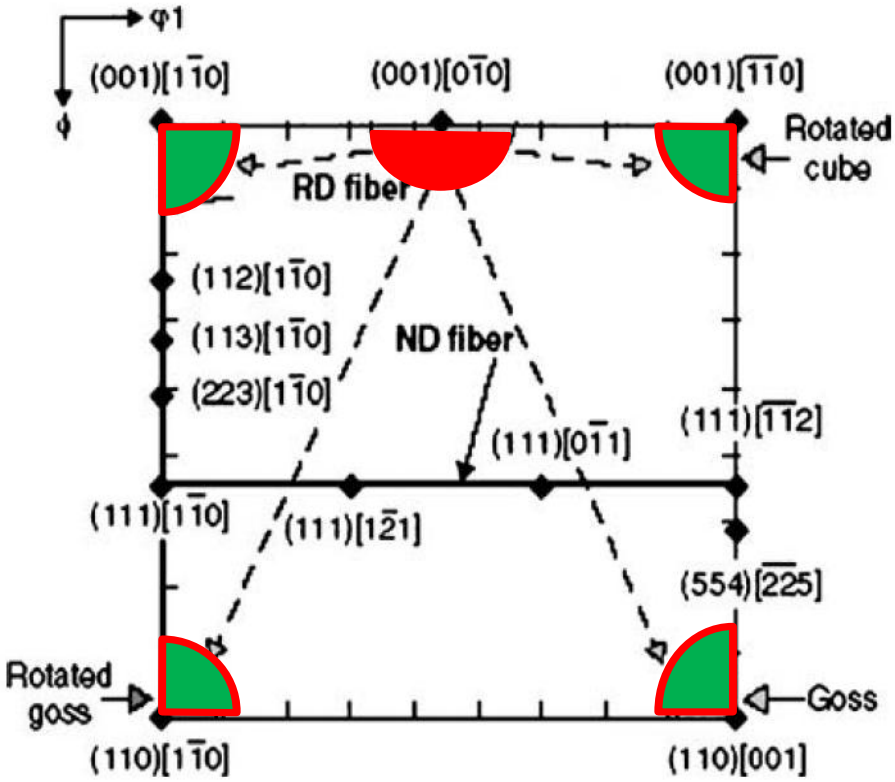

Figure II.4-3 *φ_2=45° section of Euler space showing the BCC texture components(rotated cube, Goss and rotated Goss) inherited from the FCC cube component. [95].*

Four trends can be described, namely: *(i)* The copper component transforms primarily into the {112}<110>, also known as the "transformed Cu", with a much smaller fraction appearing in the vicinity of the rotated Goss {110}<011>. The remaining K-S transformation products of Cu do not appear in the φ_2 = 45° cross-section. *(ii)* The S component transforms partially into orientations near the {112}<131>. The rest of the S transformation products are dispersed elsewhere in the 3-D Euler space and are not included in the present discussion. *(iii)* The Goss component (a minority component during rolling) transforms partly into the rotated Cu, contributing to the intensity of this component, and {111}<110> components, with the balance located outside the φ_2 = 45° cross-section. *(iv)* Finally, the brass or Br texture component transforms primarily into the "transformed Br" located in the vicinity of {111}<112> and {554}<225>, with minor amounts rotating to {112}<131> and {100}<011>.

The {100}<011> rotated cube component is detrimental to the fracture toughness anisotropy but almost always present in the textures of the pipeline steels. This component occurs with

intensities which, in general, depend on the completeness of the austenite recrystallization. The rotated cube, however, is the most intense (i.e. has the highest volume fraction) of all the texture components after the recrystallized material undergoes transformation. Conversely, when a 'pancaked' austenite grain is transformed, the {100}<011> orientation is only a minor component, since it is a low intensity by-product of just one of the four principal preferred orientations of the rolling fibre".

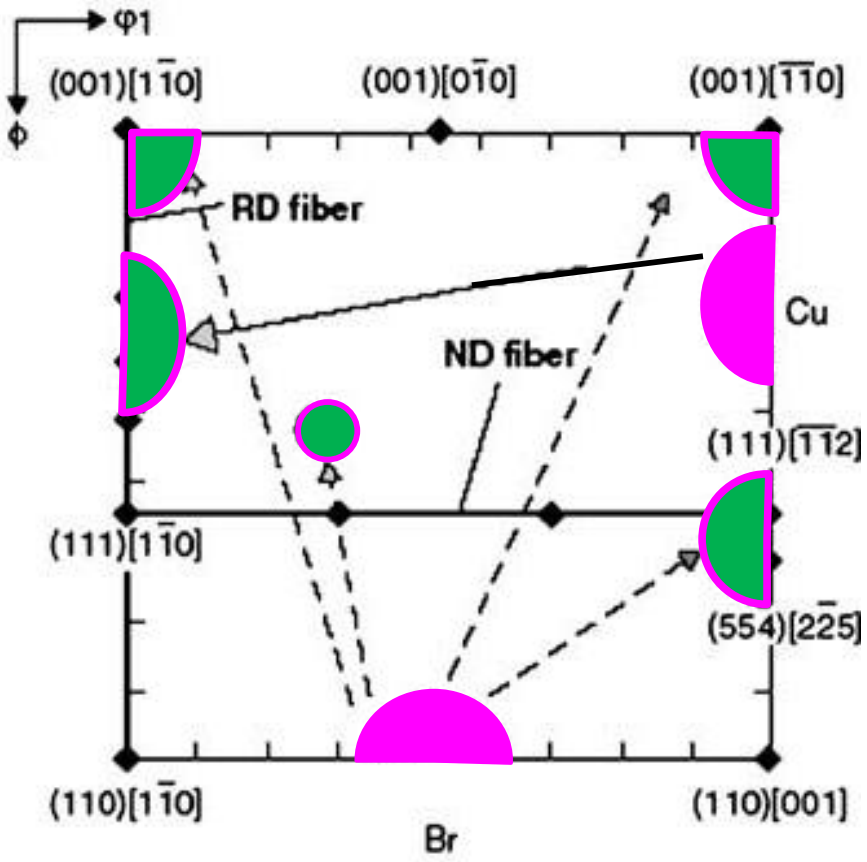

Figure II.4-4 *φ_2=45° section of Euler space showing the bcc texture components inherited from the Cu and Br components. [95].*

When the final rolling pass is carried out in the intercritical temperature range the deformation and recrystallization of the ferrite phase also contribute to the final texture. The {100}<011> texture component is part of the ferrite rolling fibre which develops (at least partially) during inter-critical rolling. Furthermore, recrystallization of the rolled ferrite gives rise primarily to the rotated cube orientation [98].

II.5 Effect of TMCP parameters on microstructure and properties of HSLA pipeline steels

Production of HSLA steels has faced many challenges owing to, among others, low operational temperature environments and demands for increased strength. These challenges have spurred the development of new steel production techniques, and as a result, significant knowledge has been acquired about the effect of different TMCP conditions on the final properties of HSLA steels (see Table II.1-2). The present survey summarizes the existing, openly available information regarding the influence of the various TMCP stages. The reheating temperature, roughing, inter-pass times, finish rolling, and cooling are discussed in view of their effect on the austenite conditioning, austenite to ferrite transformation and final transformed ferritic microstructures and properties.

II.5.1 Reheating

Dissolution of precipitates such as TiN, Nb(CN), VC, VN are time and temperature dependent [99-101]. This fact must be taken into account when the reheating parameters (temperature and time) are being adjusted. Figure II.5-1 [100] plots the amount of Nb(CN) and Ti(CN) measured in a HSLA steel after 1h of reheating at different temperatures.

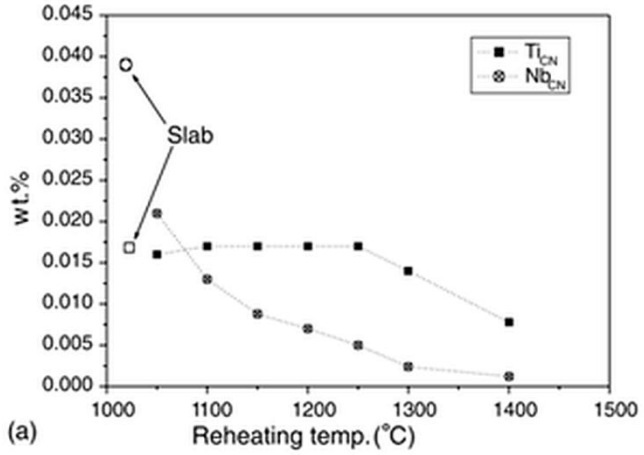

Figure II.5-1 *Amount of Nb(CN) and Ti(CN) measured in a HSLA steel after 1h of reheating at various temperatures [100].*

High reheating temperatures promote austenite grain coarsening. Coarse austenite grain sizes are, however, undesirable. The reheating temperature should, be high enough to dissolve the micro-

alloying elements (such as Nb and V) which will later contribute to precipitation strengthening. The selected temperature should result in complete dissolution of the elements (especially Nb) but simultaneously prevent significant austenite grain growth. As confirmed by *Zrnick et al.*[101], austenite grain size (in a 0.1C, 0.03Nb, 0.041Ti Wt% steel) varies with the reheating temperature and times Figure II.5-2.

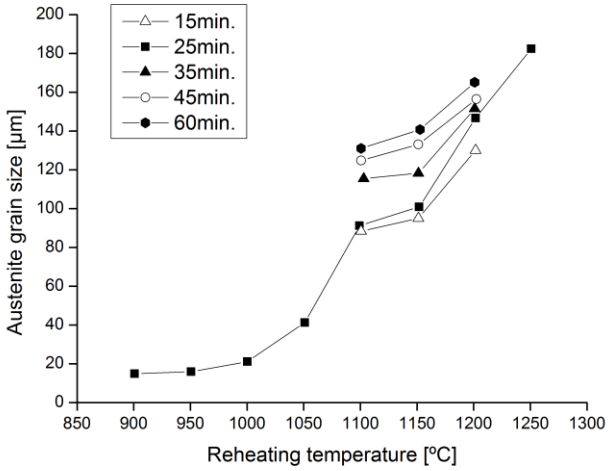

Figure II.5-2 *Change in austenite grain size with reheating temperature and time [101].*

Reheating temperatures have a clear effect on the strengths of micro-alloyed steels. For example, *Jahazi et al.* [102] observed that the YS decreases when the reheating temperature is not high enough to dissolve the micro-alloying elements Figure II.5-3. Segregation may also influence the distribution of precipitates in these steels. This segregation occurs during solidification of the continuously cast slabs. The distribution of precipitates is, therefore, another deciding factor in the choice of reheating temperature. In a recent study with low C micro-alloyed steel slabs, *Roy et al.*[103] observed that: (*i*) "Interdendritic segregation (or microsegregation) during casting can result in an inhomogeneous distribution of micro-alloy precipitates in the as-cast slabs, where precipitate-rich regions coincide with the interdendritic regions and precipitate-lean regions coincide with dendritic regions." (*ii*) "At lower reheating temperatures <1075°C, Nb precipitates effectively control the austenite grain sizes. However, at the intermediate soaking temperatures (between 1150°C and 1200°C), Nb precipitates dissolve in the dendritic regions, allowing free

austenite grain growth, while those precipitates pin down the austenite grain boundaries in the interdendritic regions, creating bimodal austenite grain structure."

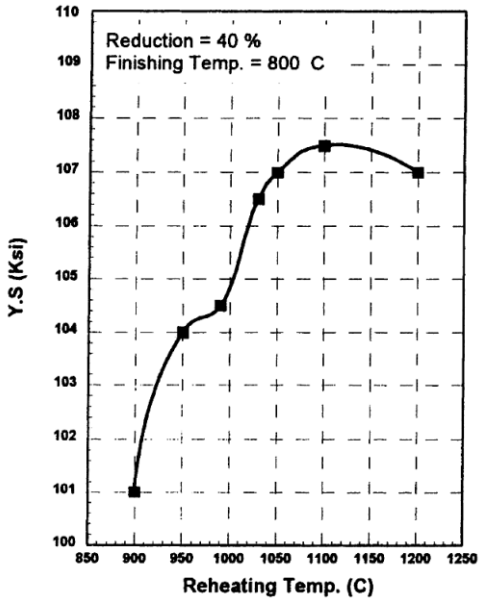

Figure II.5-3 *Correlation between yield stress and reheating temperature. [102].*

II.5.2 Rough rolling (Roughing)

After austenite deformation during rough rolling at temperatures above Tnr [32], restoration processes (static recovery & recrystallization) take place in order to lower the internal energy of the material by decreasing the density of defects. Heterogeneous austenite microstructures must be avoided at this stage of the TMCP since they can lead to detrimental heterogeneities in the final microstructure [104]. In an earlier work, *Irani et al*. [30] reported that mixed-grain microstructures (interpreted as partially recrystallized microstructures [105] were observed after holding between roughing and finishing rolling at temperatures of 1050-900°C. Finish rolling and cooling of these mixed-grain microstructures resulted in steels with low impact toughness. In contrast, plates held above 1050-1100°C had high toughness values [30] Those findings confirmed that heterogeneous microstructures are harmful to the final mechanical properties. Reductions over the whole temperature range (from a low reheating temperature to just above Tnr) were proposed [30] as an alternative to holding above 1050-1100°C. This required a roughing reduction in addition to refining the recrystallized austenite. Such reduction promoted successive homogeneous refinements of the recrystallized austenite microstructure. Furthermore,

Machida and Katsumata [106] investigated the effect of strain rate on the recrystallized grain size of austenite for rolling in the temperature range of 1200-1000°C. They observed that the parameters which control the strain rate (roll speed, roll radius, reduction per pass) could also be used to tune the subsequent recrystallized austenite grain size.

II.5.3 Inter-pass times

Figure II.5-4 plots the dependence of inter-pass time on the softening kinetics of a 0.03wt% Nb, HSLA steel during three-step compression testing at various temperatures [107]. The change in slope is related to the onset of recrystallization. Testing at high temperatures leads to complete recovery in an inter-pass time of 10s. Softening is enhanced after various deformation steps, particularly at high temperatures.

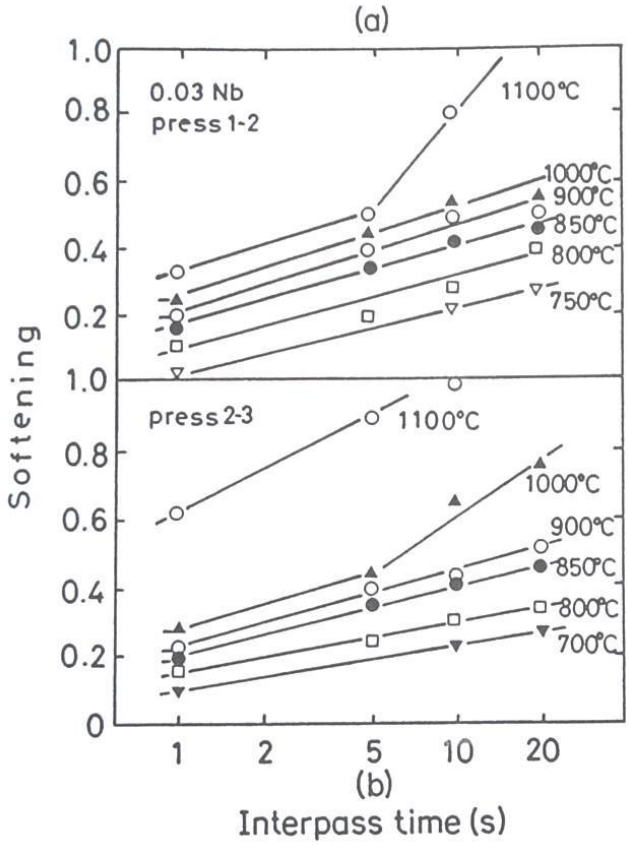

Figure II.5-4 *Softening fraction from three compression tests each with intervals of 0.1 strain per step [107].*

II.5.4 Finishing

In 1976, *Morrison and Chapman* published a paper [78] in which they described the influence of finish rolling temperature (austenitic rolling) on the final ferrite grain size of a HSLA steel (64% reduction), rolled in a laboratory line (see Figure II.5-5). The lower the temperature over which a significant part of the deformation takes place, the finer the ferrite grain size. This fine grain size stems from an increase of ferrite nucleation sites resulting from the influence of temperature-dependent precipitates on austenite recrystallization and growth (see section II.6).

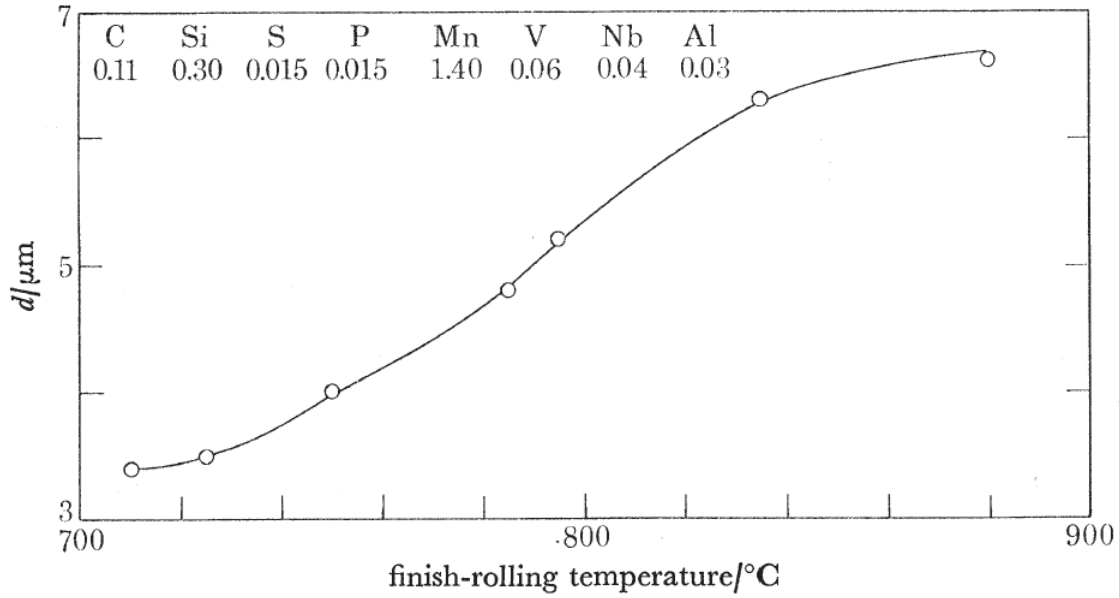

Figure II.5-5 *Final ferrite grain size vs. finish rolling temperature of HSLA materials laboratory rolled in the austenitic region [78].*

Hwang et al. [108] performed a series of trials with three HSLA steel compositions. The experiments were performed with variations of TMCP parameters namely, the FRT in the non-recrystallized and two phase regions, cooling rates, and the finish cooling temperatures. When cooling rates or finish cooling temperatures were changed, TS and UTS values varied more in specimens finish rolled in the austenite-ferrite region compared to those deformed in the non-recrystallization austenite region [108]. This observation was attributed to small difference in the phase fractions (α_p, α_{qp}, α_B,P_L) among samples rolled in the austenite region.

Baczynski et al. [58] reported that YS is higher when finishing rolling is done in the austenite-ferrite compared to the non–recrystallized region. There was, however, no significant difference

in the UTS values. *Baczynski et al.* also investigated the effect of finishing rolling temperature on the texture and YS anisotropy. The samples exhibited qualitatively similar textures and hence, similarities in anisotropic behavior. The authors concluded that the decrease in toughness at room temperature stemmed from the strong textures observed (particularly in the ND fibre) in the sheets finished in the two phase region.

Irvine and Baker [56] studied two HSLA steels containing 0.04wt% and 0.06wt% of C and Nb, respectively and observed an increase in the yield stress and the DBTT at low finish rolling temperatures (800-600°C). Deformed ferrite recovers only as a result of the strain-induced precipitation of Nb(C,N) in the substructure [4]. The strength increase was, therefore, attributed to rolling done in the ferrite phase region. However, no explanation was given for the increase of the DBTT. Conversely, in their study of ultralow carbon bainitic steels (0.02-0.03wt% C, 0.04-0.05wt%Nb), *Wang et al.* reported that the yield and tensile strengths decrease for rolling temperatures in the range of 850-775°C. This observation was attributed to the reduction of M/A constituents and accompanying increase of allotriomorphic ferrite which occurs when the finish rolling temperature is lowered [109]. The reduction of the M/A constituent with decreasing finish rolling temperature also leads to an increase in toughness and a decrease in DBTT [109].

Finish rolling temperatures also affect the fracture appearance transition temperature (FATT). *Speich and Dabkowski* [110] observed that FATTs exhibit "U"-shaped behavior (see Figure II.5-6) for finish rolling temperatures in the two phase ($\alpha+\gamma$) region. This U-shaped behavior is characterized by an initial decrease of the FATT, followed by an increase which accompanies an additional decrease in the finishing temperature. *Tanaka* [4] correlated this behavior to the recovery or change of the cellular dislocation structure into sub-grain structure, that occurs just below Ar_3, and which significantly reduces dislocation hardening in the material. Deformation at temperatures much lower than Ar_3 gives rise to non- recovered microstructures thereby increasing the dislocation hardening and consequently, the FATTs.

Zrnic et al. [101] studied the influence of different reductions during finishing. They found that increasing the finishing reduction from 50% to 60%, in air-cooled samples enhances the strength, for all coiling temperatures (cf. Figure II.5-7).

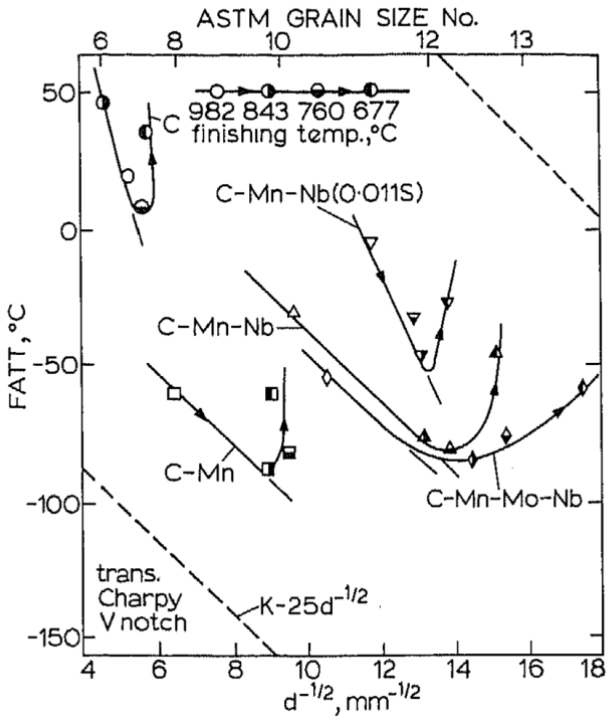

Figure II.5-6 *Effect of finishing rolling temperature on transition temperature and grain size for a series of steels [110].The data for different rolling temperatures are shown with different markers in each curve.*

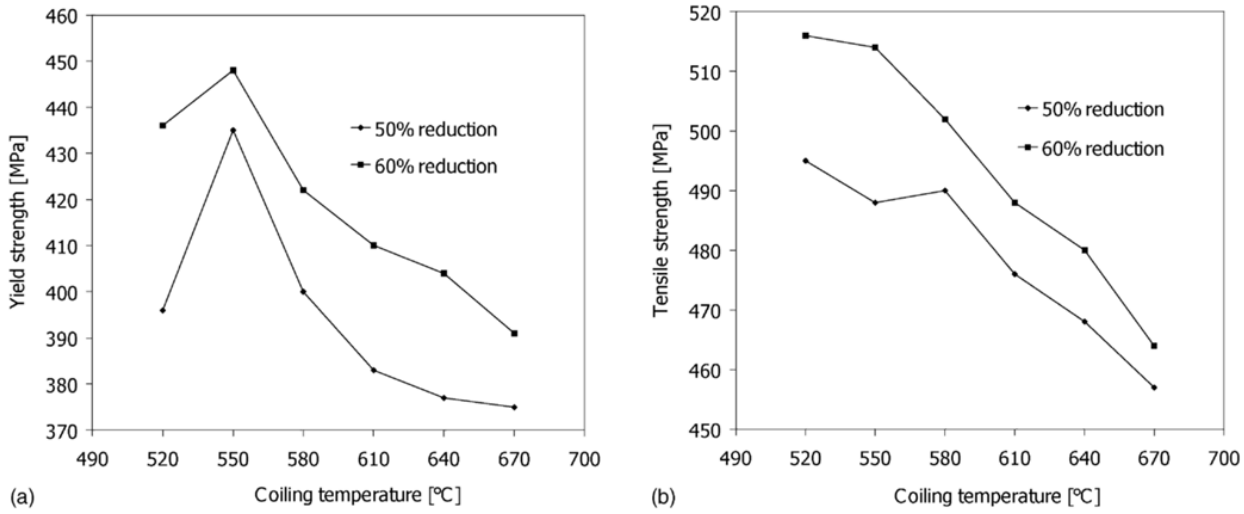

Figure II.5-7 *Variation of YS and UTS as a function of the reduction and coiling temperature [101].*

II.5.5 Cooling rate / transformation temperature

The state of the austenite prior to, and the cooling rate through the phase transformation are the two main parameters which largely impact on the grain size and morphology of the final microstructure of pipeline steels. *Ouchi et al.* [80] investigated the effects of chemical composition and different rolling conditions (rolling reduction and temperature) on single and continuous deformation schedules, Figure II.5-8 plots the austenite to ferrite transformation temperature, when air cooling is applied, as a function of the total reduction during multi pass rolling (filled points) below Tnr. Ar_3 was found to be almost constant for cumulative reductions in excess of 50%. The Ar_3 does however, depend, the chemical composition of the material.

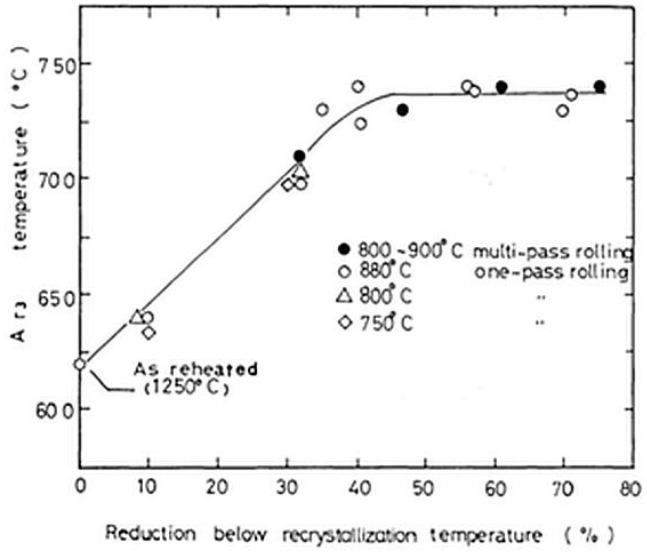

Figure II.5-8 *Relationship between rolling reduction below Tnr and the austenite to ferrite transformation temperature in HSLA Nb steel [80].*

The grain size of HSLA steels varies with the cooling rate. Equation II.5-1 [1].

$$D_\alpha = 5.7 C_R^{-0.26} D_\gamma^{0.46} \qquad \textbf{II.5-1}$$

Where $D\alpha$ is the final ferrite grain size, C_R is the cooling rate and $D\gamma$ is the austenitic grain size prior to transformation.

As previously stated, the cooling rate also influences the morphology of the grains. For example, *Yang et al.* showed that high cooling rates (above 10°C/s) preserve the deformation structures

(such as deformation bands) in bainitic steels until austenite decomposes [111]. Hence, the bainite transformation initiated at grain boundaries is suppressed owing to nucleation at intra-granular heterogeneities. This nucleation results in the formation of non-parallel plates. On the other hand, cooling rates below 5°C/s, promote partial recovery of deformed austenite during continuous cooling and, are therefore, not conducive to intra-granular nucleation.

The cooling rate influences the mechanical properties by virtue of its effect on the final microstructure. This is observed in the case of a 0.1wt% C, 0.04wt%Nb, 0.009wt%V micro-alloyed steel reheated and finished rolled in three different temperature ranges Figure II.5-9 [1]. Here, yield and tensile stress values increase while the FATTs remain almost constant or rise only slightly with increasing cooling rates.

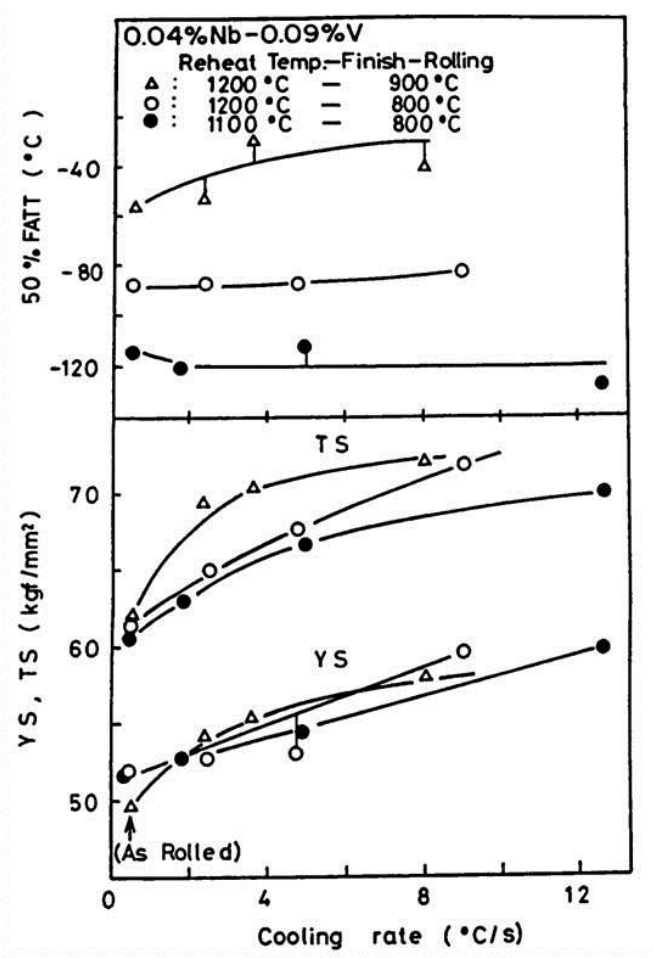

Figure II.5-9: *Effect of cooling rate on mechanical properties of a 0.1wt%C; 0.04wt%Nb, 0.09wt%V steel [1].*

The effect of the cooling rate can also vary with the thickness of the material. Particular consideration should be given to the case of heavy plates with large final thicknesses, since the cooling rates will not be spread homogeneously over the thickness of the plate. Figure II.5-10 [112] schematically illustrates the various approaches used for obtaining refined microstructures in materials with different thicknesses. Austenite conditioning combined with high cooling rates leads to fine ferritic microstructures in strips and light sections. Heavy sections, on the contrary, require additional approaches namely, particle stimulated nucleation (PSN). This approach (defined by some authors as third generation TMCP [113]) consists of adding second phase particles to steel. These particles provide additional sites for ferrite nucleation during phase transformation.

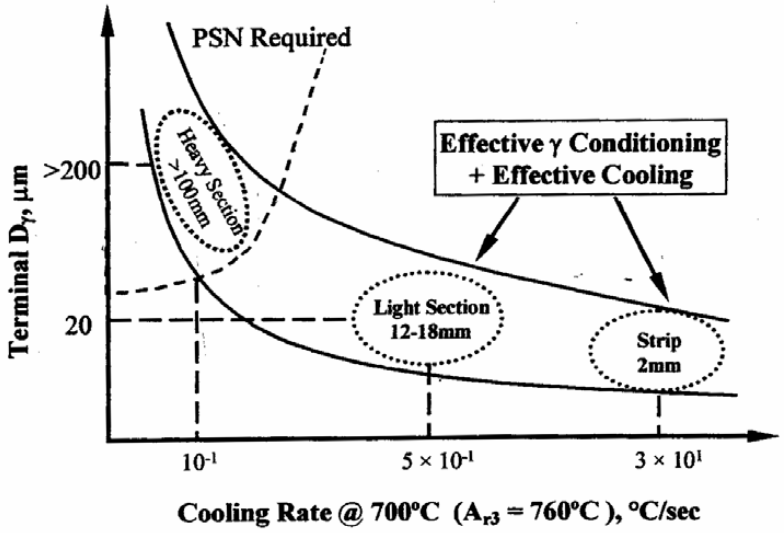

Figure II.5-10 *Correlations between final austenite grain size (D_γ), plate/strip thickness, cooling rate and corresponding grain refinement [112].*

II.6 Effect of alloying elements

HSLA steels are designed on the basis of the C-Mn alloy concept, whose base strength originates from the C content. The toughness of the material, however, deteriorates with increasing C content. Various strengthening strategies are employed in order to increase the strength of the material. Mn and Si are added as solid solution strengtheners but Nb, Mo, V, and Ti are the most important alloying elements used in HSLA steels. These four elements influence recrystallization and grain growth processes in various ways.

Nb, Mo, and V solutes retard the recrystallization of austenite by suppressing grain boundary migration. Nb and V have the most and least impact on recrystallization. The differences in the effectiveness of these solutes are attributed to differing electronic structures and atomic diameters, with respect to that of γ iron [114].

These elements further retard recrystallization by pinning grain boundaries during the final stages of rolling. Figure II.6-1 [115] verifies that austenite grain size refinement is greater in Nb-micro-alloyed steels compared to their Nb-free counterparts for temperatures in the range of 1200°C-850°C. Therefore, as it is stated in [114], "the essential function of solute retardation effect is to prevent recrystallization until precipitation retardation process can be initiated".

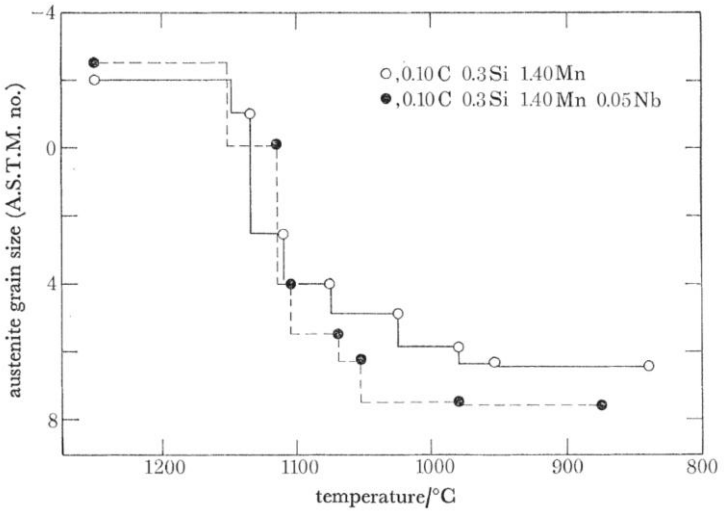

Figure II.6-1 *Differences in austenite refinement during continuous rolling (total reduction 90%) with and without Nb additions [115].*

Micro-alloying elements which remain in solid solution after final rolling decrease the austenite to ferrite transformation temperature [116]. This effect becomes more pronounced with increasing cooling rates (Figure II.6-2).

Certain amounts of Nb, Mo, or V [77] remain in solid solution after hot rolling in the recrystallization and non-recrystallization zone. These can precipitate during or after the austenite to ferrite transformation and hence contribute to an increase of the final strength of the steel.

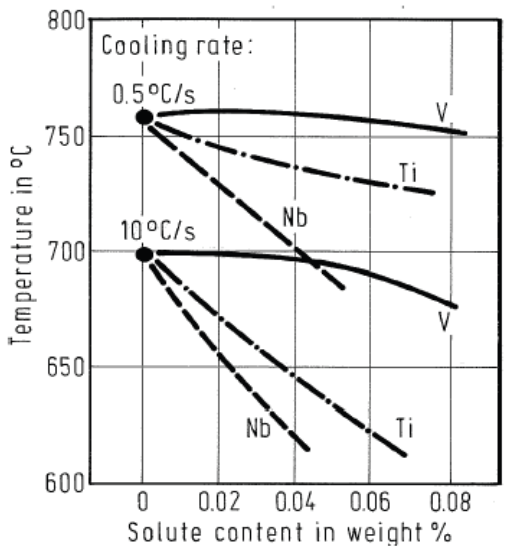

Figure II.6-2 *Effect of solute micro-alloying elements on austenite to ferrite transformation temperature [116].*

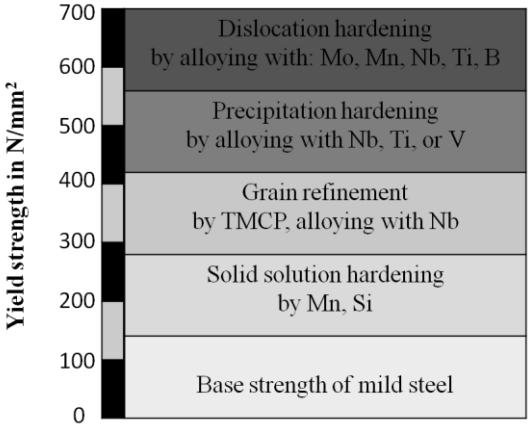

Figure II.6-3 *Strengthening contributions from different alloying elements [117].*

Ti precipitates (TiC and TiCN) [55] are the most stable of the aforementioned alloying elements over a wide range of temperatures and not surprisingly, TiN suppresses austenite grain growth during reheating.

Nb is the most widely utilized micro-alloying element in pipeline steels owing to its capacity to suppress grain boundary migration within a broad range of temperatures where rough rolling (solute drag) or finishing rolling (precipitation pinning) take place. In practice, Nb increases the Tnr and therefore expands the temperature region where pancaking (conditioning) of γ is

possible. In the solid solution, V has a weak effect on austenite recrystallization during hot controlled rolling and on the Ar_3 transformation temperature (Figure II.6-2). However, V carbides, in the form of interphase or random precipitates in ferrite, impart important strengthening to the material [55, 118].

The effect of Mo additions on the strength and toughness of high strength pipeline steel was studied in [116, 119]. Low (below 0.1wt%) additions had no effect on the microstructure. Conversely, high (above 0.1wt%) amounts resulted in progressive increases of acicular ferrite, bainite and MA fractions. Although Mo additions combined with large amounts of Nb (e.g. 0.2wt%) lead to improved YS and (especially) UTS values, the toughness was reduced owing to the large presence of MA constituents. *Lee et al*. [120] reported similar findings in the case of a 0.08C-0.03Nb wt% steel. In that case, however, an addition of 0.6wt% Mo was required in order to significantly increase the YS and UTS. This high level of Mo resulted in a considerable loss of ductility.Table II.6-1 summarizes in condensed form the guidelines for alloying strategy of HSLA steels designed for pipeline applications.

Element	Purpose
C< 0.06 wt%	High impact toughness, good weld ability
Mn	Transformation control, solid solution strengthening
Mo	Transformation control, solid solution strengthening
Ti	Grain growth control during recrystallization rolling
Nb	Inhibit recrystallization, transformation control, precipitation strengthening
S<0.004 wt%	Impact toughness

Table II.6-1 *Summary of the alloying strategy for high strength steels [121].*

II.6.1 Precipitation behavior (Austenite/ ferrite)

Recrystallization may interact with, and compete against, deformation-induced precipitation during hot rolling. The observed correlation between precipitation and recrystallization [122, 123] can be explained as depicted in Figure II.6-4) [114]. Zone 1: recrystallization takes place during high temperature rolling. Zone 2: onset of recrystallization followed by precipitation at the

grain boundaries of previously recrystallized grains. Zone 3: precipitation occurs first and subsequently retards or suppresses recrystallization.

The effect of different micro-alloying combinations on recovery, recrystallization and precipitation behavior in the austenitic region of HSLA steels was studied in detail by *Akben et al.* [124] and *Hua el al.* [125]. In addition, *Jang et al.[126] and Charleux et al*. [127] explained the interphase precipitation behavior and the ferrite precipitation, respectively of various Ti-Nb-Mo micro-alloyed steels.

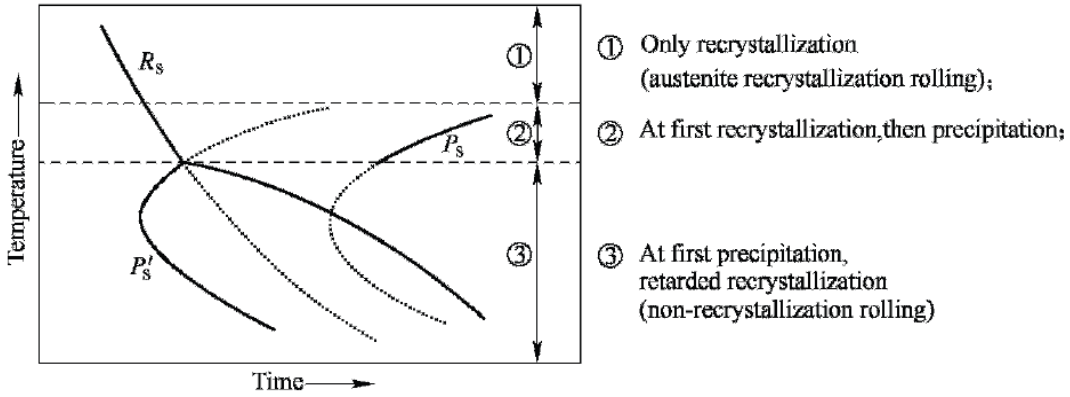

Figure II.6-4 *Schematic precipitation-recrystallization interaction diagram. P_s and $P_{s'}$ symbolize the onset of precipitation in undeformed and deformed austenite respectively. R_s represents the start of recrystallization [114].*

II.7 Strengthening mechanisms

The strength is one of the most important properties of HSLA pipeline steels. It is defined as the ability of the metal to withstand an applied stress without failure. Combinations of findings, delineated along the history of steel research, support the fundamental statement that the mechanical properties are sensitive to changes (of defect presence) at various structural levels of the material, from the atomic to the macroscopic level. Figure II.7-1 outlines the historical progress of TMCP and the classical mechanisms utilized to increase the strength of steels.

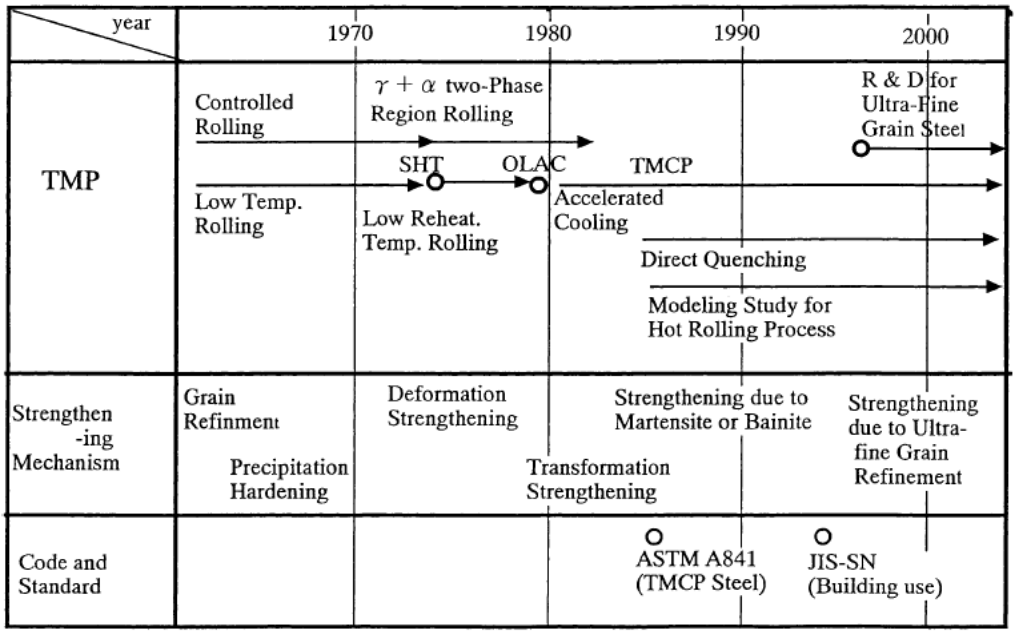

Figure II.7-1 *Historical progress of TMCP and the strengthening mechanisms utilized [36].*

Therefore, strengthening implies an increased resistance to plastic deformation by means of blocking dislocation motion. Strengthening can be achieved by introducing obstacles in the form of grain refinement, work hardening via dislocation interactions, solid solution elements, precipitates, and second phases. The contributions of different strengthening mechanisms will now be briefly discussed.

II.7.1 Grain size strengthening

Grain boundaries can sometimes impede the motion of dislocations. This is achieved through grain refinement which increases the boundary area per unit of volume, and hence, reduces the free path for continuous slip. The yield strength depends, therefore, on the grain size of the material. *Hall* [128] and *Petch* [129] defined this dependency as:

$$\sigma_Y = \sigma_0 + K_Y d^{-0.5} \qquad \textbf{II.7-1}$$

where σ_0 is the intrinsic lattice friction stress, which represents the stress necessary to move free dislocations along the slip planes in iron BCC crystals. σ_0 depends on both temperature and chemical composition. K_Y is a constant referred to as the "grain boundary unlocking term", which

represents the difficulty of unlocking or generating dislocations in the neighboring grains. *d* is the mean grain size in meters. The *Hall-Petch* relationship cannot be singularly used if other microstructural features influence the mean free path of dislocation movement. The yield strength of polycrystalline materials, particularly the HSLA steels, results from various contributory sources including solid solution, grain size, precipitation, dislocation and texture strengthening [78]. Several authors [78, 130] posit a simple summation law of the strengthening contributions. *Koppenaal* [131] and latter *Irvine, Kocks* and *Majta* [132-134] obtained a better agreement between calculated and experimental results by using root mean square (r.m.s) summation of the operating strengthening contributions. Therefore, compared to the simple summation law, the r.m.s results in a lower quantification error when two microstructural obstacles of the same order of magnitude are measured. A thorough explanation of the theory of obstacle-controlled yield strength can be found in [134].

II.7.2 Dislocation strengthening, work hardening

The yield stress *(σ)* also depends on, and is positively correlated to, the dislocation density of the material. *Bhadeshia and Honeycombe* [135] expressed the interaction of dislocations with short [136] and long angle obstacles as:

$$\sigma = \sigma^* + \sigma_i$$

$$\sigma^* = \frac{1}{V}[\Delta H_0 + KTln\frac{l\,\dot{\varepsilon}}{\rho m A b \gamma}] \qquad \textbf{\textit{II.7-2}}$$

$$\sigma_i = \alpha \mu b \rho^{0.5}$$

Where V = activation volume; ΔH_0 = activation enthalpy at $\sigma = 0$; k = Boltzmann's constant; T = temperature; l = length of activated dislocation line; $\dot{\varepsilon}$ = strain rate; m = mobile dislocation density; A = area of glide plane covered by dislocation; α and μ are constants; b is the Burgers vector and ρ is the dislocation density.

Equation II.7-2 indicates that the shear stress for further deformation depends on a temperature-dependent, effective shear stress (including short range obstacles such as isolated dislocations) and an internal stress (including long range obstacles such as cell walls).

The strengthening contribution of dislocations can be also quantified using the *Taylor* approach [137], which expresses the additional stress needed to cut through the dislocation "forest" as:

$$\sigma_d = \alpha M G b \sqrt{\rho} \qquad \textbf{(II.7-3)}$$

where α is a constant that depends on the crystal structure, M is the average Taylor factor, G [MPa] is the shear modulus, b [m] is the Burgers vector and ρ [m^{-2}] is the dislocation density.

Takahasi and Bhadeshia [138] described empirically the relationship between the density of dislocations in ferritic/bainitic microstructures and the transformation temperature (see Figure II.7-2). It is clear from Figure II.7-2 that, as expected, the dislocation density (and hence, the corresponding contribution to strengthening) decreases with increasing transformation temperature.

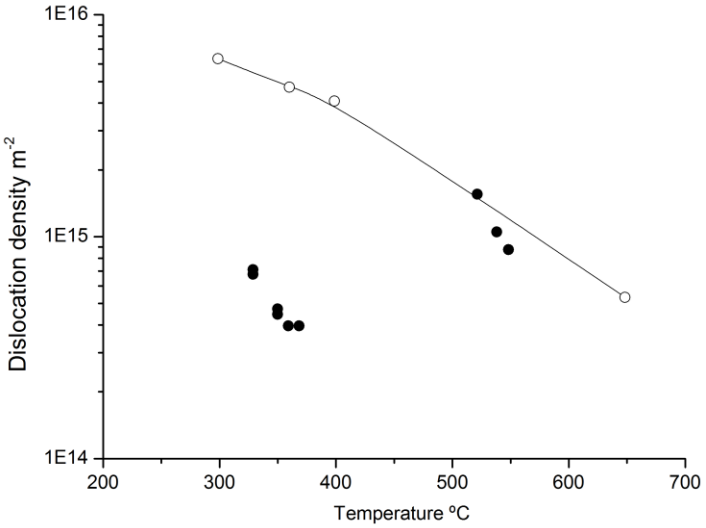

Figure II.7-2 *Changes in dislocation density of bainitic ferrite (open circles) and martensite (solid circles) as a function of transformation temperature, points from different studies [138].*

II.7.3 Precipitation strengthening

Volume defects such as precipitated particles (i.e. metallic carbonitrides M(CN)) initiate precipitation strengthening. The magnitude of strengthening depends on the morphology, size, coherency with the matrix, distribution and volume fraction of the precipitates. Two types of particle-dislocation mechanisms are possible. Dislocations can loop between, and therefore bypass, hard and non-deformable particles (known as *Orowan* mechanism [139]). Alternatively, dislocations can glide through and shear particles (known as *Friedel* mechanism [140]). Bypassing and shearing depend inversely on and are proportional to the particle size, respectively. The *Orowan* mechanism, was extended by *Ashby* [141] for a random arrangement of particles. The resolved shear stress τ to overcome the effect of the precipitates can be expressed as:

$$\tau = \frac{1}{1.18}\left(\frac{1.2Gb}{2\pi\left(\frac{1}{\sqrt{n_s}} - x\right)}\right)[\ln(\frac{x}{2b})] \qquad \textbf{(II.7-4)}$$

Where x = the mean planar intercept diameter of a precipitate, n_s the number of precipitates per unit area of slip plane, G = the shear modulus, b = the Burgers vector.

Precipitation strengthening, $\sigma_{p,}$ can be quantified using a modified form of the *Ashby-Orowan* equation [56].

$$\sigma_p = \frac{0.3Gbf^{0.5}}{\bar{x}} ln\frac{\bar{x}}{2b} \qquad \textbf{(II.7-5)}$$

Where G is the shear modulus in GPa, b is the Burgers vector in nm, f is the volume fraction of particles and x is the average particle size in mm.

II.7.4 Solid solution strengthening

Interstitial and substitutional elements contribute to an increase in the yield strength. Interstitial elements, such as carbon and nitrogen introduce asymmetric lattice distortion [142] which promote dislocation immobilization. Interstitial solutes are better strengtheners than substitutional

ones but C and N, for example, have low solubilities, especially at room temperature. Interstitial solute strengthening is, therefore, limited. Metallic substitutional solute atoms cause a symmetric distortion of the solvent lattice arising from the atomic size mismatch, difference in elastic modulus, and electronegativity [142] [143]. The solid solution hardening contribution can be quantified by using the analytical relationships developed in the literature for different types of steels [142-145].

II.7.5 Second phase strengthening

Phases such as pearlite, which is a mixture of ferrite and cementite, also influence the strengths of multi-phase steels. The literature [133, 146] contains numerous empirical equations describing the yield stress of steels which have more than 25-30% of pearlite. Generally these equations include two extra parameters: *(i)* the volume fraction of ferrite and *(ii)* the mean true inter-lamellar spacing, which is the main parameter affecting the strength of pearlite [143].

II.8 Fracture Mechanics

Fracture mechanisms, like the mechanical properties, depend on the microstructural features of the steels. This is important since the structural integrity of the pipelines will depend on the underlying microstructures. The structural integrity of a pipeline should be addressed in various steps: design of the pipeline route, steel pipe production, line pipe construction and maintenance during operation in order to avoid failure. This section gives a brief overview of fracture related mechanisms in pipeline steels, and the role of microstructure in each. Please see [147-150] for detailed analyses and reviews of fracture mechanisms from the viewpoint of fracture mechanics.

Pineau [151] in a recent review mentioned that, two types of approaches have been developed to assess the integrity of flawed, mechanical structures. These are:

(a) “Global” approach, which characterizes fracture resistance in terms of one or two global parameters, such as K_{IC}, J_{IC} [152], K_{Id} J_{Id} [153] Crack Tip Opening Angle, CTOD, J integral or Q field parameter stress. This approach is based on linear elastic fracture, and elastic-plastic fracture mechanics.

(b) "Local" approach. A more recent methodology developed to overcome the limitations of the global approach. These limitations include size dependency [154] or transferability between different geometries [155]. This approach consists of modeling local fracture by micromechanical models [156, 157]. The local fracture criteria are established from tests on notched specimens.

The main points addressed in the current local fracture methodology are schematically illustrated in Figure II.8-1.

One of the goals of the current study is to observe, identify and quantify the microstructural features (blocks I and III Figure II.8-1), which should be considered when designing damage models in HSLA steels (block II Figure II.8-1).

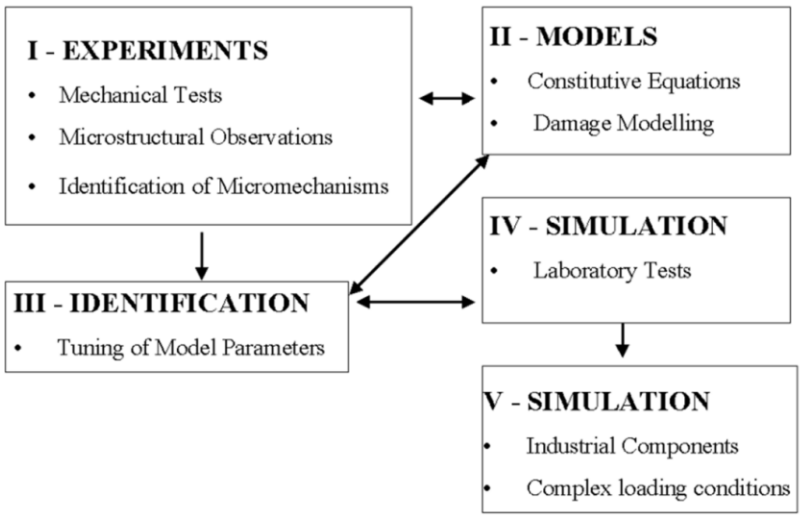

Figure II.8-1 *Methodology followed in the local approach of fracture mechanics [151].*

In his survey of fracture control in gas pipelines *Fearnehough* [158] states that fracture behavior is generally characterized as either brittle or ductile, and uses the transition temperature as the boundary between both. However, fracture propagation frequently consists of combinations of both behaviors. Table II.8-1 summarizes the possible means of fracture in pipeline steels.

Definition	Description	Fractography
Brittle	Little deformation, takes place in specific planes by cleavage. Appears at temperatures from the lower shelf of the transition curve.	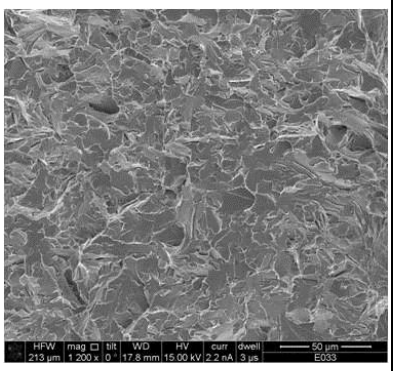
Ductile	Large deformation produced via void nucleation and coalescence. Appears at temperature from the upper shelf of the transition curve	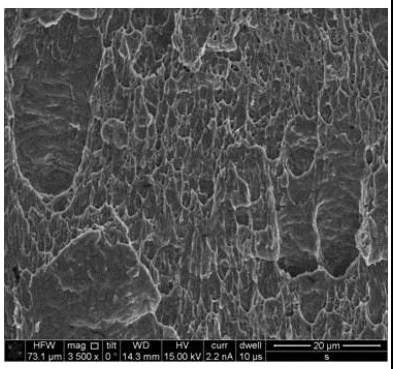
Mixed	Occurring mainly within the transition temperature range. Central brittle region due to triaxiality stresses and shear lips on the edges. Appears at temperatures between the upper and lower shelf (transition temperatures)	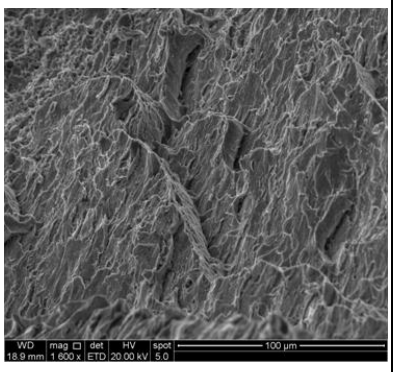
Delamination	Overall ductile fracture resistance is decreased due to inclusions or cleavage in planes parallel to the plate surface. Appears in the transition and upper shelf region.	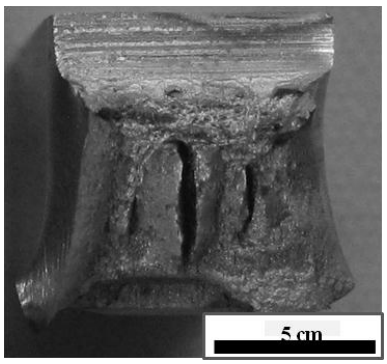

Table II.8-1 *Illustration of the different types of fracture in pipeline steels.*

Cleavage fracture occurs favorably over {100} planes for BCC structures. As observed in Figure (a) of Table II.8-1, steps appear in the fracture surface as a result of changes in the orientation of the cleavage planes when cracks cross the grain boundaries. Cleavage fracture in ferritic steels is initiated by the cracking of carbides [159, 160], or from brittle second phases (for example, MnS inclusions elongated and flattened by rolling) [161-163]. Pearlite colonies in ferrite-pearlite banded microstructures [164] or M/A constituents in bainitic structures [165] are also potential cleavage fracture initiators. Fracture initiation results from the combination of three events [147]:

- Slip-induced micro-cracking on a brittle second constituent
- Propagation of the micro-crack under the local stress state
    - (I) Across the second constituent/matrix interface
    - (II) Along a cleavage plane of the neighboring matrix grain
- Propagation of the grain-sized-crack through neighboring grains across the grain boundary (transgranular propagation).

Fracture in HSLA pipeline steels is growth controlled by the presence of microstructural barriers such as grain boundaries. According to fracture mechanics theory, fracture propagation occurs when the stress created by a crack of given size reaches the *Griffith* [166] stress.

Inter-granular brittle fracture may also occur in the material. This mode of fracture is especially favored when impurities such as phosphorous (which decreases the critical inter-granular fracture stress [167] segregate along the grain boundaries.

Brittle and ductile fracture clearly differ from each other and can be defined by different initiating events. Ductile fracture is defined by [147] as a process of damage nucleation followed by growth and coalescence driven by plastic deformation. Several models have been developed to simulate void nucleation and coalescence. The main parameters in these models are the critical cavity volume fraction and the acceleration factor to simulate coalescence introduced by *Gurson, Tvergaard and Needleman* [168].

Plastic deformation is often localized in microstructrually heterogeneous materials in which hard and soft phases are distributed. Ductile fracture is, therefore, controlled by microstructural heterogeneities present in the material. During ductile crack growth the material is able to preserve, to some extent, its load capacity. The onset of cleavage, however, drastically diminishes

the load-bearing capacity of the material. Consequently, the volume fractions of microstructural factors affecting the balance between the above phenomena (demonstrated as DBTT) are of major importance in the design and production of HSLA steels.

Pipelines can fail in various ways through axial overload, buckling (structural collapse), puncture, fatigue, internal pressure loading on a wall defect, etc. Failure occurs most frequently through internal pressure loading on a wall defect. Propagating fractures start at existing material flaws, and the stresses in the neighbourhood of the defect provide the driving force for fracture propagation. In general, flaws which are sufficiently deep and short will result in stable leaks after penetrating the wall thickness. Sufficiently long and shallow flaws, on the other hand, propagate along the length of the pipe after penetrating just enough of the wall thickness [169].

Pipelines must withstand a number of loads, including those imposed during the construction phase. The most important stress, however, is imposed by the internal pressure. Therefore, the crack-arrest (or crack-propagation) phenomenon is in essence a race between the decompression gas and the fracture velocity in the material [170].

Generally hoop stress (higher acting stress) is expressed as:

$$\sigma_h = PD/2t \qquad \textbf{\textit{II.8-1}}$$

where: *P* pipeline pressure; *D* outside pipe diameter; *t* pipe wall thickness.

For a safe operation, the hoop stress in the line should be lower than the Specified Minimum Yield Strength (SMYS) of the steel grade through a design or safety factor ϕ:

$$\sigma_h \leq \phi\ SMYS \qquad \textbf{\textit{II.8-2}}$$

Normally, a maximum design factor of ϕ=0.72 is used in most of the pipeline codes around the world (i.e. ASME B31.4) but in some countries such as Canada (CSA Z662), the pipeline standards allow a maximum design factor of ϕ=0.8. Nevertheless, the design factor is lowered in certain situations or locations (i.e. populated areas, transport of hazardous products). Pipelines also experience axial stresses. The magnitude of the axial stress (σ_L) depends on the constraints (obstacles against plastic deformation) imposed by the surroundings. If the pipe is buried σ_L is about 30% of the hoop stress, and 50% [171] in the case of freedom to expand.

Laboratory tests were developed in order to evaluate fracture resistance of pipeline steels. Experimental crack arrest methods can be divided into three groups [172]: *(i)* large or full scale test, *(ii)* structurally representative test and *(iii)* small scale test [173]. Owing to the high costs associated with the full burst test, a small scale test method was developed which would result in structurally representative crack arrest outputs. Classically, the data obtained from small laboratory tests are used to determine analytical correlations with the operational toughness behavior. Laboratory tests can also be used to compare fracture resistance with material specifications such as the microstructure and texture.

Charpy V-notch impact (CVN) and drop-weight tear test (DWTT) are the laboratory tests most frequently used to assess fracture toughness. Since triaxiality, low temperatures and high strain rates promote brittle fracture, pipeline steels are subjected to impact tests (i.e. CVN or DWTT) over a range of temperatures and geometries which include a notch. In an impact test, the toughness and ductility are related to the energy absorbed by the material and the shear area of the fracture surface, respectively. A descriptive model for brittle fracture was established after a series of brittle fractures in the 1950s and 1960s. This model correlates DWTT and Charpy energy with the full scale burst test [170]. In short, if the pipe is operating below the transition temperature (defined as the temperature at which the fracture surface of DWTT samples contains 85% of the shear area) the fracture is considered brittle and the crack will propagate long distances at speeds above 450m/s. In contrast, if the pipe operates at higher temperatures than the previously defined transition temperature, then the fracture propagation will depend on defined criteria which are based on the energy absorbed during the V-notch impact test [169].

Steel producers are currently able to fabricate steels which behave ductile within the operational conditions window at low transition temperatures. Pipeline steel compositions (steel cleanliness) and TMCP routes are designed in order to make steels which are ductile at low temperatures. These designs ensure that the steels fall in the upper shelf region of the DBTT curve for all the operating temperatures. Pipeline producers, nowadays, are mainly concerned about brittle fracture and the prevention of running ductile fractures.

Crack arrestability can be addressed [158] by either focusing on fracture initiation and/or designing steels which are resistant to fracture propagation. The prevention of fracture initiation (through pre-service inspection or in-service surveillance) is of utmost importance. Pipeline steels

are, however, inherently "flawed" by virtue of TiN, non-metallic inclusions, phase interfaces or material constituents present in the steel. Fracture initiation (on the microscopic level) is highly possible (or even probable) owing to the presence of these flaws.

Fearnehough [158] reviewed the literature from the period of 1953 to 1974 and established the fundamental concepts of crack propagation. Crack arrest behavior is defined as the resistance against continuous crack propagation. This resistance can be qualitatively expressed in various ways including the crack arrest temperature (CAT) [172], below which brittle crack propagation is possible for a given flaw size and stress level. Crack arrest behavior may also be directly determined by measuring the ductile fracture resistance through the fundamental parameter R. R characterizes the resistance against crack propagation (slowly or dynamically) during shear deformation [158]. Historical developments of theoretical and empirical ductile fracture propagation models are described in [147, 174]. Recent, representative works can be found in [155, 175-178]. These studies typically compare full scale behavior to the results from laboratory mechanical testing. This is achieved through correlations of the propagation toughness to the energy-fracture appearance measured in Drop Weight Tear Tests (DWTT) or through an equivalence with the shelf energy of Charpy V-notch impact tests [179]. The Battelle Two Curve (BTC) model [180, 181] is one such example which relates the pipe geometry to the loading conditions. The corresponding relation is given as:

$$(C\,V)_{2/3} = 2.382 \cdot 10^{-5} \sigma_h^2 (R_t)^{1/3} \qquad \textbf{\textit{II.8-3}}$$

Where $(C\,V)_{2/3}$ is the Charpy energy (J) for fracture arrest measured on 2/3 thickness of the plate, σ_h is the hoop stress (MPa), R is the radius of the pipe (mm) and t is the thickness (mm). The full size Charpy V-notch energy is calculated by multiplying equation II.8-3 multiplied by a factor of 1.5.

Fracture propagation is also linked to the decompression behavior of the pressurized gas contained within the pipe. The pressurized gas provides the driving force necessary for continued propagation of both brittle and ductile fractures. Various models ([179, 182]), for example the BTC model, simultaneously integrate gas decompression and dynamic crack propagation. Figure II.8-2 [182] schematically illustrates the go or no(t) go criteria for crack propagation according to the BTC method. These criteria are based on the empirical derivation of two curves which

describe the dependence of fracture velocity and gas decompression wave velocity on pressure. Figure II.8-2 presents three possible scenarios: (1) pressure decompression decreases until $P_{A,}$ and the fracture propagates continuously with the correspondent velocity. In the case where the curves do not intersect each other (2), the faster pressure decompression velocity results in a crack arrest scenario. For case (3), the gas pressure lags behind the crack tip and continuously decreases until the equilibrium tangent point is reached (equal decompression and crack velocities). This equilibrium tangent point corresponds to the minimum arrest toughness for any specific pipeline [182]. In other words, the fracture front always experiences the total line pressure if the crack propagates at higher speeds than that at which the gas decompresses. In such a scenario, the crack can only be arrested by a major geometrical or metallurgical barrier.

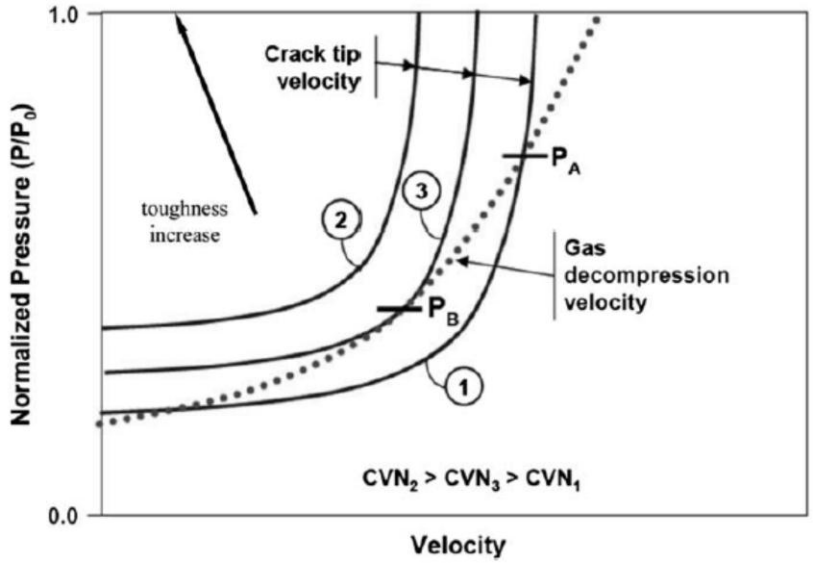

Figure II.8-2 *Schematic representation of the go or no(t) go criteria for crack propagation according to the BTC method [57]. Red and blue curves show the gas decompensation speed and the different crack tip velocities depending on the CVN toughness.*

The BTC method works well for pipeline steel grades up to X65. This limitation exists because equations such as. II.8-3 are empirical relationships which were established with low pipeline grades. Questions have been raised [181, 182] about the applicability of these equations to modern TMCP steels which have higher toughness values than the low pipeline grades. Correction factors are therefore needed in order to properly estimate the fracture initiation and propagation energies of the higher grades. The *Leis*, *Wilkowski*, and *Centro Sviluppo Materiali* (CSM) corrections [169] are generally accepted for use in this regard.

Poynton et al. [183] proposed an alternate solution based on energy balance rate during fracture. This approach was later adopted by others, for example, the British Gas Corporation. The fundamental idea is that for a constant velocity fracture, the energy involved in expanding the gas is equal to the sum of kinetic energy imparted to the deforming wall and the fracture energy absorbed by the pipeline steel (at the crack tip region).

$$E_{g.} = E_k + E_f$$

$$E_f = E_i + E_p \qquad \textbf{\textit{II.8-4}}$$

The fracture energy (E_f) can be expressed in terms of the energies absorbed during crack initiation (E_i) and propagation (E_p). E_p can be controlled through microstructural steel design, which plays an important role in the control of crack propagation. The current work will, therefore, focus on E_p. The pipeline fracture mechanics experts, who attended the last Pipeline Technology conference hosted in Ostend in 2013, agreed that other approaches, tools, experiments, means, etc. are needed in order to predict ductile crack propagation of new pipeline steel grades. *Horsley* [170] stated that "the problem is not one of fracture mechanics alone. Rather, solutions require description of both driving force (stresses applied by pressure of the fluid in the pipe at near the crack tip) and material resistance." *Pineau and Pardoen* [147] stated in their review of failure of metals that "despite of all the researchers devoted to the study of fracture in metals many questions remain open and both experimental and theoretical investigations are still needed to understand and solve real life engineering problems".

Murty et al. (1983) [184] compared the load-time traces relating to different fracture behaviors during an instrumented Charpy test. Although that study was done with a different type of steel, an extrapolation is possible, as can be appreciated from the work of *Yoshida et al.* [185].

Figure II.8-3 provides the correlations between the load-time record and the crack propagation mode. During pure brittle fracture (Figure II.8-3 a) the load increases linearly to a maximum, where fracture occurs and falls suddenly afterwards. The curve is bell-shaped in the case of pure ductile behavior (Figure II.8-3 c) and the occurrence of a pronounced shear lip leads to a similar shape but now with an extended tail (Figure II.8-3 d).

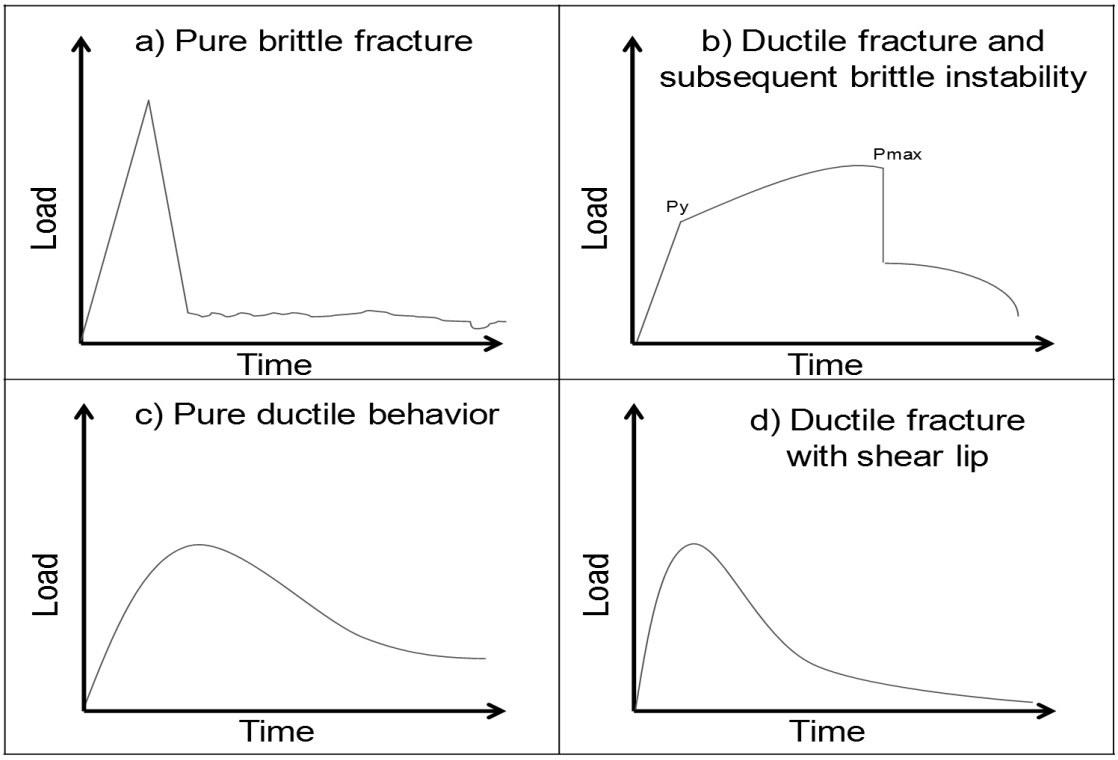

Figure II.8-3 *Correlations between load-time curves and fracture type, during instrumented impact Charpy test; adapted from [184]***.**

Nevertheless, fracture instability, in practice, is manifested in the type of curve shown in Figure II.8-3 b, where crack initiation occurs between the yield point and the maximum load [186, 187]. Crack initiation can also be assumed to occur at the maximum load, at $0.8P_{max}$ [188], or at the average between P_{max} and the load at yielding P_{yield} [186, 187]). In addition, the event of semi-brittle instability is identified by a sudden drop in the load.

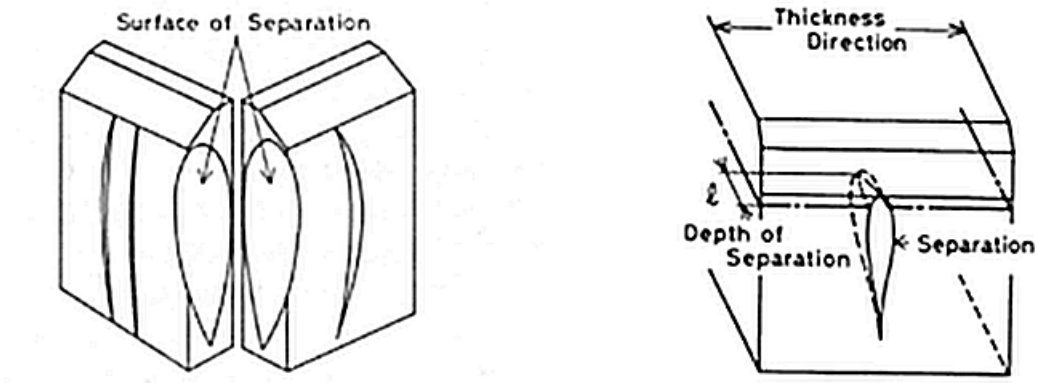

Figure II.8-4 *Schematic representation of separations/splits on Charpy specimens [189, 190]*.

Impact testing of TMCP steels in the transition temperature range result in the appearance of additional fracture planes which are perpendicular to the main fracture plane. This phenomenon is known as separation, delamination or splitting (Figure II.8-4). Initial classifications of this phenomenon, based on the characteristic microstructural features and the causes of appearance, were designated as inclusion type, grain boundary type and cleavage type [189]. Extensive research proposed two interpretations of the separation occurrence:

(a) <u>*Critical cleavage stress criterion [191-193].*</u> When a Charpy specimen withstands a bending force, the maximum stresses (under plane strain condition) are induced at the plastic elastic interface (see Figure II.8-5) [193]. Knowing the stress distribution beneath the notch of a Charpy-V specimen, the condition for the occurrence of separations is given by [191]:

$$\sigma_{cf}^{y} - \sigma_{cf}^{z} \geq \sigma_{yy} - \sigma_{zz} \qquad \textbf{\textit{II.8-5}}$$

where $\sigma_{cf}^{y}, \sigma_{cf}^{z}$ are the cleavage fracture strengths in Y (longitudinal) and Z (through thickness) directions and σ_{yy}, σ_{zz} are the stresses acting in the Y and Z directions, respectively (Figure II.8-5). According to this interpretation separations occur only if the fracture strength in Y exceeds that of the Z direction (i.e. triaxiality decreases).

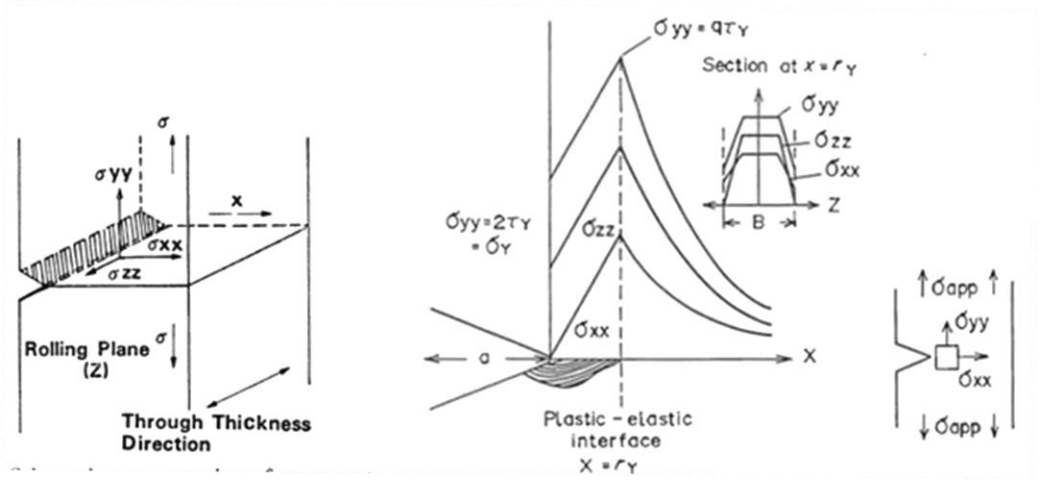

Figure II.8-5 *(a) Schematic representation of stresses at the notch; (b) Distribution of principal stresses in a Charpy specimen in plane strain condition [193]***.**

(b) <u>*Texture type cleavage separations approach*</u> [189, 190]. *Kunhe et al*. [189, 190] identified the (100)[011] orientation as the reason for separation in X70 pipeline steel. Alternatively

Matsuda et al. [189, 190] proposed that delamination occurs as a result of the strain anisotropy of grains which neighbor the {100}<uvw> and {111}<uvw> orientations (see Figure II.8-6). They claimed that {100}<uvw> and {111}<uvw> orientations contract easily in the Z and X directions, respectively during bending of the Charpy sample. Cracks could, therefore, originate at the grain boundaries between these orientations. Once initiated, cracks propagate along either colony boundaries of strongly textured grains, or {100} planes in a brittle manner.

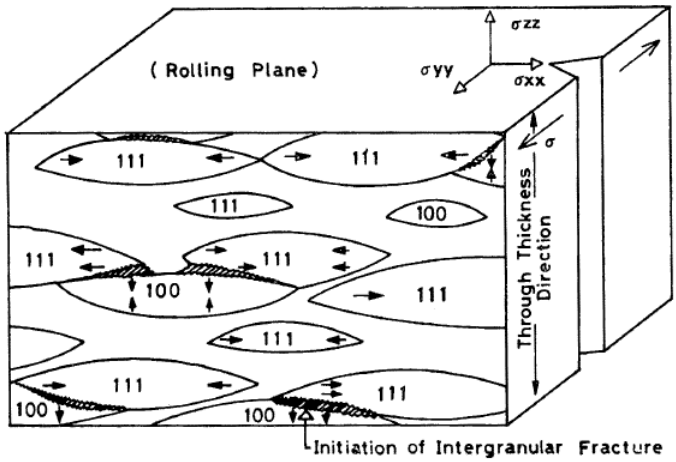

Figure II.8-6 *Schematic representation of the separation mechanism. Crystallographic banding through the thickness. Cracks initiated owing to strain anisotropy at boundaries between colonies with {100} and {111} orientations are shown as thick black regions [189, 190]. Arrows indicate the directions of maximum shear strains.*

The occurrence of separations influences both the fracture appearance transition temperature (FATT) and the energy absorbed energy in the ductile fracture region [194]. Both values decrease with increasing number of separations.

II.9 Definition of unresolved issues

Despite the significant strides made in the last decades, much remains unresolved as it relates to the prediction of microstructures and, by extension, the resulting mechanical properties of pipeline steels. Modeling the correlation between the thermo-mechanical history and the final microstructures and mechanical properties is a “hot topic” which requires further attention.

The existing models/equations are, to a certain extent, able to reproduce the hot deformation behavior of steels. Fine-element methods developed in the last few decades allow accurate calculations of strain, strain rates and temperature distributions in the material. These data could be linked to existing semi-empirical microstructural equations. The limitation is that, the semi-empirical equations are based on experiments carried out on steels of a given chemical composition which were deformed under laboratory simplified conditions. However, TMCP implies several deformation stages in non-isothermal conditions either above Tnr, below Tnr or in the intercritical region followed by continuous cooling transformations. In addition, recovery-recrystallization-precipitation phenomena during rough rolling, finishing rolling and cooling of pipeline steels (particularly those containing Nb) are still not completely understood.

It is true that the YS can, to a certain extent, be predicted based on analytical equations which depend on the chemical composition, (predicted) ferrite grain size, applied strains, etc. Each analytical equation, however, is valid only for a given composition or short compositional range under limited processing conditions. This fact indicates the lack of a complete understanding of the physical basis underlying these equations.

Fracture propagation and arrest phenomena have been studied for about five decades. The resistance of the material to these phenomena has historically been characterized by means of the Charpy V-notch or drop weight tear test [170]. Latest developments in pipeline steel practices have led to increases in strength and toughness. However, the Battelle two curve model (BTCM) used to determine the arrest toughness for ductile gas transmission pipelines is only accurate for the steel with low toughness [195] [196-198]. *Zhu and Leis* [195] reviewed the different correction methods used to match full experimental data with the CVN and DWTT energy-based empirical equations. They concluded that the BTCM type approaches are questionable. From a materials scientist point of view, an approach which includes a fundamental understanding of the role of microstructure and texture heterogeneities in ductile crack propagation is needed.

The present study relates to the previously enumerated unresolved issues. The particular objectives of current work are included in Chapter III.

References

[1] I. Tamura, C. Ouchi, T. Tanaka, and H. Senike, *Thermomechanical Processing of High Strength Low Alloy Steels*. London: Butterworth, 1988.

[2] H. Vergote, "Current status of TMP in Hot Strip Mill," in *2nd International Conference on Thermomechanical Processing of Steels*, Liege (Belgium), 2004, pp. 9-18.

[3] Y. Weng, *Ultra-fine grained steels*: Springer, 2009.

[4] T. Tanaka, "Controlled rolling of steel plate and strip," *International metals reviews*, vol. 26, pp. 185-212, 1981.

[5] W. B. Morrison, "Microalloy steels - the beginning," *Materials Science and technology*, vol. 25, pp. 1066-1073, 2009.

[6] R. Song, D. Ponge, D. Raabe, and R. Kaspar, "Microstructure and crystallographic texture of an ultrafine grained C–Mn steel and their evolution during warm deformation and annealing," *Acta Materialia*, vol. 53, pp. 845-858, 2// 2005.

[7] D. H. Shin, B. C. Kim, Y.-S. Kim, and K.-T. Park, "Microstructural evolution in a commercial low carbon steel by equal channel angular pressing," *Acta Materialia*, vol. 48, pp. 2247-2255, 5/29/ 2000.

[8] N. Tsuji, Y. Saito, H. Utsunomiya, and S. Tanigawa, "Ultra-fine grained bulk steel produced by accumulative roll-bonding (ARB) process," *Scripta Materialia*, vol. 40, pp. 795-800, 3/5/ 1999.

[9] A. Belyakov, K. Tsuzaki, H. Miura, and T. Sakai, "Effect of initial microstructures on grain refinement in a stainless steel by large strain deformation," *Acta Materialia*, vol. 51, pp. 847-861, 2/7/ 2003.

[10] P. D. Hodgson, M. R. Hickson, and R. K. Gibbs, "Ultrafine ferrite in low carbon steel," *Scripta Materialia*, vol. 40, pp. 1179-1184, 4/23/ 1999.

[11] Y. Matsumura and H. Yada, *ISIJ International*, vol. 27, 1987.

[12] S. Nanba, M. Nomura, N. Matsukura, K. Makii, and Y. Shirota, presented at the International symposium on ultrafine grained steels (ISUGS 2001), Fukuoka, Japan 2001.

[13] A. Najafi-Zadeh, J. J. Jonas, and S. Yue, "Grain refinement by dynamic recrystallization during the simulated warm-rolling of interstitial free steels," *Metallurgical Transactions A*, vol. 23, pp. 2607-2617, 1992/09/01 1992.

[14] P. Schmidt and D. H. Avery, "Complex Iron Smelting and Prehistoric Culture in Tanzania," *Science*, vol. 201, pp. 1085-1089, 1978.

[15] T. Rehren, T. Belgya, A. Jambon, G. Káli, Z. Kasztovszky, Z. Kis, *et al.*, "5,000 years old Egyptian iron beads made from hammered meteoritic iron," *Journal of Archaeological Science*, 2013.

[16] R. W. Vanderbeck, "Controlled Low Temperature Hot Rolling as Practice in Europe," *Journal of the Japan Welding Society*, vol. 37, pp. 114-s-116-s, 1958.

[17] C. Hatchett, "An Analysis of a mineral Substance from North America, containing a metal hitberto unknown," *Phil. Trans. R. Soc. Lond. A*, vol. 92, pp. 49-66, 1802.

[18] A. Arrowsmith, *J. Iron and Steel Inst.*, vol. 110, pp. 317-319, 1924.

[19] H. H. and L. F., *Stahl u. Eisen*, vol. 45, 1925.

[20] F. M. Becket and R. Franks, U.S Patent, 1939.

[21] W. Barr and C. F. Tipper, *J. Iron and Steel Inst.,* vol. 157, pp. 223-238, 1947.

[22] G. L. S. Corporation, *Steel,* vol. 116, 1960.

[23] C. A. Beiser, "The effect of small columbium additions to semi-killed medium-carbon steels," vol. 138, ed. ASM Preprint, 1959.

[24] C. L. Altenburger, Dearborn, and F. A., "Columbium containing steels, process for their manufacture and articles prepared therefrom," United States Patent, 1961.

[25] W. B. Morrison, *J. Iron and Steel Inst.,* vol. 201, pp. 317-325, 1963.

[26] N. J. Petch, "The upper yield stress of policristallyne iron," *Acta Metallurgica,* vol. 12, pp. 59-65, 1964.

[27] R. A. Grange, "Fundamentals of deformation processing," *Syracuse University Press,* pp. 229-230, 1964.

[28] K. J. Irvine, "Strong tough structural steels," *London, The Iron and Steel Institute,* pp. 1-10, 1967.

[29] R. Phillips, W. E. Duckworth, and P. E. L. Copley, *Iron and Steel Institute,* vol. 201, p. 593, 1964.

[30] J. J. Irani, D. Burton, J. D. Jones, and A. B. Rothwell, in *Strong touh structural steels*, London, 1967.

[31] K. Tsukada, K. Matsumoto, K. Hirabe, and K. Takeshige, *IS&M,* vol. 9, pp. 21-28, 1982.

[32] T. M. Maccagno, J. J. Jonas, S. Yue, B. J. McCrady, R. Slobodian, and D. Deeks, "Determination of recrystallization stop temperature from rolling mill logs and comparison with laboratory simulation results," *ISIJ International,* vol. 34, pp. 917-922, 1994.

[33] C. Ghosh, V. V. Basabe, J. J. Jonas, Y.-M. Kim, I.-H. Jung, and S. Yue, "The dynamic transformation of deformed austenite at temperatures above the Ae3," *Acta Materialia,* vol. 61, pp. 2348-2362, 4// 2013.

[34] J. M. Gray and F. Siciliano, "High strength microalloyed linepipe: half a century of evolution," presented at the 5th International Conference on Pipeline Technology, Ostend, Belgium, 2009.

[35] H. J. McQueen, "Historical aspects of thermomechanical processing for steels," *Materials Science Forum,* vol. 539-543, pp. 4397-4404, 2007.

[36] C. Ouchi, "Development of Steel Plates by Intensive Use of TMCP and Direct Quenching Processes," *ISIJ International,* vol. 41, pp. 542-553, 2001.

[37] H. G. Hillenbrand, A. Liessem, K. Biermann, C. J. Hecmann, and V. Schwinn, "Development of grade X120 pipe material for high presure gas transportation lines," in *4th International Conference on Pipeline Technology*, Ostend (Belgium), 2004.

[38] I.M.O.A. *High Strength Low Alloy (HSLA) Steel*. Available: http://www.imoa.info/moly_uses/moly_grade_alloy_steels_irons/high_strength_lowAlloySteel.php

[39] D. N. V. AS, "Submarine Pipeline Systems," in *Offshore Standard DNV-OS-F101*, ed, 2012.

[40] W. T. I. C. o. T. J. W. E. Society. *Carbon equivalents*. Available: http://www-it.jwes.or.jp/weld_simulator/en/cal1.jsp

[41] D. J and O. N. H, "A guide to selection and welding of low alloy structural steel," *Transactions of the Insitute of Welding,* vol. 3, pp. 203-214, 1940.

[42] N. Yurioka and H. Suzuki, "Hydrogen assisted cracking in C-Mn and low alloy steel weldments," *International Materials Reviews,* vol. 35, pp. 217-249, // 1990.

[43] D. C. F, "Prediction of the hardness in the HAZ of HSLA steels by means of the C-equivalent," presented at the Select Conference on Hardenability of Steels, Debry, UK, 1990.

[44] Y. Ito and K. Bessyo, *Weldability Formula of High Strength Steels: Related to Heat-affected Zone Cracking*: IIW, 1968.

[45] Y. N., S. S., O. S., and S. S, "Determination of Necessary Preheating Temperature in Steel Welding," *Welding Reseach Supplement,* vol. 62, pp. 147-153, 1983.

[46] W. C. Kan, M. Weir, M. M. Zhang, D. B. Lillig, S. T. Barbas, M. L. Macia, *et al.*, "Strain-based pipelines: design consideration overview," in *Proceedings of the 18th International Offshore and Polar Engineering Conference*, 2008, pp. 174-181.

[47] A. Liessem, G. Knauf, and S. Zimmermann, "Strain based design—What the contribution of a pipe manufacturer can be," in *Proceedings of the 17th International Offshore and Polar Engineering Conference (ISOPE), Lisbon, Portugal*, 2007.

[48] B. Liu, X. J. Liu, and H. Zhang, "Strain-based design criteria of pipelines," *Journal of Loss Prevention in the Process Industries,* vol. 22, pp. 884-888, 11// 2009.

[49] N. G. Kolbasnikov, O. G. Zotov, I. S. Martyashov, and R. V. Sulyagin, "The Bauschinger effect and the formation of microalloyed-steel properties in pipe manufacture," *Steel in Translation,* vol. 42, pp. 657-662, 2012/08/01 2012.

[50] I. Y. Pyshmintsev, D. Pumpyanskyi, L. Marchenko, and V. Stolyarov, "Strength and Bauschinger effect in TMCP Line Pipe Steels," *Publication of Russian Research Institute for the Tube and Pipe Industries, Russia,* pp. 1-5, 2004.

[51] S. Sohn, S. Han, S. Shin, J.-h. Bae, and S. Lee, "Effects of microstructure and pre-strain on Bauschinger effect in API X70 and X80 linepipe steels," *Metals and Materials International,* vol. 19, pp. 423-431, 2013/05/01 2013.

[52] R. Sowerby, D. K. Uko, and Y. Tomita, "A review of certain aspects of the Bauschinger effect in metals," *Materials Science and Engineering,* vol. 41, pp. 43-58, 11// 1979.

[53] S. Vervynckt, "Control of the non-recrystallization temperature in high strength low alloy (HSLA) steels," Doctor in Materials Science, Department of Materials Science and Engineering, Ghent University Gent, 2010.

[54] G. E. Dieter, *Mechanical Metallurgy*, 1988.

[55] S. Zajac and B. Jansson, "Thermodynamics of the Fe-Nb-C-N System and the Solubility of Niobium Carbonitrides in Austenite," *Metallurgical and Materials Transactions B,* vol. 29B, pp. 163-176, 1998.

[56] J. Irvine and T. N. Baker, "The influence of rolling variables on the strengthening mechanisms operating in niobium steels," *Materials Science and Engineering,* vol. 64, pp. 123-134, 1984.

[57] D. Stalheim, "The Evolution, review and optimization next steps related to the high temperature processing (HTP) alloy design for pipeline steels in china," in *International Pipeline Technology Conference*, Beijing, China, 2010.

[58] G. J. Baczynski, J. J. Jonas, and A. E. Collins, "The influence of rolling practice on notch toughness and texture development in high-strength linepipe," *Metallurgical and Materials Transactions A*, vol. 30A, pp. 3045- 3054, 1999.

[59] J. Patel, "Microalloyed hot strip mill products-processing and properties."

[60] K. Nishioka and K. Ichikawa, "Progress in thermomechanical control of steel plates and their commercialization," *Sci. Technol. Adv. Mater.*, vol. 13, 2012.

[61] J. K. Patel and B. Wilshire, "The challenge to produce consistent mechanical properties in Nb-HSLA strip steels," *Journal of Materials Processing Technology*, vol. 120, pp. 316-321, 2002.

[62] C. M. Sellars, "Modelling microstructural development during hot rolling," *Materials Science and Technology*, vol. 6, pp. 1072-1081, 1990.

[63] F. Siciliano Jr, K. Minami, T. M. Maccagno, and J. J. Jonas, "Mathematical modeling ot the mean flow stress, fractional softening and grain size during the hot strip rollig of C-Mn Steels," *ISIJ International*, vol. 36, pp. 1500-1506, 1996.

[64] P. Uranga, A. I. Fernandez, B. Lopez, and J. M. Rodriguez-Ibabe, "Transition between static and metadynamic recrystallization kinetics in coarse Nb microalloyed austenite," *Materials Science and Engineering* vol. A354, pp. 319-327, 2003.

[65] T. Sakai and J. J. Jonas, "Dynamic recristallization mechanical and microstructural considerations," *Acta Materialia*, vol. 32, pp. 189-209, 1984.

[66] H. J. McQueen and N. D. Ryan, "Constitutive analysis in hot working," *Materials Science and Engineering A*, vol. 322, pp. 43-63, 2002.

[67] W. Roberts, A. Sandberg, T. Siwecki, and T. Werlefors, "Prediction of Microstructure Development During Recrystallization Hot Rolling of Ti--V Steels," *HSLA Steels, Technology and Applications*, pp. 67-84, 1983.

[68] P. Choquet, P. Fabregue, J. Giusti, B. Chamont, J. Pezant, and F. Blanchet, "Modelling of forces, structure, and final properties during the hot rolling process on the hot strip mill," *Mathematical Modelling of Hot Rolling of Steel*, pp. 34-43, 1990.

[69] P. Hodgson, "Models of the recrystallisation behaviour of C-Mn and Nb microalloyed steels during hot working processes," in *Materials forum*, 1993, pp. 403-408.

[70] A. Laasraoui and J. Jonas, "Recrystallization of austenite after deformation at high temperatures and strain rates-analysis and modeling," *Metallurgical transactions. A, Physical metallurgy and materials science*, vol. 22, pp. 151-160, 1991.

[71] H. Sekine and T. Maruyama, "Fundamental Reseach on Manufacturing of High-Tough, High Tension Steel by Controlled Rolling," *Seitetsu Kenkyu* vol. 289, pp. 43-61, 1976.

[72] A. J. DeArdo. Fundamental metallurgy of niobium steel.

[73] R. K. Ray and J. J. Jonas, "Transformation textures in steels," *International Materials Reviews*, vol. 35, pp. 1-36, 1990.

[74] A. Bodin, J. Sietsma, and S. V. D. Zwaag, "Texture and microstructure development during intercritical rolling of Low-Carbon Steels " *Metallurgical and Materials Transactions A,* vol. 33A, pp. 1589-1603, 2002.

[75] D. Vanderschueren, L. Kestens, P. Van Houtte, E. Aernoudt, J. Dilewijns, and U. Meers, "Influence of transformation induced recrystallisation on hot rolling textures of low carbon steel sheet," *Materials Science and Technology,* vol. 6, pp. 1247-1250, 1990.

[76] H. K. D. H. Bhadeshia, *Bainite in Steels*.

[77] R. Lagneborg, T. Siwecki, S. Zajac, and B. Hutchinson, "The role of vanadium in microalloyed steels," *Scandinavian Journal of Metallurgy,* vol. 28, pp. 186-241, 1999.

[78] W. B. Morrison and J. A. Chapman, "Controlled Rolling," *Phil. Trans. R. Soc. Lond. A,* vol. 282, pp. 289-303, 1976.

[79] K. J. Kurzydlowski and B. Ralph, *The quantitative description of the microstructure of materials*, 1995.

[80] C. Ouchi, T. Sampei, and I. Kozasu, "The effect of hot rolling condition and chemical composition on the onset temperature of γ-α transformation after hot rolling," *Transactions of the Iron and Steel Institute of Japan,* vol. 22, pp. 214-222, 1982.

[81] B. K. Panigrahi, "Processing of low carbon steel plate and hot strip—An overview," *Bulletin of Materials Science,* vol. 24, pp. 361-371, 2001/08/01 2001.

[82] C. Sellars and J. Beynon, "Microstructural development during hot rolling of titanium microalloyed steels," *High strength low alloy steel,* pp. 142-150, 1984.

[83] P. D. Hodgson and R. K. Gibbs, "A mathematical model to predict the mechanical properties of hot rolled C-Mn and microalloyed steels," *ISIJ International,* vol. 32, pp. 1329-1338, 1992.

[84] Y. H. Bae, J. S. Lee, J.-K. Choi, W.-Y. Choo, and S. H. Hong, "Effects of austenite conditioning on austenite/ferrite phase transformation of HSLA Steel," *Materials Transactions,* vol. 45, pp. 137-142, 2004.

[85] G. Krauss and S. W. Thompson, "Ferritic microstructures in continuously cooled low- and ultralow-carbon steels," *ISIJ International,* vol. 35, pp. 937-945, 1995.

[86] M. P. Aarnts, R. A. Rijkenberg, F. A. Twisk, D. Wilcox, M. J. Zuijderwijk, A. Arlazarov, *et al.*, "Microstructural quantification of multi phase steels (Micro-quant)," European commission2011.

[87] B. R. Commitee, *Atlas for bainitic microstructures* vol. 1: Iron and Steel Institute of Japan 1992.

[88] M. Sánchez-Araiza, S. Godet, P. J. Jacques, and J. J. Jonas, "Texture evolution during the recrystallization of a warm-rolled low-carbon steel," *Acta Materialia,* vol. 54, pp. 3085-3093, 2006.

[89] P. Chapellier, R. K. Ray, and J. J. Jonas, "Prediction of transformation textures in steels," *Acta metall. mater,* vol. 38, pp. 1475-1490, 1990.

[90] J. J. Sidor and L. A. I. Kestens, "Analytical description of rolling textures in face-centred-cubic metals," *Scripta Materialia,* vol. 68, pp. 273-276, 3// 2013.

[91] G. Kurdjumow and G. Sachs, "Über den Mechanismus der Stahlhärtung," *Zeitschrift für Physik,* vol. 64, pp. 325-343, 1930/05/01 1930.

[92] Z. Nishiyama, *Martensitic transformation*: Academic Press, 1978.

[93] B. E.C. and D. N.Y., "The nature of martensite," vol. 70, pp. 25-46, 1924.

[94] L. Sandoval, H. M. Urbassek, and P. Entel, "The Bain versus Nishiyama–Wassermann path in the martensitic transformation of Fe," *New Journal of Physics*, vol. 11, p. 103027, 2009.

[95] J. J. Jonas, "Transformation textures associated with steel processing," in *Microstructure and Texture in Steels*, Springer, Ed., ed, 2009.

[96] R. A. Vandermeer and D. J. Jensen, "Quantifying recrystallization nucleation and growth kinetics of cold-worked copper by microstructural analysis," *Metallurgical and Materials Transactions A*, vol. 26, pp. 2227-2235, 1995/09/01 1995.

[97] R. Petrov, J. J. Jonas, L. Kestens, and M. Gray, "Microstructure and texture development in pipeline steels," in *Oil and Gas Pipelines: Integrity and Safety Handbook*, R. W. Revie, Ed., ed: JohnWiley & Sons, Inc., 2014.

[98] R. Ray, J. J. Jonas, and R. Hook, "Cold rolling and annealing textures in low carbon and extra low carbon steels," *International materials reviews*, vol. 39, pp. 129-172, 1994.

[99] K. E. Esterling, *Introduction to the physical metallurgy of welding*, 1983.

[100] S. G. Hong, H. J. Jun, K. B. Kang, and C. G. Park, "Evolution of precipitates in the Nb–Ti–V microalloyed HSLA steels during reheating," *Scripta Materialia*, vol. 48, pp. 1201-1206, 4/14/ 2003.

[101] J. Zrnik, T. Kvackaj, D. Sripinproach, and P. Sricharoenchai, "Influence of plastic deformation conditions on structure evolution in Nb–Ti microalloyed steel," *Journal of Materials Processing Technology*, vol. 133, pp. 236-242, 2/1/ 2003.

[102] M. Jahazi and B. Egbali, "The influence of hot rolling parameters on the microstructure and mechanical properties of an ultra-high strength steel," *Journal of Materials Processing Technology*, vol. 103, pp. 276-279, 6/15/ 2000.

[103] S. Roy, D. Chakrabarti, and G. K. Dey, "Austenite Grain Structures in Ti- and Nb-Containing High-Strength Low-Alloy Steel During Slab Reheating," *Metallurgical and Materials Transactions A*, vol. 44, pp. 717-728, 2013/02/01 2013.

[104] J. M. R.-I. e. al., "Some aspects regarding microstructural heterogeneities during steel processing," *Materials Science Forum*, vol. 706-709, pp. 157-164, 2011.

[105] J. D. Jones and A. B. Rotwell, "Deformation under hot working conditions," Iron and Steel Institute1968.

[106] M. Machida and M. Katsumata, "Effect of rolling strain rate on the grain size of austenite recrystallized immediately after hot rolling," *Tetsu-to-Hagane*, vol. 70, 1984.

[107] C. Ouchi, T. Okita, T. Ichihara, and Y. Ueno, "Hot deformation strength of austenite during controlled rolling in a plate mill," *Trans. Iron Steel Inst. Jpn.*, vol. 20, pp. 833-841, 1980.

[108] B. Hwang, Y. Kim, S. Lee, N. Kim, and J. Yoo, "Effects of microstructure on inverse fracture occurring during drop-weight tear testing of high-toughness X70 pipeline steels," *Metallurgical and Materials Transactions A*, vol. 36, pp. 371-387, 2005/02/01 2005.

[109] S.-C. Wang, R.-I. Hsieh, H.-Y. Liou, and J.-R. Yang, "The effects of rolling processes on the microstructure and mechanical properties of ultralow carbon bainitic steels," *Materials Science and Engineering,* vol. A157, pp. 29-36, 1992.

[110] G. R. Speich and D. S. Dabkowski, "Effect of deformation in the austenite and austenite-ferrite regions on the strength and fracture behavior of C, C-Mn, C-Mn-Cb and C-Mn-Mo-Cb steels," in *The hot deformation of Austenite,* ed. AIME: AIME, 1979, pp. 557-579.

[111] J. R. Yang, C. Y. Huang, and C. S. Chiou, "The influence of plastic deformation and cooling rates on the microstructural constituents of an ultra-low carbon bainitic steel," *ISIJ International,* vol. 35, pp. 1013-1019, 1995.

[112] A. J. De Ardo, C. I. Garcia, W. Gao, and M. HUA, "Thermomechanical processing of microalloyed steels: grain refinement revisited," presented at the International Conference on Thermomechanical Processing: Mechanics, Microstructure & Control, Sheffield, 2003.

[113] T. Kimura, F. Kawabata, K. Amano, A. Ohmori, M. Okatsu, K. Uchida, *et al.*, "Heavy Gauge H-Shapes with Excellent Seismic-Resistance for Building Structures Produced by the third generation TMCP," presented at the Steel for fabricated structures international symposium, 1999.

[114] M. G. Akben, I. Weiss, and J. J. Jonas, "Dynamic precipitation and solute hardening in A V microalloyed steel and two Nb steels containing high levels of Mn," *Acta Metallurgica,* vol. 29, pp. 111-121, 1// 1981.

[115] S. H and M. T, "Controlled rolling for obtaining a fine uniform structure in high strength steels," in *Third International Conference on The Strength of Metals and Alloys* Cambridge, England 1973, pp. 85-88.

[116] H. Mohrbacher, "Principal effects of Mo in HSLA steels and cross effects with microalloying elements," *Central Iron and Steel Research Institute (CISRI),* pp. 75-96, 2010.

[117] J. Patel, "Microalloyed hot strip mill products-processing and properties."

[118] T. Baker, "Processes, microstructure and properties of vanadium microalloyed steels," *Materials Science and Technology,* vol. 25, pp. 1083-1107, 2009.

[119] K. Junhua, Z. Lin, G. Bin, L. Pinghe, W. Aihua, and X. Changsheng, "Influence of Mo content on microstructure and mechanical properties of high strength pipeline steel," *Materials & Design,* vol. 25, pp. 723-728, 12// 2004.

[120] W. B. Lee, S. G. Hong, C. G. Park, K. H. Kim, and S. H. Park, "Influence of Mo on precipitation hardening in hot rolled HSLA steels containing Nb," *Scripta Materialia,* vol. 43, pp. 319-324, 7/28/ 2000.

[121] L. Collins, "Processing of niobium-containing steels by steckel mill rolling."

[122] R. Wang, C. I. Garcia, M. Hua, K. Cho, H. Zhang, and A. J. DeArdo, "Mirostructure and precipitation behavior of Nb, Ti complex microalloyed steel produced by compact strip processing," *ISIJ International,* vol. 46, 2006.

[123] S. Vervynckt, K. Verbeken, P. Thibaux, and Y. Houbaert, "Recrystallization–precipitation interaction during austenite hot deformation of a Nb microalloyed steel," *Materials Science and Engineering: A,* vol. 528, pp. 5519-5528, 2011.

[124] M. G. Akben, B. Bacroix, and J. J. Jonas, "Effect of vanadium and molybdenum addition on high temperature recovery, recrystallization and precipitation behavior of niobium-based microalloyed steels," *Acta Metallurgica,* vol. 31, pp. 161-174, 1// 1983.

[125] M. Hua, C. I. Garcia, and A. J. DeArdo, "Precipitation behavior in ultra-low-carbon steels containing titanium and niobium," *Metallurgical and Materials Transactions A,* vol. 28, pp. 1769-1780, 1997/09/01 1997.

[126] J. Jang, Y. Heo, C. Lee, H. Bhadeshia, and D.-W. Suh, "Interphase precipitation in Ti-Nb and Ti-Nb-Mo bearing steel," *Materials Science and Technology,* vol. 29, pp. 309-313, 2013.

[127] M. Charleux, W. J. Poole, M. Militzer, and A. Deschamps, "Precipitation behavior and its effect on strengthening of an HSLA-Nb Ti Steel," *Metallurgical and Materials Transactions A,* vol. 32A, pp. 1635-1647, 2001.

[128] E. O. Hall, "The deformation and ageing of mild steel: III discussion of results," *Proceedings of the Physical Society. Section B,* vol. 64, p. 747, 1951.

[129] N. J. Petch, "The cleavage strength of polycrystals," *J. Iron and Steel Inst.,* vol. 174, 1953.

[130] Y. Hai-Iong, D. Lin-xiu, W. Guo-dong, and L. Xiang-hua, "Development of Nb-V-Ti hot-rolled high strength steel with fine ferrite and precipitation strengthening," *Journal of Iron ans Steel Research International,* vol. 16, pp. 72-77, 2009.

[131] T. J. Koppenaal and D. KuhlmannWilsdorf, "The effect of prestressing on thestregth of neutronirradiated copper single crystals," *Applied Physics Letters,* vol. 4, 1964.

[132] K. J. Irvine, "Keynote Speech physical metallurgy of steel," *Phil. Trans. R. Soc. Lond. A,* vol. 282, pp. 339-346, 1976.

[133] J. Majta, J. G. Lenard, and M. Pietrzyk, "A study of the effect of the thermomechanical history on the mechanical properties of a high niobium steel," *Materials Science and Engineering,* vol. A208, pp. 249-259, 1996.

[134] U. F. Koks, "The Theory of an obstacle-controlled yield strength," *Materials Science and Engineering,* vol. 27, pp. 291 - 298, 1977.

[135] H. K. D. H. Bhadeshia and R. W. K. Honeycombe, *Steels microstructure and properties,* 2006.

[136] H. Conrad and S. Frederick, "The effect of temperature and strain rate on the flow stress of iron," *Acta Metallurgica,* vol. 10, pp. 1013-1020, 11// 1962.

[137] G. I. Taylor, "The mechanism of plastic deformation of crystals," *Proceedings of the Royal Society of London. Series A,* vol. 145, pp. 362-388, 1934.

[138] M. Takahashi and H. K. D. H. Bhadeshia, "Model for transition from upper to lower bainite " *Materials Science and Technology,* vol. 6, pp. 592-603, 1990.

[139] E. Orowan, "The theory of yield without particle shear," in *Symposium on Internal Stresses in Metals and Alloys,* London - United Kingdom, 1948, pp. 451-453.

[140] B. Bilby, "Les dislocations by J. Friedel," *Acta Crystallographica,* vol. 10, p. 488, 1957.

[141] M. F. Ashby, "The theory of the critical shear stress and work hardening of dispersion-hardened crystals," in *Metallurgical Society Conference Oxide Dispersion Strenghening,* New York - USA, 1966, pp. 143-205.

[142] F. B. Pickering, *Physical metallurgy and the design of steels*. London: Applied Science Publishers, 1978.

[143] T. Gladman, *The physical metallurgy of microalloyed Steels*: Maney for the Institute of Materials, 2002.

[144] W. C. Leslie, "Iron and its dilute substitutional solid solutions," *Metallurgical Transactions,* vol. 3, pp. 5-26, 1972/01/01 1972.

[145] M. J. Cancio, G. Echaniz, and T. E. Perez, "Characterisation of microalloy precipitates in the austenitic range of high strength low alloy steels," *Steel research,* vol. 73, pp. 340-346, 2002.

[146] T. Gladman, I. D. mclvor, and E. B. Pickering, "Some aspects of the structure-property relationships in high-carbon ferrite-pearlite steels," *Iron and Steel Institute,* vol. 210, pp. 916-930, 1972.

[147] A. Pineau and T. Pardoen, "2.06 - Failure of metals," in *Comprehensive Structural Integrity*, I. Milne, R. O. Ritchie, and B. Karihaloo, Eds.,Oxford: Pergamon, 2007, pp. 684-797.

[148] V. Tvergaard, "Ductile fracture: micromechanisms," in *Encyclopedia of Materials: Science and Technology (Second Edition)*, K. H. J. Buschow, R. W. Cahn, M. C. Flemings, B. Ilschner, E. J. Kramer, S. Mahajan, *et al.*, Eds., Oxford: Elsevier, 2001, pp. 2355-2362.

[149] R. W. Hertzberg, *Deformation and fracture mechanics of engineering materials*: John Wiley & Sons, 1989.

[150] H. G. F. Wilsdorf, "The ductile fracture of metals: A microstructural viewpoint," *Materials Science and Engineering,* vol. 59, pp. 1-39, 5// 1983.

[151] A. Pineau, "Development of the local approach to fracture over the past 25 years: theory and applications," *International Journal of Fracture,* vol. 138, pp. 139-166, 2006/03/01 2006.

[152] J. R. Rice, "A path independent integral and the approximate analysis of strain concentration by notches and cracks," *Journal of Applied Mechanics,* vol. 35, pp. 379-386, 1968.

[153] K. Toshiro, Y. Isamu, and N. Mitsuo, "Evaluation of dynamic fracture toughness parameters by instrumented Charpy impact test," *Engineering Fracture Mechanics,* vol. 24, pp. 773-782, // 1986.

[154] W. Guo, H. Dong, M. Lu, and X. Zhao, "The coupled effects of thickness and delamination on cracking resistance of X70 pipeline steel," *International Journal of Pressure Vessels and Piping,* vol. 79, pp. 403-412, 6// 2002.

[155] B. Tanguy, T. T. Luu, G. Perrin, A. Pineau, and J. Besson, "Plastic and damage behaviour of a high strength X100 pipeline steel: Experiments and modelling," *International Journal of Pressure Vessels and Piping,* vol. 85, pp. 322-335, 5// 2008.

[156] A. L. Gurson, "Continuum theory of ductile rupture by void nucleation and growth: Part I—yield criteria and flow rules for porous ductile media," *Journal of Engineering Materials and Technology,* vol. 99, pp. 2-15, 1977.

[157] G. Rousselier, "Ductile fracture models and their potential in local approach of fracture," *Nuclear Engineering and Design,* vol. 105, pp. 97-111, 12// 1987.

[158] G. D. Fearnehough, "Fracture propagation control in gas pipelines: A survey of relevant studies," *International Journal of Pressure Vessels and Piping,* vol. 2, pp. 257-282, 10// 1974.

[159] C. J. McMahon Jr and M. Cohen, "Initiation of cleavage in polycrystalline iron," *Acta Metallurgica,* vol. 13, pp. 591-604, 6// 1965.

[160] A. Echeverria and J. M. Rodriguez-Ibabe, "Cleavage micromechanisms on microalloyed steels. Evolution with temperature of some critical parameters," *Scripta Materialia,* vol. 50, pp. 307-312, 1// 2004.

[161] M. Fukuda, K. Kunishige, and S. Sugisawa, "Separations occurring at the fracture surfaces of controlled rolled hot-strips," *Tetsu-to-Hagane,* vol. 64, pp. 740-748, 1978.

[162] M. Iino, H. Mimura, and N. Nomura, "Delamination in linepipe steels" *Transactions of the Iron and Steel Institute of Japan,* vol. 17, pp. 450-458, 1977.

[163] I. Kozasu, H. Kubota, and T. Shimizu, "Recrystallization of austenite of Si-Mn steels with minor allowing elements after hot-rolling," *Transactions of the Iron and Steel Institute of Japan,* vol. 11, pp. 367-&, 1971.

[164] M. T., E. T., F. T., and O. R., *Tetsu-to-Hagane,* vol. 63, 1977.

[165] A. Lambert-Perlade, T. Sturel, A. F. Gourgues, J. Besson, and A. Pineau, "Mechanisms and modeling of cleavage fracture in simulated heat-affected zone microstructures of a high-strength low alloy steel," *Metallurgical and Materials Transactions A,* vol. 35, pp. 1039-1053, 2004/03/01 2004.

[166] A. A. Griffith, "The phenomena of rupture and flow in solids," *Philosophical Transactions of the Royal Society of London. Series A, Containing Papers of a Mathematical or Physical Character,* vol. 221, pp. 163-198, January 1, 1921 1921.

[167] J. Kameda and C. J. McMahon, "Solute segregation and brittle fracture in an alloy steel," *Metallurgical and Materials Transactions A,* vol. 11, pp. 91-101, 1980/12/01 1980.

[168] V. Tvergaard, "Material failure by void growth to coalescence," *Advances in applied Mechanics,* vol. 27, pp. 83-151, 1990.

[169] O. a. G. Journal. (2008). *Fracture propagation, Conclusion: Prediction steel grade dependent*. Available: http://www.ogj.com

[170] D. J. Horsley, "Background to the use of CTOA for prediction of dynamic ductile fracture arrest in pipelines," *Engineering Fracture Mechanics,* vol. 70, pp. 547-552, 2// 2003.

[171] P. Hopkins, *The structural integrity of oil and gas transmissiion pipelines*: Elsiever publishers, 2002.

[172] C. S. Wiesner, "Predicting structural crack arrest behaviour using small-scale material characterisation tests," *International Journal of Pressure Vessels and Piping,* vol. 69, pp. 185-196, 12// 1996.

[173] T. Kobayashi, "Impact Testing," in *Encyclopedia of Materials: Science and Technology (Second Edition)*, K. H. J. B. Editors-in-Chief: , W. C. Robert, C. F. Merton, I. Bernard, J. K. Edward, M. Subhash, *et al.*, Eds., ed Oxford: Elsevier, 2001, pp. 4027-4031.

[174] A. B. Rothwell, M. Urednicek, and A. Gilroy-Scott, "Requirements for control of ductile fracture propagation in large-diameter gas transmission pipelines," *J. Materials for Energy Systems,* vol. 2, pp. 30-40, 1980.

[175] K. C. Koppenhoefer and R. H. Dodds Jr, "Ductile crack growth in pre-cracked CVN specimens: numerical studies," *Nuclear Engineering and Design,* vol. 180, pp. 221-241, 4// 1998.

[176] G. Bernauer, W. Brocks, and W. Schmitt, "Modifications of the Beremin model for cleavage fracture in the transition region of a ferritic steel," *Engineering Fracture Mechanics,* vol. 64, pp. 305-325, 10// 1999.

[177] T. Varga, "Crack initiation, propagation and arrest criteria for steel structure safety assessment," *Structural Safety,* vol. 12, pp. 93-98, 6// 1993.

[178] S. Y. Shin, B. Hwang, S. Kim, and S. Lee, "Fracture toughness analysis in transition temperature region of API X70 pipeline steels," *Materials Science and Engineering: A,* vol. 429, pp. 196-204, 8/15/ 2006.

[179] R. Higuchi, H. Makino, and I. Takeuchi, "New concept and test method on running ductile fracture arrest for high pressure gas pipeline," presented at the 24th World gas conference, Buenos Aires (Argentina), 2009.

[180] A. B. Rothwell, "Fracture propagation control for gas pipelines – past, present and future," in *Pipeline Technology*, Brugge (Belgium), 2000.

[181] S. H. Hashemi, "Apportion of Charpy energy in API 5L grade X70 pipeline steel," *International Journal of Pressure Vessels and Piping,* vol. 85, pp. 879-884, 12// 2008.

[182] S. H. Hashemi, "Correction factors for safe performance of API X65 pipeline steel," *International Journal of Pressure Vessels and Piping,* vol. 86, pp. 533-540, 8// 2009.

[183] W. A. Poynton and G. D. Fearnehough, "An analysis of shear fracture propagation in gas pipelines," presented at the Lehigh Conf. on Dynamic Crack Propagation, 1972.

[184] K. N. Murty, N. K. Rao, and H. Krishnan, "Application of instrumented impact testing for studying dynamic fracture behaviour of rotor steels," *Engineering Fracture Mechanics,* vol. 18, pp. 1173-1184, // 1983.

[185] H. Yoshida, K. Miyata, Y. Hayashi, M. Narui, and H. Kayano, "Instrumented charpy impact tests of austenitic and ferritic steels," *Journal of Nuclear Materials,* vol. 133–134, pp. 317-320, 8// 1985.

[186] L. H. Zhu, Q. X. Zhao, H. C. Gu, and Y. S. Lu, "Application of instrumented impact test for studying dynamic fracture property of 9Cr-1Mo-V-Nb-N steel," *Engineering Fracture Mechanics,* vol. 64, pp. 327-336, 10// 1999.

[187] P. R. Sreenivasan, A. Moitra, S. K. Ray, S. L. Mannan, and R. Chandramohan, "Dynamic fracture toughness properties of a 9Cr•1Mo weld from instrumented impact and drop-weight tests," *International Journal of Pressure Vessels and Piping,* vol. 69, pp. 149-159, 12// 1996.

[188] T. Kobayashi, "Analysis of impact properties of A533 steel for nuclear reactor pressure vessel by instrumented Charpy test," *Engineering Fracture Mechanics,* vol. 19, pp. 49-65, // 1984.

[189] K. Kuhne, H. Dunnewald, and W. Dahl, "Reasons for the appearance of separations in HSLA-steels," presented at the 4th European Conference on Fracture E.C.F. , Leoben, Austria, 1982.

[190] S. Matsuda, Y. Kawashima, S. Sekiguchi, and M. Okamoto, "Mechanism of Separation of A Low-carbon Low Alloy Steel Control-Rolled in Austenite and Ferrite Two Phase Regions," *Tetsu-to-Hagane*, vol. 68, pp. 435-443, 1982.

[191] G. Baldi and G. Buzzichelli, "Critical stress for delamination fracture in HSLA steels," *Metal Science*, vol. 12, pp. 459-472, 1978.

[192] F. DE Kazinczy and W. Backofen, *Influence of Hot-rolling Conditions on Brittle Fracture in Steel Plate*: Defense Technical Information Center, 1960.

[193] K. J.F., in *Effect of Second phase particles on the mechanical properties of steel*, London, England, 1971.

[194] T. Tanaka, T. N., H. T., and S. C., in *Microalloying '75*, New York, 1977, p. 107.

[195] X.-K. Zhu and B. N. Leis, "CVN and DWTT energy methods for determining fracture arrest toughness of high strength pipeline steels," in *9th International Pipeline Conference*, 9th International Pipeline Conference, 2012.

[196] B. N. Leis, "Alternative view of fracture propagation in pipelines," in *6th International Pipeline Technology Conference*, Ostend, Belgium, 2013.

[197] G. Wilkowski, Y. Hioe, and D.-J. Shim, "Methodology for brittle fracture control in modern line pipe steels," in *6th International Pipeline technology Conference* ostend, Belgium, 2013.

[198] G. Wilkowski, Y. Hioe, P. Mincer, B. Tosi, G. Wall, S. Igi, *et al.*, "West Jefferson burst test results to assess abnormal fracture appearance in DWTT for X65 TMCP steel pipe," in *6th International Pipeline Technology Conference*, Ostend, Belgium, 2013.

"Simplicity is the ultimate sophistication."

Leonardo da Vinci (1452-1519)

CHAPTER III

Statement of objectives

III.1 Issues

Knowledge evolves with time; early studies on the topic of the present PhD thesis were constrained by the steel grades produced and the characterization techniques of each epoch. However, fundamental knowledge is updated as needed, as materials and available production technologies are improved. Many functional properties of HSLA steels, such as the strength, toughness, and crack arrestability are determined by the microstructure. The control of these microstructures depends on both our knowledge concerning technology and concerning physical-mechanical metallurgy. Furthermore, an understanding of the relation between the microstructure and the properties of the steel is essential in order to optimize the TMCP with regards to technological, economic, and environmental constraints. Fundamental to this optimization is an understanding of how the HSLA pipeline steel is affected by the deformation path in different temperature ranges, and in addition, how the subsequent cooling route influences the microstructure evolution of the hot deformed material.

III.2 Goal definition

Consequently, this thesis is aimed at elucidating the correlation among the composition, processing, microstructure, mechanical properties, and performance of pipeline steels, particularly with regards to the following aspects (points):

- Understanding the influence of the chemical composition and processing parameters during final rolling on the microstructure of the pipeline steel sheets.
- Understanding the microstructure – properties relation in loading conditions which are specific for pipeline steel skelp.

III.3 General methodology

To achieve the aforementioned goal, the current study focused on the influence of processing parameters on the microstructural formation, and by extension the mechanical performance, based on the philosophy of continual upgrade of knowledge. Figure III.3 1 illustrates the strategy developed in the progress of the complete PhD thesis project.

Relevant studies related to the field of TMCP of HSLA pipeline steels were used as a starting point in order to identify the particular process stage on which the research should be focused. Key issues regarding the control of the non-recrystallization temperature in HSLA steels (S. Vervynckt thesis [1]), and the control of mechanical anisotropy of pipeline steels (N. Sanchez Mourino thesis [2]) were successfully investigated within the research group during the recent years. However, a quantitative description of the microstructure formation during the final rolling stage and their influence on the properties remained elusive.

Hence, it was decided to pay particular attention to the *influence of processing conditions during finishing rolling on the microstructure and final mechanical properties*. For this purpose, a series of steel grades and thermo-mechanical processing schedules were designed and performed in collaboration with an industrial partner (ArcelorMittal Global R&D Gent, OCAS NV).

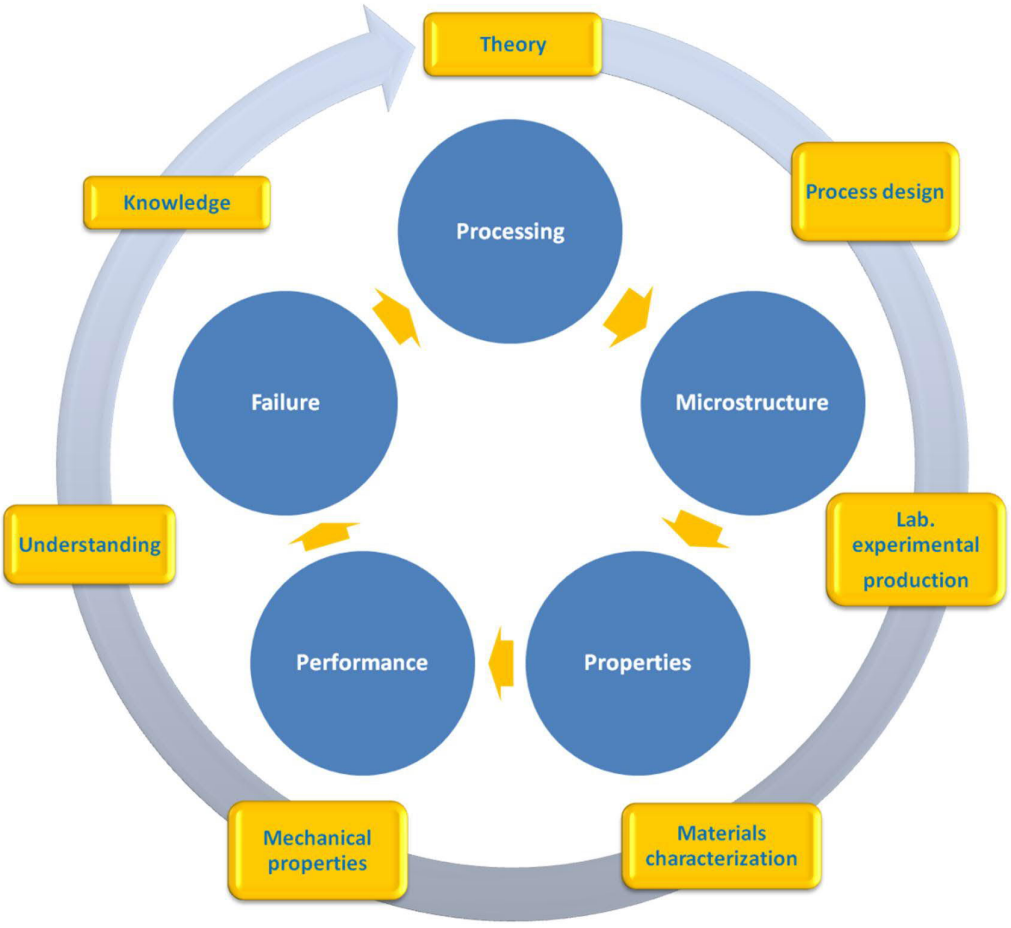

Figure III.3-1 *PhD project strategy. The figure highlights that the microstructure of a material will depend on how it is processed. The properties are, determined by the microstructure. Furthermore, the performance of the material will be a function of its properties. In particular cases, failure or the response of the material during failure, can be interconnected to the microstructure and, by extension, to the processing condition. With a focus on HSLA pipeline steels, the study addresses the influence of processing parameter on the performance by combining: (i) existing know how, (ii) expertise in TMCP process design, (iii) experimental laboratory production of materials, (iv) advanced characterization techniques, and (iv) analytical study of the experimental outcomes. The ultimate goal is to understand how the changes in one or more parameters influence the microstructure and the respective properties of specific grades of HSLA steels. The approach was formulated in a cyclic manner, since the output of the first set of experiments were used to design and guide subsequent process designs.*

Using the available techniques and equipment at the Department of Materials Science and Engineering and at OCAS NV, detailed characterizations of the steels at each processing step were carried out in order to correlate the microstructure with the measured mechanical properties (strength & toughness).

Cross correlations between processing parameter-microstructure-properties were subsequently identified and analysed in depth. A series of hypotheses was formulated at this point. Those which respected the established laws & conditions of fundamental metallurgy and simultaneously concurred with earlier works within the field, (not necessarily the same type of studies but studies with some common points), were considered in further detail. As a result, concluding statements about the impact of a given process parameter on the microstructure and mechanical properties were presented. Complementary hypotheses regarding microstructure and texture evolution were evaluated and/or validated by means of parallel, independent experimental techniques and model simulations.

Moreover, in some cases, a more complete understanding of the existing knowledge was provided. In other cases, a completely new understanding of the phenomenological events which occur during the variation of certain TMCP parameters and their effect on final properties were obtained.

III.4. Structure of the work

The PhD thesis is organised into 8 chapters; Chapter I introduces the subject and describes the importance of the pipeline steel with regards to societal needs; prognoses for the future are also considered. Chapter II includes an overview of the most relevant advances in the field of TMCP (with special emphasis on HSLA pipeline steels). Chapter III states the objectives and the general methodology of the work. Chapter IV briefly describes the experimental procedures. Chapter V describes and discusses the microstructure and texture evolution which occur during the studied TMCP. The effects of variations in the TMCP parameters on mechanical properties were also investigated. In addition, the mechanical behavior was analyzed as a function of the chemical composition. An analysis of the process parameters (i.e. finishing rolling reduction draught, cooling condition) is also described. The third section of Chapter V focuses on the investigations into microstructural control of the fracture toughness. Furthermore, the determination of the strengthening mechanism under different rolling parameters is described in the last part of Chapter V. Chapter VI provides a comprehensive assessment of the correlations among processing parameters, microstructure, and properties. In this general discussion chapter, a number of explanations will be given to clarify the variability of the mechanical properties presented in chapter V. The aforementioned discussion includes particular implications of recrystallization-precipitation interactions on

the TMCP schedules used in the thesis. An interpretation of the synergies between different strengthening mechanisms is also included. To finalize, Chapter VI incorporates a description of the proposed variables governing fracture resistance in HSLA pipeline steels. Chapter VII summarizes the main conclusions of the thesis, and Chapter VIII enumerates the suggestions for further studies.

References

[1] S. Vervynckt, "Control of the non-recrystallization temperature in high strength low alloy (HSLA) steels," Doctor in Materials Science, Department of Materials Science and Engineering, Ghent University Gent, 2010.

[2] N. S. Mouriño, "Crystallographically controlled mechanical anisotropy of pipeline steels," Doctor in de Ingenieurswetenshappen, Department of Materials Science and Engineering, Ghent University, Gent, 2010-2011.

"Although nature commences with reason and ends in experience it is necessary for us to do the opposite that is to commence with experience and from this to proceed to investigate the reason".

Leonardo da Vinci (1452-1519)

CHAPTER IV

Experimental procedure

IV.1 Materials

Table IV.1-1 shows the chemical compositions of the steels studied in this work. This broad range compositions was used to determine the effect of the chemical composition on the technological properties; however, owing to confidentiality agreements, the exact composition of the steels cannot be disclosed. The relative amounts of C and Nb for the five investigated compositions are indicated in Table IV.1-2. Steel 1 was used as the reference material. The reference HSLA steel was delivered in the shape of an industrial slab, and was cut into 75mm-thick pieces. Special attention was paid during cutting of the material so that a region free of centre line segregation could be obtained. This material is referred, within the frame of the thesis, to as Medium carbon – High niobium (cf. Table IV.1-2).

C	Mn	P	S	Nb+V+Ti	Mo+Ni+Cu+Cr
0.02-0.1	1.6	<0.02	<0.003	<0.1	<0.1

Table IV.1-1 *Generic chemical composition (mass %).*

Chemistry	Relative C content	Relative Nb content
Steel 1	Medium	High
Steel 2	Low	Low
Steel 3	Low	Medium
Steel 4	High	Low
Steel 5	High	Medium

Table IV.1-2 *Relative amounts of C and Nb elements for the five steel grades investigated in this PhD thesis.*

The reference steel with medium C and high Nb content was used to study the influence of Finish Rolling Temperature (FRT), cooling condition (ACC or air cooling), and finish rolling reduction draught (constant, increasing, decreasing) on the microstructural features (grain size, phase distribution, texture) and mechanical properties (V-Charpy impact toughness, tensile strength, and elongation).

The same reference steel was used to trace the changes in material microstructure and properties during TMCP, in particular:

- Austenitic microstructure evolution (grain size, morphology, and texture);
- Precipitate evolution in austenite and ferrite/bainite;
- Influence of different austenite conditioning on the toughness.

Steels 2 to 5 (see Table IV.1-2) were specially designed to meet the needs of the research work as it relates to variations of C and Nb. They were prepared in different heats in an induction melting and cast unit under vacuum. Steels 1 to 5 were used to study the effect of C – Nb contents on microstructure and mechanical properties under four common rolling schedules (draughts), namely constant reduction per pass combined with high/low FRT and ACC/air cooling.

IV.2 Materials processing

A summary of the TMCP schedules used for each steel composition is shown in Table IV.2-1.

TMCP schedules were designed based on constraints imposed by a series of metallurgical events. For the purposes of TMCP design, preliminary values of the reheating temperature of the slabs, the T_{nr} (recrystallization stop temperature of austenite), and the A_{r3} (the γ to α transformation start temperature) were determined for the strained and non-strained austenite. This was done by using the empirical equations available in the literature [1-3], which allow estimation of the Tnr for predefined deformation conditions based on the steel compositions.

Chem. 1		Chem. 2		Chem. 3		Chem. 4		Chem. 5		Reheat Tem. ºC	Rough Temp. Out	Reduction PER PASS	FRT	Cooling	Coiling T. ºC
1	Med. C High Nb	13	Low C Low Nb	17	Low C Med. Nb	21	High C Low Nb	25	High C Med. Nb	1250	1180	=	1000	AIR	
2		14		18		22		26					800		
3		15		19		23		27					1000	ACC	560
4		16		20		24		28					800		
5												↗	1000	AIR	
6													800		
7													1000	ACC	560
8													800		
9												↘	1000	AIR	
10													800		
11													1000	ACC	560
12													800		

Table IV.2-1 *Summary of the TMCP schedules used for the different chemical compositions.*

IV.2.1 Laboratory rolling mill and ancillary equipment

The TMCP was performed on a 2-high Carl Wezel BW 400 (400mm roll diameter, and 400t rolling force) laboratory rolling mill, complemented with a reheating furnace, an ACC cooling bed line, and a coiling simulation furnace. A general view of the rolling mill facilities is presented in Figure IV.2-1. A programmable heating furnace was used to soak the blocks for 2h at 1250ºC. The rolling schedules were computer-controlled and the rolling data (load, torque, speed, roll gap) were recorded as a function of time. The cooling rate during ACC was settled by controlling the nozzle diameter and water flow on the ACC cooling bed. In addition, the temperature was monitored with thermocouples which were inserted at the mid-thickness of the block; the surface temperature during rolling was monitored by pyrometers. The accuracy of the temperature measurements was ±2°C.

Figure IV.2-1 *Rolling facilities at the Metal Processing Centre.*

IV.3 Experimental techniques

Plates after TMCP were sampled according to the scheme shown in Figure IV.3-1. Metallography characterization was carried out in samples obtained from the pink region (nearest to the thermocouple).

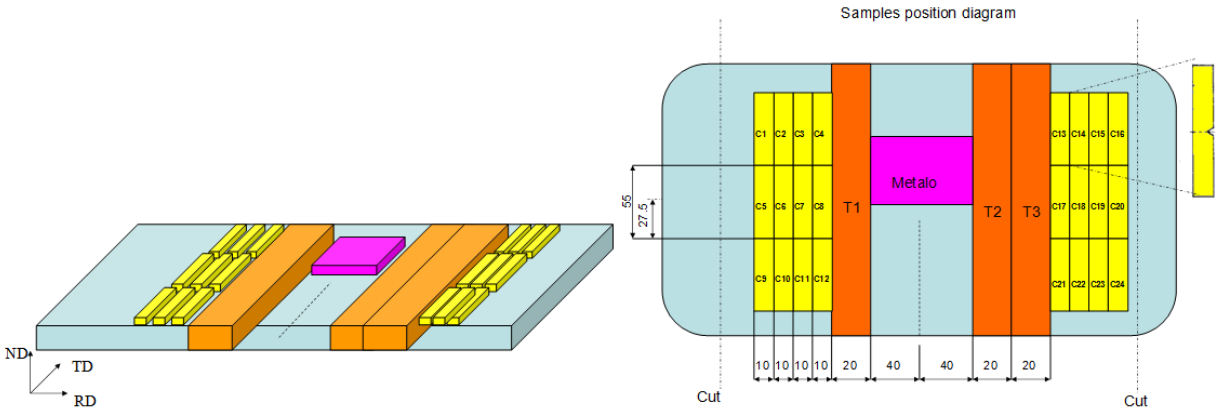

Figure IV.3-1 *Schematic view of the sampling regions for: metallographic characterization, tensile test, and V-notch Charpy test.*

Three tensile test samples (T1-3) were taken from the areas in orange, whereas the V-notch Charpy specimens are schematically represented in yellow (C1-24).

A number of techniques were employed in order to characterize the microstructure at all length scales. Figure IV.3-2 schematically displays the methods used to identify the correlations between the mechanical properties and the microstructural features after each particular TMCP schedule.

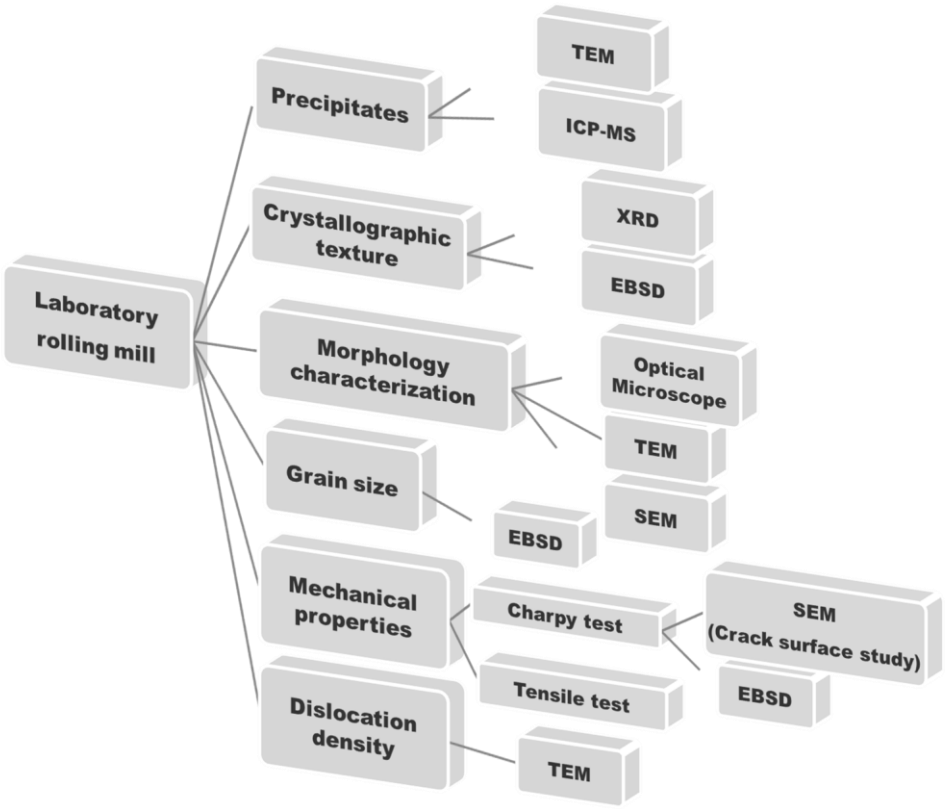

Figure IV.3-2 *Schematic view of the employed characterization techniques.*

IV.3.1 Microstructural characterization

Several characterization techniques, including optical microscopy (OM), scanning electron microscopy (SEM), electron back scatter diffraction (EBSD), X-Ray diffraction, Inductively-Coupled Plasma Mass Spectrometry (ICP-MS), and transmission electron microscopy (TEM) were used in this work. Specimens for OM, SEM, and EBSD were prepared such that the longitudinal (rolling direction) and the normal (through-thickness direction) could be observed i.e., the observation is in a plane perpendicular to the plate transverse direction (see Figure IV.3-3). In most cases, the characterization was done at ¼ thicknesses, which is considered representative of the microstructure of the rolled plates. However, through-

thickness measurements were performed in a number of samples in order to determine the corresponding distribution of microstructural features.

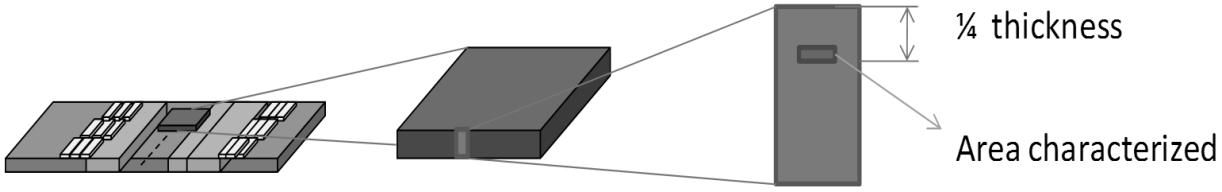

Figure IV.3-3 *Schematic view of the region of the TMCP plate that was characterized.*

Samples for XRD and TEM characterization were obtained at ¼ thickness and ½ thickness for XRD and ¼ thickness for TEM in such a way that the longitudinal (rolling direction) and transversal directions could be observed i.e., the characterization is done in the plane parallel to the rolling plane.

Cubic-shaped (5-7mm side) samples for ICP-MS were obtained from the ¼ thickness.

IV.3.1.1 Optical microscopy

Samples for optical metallography were cut and mounted in bakelite, ground on 80, 180, 240, 320, 400, 600, and 1200 grit silicon carbide papers, and finally polished with 3µm and 1µm diamond paste. The microstructure was investigated using a ZEISS JENAVERT microscope. Two different etching procedures were used to reveal the prior austenite microstructures, and the austenite transformation products:

(I) The former austenite grains of the as-quenched specimens (intermediate-quenched samples at different stages of TMCP) were revealed by Bechet and Beaujard's etching [4]. The quantification of the grain size was made following the mean linear intercept method according to ASTM E112-12 [5].

(II) The ferritic-bainitic-pearlitic microstructures were revealed using a 2% solution of HNO_3 in ethanol (nital) for 6-10s at room temperature.

After optical microscopy, the volume fraction of the second phase constituents (pearlite, MA, etc.) was determined using Image J® software.

IV.3.1.2 Scanning Electron Microscopy (SEM)

The microstructures were characterized by scanning electron microscopy (SEM). SEM samples were prepared using the same steps as OM. The analyses were conducted using a FEI® Nova Nanolab Dual-Beam Focused Ion Beam (FIB) and a FEI® Quanta, each equipped with a Field Emission Gun FEG-SEM column. The FEI® Quanta was interfaced with an EDAX energy dispersive x-ray spectrometer in order to determine the steel and precipitate compositions.

IV.3.1.2.1 Electron Backscatter Diffraction (EBSD)

Electron Backscatter Diffraction (EBSD) analysis was used to determine the crystallographic texture, grain boundary misorientation, and to accurately measure the ferrite grain size of the final TMCP samples. The EBSD samples were prepared using the same steps as for the OM samples. After mechanical polishing, samples were electrolytically polished (parameters: flow rate 7; voltage 22V; time 11s; temperature 22°C; sample area ½ cm^2) with A2 Struers® electrolyte. Further, wet polishing was carried out with OP-U suspension (~35nm particle size) for 20-30min, with an applied force of ~5N, especially in the case of samples whose response to the A2 electrolyte was not satisfactory. The EBSD data were acquired on a rectangular scan grid with step sizes of 0.2µm and 0.5µm (depending on the scan size). Data were post-processed with OIM-TSL® Data analysis 4.6 software. The grains were defined according to 15° misorientation criteria; i.e., any two pixels in a grain are misoriented by a maximum 15° from each other and each grain consists of a minimum five and two pixels, respectively, for scans performed at step sizes of 0.2 µm and 0.5 µm step. The EBSD technique and texture analysis methods are described in detail elsewhere [6, 7].

IV.3.1.2.1.1 Critical assessment of the accuracy of the EBSD measurements

EBSD data acquisition strongly depends on the time constraints linked to equipment availability. During the experimental phases of the present work, EBSD scans could be performed in only the uneven blocks of time which were available. Therefore, two step size criteria were chosen in order to cover similar areas when time constraints were different. In order to quantify the impact of step size on the grain size determination, the following experiment was carried out: *(i)* a random region was selected; *(ii)* a first scan with 0.5µm step

size was acquired; *(iii)* a second scan of the aforementioned area was acquired with 0.2µm step size; all other acquisition parameters remained unchanged. As shown in Figure IV.3-4, the impact on grain size quantification (either average grain size or area fraction of grains) is very small. Consequently, it was decided that data obtained from those two step sizes were perfectly comparable.

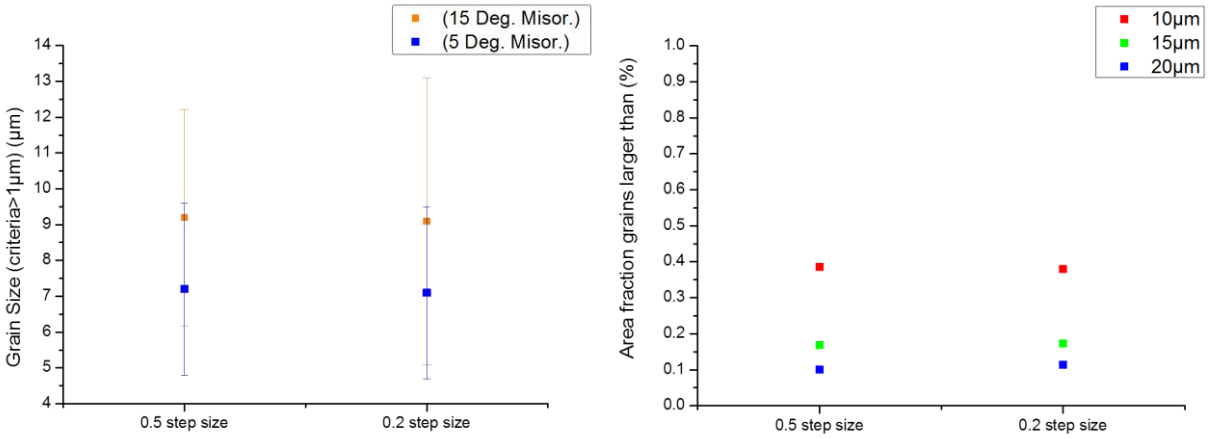

Figure IV.3-4 *Quantification of impact on grain size when different acquisition step sizes (0.5 and 0.2µm) were used.*

IV.3.1.3 X-ray Diffraction

Macro-texture data were obtained via X-ray diffraction a (Siemens D5000® X-ray diffractometer) with Mo Kα radiation (λ=0.071nm) at 40kV and 50mA. Orientation distribution functions (ODFs), for Lmax =16, were calculated from the (110), (200), (211), and (310) incomplete pole figures using FHM-MTM software developed by Van Houtte [8, 9]. This software employs Ghost correction algorithms [10] and is based on the conventional Bunge method of pole figure inversion. For further reading on these topics, please see [11, 12].

IV.3.1.4 Transmission Electron Microscopy (TEM)

Detailed microstructural analysis (austenite product morphology, precipitate analysis, and measurement of dislocation density) was conducted using the JEOL® JEM-2200FS transmission electron microscope (TEM) operated at a high tension of 200kV and equipped with an in-column omega filter. This filter reduces image blurring, caused by chromaticity of inelastically-scattered electrons when observing thick sample areas. The micrographs and electron diffraction patterns were taken from (¼ thickness) thin foils and carbon extractive replicas using the following microscope modes: bright field (BF) imaging in scanning

transmission regime (STEM), selected area electron diffraction (SAED), and convergent beam electron diffraction (CBED). Additional details about the observation parameters are mentioned in the discussion of each image.

TEM foil specimens were prepared by grinding and polishing (up to 100µm thickness) of the material, followed by punching a 3mm diameter disk by a dedicated device that prevents the introduction of plastic deformation in the central part of the sample. The disks were subsequently thinned using the twin-jet electro-polishing setup of Struers® -Tenupol-5 with 10 vol.% solution of perchloric acid in methanol (parameters: voltage 14V; at 25°C, single flow, flow rate 20).

Carbon replicas were taken from ¼ thickness ground and polished samples. After cleaning the surface of interest with ethanol, the samples were etched with 2% nital solution. A 20 nm-thick carbon film was then deposited on the surface and the carbon replicas were submerged into 4% nital solution. The replicas were extracted from the solution by rinsing with ethanol and demi water before being collected on Cu grids suited for TEM observation. Detailed explanation of the procedure used for determination of the dislocation density is given in chapter V.4.1.2.

IV.3.1.5 Inductively Coupled Plasma Mass Spectrometry (ICP-MS)

Small 7x7x7mm cubic specimens were cut from the ¼ thickness region of the strip and selectively dissolved in order to determine the amount of Nb and Ti precipitated. The resulting solution, which consists of base metal and precipitated micro-alloying elements, was filtered; undissolved precipitates were trapped with the filter whereas the dissolved iron matrix and the remaining elements in solid solution were filtrated. The fraction of Nb and Ti -containing particles which were attached to the filter, contained in the residue solution, and precipitated, were determined via Inductively Coupled Plasma Mass Spectroscopy (ICP-MS). ICP-MS is typically used to quantitatively measure the elemental composition of materials. During ICP-MS, a high-temperature Inductively Coupled Plasma (ICP) source is used to ionize the atoms of the elements and these ions are then separated and detected by a mass spectrometer. The ICP-MS technique is described in detail elsewhere [13, 14].

IV.3.1.6 Dilatometry

Dilatometry is a technique used to measure the expansion or shrinkage in one direction of a material that is subjected to temperature variations. In steel, dilatometry is of special importance since the mentioned change in volume can be correlated with the solid–solid phase transformations [15]. Moreover, dilatometry coupled with uniaxial compression can be used to study austenite softening and recrystallization behavior at high temperatures [16, 17]. In this work, double deformation tests were conducted using a Bähr® DIL 805 plastodilatometer. The tests were conducted according to the standard procedure described elsewhere [18, 19]. The principle of the test is explained in details in [16, 17]. It consists of measuring the resistance of the material to deformation in two steps which are separated by an inter-deformation time. Both deformations are performed at the same pre-defined temperature. The softening fraction is determined by comparing the stress strain curves of each deformation step. In addition, the 2% offset method (see Figure IV.3-5) was used to quantify the softening.

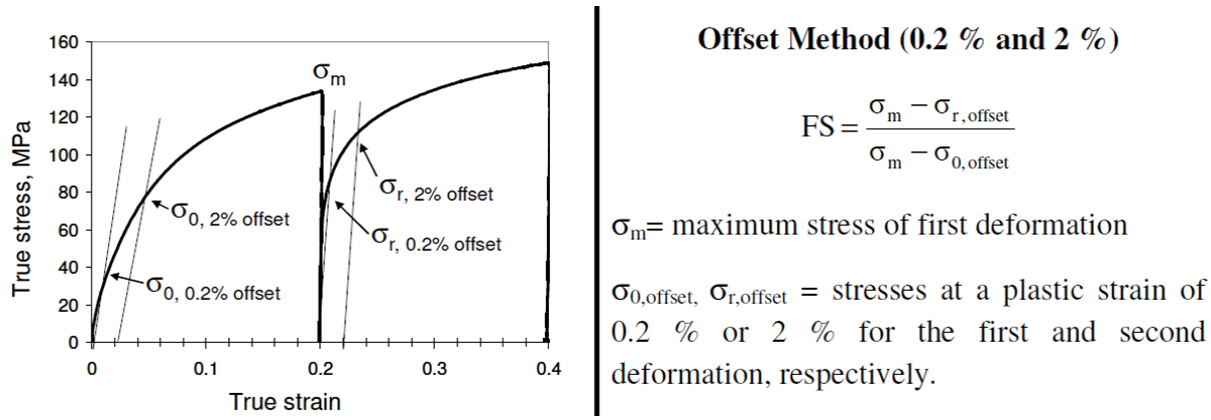

Figure IV.3-5 *Schematic representation of and equation used for the fractional softening calculation according to the 0.2% and 2% methods [16].*

Cylindrical samples for the double deformation test were machined by spark erosion. The dimensions of the sample were ∅5mm × 10mm (diameter × length).

IV.3.2 Mechanical properties characterization

IV.3.2.1 Tensile test

Tensile tests were performed in order to quantify the impact of different TMCP conditions on the strength. The long axis of each 12-mm-thick specimen was oriented along the plate

transverse direction, in accordance with the ASTM-E8 specification [20]. The specimens were tested at room temperature at strain rates of 0.03 and $1s^{-1}$. The dimensions of the tensile specimens are shown in Figure IV.3-6.

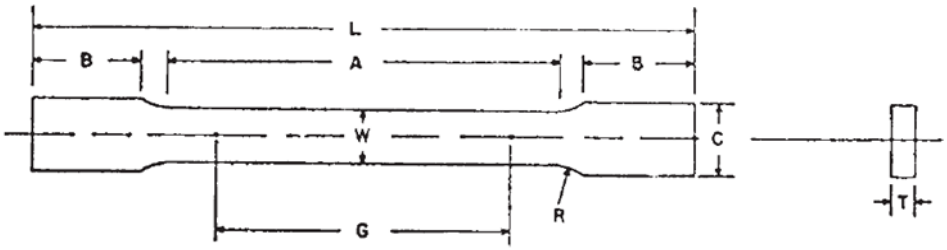

A	B	C	G	L	R	T	W
57	50	20	50	200*	12.5	**	12.5

* Length of the specimen between 220-230mm; ** Thickness of material

Figure IV.3-6 *Tensile test specimen dimensions.*

IV.3.2.2 Impact toughness

Standard full-sized Charpy specimens were cut from the TMCP steels along the plate transverse direction, i.e. with the V-notch parallel to the normal direction (Figure IV.3-1), and tested in accordance with the ASTM-E23 [21] standard. The instrumented impact Charpy hammer, shown in Figure IV.3-7, had a total capacity of 750J and was swung at a velocity of 5.4m/s. In addition, the hyperbolic tangent function, which is believed to be a reliable method of determining the transition temperature, was fitted to the plot of the energy absorbed at impact versus temperature [22, 23].

The ductile to brittle transition temperature (DBTT) is defined as the temperature at which the impact energy equals the energy at the midpoint of the upper and lower shelf energies (USE and LSE, respectively). The corresponding transition curve is described by a hyperbolic tangent function (Eq.IV.3-1) [23] which is given as.

$$y = \frac{a_1}{2}\left[1 - tanh\left(\frac{T - a_3}{a_4}\right)\right] + \frac{a_2}{2}\left[1 + tanh\left(\frac{T - a_3}{a_4}\right)\right] (IV.3-1)$$

$$E = \frac{USE + LSE}{2} + \frac{USE - LSE}{2} \cdot tanh\left[\frac{T - T_{50}}{C}\right] (IV.3-2)$$

Where y, T, and a_i are the Charpy energy, temperature, and fitting parameters, respectively. Eq. 1 can be re-written as Eq. IV-3-2 [22] from which the transition temperature can be reliably determined. In Eq. IV.3-2, E is the absorbed energy, [J]; *USE* is the upper shelf energy, [J]; *LSE* is the lower shelf energy, [J];

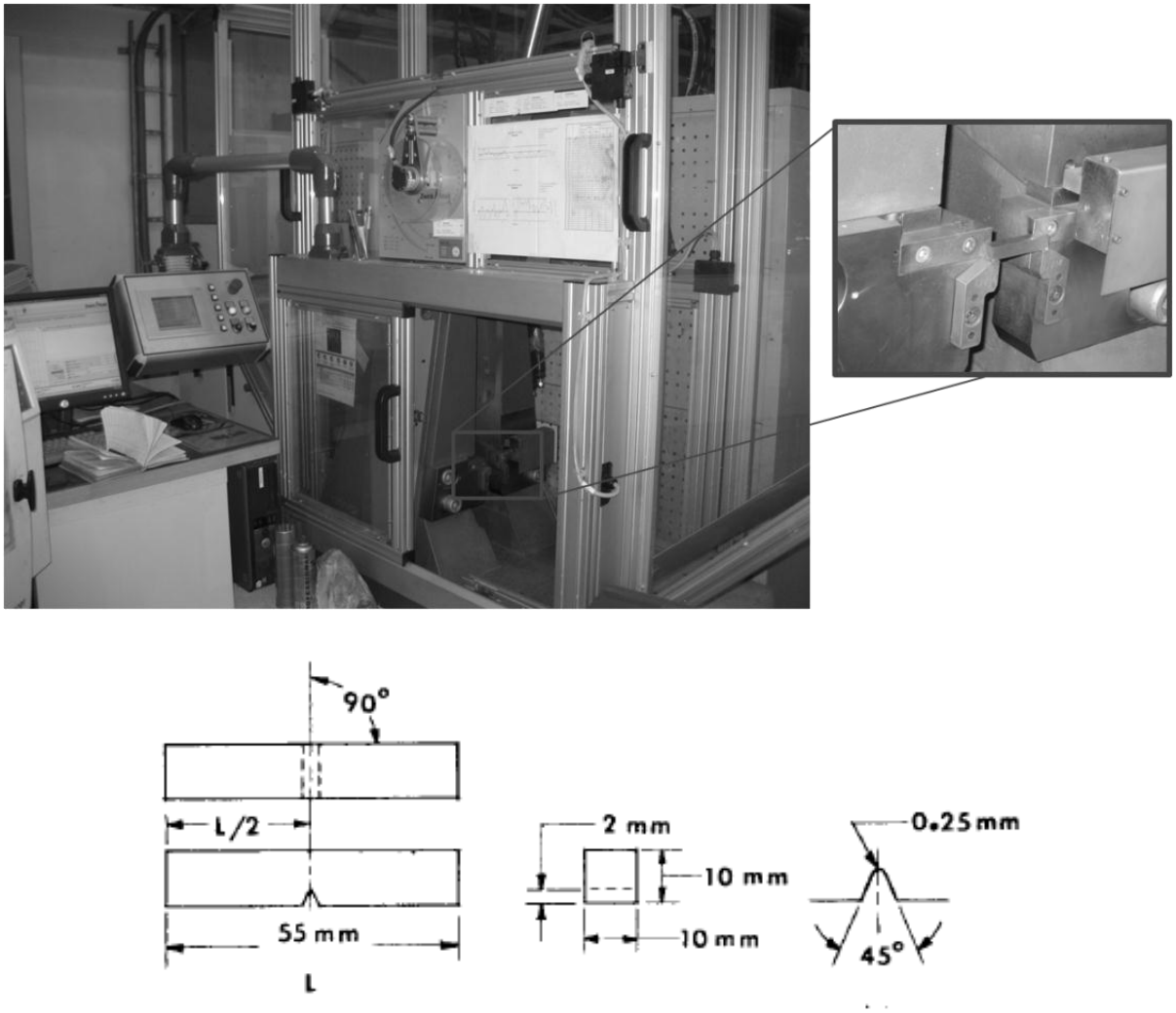

Figure IV.3-7 *Instrumented V-notch Charpy test facilities (a), and (b) geometry of the V-notch Charpy specimen.*

T_{50} is the mid-transition temperature, [°C]; and C is a measure of the temperature range over which the transition behavior occurs. The energy absorbed by the material during crack propagation was determined by integrating the load displacement curves obtained in the ductile region (upper shelf temperature range of 20 °C to -40 °C).

Figure IV.3-8 represents the plane (in red) where fracture propagates during V-notch impact testing. As will be shown in the details in section VI.7, the volume fraction of {001} planes parallel to the fracture surface was measured in order to understand the influence of the crystallographic texture on the toughness.

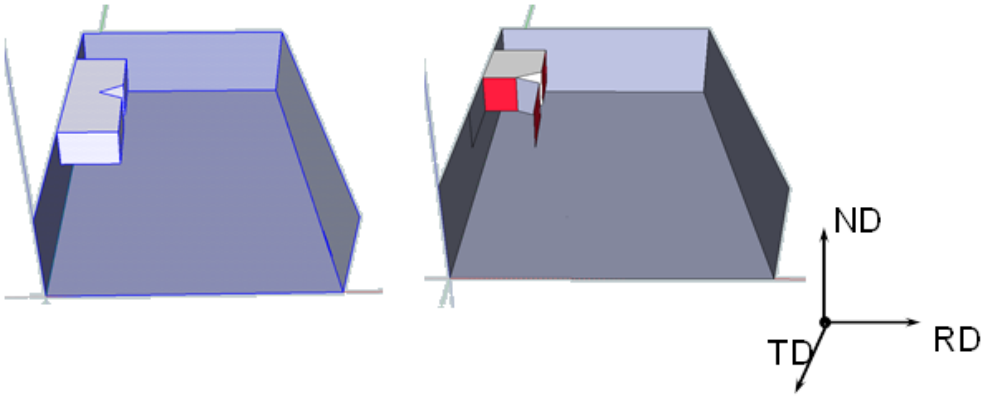

Figure IV.3-8 *Schematic representation of the fracture plane in a V-notch Charpy impact test sample.*

References

[1] T. M. Maccagno, J. J. Jonas, S. Yue, B. J. McCrady, R. Slobodian, and D. Deeks, "Determination of recrystallization stop temperature from rolling mill logs and comparison with laboratory simulation results," *ISIJ International,* vol. 34, pp. 917-922, 1994.

[2] C. Ouchi, T. Sampei, and I. Kozasu, "The Effect of hot rolling condition and chemical composition on the onset temperature of γ-α; tansformation after hot rolling," *Transactions of the Iron and Steel Institute of Japan,* vol. 22, pp. 214-222, 1982.

[3] K. J. Irvine, F. B. Pickering, and T. Gladman, *Iron and Steel Institute*, vol. 205, p. 161, 1967.

[4] B. Sum-Met, *The Science Behind Material Preparation*, 2004.

[5] ASTM, "Standard test methods for determining average grain size," in *ASTM E112 - 12*, ed.

[6] O. Engler and V. Randle, *Introduction to texture analysis: macrotexture, microtexture, and orientation mapping*: CRC press, 2010.

[7] A. J. Schwartz, *Electron backscatter diffraction in materials science*: Springer, 2009.

[8] P. V. Houtte, "The "MTM-FHM" software system Version 2," ed. Katholieke Universiteit Leuven, Belgium: Department of Metallurgy and Materials Engineering, 1995.

[9] P. V. Houtte, "A new method for the determination of texture functions from incomplete pole figures - comparison with older methods," *Textures and Microstructures,* vol. 6, pp. 137-161, 1984.

[10] P. Van Houtte, " A method for the generation of various ghost correction algorithms—the example of the positivity method and the exponential method," *Textures and Microstructures*, vol. 13, pp. 199-212, 1991.

[11] B. D. Cullity, *Elements of X Ray Diffraction*: BiblioBazaar, 2011.

[12] J. Gautam, "Control of surface graded trasformation textures in steels for magnetic carrying applications," Doctor, Department of Material Science and Enginnering, at Delft University of Technology, Delft, Delft, 2011.

[13] A. Montaser, *Inductively coupled plasma mass spectrometry* vol. 515: Wiley-vch New York, 1998.

[14] A. A. Ammann, "Inductively coupled plasma mass spectrometry (ICP MS): a versatile tool," *Journal of Mass Spectrometry*, vol. 42, pp. 419-427, 2007.

[15] Garcı, amp, x, C. a de Andrés, F. G. Caballero, C. Capdevila, *et al.*, "Application of dilatometric analysis to the study of solid–solid phase transformations in steels," *Materials Characterization*, vol. 48, pp. 101-111, 2002.

[16] S. Vervynckt, "Control of the non-recrystallization temperature in high strength low alloy (HSLA) steels," Doctor in Materials Science, Department of Materials Science and Engineering, Ghent University Gent, 2010.

[17] S. Vervynckt, K. Verbeken, P. Thibaux, and Y. Houbaert, "Characterization of the austenite recrystallization by comparing double deformation and stress relaxation tests," *Steel research international*, vol. 81, pp. 234-244, 2010.

[18] ASTM, "Standard test method for linear thermal expansion of solid materials by thermomechanical analysis," in *ASTM E831-12*, ed.

[19] ASTM, "Standard test method for linear thermal expansion of solid materials with a push-rod dilatometer," in *ASTM E228-11*, ed.

[20] A. International, "Standard test methods for tension testing of metallic materials," ed. United States: ASTM International, 2004.

[21] ASTM, "ASTM E23-0.2 Standard test methods for motched bar impact testing of metallic materials," in *Annual Book of ASTM Standards 2002*, ed. USA: ASTM International.

[22] Q.-m. Wan, R.-s. Wang, G.-g. Shu, H. Ding, P. Huang, F. Lv, *et al.*, "Analysis method of Charpy V-notch impact data before and after electron beam welding reconstitution," *Nuclear Engineering and Design*, vol. 241, pp. 459-463, 2011.

[23] W. Oldfield, "Curve fitting impact test data. A statistical procedure," *ASTM Standardisation*, vol. 3, pp. 24-29, 1975.

"Diligence is the mother of good fortune, and idleness, its opposite, never brought a man to the goal of any of his best wishes."

Miguel de Cervantes (1547 -1616) El Quijote

CHAPTER V

Results

V.1 Microstructure and texture changes during TMCP

Interrupted quenching and sampling was performed on the reference material: medium carbon – high niobium (steel 1, Chapter IV.1) in order to study the evolution of the microstructure, precipitation, recrystallization/softening, and texture states during TMCP. Quenching of smaller samples which undergo exactly the same rolling treatment as the plates was done at different stages during processing. This was done in order to prevent, as much as possible, precipitation which occurs at high temperatures, from occurring at room temperature and to reveal the prior austenite grain size. The samples are denominated as follows: Quench 0 (Q0) after reheating at 1250°C for 2h, Quench 1 (Q1) after rough rolling, Quench 2 (Q2) after rough rolling and the additional transfer time between roughing and finishing at high temperature, Quench 3 (Q3) after finishing at high FRT, and Quench 4 (Q4) after finishing at low FRT (see *Table V.1-1*. and *Figure V.1-1*).

	Q0	**Q1**	**Q2**	**Q3**	**Q4**
Quench after:	Reheating	Roughing	Roughing + air cooling up to entry temp. at high FRT	Finishing at high FRT	Finishing at low FRT
Temp. Quenching °C	1250	1180	1060	980	800
Microstructure state	Recrystallized	Recrystallized	Recrystallized	Semi-Pancaked	Pancaked
Austenitic recrystallized grain size (µm)	58	26	34	-	-

Table V.1-1 *Outline of the intermediate-quenched sample status at different TMCP stages.*

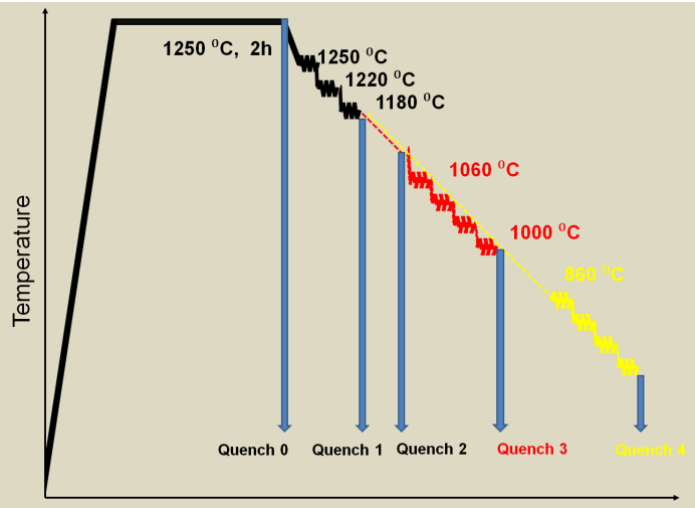

Figure V.1-1 *Scheme of TMCP schedule with intermediate quench points.*

V.1.1 Microstructure

Micrographs and EBSD scans were obtained from the quenched samples described in *Table V.1-1* at Q0, Q1, Q2, Q3, and Q4 stages. *Figure V.1-2* illustrates the evolution of the austenite grain size and morphology during the thermo-mechanical treatment. The microstructures of the samples were characterized in the plane containing the longitudinal and normal directions, at the ¼ of the thickness, by means of optical microscopy and SEM after appropriate sample preparation and/or etching (read chapter IV.3.1). The former austenite grains of the samples, after different stages (intermediate quenched samples), were revealed by Bechet and Beaujard's etching [1]. The average austenite grain diameter (presented in *Table V.1-1*) was estimated according to the ASTM E112-88 linear intercept procedure. Furthermore, certain areas were also scanned by means of the EBSD technique, in order to identify the microstructure, prior to transformation, by means of parent – product transformation relationships (recognizing martensitic lath-packets inside a former austenite grain). An example of this technique is shown in Annex I.

Q0, Q1, and Q2 microstructures were comprised of equiaxed grains, indicating that softening occurred during or after deformation, presumably as static recrystallization, since as explained in Chapter II.2, this is the dominant softening process that occurs during rough rolling. It is well established (c.f. Chapter II.1.2; II.5.1; II.6) that Ti, which is one of the important micro-alloying elements in steel, forms stable TiN precipitates (stable even at high temperatures), which controls

austenite grain growth during reheating. As a result, the average austenite grain size of the reference material after 2h at 1250°C is only 60µm. A priori, the value could be considered small in comparison to the results obtained from a model [2] that is used to predict the evolution of austenite during rolling in conventional and HSLA steels. However, based on experimental measurements, *Roy et al.* [3] explained that it is perfectly possible to obtain such small austenite grain sizes after reheating. Later on, after rough rolling, the effect of the transfer time, between the roughing and the finishing mill, resulted in the growth (quantitatively measured) of the recrystallized austenite (see also *Table V.1-1*). The γ-grain growth, during transfer, was also predicted by the previously cited model [2], which was developed by ArcelorMittal and Nippon Steel Corporation.

TMCP stage	*Optical Micrograph*	*IPF colour +IQ map*
Quench 0 (after reheating)	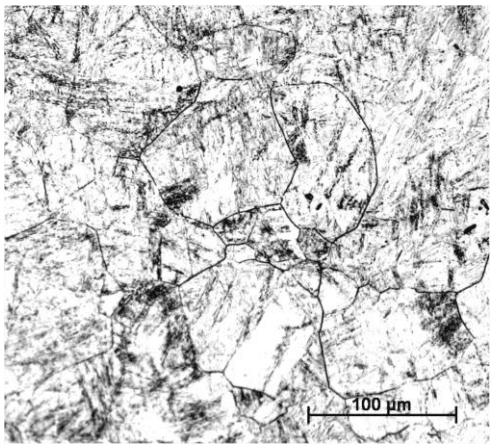	
Quench 1 (after roughing)	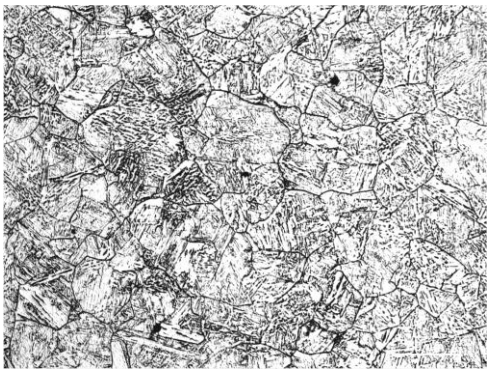	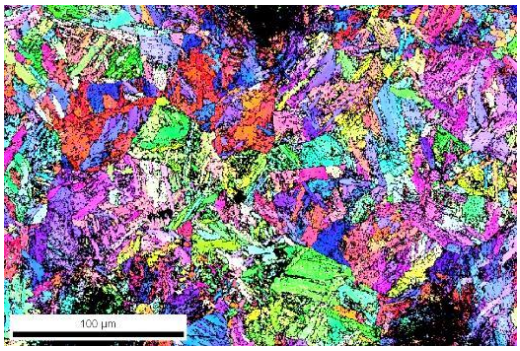

Quench 2 (after roughing + air cooling up to entry tem. At high FRT)		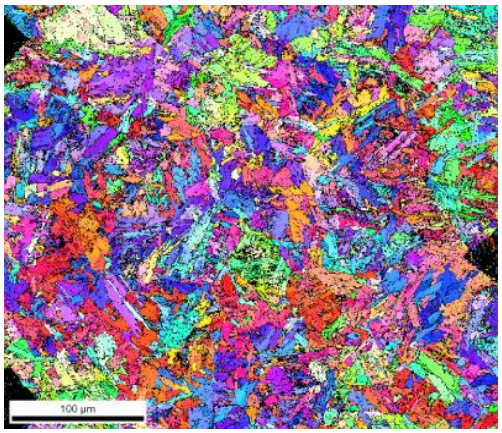
Quench 3 (after finishing at high FRT)	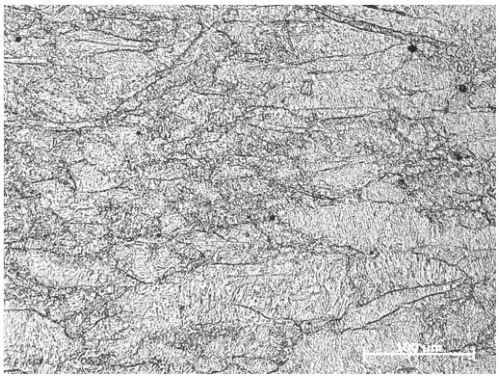	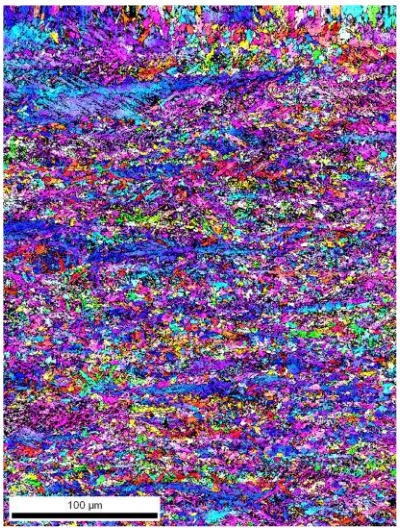
Quench 4 (after finishing at low FRT)	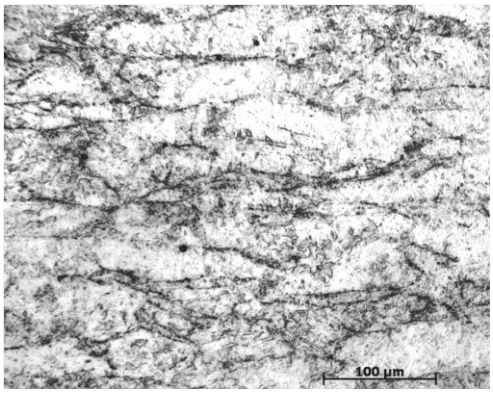	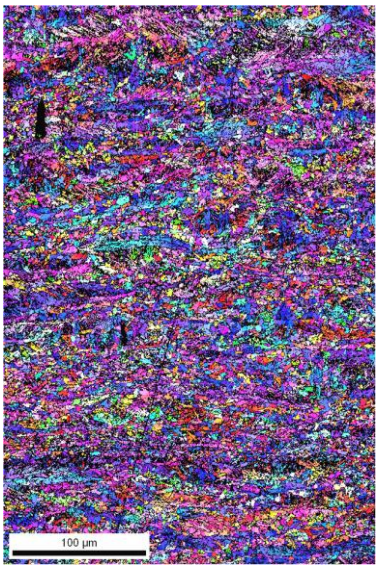

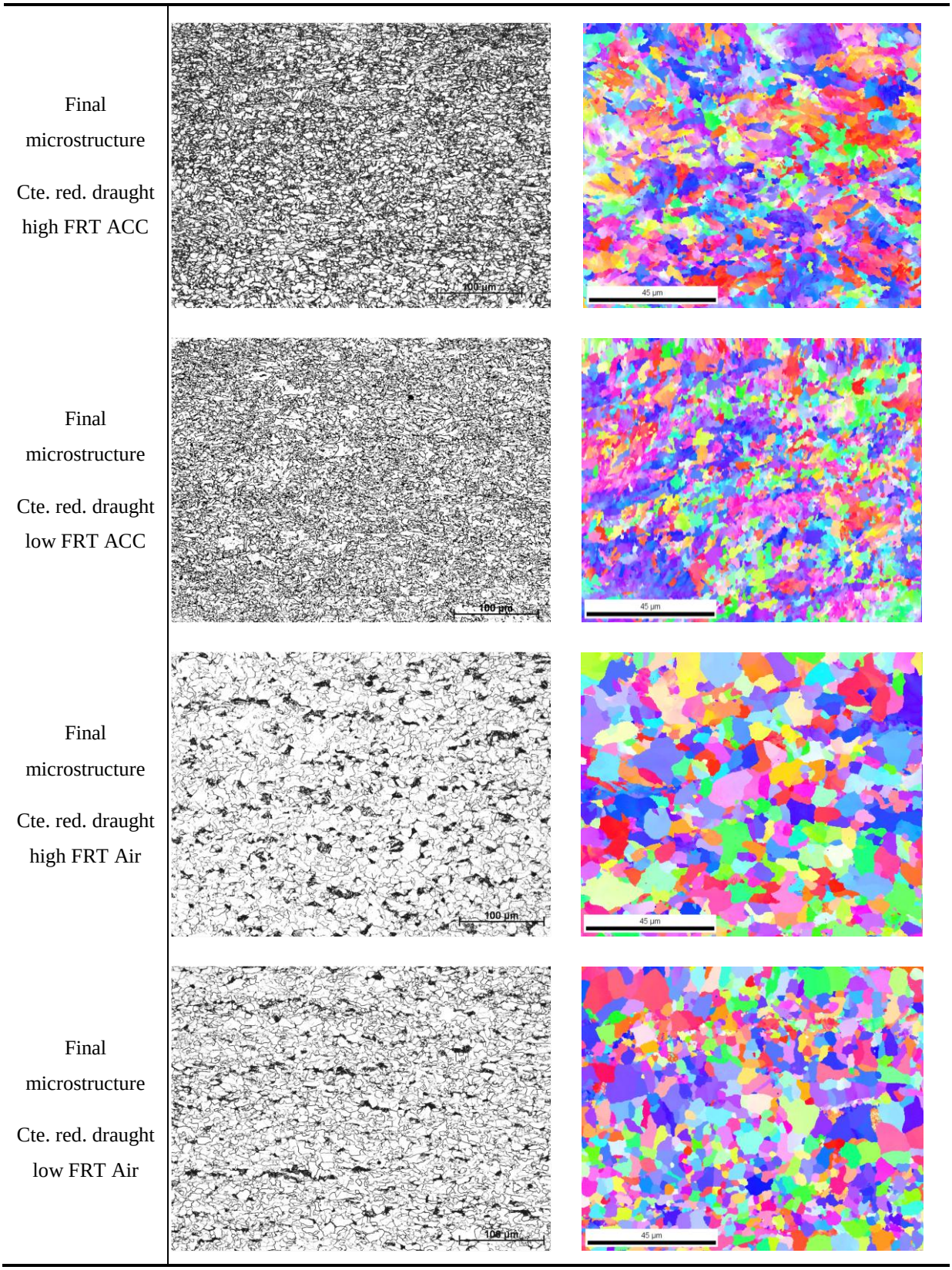

Figure V.1-2 *Optical micrographs (column 2) and IPF+IQ maps (column 3) illustrating the microstructure at various stages of TMCP.*

The microstructure of austenite evolved to a pancake-like morphology immediately after finish rolling at high and low FRT, Q3, and Q4 respectively. The pancaking at Q4 seemed to be more severe than at Q3. This difference may be attributed to the lower FRT for Q4 samples and to the extra grain-boundary pinning that results from the larger amount of precipitated Nb compared to that of Q3 (see *Table V.1-1* and *Table V.1-2*).

Four final TMCP microstructures (combination of constant reduction draught together with high/low FRT and Air/ACC) are included in *Figure V.1-2* as illustrations of the final microstructural stage. These microstructures consist primarily of granular bainitic ferrite $\alpha_{B(G),}$ and bainitic-ferrite α_B together with quite small islands of Martensite-Austenite (MA), particularly for the routes employing ACC. However, polygonal ferritic (α_p) and quasi-polygonal ferritic (α_{qp}) microstructures, together with lamellar (P_L) and degenerated (P_D) pearlite islands, were developed for the routes using Air cooling. Detailed optical, SEM, and TEM images of representative final TMCP microstructures are shown in Annex I. The α_B , $\alpha_{p,}$ $\alpha_{qp,}$ and P_L phases constitute only a few of the potential γ-transformation products which are described in chapter II.3.3.

V.1.2 Precipitation

It can be seen from the data in *Table V.1-2* that Ti did not dissolve completely even after 2h of reheating at 1250°C and remains as Ti (C,N) precipitates in all quenched samples. On the other hand, the measured amount of precipitated Mn was quite low, indicating that most of the Mn remained in solid solution during the austenitic rolling stages. As previously discussed in chapter II.6, Nb plays an important role during TMCP and *Table V.1-2* is quite revealing in this regard. First, the measurements (at Q0) indicate that there is a residual amount of Nb that was not dissolved during reheating. These values are concur with those measured by *Hong et al*. [4] in a similar micro-alloyed steel. Second, Q1 makes clear that precipitation did not occur through roughing. This detail is important, since precipitation of Nb is desired, mainly during the final stages of rolling, for the retardation of recrystallization by pinning mechanisms, and after phase transformation in order to contribute to strengthening by precipitation hardening. When the material was transferred from roughing to finishing rolling at high FRT, a small amount (≈7%) of Nb precipitates was measured, which probably contributed to the control, but not suppression,

(see *Table V.1-1*) of γ grain growth at the said processing stage. Unfortunately, records from the material quenched before being rolled at low FRT are unavailable owing to a technical problem during TMCP of the aforementioned material.

	Q0	**Q1**	**Q2**	**Q3**	**Q4**
Quench after:	Reheating	Roughing	Roughing + air cooling until entry at HFRT	Finishing at HFRT	Finishing at LFRT
T Quenching (°C)	1250	1180	1060	980	800
Ti precipitated (%)	96	94	97	100	100
Mn precipitated (%)	0.4	0.2	0.2	0.1	0.1
Nb precipitated (%)	16	15	23	33	40

Table V.1-2 *Outline of the precipitated amounts of Ti, Mn, and Nb at different TMCP stages.*

The high FRT route resulted in the precipitation of about 10% of Nb during finishing. These precipitates contributed to the pinning of austenite grain boundaries, which, as observed in *Figure V.1-2*, presents pancaking of austenite grains before transformation (see image for Q3). However, the total amount of Nb precipitated immediately after finishing rolling at low FRT was 7% larger than its high FRT counterpart. This difference contributed to an increase in the pancaking of the microstructure (see *Figure V.1-2*).

Further TEM analysis, on carbon replicas of the quenched materials, showed that the precipitate size distribution changed throughout the TMCP course (see *Figure V.1-3*). From these data one can see that Q0 resulted in a bell-shaped precipitate size distribution skewed to the right, with a large percentage of precipitates having an equivalent radius between 10 and 50nm. After roughing, at Q1, some of the precipitates have grown; hence the size distribution displays a broad, flat- (platykurtic) shaped curve. The reason for the growth of precipitates can be explained by analyzing the results in Figures V.1-4 and V.1-5. Originally, only cuboidal-shaped Ti precipitates were present at Q0. During the TMCP, however, they act as nucleation sites for the Nb-rich precipitates.

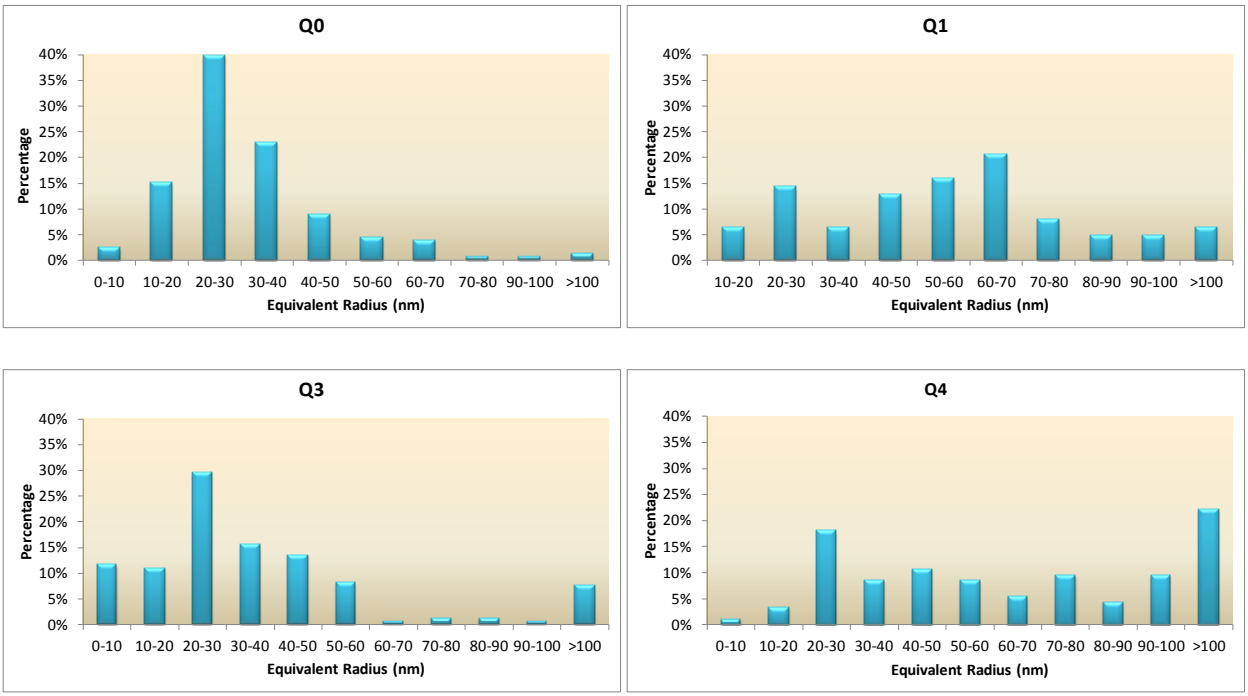

Figure V.1-3 *Experimentally determined precipitate size distribution at various TMCP stages.*

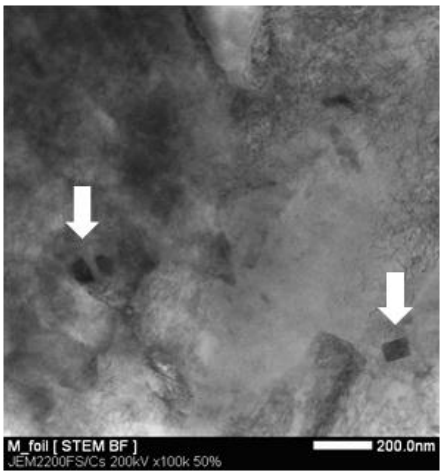

Figure V.1-4 *STEM micrograph showing various cuboidal-shaped Ti precipitates at the Q0 stage.*

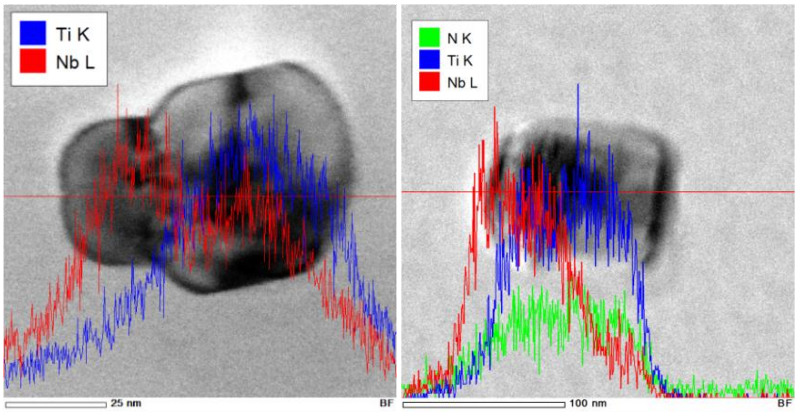

Figure V.1-5 *TEM micrograph showing two examples of body-cup precipitates. Ti-rich precipitates act as nucleation sites of the Nb-rich precipitates. The distribution of Nb, Ti, and N along a line crossing the precipitate is shown by curves of different colors.*

As indicated in Table V.1-2, Nb precipitates continuously during the finishing rolling. At this stage, dislocations, shear bands, grain boundaries, and previously formed TiN precipitates start

acting as nucleation sites for the new precipitates. Therefore, at Q3, the precipitate size distribution shows relatively large fractions of new, fine Nb precipitates (see ***Figure V.1-6***) together with old, large precipitates which have grown owing to the fact that they nucleated earlier (see *Figure V.1-7*). Precipitates at the Q4 exhibit a clear bi-modal size distribution which developed in a similar manner to that of the Q3 samples. However, the extended transfer time between roughing and finishing resulted in additional precipitation before the start of the finishing rolling. During the transfer from rough to finish rolling, the microstructure of the material consisted of recrystallized austenite. The preferential sites for precipitate nucleation were, therefore, the γ grain boundaries and the previously formed TiN or Nb precipitates. This explains the shift of the maxima in *Figure V.1-3* (Q4) towards large precipitates. As *Figure V.1-3* shows, there is a significant difference between the fractions of large equivalent radius of the two FRT conditions (Q3-fraction of ppm >100 = 8%, Q4-fraction of ppm >100 = 24%).

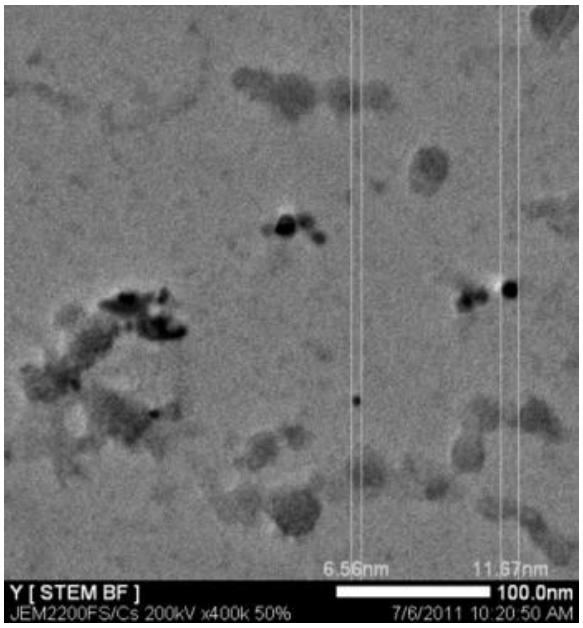

Figure V.1-6 *Fine Nb precipitates measured at the Q3 stage.*

It was observed that, at high FRT, the difference in the amount of Nb precipitated between the samples quenched immediately after finishing, and those following the complete ACC simulation was only of 6%. When low FRT is utilized, the divergence between the quenched sample immediately after finishing and the sample after complete ACC simulation was of 12%. This divergence can be related to the increased ability for strain-induced precipitation at lower temperatures. In addition, there was significant correlation between materials processed with ACC and those which were air-cooled. In both cases the difference of Nb precipitated at high and low FRT was exactly the same, i.e., ≈13%. Interestingly, this correlation may be related to the original difference in the fractions of Nb precipitated in Q3 and Q4, i.e. ≈7%, quenched just after finishing at the mentioned different FRTs. In other words, at high or low FRT, the differences in precipitation during finishing rolling and the different strain induced precipitation response, are both insensitive to the cooling condition.

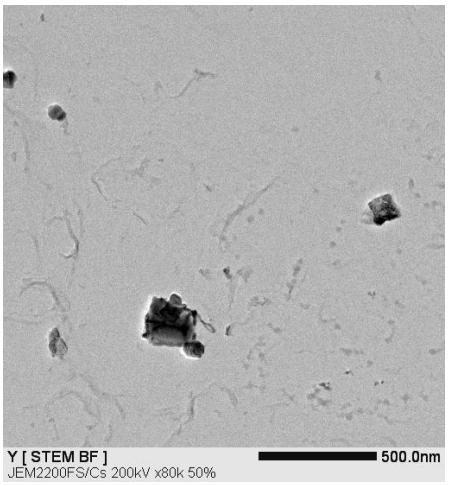

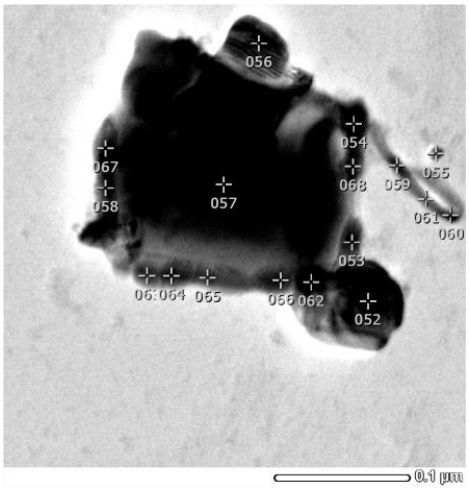

Memo	N	Ti	Mn	Nb
52	7.7	26	0	65.3
53	0	20.2	0	76.5
54	0	11.6	0	86.7
55	0	0.9	0	93.2
56	4.2	19.4	0	75.5
57	20.1	48.9	0	30.7
58	21.9	35.9	0	41.2
59	0	1.8	0.1	93.6
60	0	1.8	0	96
61	0	1.6	0	96.4
62	14.8	37.6	0	46.2
63	6.5	29.6	0	63
64	9.2	31	0	58.9
65	8.2	36.9	0	54.4
66	9.4	40.5	0.1	49.2
67	21.8	32.7	0	44.8
68	0	20.2	0.2	77.6

a b c

Figure V.1-7 *(a) General view of various coarse body-cup precipitates; (b) detail of how a Ti cubic precipitate is surrounded by Nb precipitates;(c) EDX point analysis data of the precipitates with main constituting elements listed in atomic%.*

Figure V.1-9 compares the results obtained from the precipitate size distribution measurements after the four final TMCP schedules (denoted by red marks in *Figure V.1-8*). There was a significant difference between the two cooling conditions. Air-cooled samples have a much higher percentage of precipitates with equivalent radius larger than 100nm compared to those cooled by other methods. Moreover, under the same cooling condition, greater fraction of large precipitates was found in low FRT processed materials. This behavior was already observed in the quenched sample Q4 after low FRT (see *Figure V.1-3*) and might be related to the difference in transfer time between roughing and finishing. The presence of large precipitates after air cooling also concurs with our earlier observations of the fracture surface after V-notch Charpy impact tests. SEM fractographs (see *Figure V.1-10*) showed that void nucleation in air-cooled samples, occurred in regions containing significant fractions of large precipitates.

There are similarities between the precipitate size distributions displayed in the quenched samples Q3 and Q4 in *Figure V.1-3* and those in the materials after complete TMCP. In contrast, the plates rolled at low FRT formed fine particles, but the dominant size of precipitates seemed to shift towards a slightly higher equivalent radius.

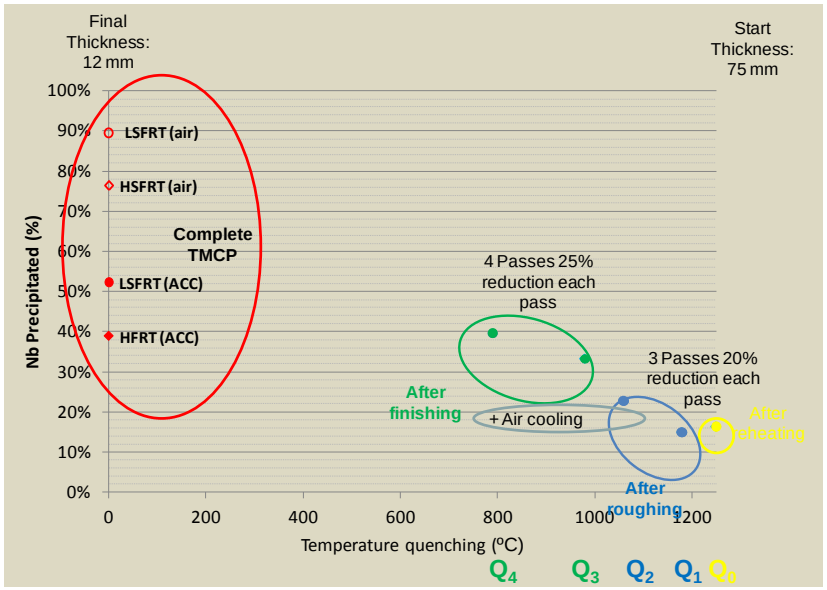

Figure V.1-8 *Evolution of Nb precipitated (%) after different stages of TMCP for the Med. C–High Nb steel.*

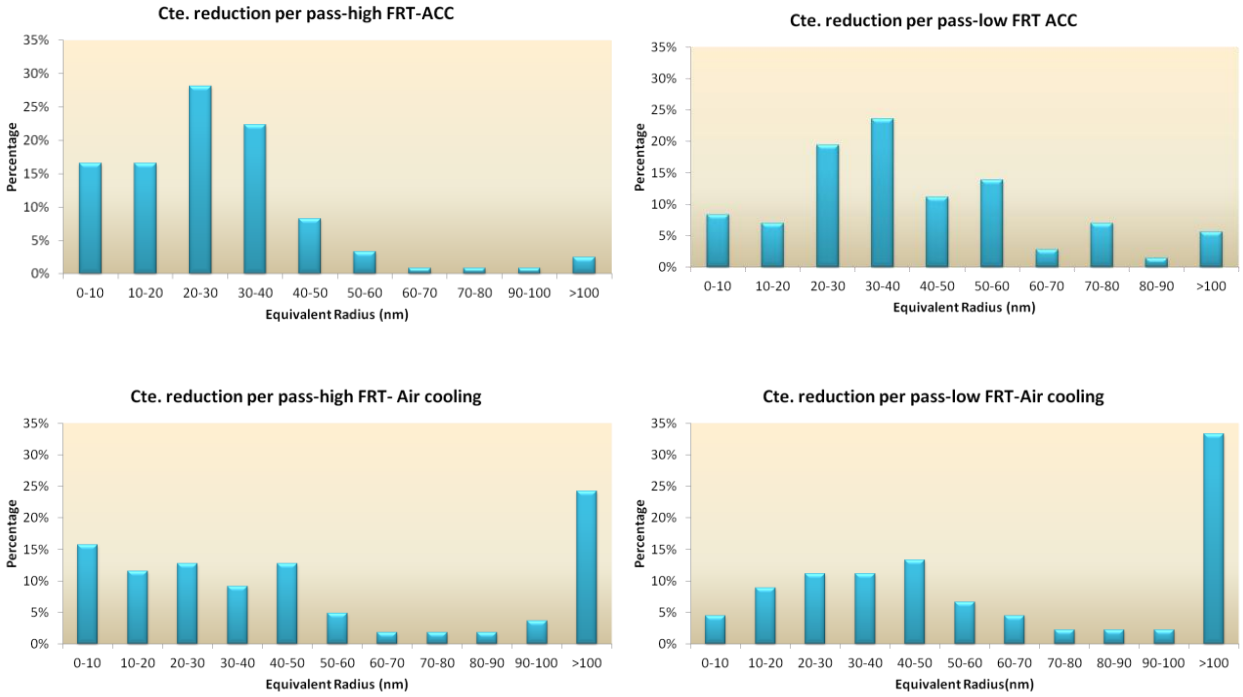

Figure V.1-9 *Experimentally determined precipitate size distribution at the end of four different TMCP routes.*

Part of the Nb available in the solid solution at the transformation temperature Ar_3 may precipitate during or after the γ to α transformation as very fine dispersoids in the ferritic matrix. Extremely fine precipitates are difficult to detect with STEM imaging. As such, complementary

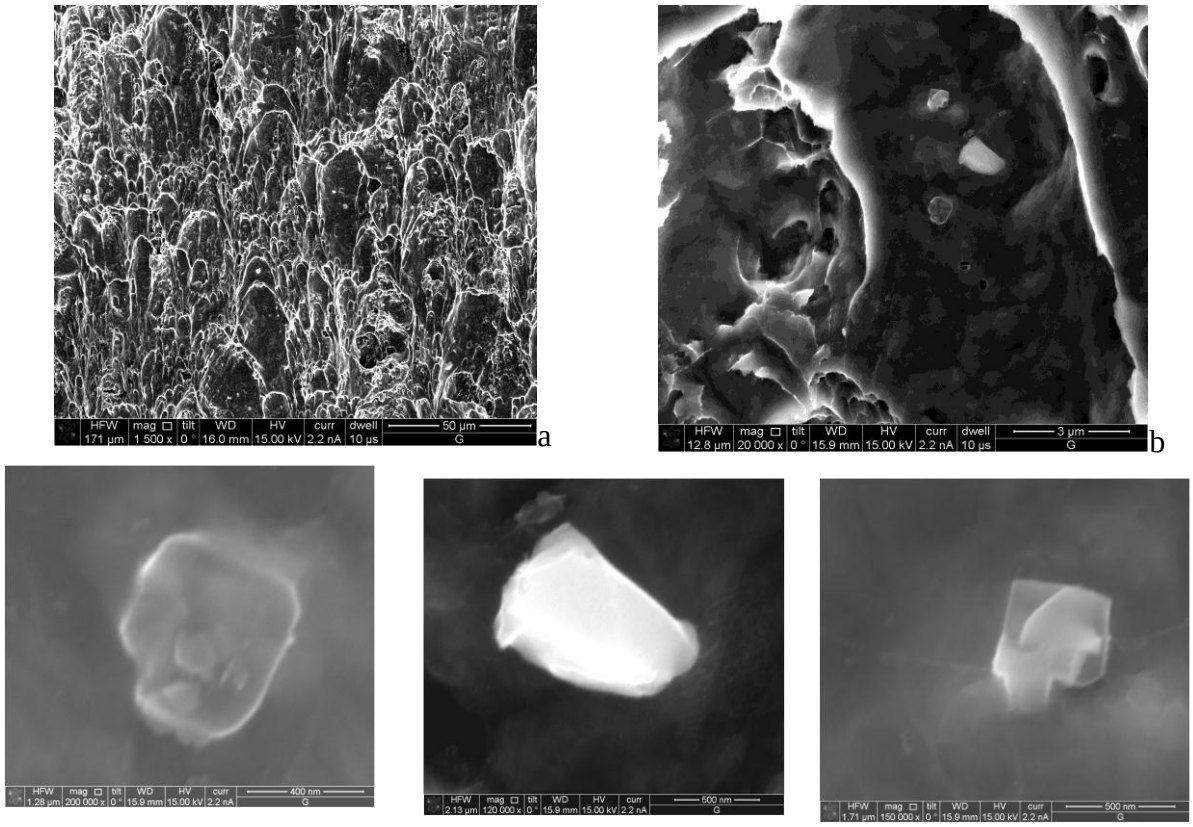

a b c d e

Figure V.1-10 *(a) SEM fractography, showing voids generated during ductile fracture of a V-notch Charpy specimen; (b) Detailed view of an elongated void containing a cluster of precipitates; (c),(d),and (e) view of each large precipitate.*

High Resolution TEM (HRTEM) analysis was performed with the aim of proving the existence of tiny precipitates. Care was taken to verify that the orientation relationship between the carbide particles and ferrite exhibited one of the three variants of the Baker-Nutting [5] relationship. In order to identify the precipitates, the following works [6-8] were used as guidelines. *Figure V.1-11* shows the dark and/or bright field images of representative areas corresponding to the previously discussed four different TMCP routes. As can be seen from Figure V.1-11, minute precipitates (radius <5nm) were found in the plates processed by all four reference TMCP schedules. Comparison of the data in Figure V.1-11, indicates that it was possible to identify even smaller precipitates at low FRT, particularly in the ACC steels. The fine precipitates after ACC offer, therefore, an additional strengthening mechanism, in the pipeline steel, which can be controlled by the cooling rate at this processing stage.

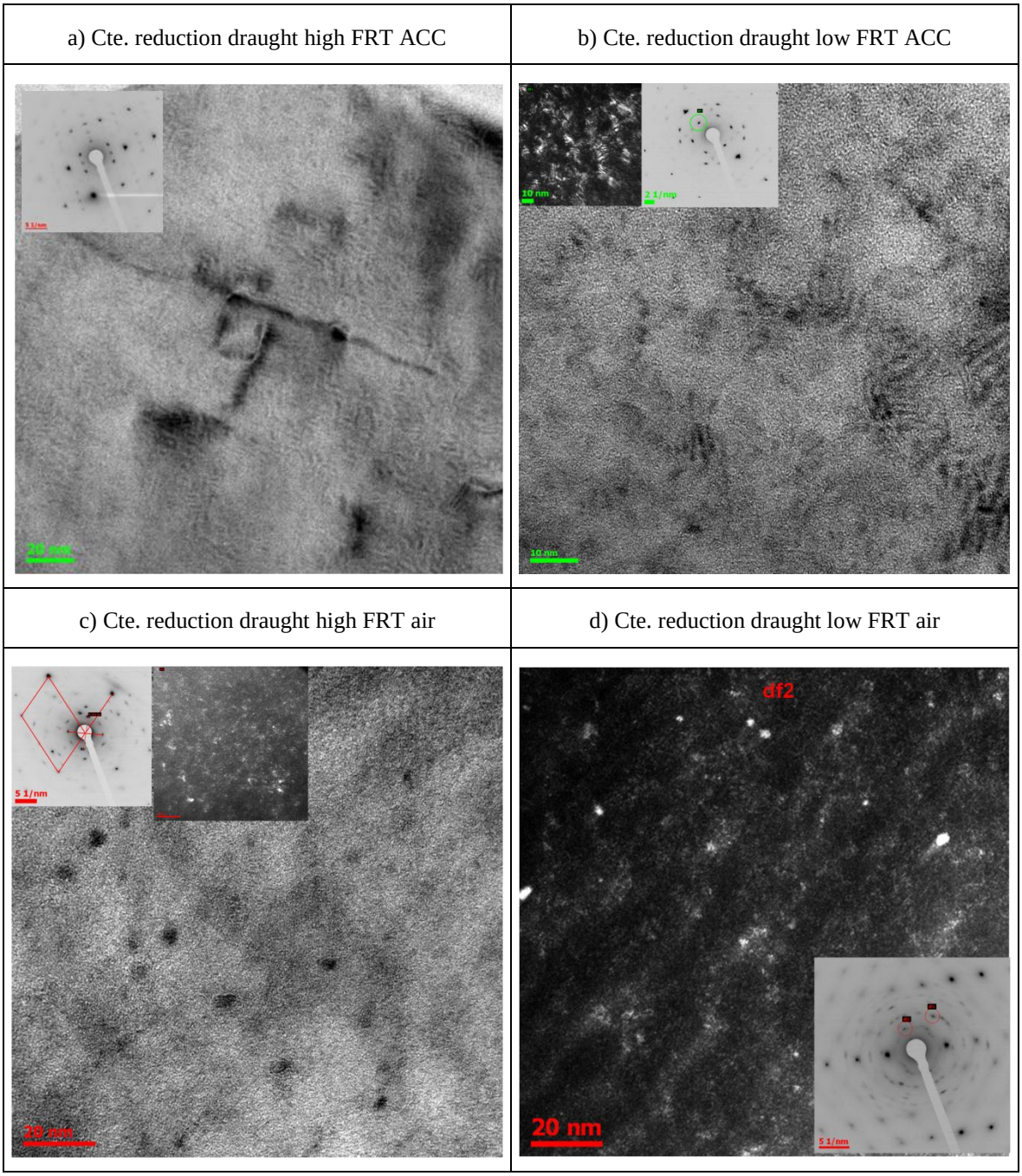

Figure V.1-11 *HRTEM analysis of four samples after different TMCP schedules. Representative bright field and/or dark field images showing the presence of fine precipitates. a) Cte. reduction draught high FRT ACC; b) Cte. reduction draught low FRT ACC; c) Cte. reduction draught high FRT air; d) Cte. reduction draught low FRT air A) BCC Z.A. <1,0,2>, ZA <112>; B) BCC Z.A. <1,0,4> ZA <1,1,4>; C) BCC Zone axis Z.A. <2,1,6> ZA <2,1,5>; D) BCC Z.A <3,3,1> lattice parameter carbide 0.846 nm ordered NaCl type structure. Space group Fm$\bar{3}$m.*

Symbol	Wyckoff	x	y	z	Occupancy
C	a	0	0	0	1
Nb	b	0.5	0.5	0.5	1

V.1.3 Texture

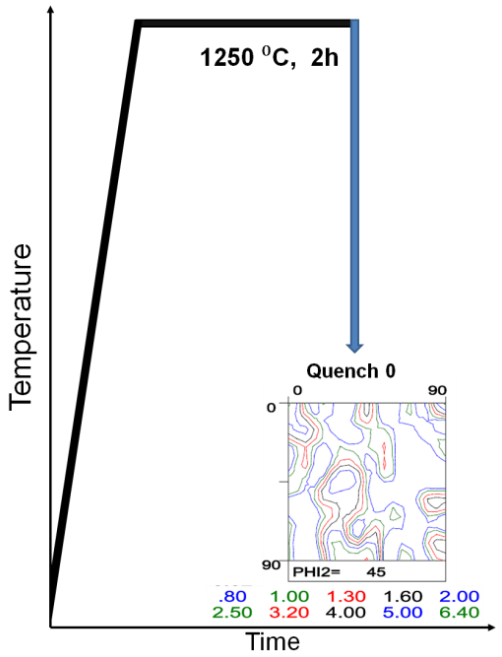

Figure V.1-12 *φ2=45° ODF section representing the transformed texture at Q0 stage of the TMCP.*

During the TMCP schedules, the crystallographic texture underwent a number of changes related to the occurrence of various events namely, γ deformation, γ recrystallization, γ to α transformation, and, although limited, the possible deformation of α at the surface of the materials owing to the temperature gradient. The exhaustive examination of the recrystallization and deformation textures in γ and their correspondent transformation products in ferrite, described by *Jonas* [9] and *Ray* [10], was used as the basis for determining the recrystallization-deformation status of steels at each stage of the processing route.

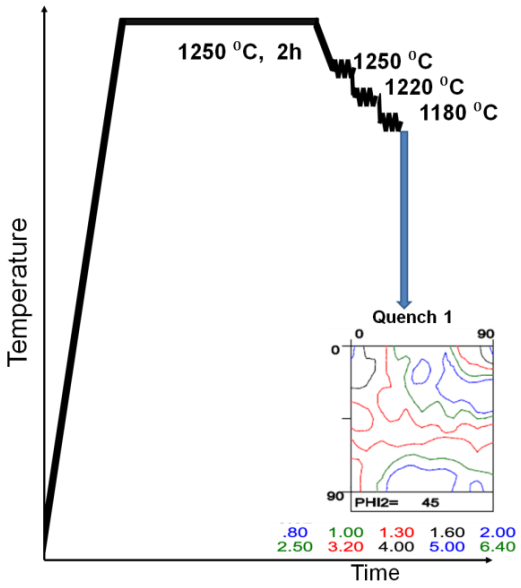

Figure V.1-13 *φ2=45° ODF section representing the transformed texture at the Q1 stage of the TMCP.*

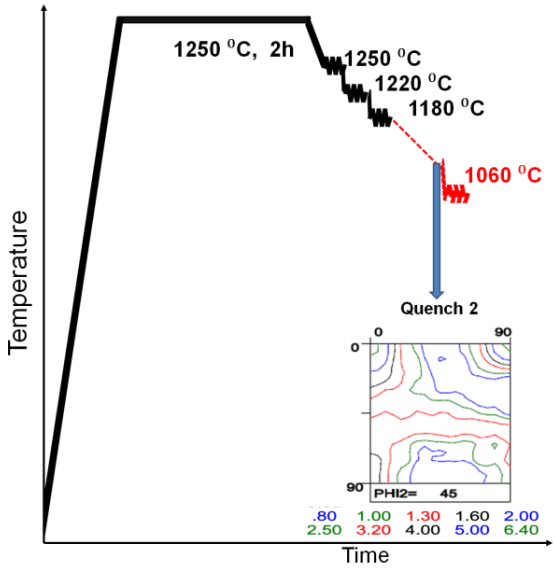

Figure V.1-14 *φ2=45° ODF section representing the transformed texture at the Q2 stage of the TMCP*

The theoretical fundamentals of the mentioned works were summarized in Chapter II.4. Figure V.1-12 shows the transformation BCC texture developed during reheating up to 1250°C, holding for 2h and subsequent water quenching. The BCC texture is relatively weak and represents transformation products which originate from recrystallized austenite namely, rotated cube, Goss, and rotated Goss with intensity of 2.5 multiples of random density (mrd) and 2 mrd, respectively. The transformation products of austenite which have the brass orientation occur with an intensity of 2 mrd. The transformation texture shown in Figure V.1-13 shows even more clearly the same principal texture components which originate from the recrystallized austenite, i.e. {100}<110> (rotated cube) with intensity of 2 mrd and a weak (intensity of 1.3 mrd) transformation product of the austenite β fiber texture. The observed texture is a clear indication that the austenite recrystallizes almost completely after rolling above Tnr and the transformation follows the Kurdjumov-Sachs (K-S) orientation relationship between the parent and the product orientations (see Chapter II.4). The rotated cube, rotated Goss, and Brass texture components are K-S transformation products from the parent cube orientation. Therefore, the formation of these components confirms that the transformation started with recrystallized austenite grains which have the cube orientation. Since the Q1 was done immediately after the third rough rolling pass, traces of deformed γ were also present in the BCC texture (β-fiber transformation texture), as there was not enough time for recrystallization to be completed after this pass. Therefore, the φ_2=45° section presented in Figure V.1-13 shows a weakly textured material composed primarily of the rotated cube {100}<011>, rotated Goss {110}<110>, and the gamma fiber which occur with intensities of 2, 1.3, and 1.3 mrd, respectively. Furthermore, the Goss {110}<001> component occurred with an intensity lower than 1 mrd.

The intensities of the rotated cube, Goss, and rotated Goss components increased slightly (by ≈ 0.5 mrd) at Q2 (Figure V.1-14). In addition, the recrystallized transformation textures, although small, are possibly an indication of microstructural evolution during the transfer time. This evolution can be attributed to the γ grain growth measured during the aforementioned transfer stage of the TMCP.

As shown in *Figure V.1-15*, at Q3 and Q4 (just after finishing rolling at two different high/low FRTs, and in both cases, below Tnr) the textures sharpened and changed as follows: the copper,

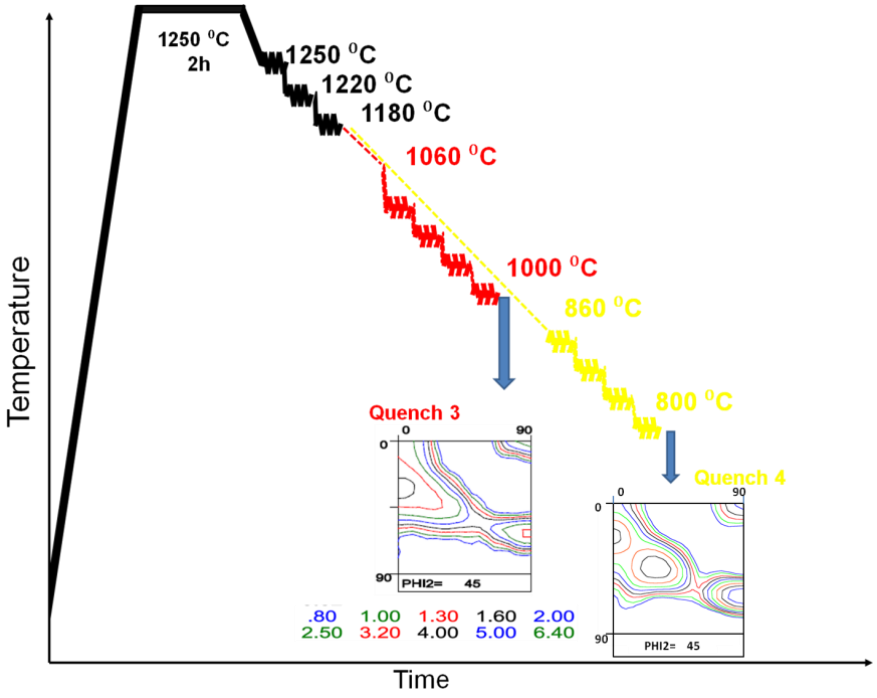

Figure V.1-15 *φ2=45° ODF section representing the transformed texture at Q3 and Q4 stages of the TMCP.*

brass, and Goss austenite components resulting from finishing rolling of γ below Tnr transformed to (see Chapter II.4 for reference φ2=45° ODF section): {114}<110>, {113}<110>, {112}<131>, {111}<132>, {111}<011>, {111}<123>, {554}<225>, {332}<113>, and {001}<110> texture components. In both cases, the maximum occurs in the vicinity of the {114}<110> and {113}<110> texture components, which are K-S transformation products of copper-oriented austenite. Since the rolling was executed below the assumed Tnr and the plate was immediately quenched, then the increase of the rotated cube intensity can no longer be attributed to an increase in the fraction of recrystallized austenite. This increase most probably resulted from the transformation of the deformed austenite, which had a strong brass texture, to the rotated cube component.

V.1.3.1 Analysis of through-thickness texture gradients

In the current study, various materials were analyzed by means of through-thickness EBSD scans. These scans were performed with the aim of assessing the texture evolution across the thickness of the material for both high and low FRT conditions. Figure V.1-16 shows the experimental data containing the φ_2=45° ODF sections when the thickness of the final TMCP processed material is divided into 10 regions. The length of each region along the ND is, therefore, 600μm. It is

interesting to note that a pronounced texture gradient was developed through the plate thickness in both FRT schedules. In addition, the central part of the plates exhibit the characteristic texture that results from the transformation of austenite which underwent plane strain deformation prior to the transformation. The texture weakens towards the ¼ thickness of the material. At 2400µm to 3600µm from the center, only a somewhat strong rotated cube component (in the case of high FRT) or {113}⟨110⟩ and {112}⟨110⟩ (in the case of low FRT) could be distinguished among a quasi-random texture. Starting at approximately 3600µm from the center, and ending at the surface, the φ2=45° ODF sections were found to consist of Copper, Goss, and Brass texture components, which are related to the shear deformation mode of the γ or α phase [11]. The low and high FRT materials exhibited some differences in texture. It is encouraging to compare the localised texture components which arose at this two conditions, (see *Figure V.1-17*).

Material	Through-thickness texture	Legend
Low C Med. Nb Cte. Reduction Per Pass HFRT	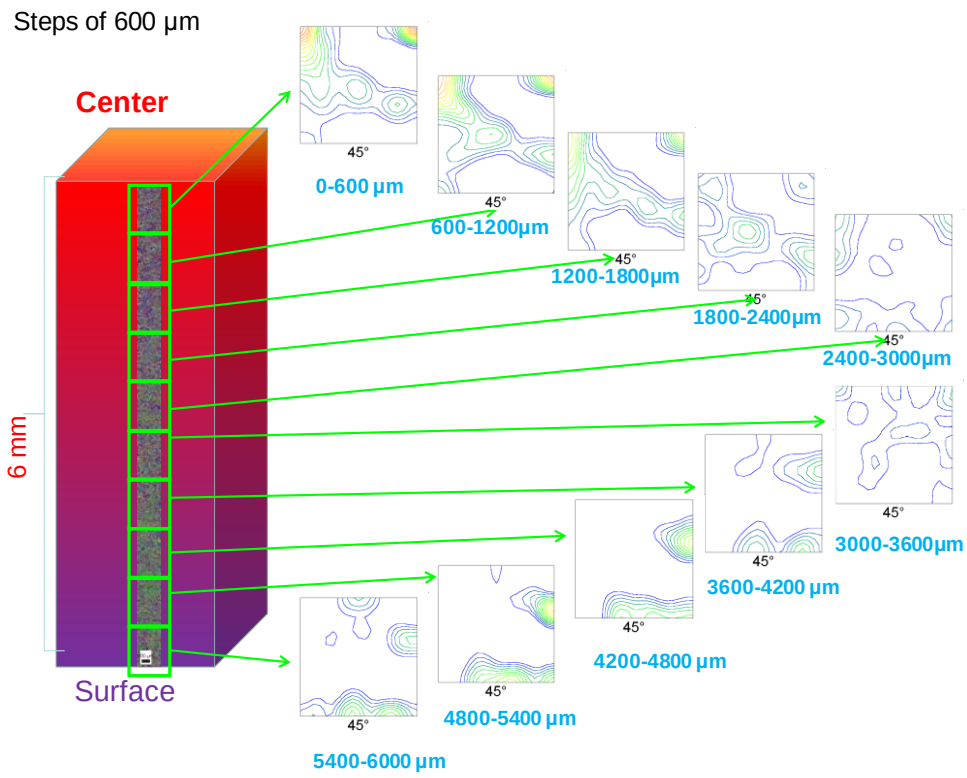	5.500 5.263 5.026 4.789 4.553 4.316 4.079 3.842 3.605 3.368 3.132 2.895 2.658 2.421 2.184 1.947 1.711 1.474 1.237 1.000

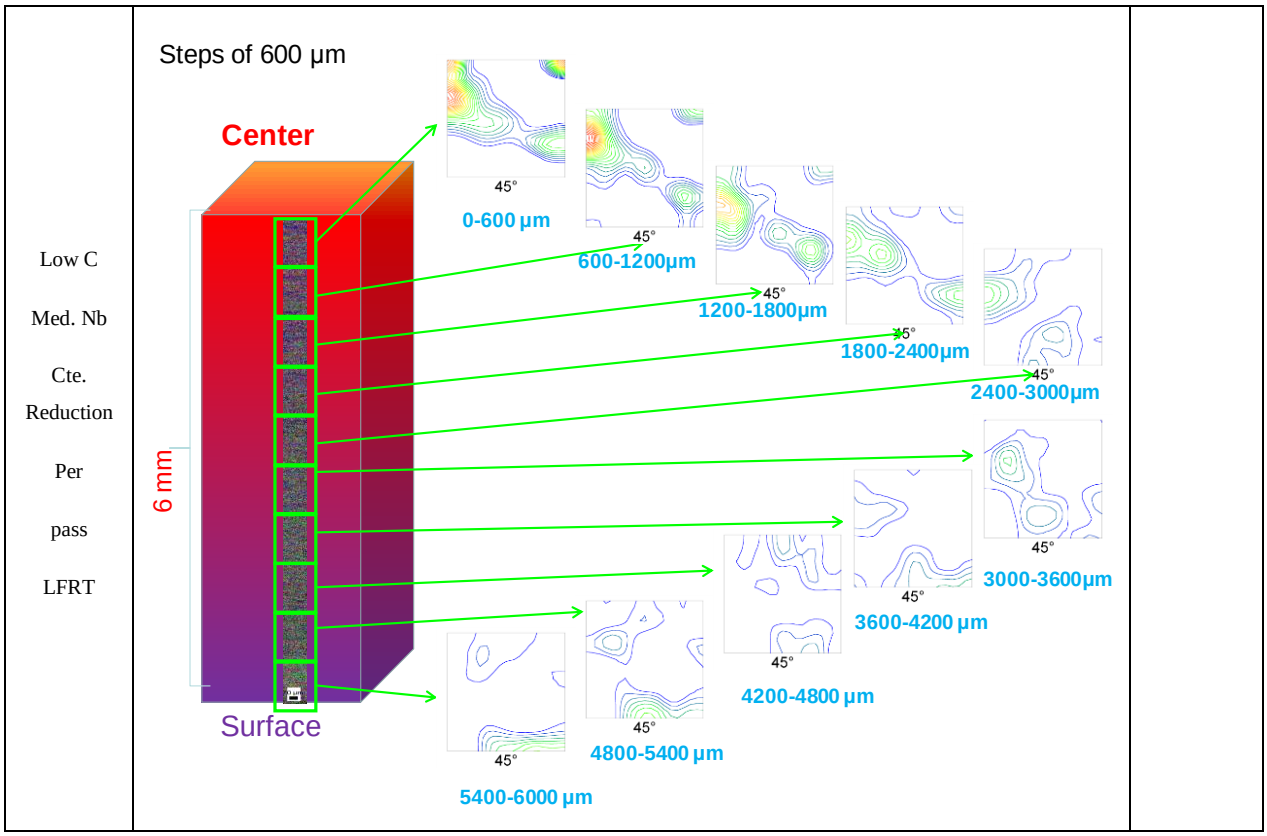

Figure V.1-16 *Illustrations of through-thickness texture gradients for (a) high FRT, and (b) low FRT(b). φ2=45° ODF sections with steps of 600µm.*

Figure V.1-17 compares the qualitative (texture components) and quantitative (intensity levels) differences between two steels processed at similar TMCP conditions but with different FRT. The comparison is done locally (steps of 600µm length along the ND). *Figure V.1-17* also shows, inside the central columns, the φ2=45° sections of the global ODF of the aforementioned steels. The ODF sections from the central regions reveal that the route with high FRT resulted in the highest relative intensity of the rotated cube {100} ⟨011⟩ component. In contrast, the low FRT resulted in maxima at the {113}⟨110⟩ and {112}⟨110⟩ transformation components. In terms of intensity, the low FRT route produces sharper textures in the central regions than the high FRT. At ¼ thicknesses, similar intensities were found for both conditions. The texture in this region (¼ thicknesses) mimics, in a weaker manner, the main components present at the central region (1/2 thicknesses) of both steels.

As previously mentioned, the two FRT conditions resulted in the formation of the typical shear texture components close to the surface of the materials. However, the copper component was only observed at high FRT.

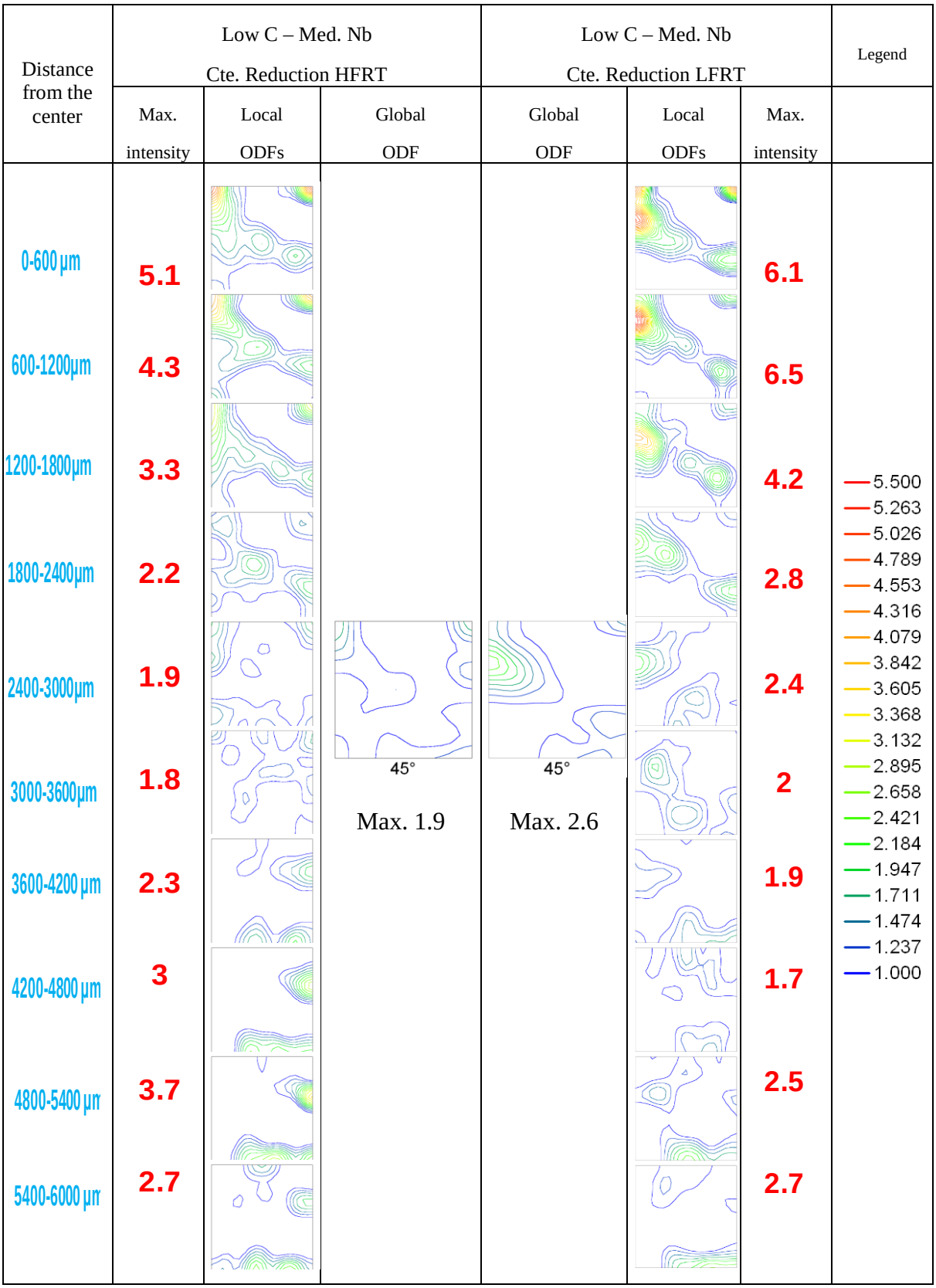

Figure V.1-17 *Crystallographic texture comparison between two steels processed at similar TMCP conditions, with the exception of the FRT.*

The reason for this is not clear. Two possible explanations/hypotheses are considered:

(i) The presence of a strong Brass component at high FRT may be the result of shear deformation of ferrite at the surface of the material. After rolling at high FRT, those deformed ferrite components may have recrystallized and strengthened the Copper and Brass components. At low FRT the shear ferrite components did not recrystallize and strengthen and, therefore, a weak Copper component developed.

(ii) The differences in the shear texture components might be related to the different friction behavior at high or low FRT. For example, *Wusatowski* [12] reported that the coefficient of friction during hot rolling is sensitive to the type of steel, the roll surface velocity, and the rolling temperature. *Figure V.1-18* shows the temperature distribution of the friction coefficient for various carbon steels at a roll surface velocity similar to those used in the present work. The larger friction coefficients at high FRT may explain the occurrence of a strong intensity of Copper component in BCC.

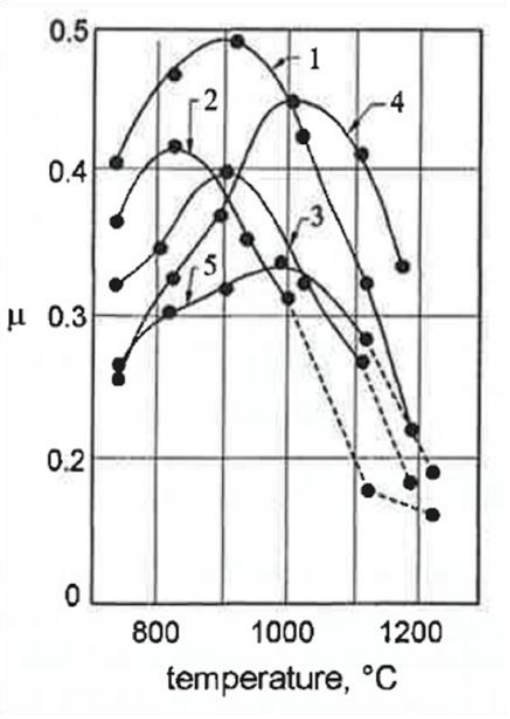

Figure V.1-18 *Friction coefficient inferred during hot rolling of various carbon steels [12].*

Furthermore, the global through-thickness textures were similar to those observed at around the ¼ thickness, particularly between distances of 2400µm to 3000µm from the center of the samples. This comparison neglects, however, the contribution (components and or intensities) from the center or surface. This suggests that important information can be lost in many cases, where either only local or global regions are considered without focusing on their diverse local peculiarities. It should be noted that, the average balance of texture components depends on the friction conditions. Therefore, different texture components may develop when the friction conditions are changed.

Complementary XRD measurements were made at various layers of two materials. These two materials were processed with an increasing and a decreasing strain deformation path, respectively and ACC was utilized in both cases. The results are presented together in *Figure V.1-19*. The first row schematically illustrates the distance from the sample surface whose area was subjected to XRD analysis. At the center of the plate (i.e. 6mm from surface), the φ2=45° ODF sections consist of the aforementioned "*beta*" deformation fiber components with absolute maxima at {113}⟨110⟩ and {112}⟨110⟩. Local maxima occur at {554}<225>, {332}<113>, and {001}<110> (cf. Figure V.1-19).

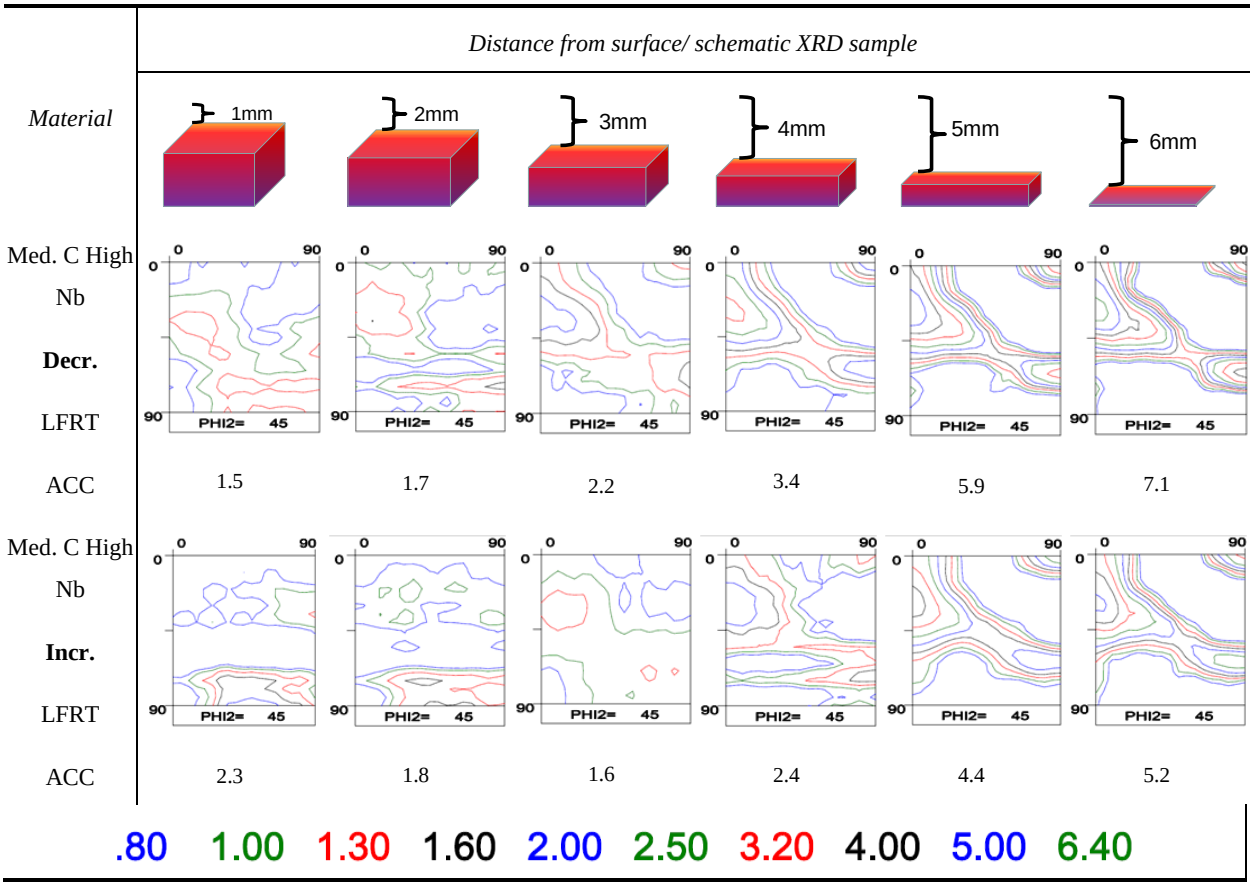

Figure V.1-19 *Texture at various thicknesses. ODF section at φ2 = 45°. Iso-intensity lines: 0.8x - 1x -1.3x -1.6x -2x -2.5x -3.2x -5x -6.4x random.*

The strength of the texture components differ based on the strain path. Decreasing reduction per pass resulted in a stronger texture than its increasing strain counterpart. The texture weakened towards the ¼ thickness in both conditions and the Goss and Brass components developed near the surface (starting from 2mm distance from the surface) of the samples. Interestingly, the

increasing reduction draught exhibited only shear texture components (Goss, Brass, and Copper). Similarly, the decreasing draught consisted of a slightly weaker texture resulting from the combination of Brass and Goss together with a "*beta*"-FCC deformation fiber. This finding concurs with the fact that the friction coefficient should increase with increasing reduction draught and hence, the intensity of the shear texture components can increase. The "weak transition texture" that developed at 3mm from the surface in the increasing draught is particularly surprising.

V.1.4 Comparison of measured and modelled textures

There are a number of published studies which predict the microstructural changes which occur during hot rolling (γ deformation behavior, the γ to α transformation behavior, precipitation behavior, the final α grain size...), for e.g. [2], [13], [14]. The comparison of experimentally produced data with these types of models goes beyond the scope of the present study. However, the acquired crystallographic data were used to evaluate the correspondence between the measured and corresponding simulated textures at certain TMCP stages.

V.1.4.1 Texture

In their analysis of the crystallographic texture changes in aluminum, *Sidor et al.* [15] developed a recrystallization model based on nucleation and growth selection. The details of the model can be found in the original paper [15]. In the current work, an attempt was made to further understand the evolution of the γ texture and therefore verify the corresponding mechanisms involved during the TMCP of HSLA pipeline steels. For that purpose, the same methods and model described in the aforementioned work [15] were followed. The model (ALAMEL) was inspired by the work of *Kestens and Jonas* [16], and is based on the preferential nucleation and growth of grains with low Taylor factor.

Since the goal of the thesis was to understand the influence of the processing variables of TMCP, particularly during finishing rolling, the initial stage of the model was set at Q2 (c.f. *Figure V.1-1*). In other words, the assumed initial γ texture was created with the aim of reproducing the texture observed after rough rolling and the transfer up to the finishing rolling (based on the

experimental characterization results of the material at the point described in *Figure V.1-1* as Q2).

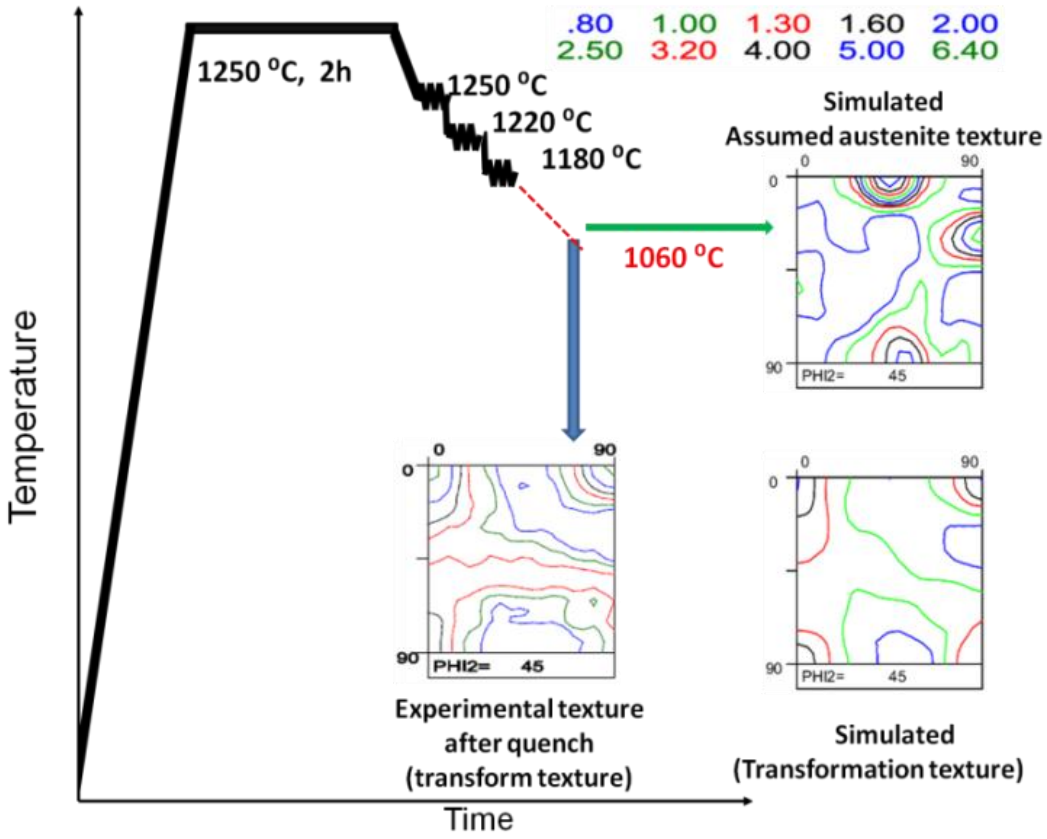

Figure V.1-20 *Illustration of the simulated and measured textures (φ2=45° ODF sections) at the indicated stage of TMCP.*

Hence, ***Figure V.1-20*** illustrates the initial simulated austenite texture (φ2=45° ODF) at 1060°C just before finishing rolling. Additionally, the experimentally measured, transformed texture at that point is compared with the modelled transformation texture. The initially introduced texture was a mixture of the following textures: a) weak β-fiber – γ deformation texture component; b) strong cube component-austenite recrystallization texture component; c) boundaries which possess high mobility <111>40° orientation relations with the deformed matrix grains; d) random texture. There is a clear resemblance between the experimental and the simulated textures although the latter is slightly weaker than the former and there is only a minor difference, of around 0.5 mrd, in the intensities of the simulated texture which appears to be weaker.

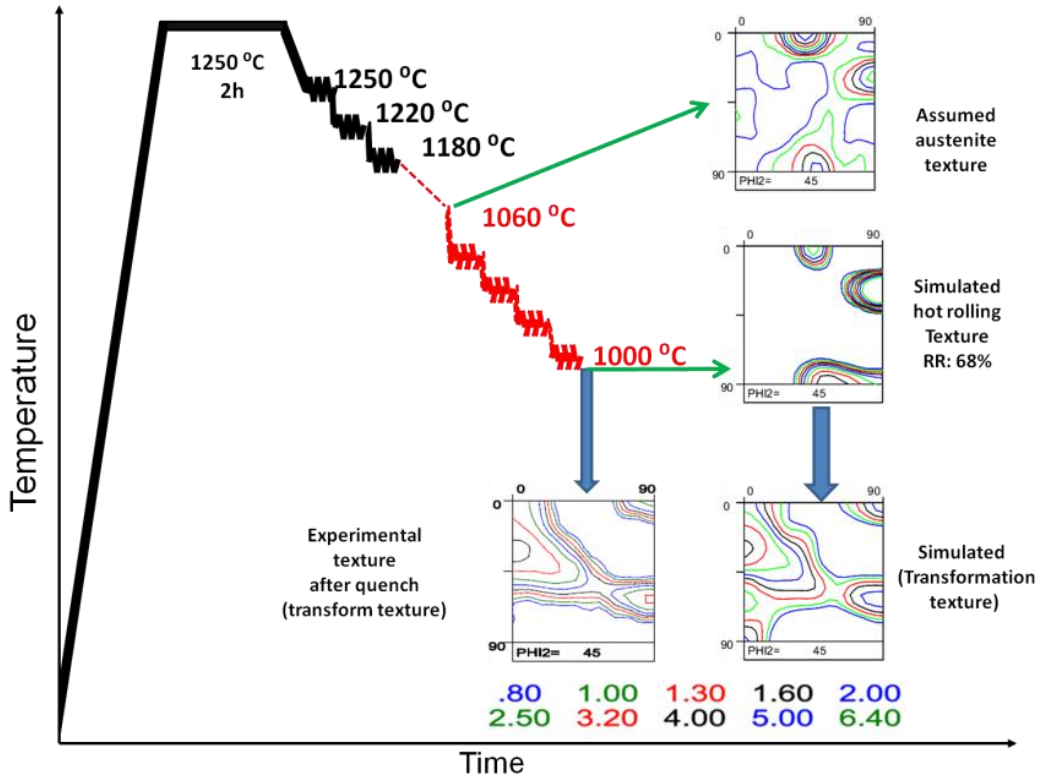

Figure V.1-21 *Illustration of the simulated and measured textures (φ2=45° ODF sections) at the indicated stage of TMCP.*

ALAMEL [17, 18] is a poly-crystal plasticity model which was used to predict the plastic behaviour of the material during finishing rolling. A rolling simulation of 68% reduction was applied. The resulting γ texture is shown in Figure V.1-21. Copper and Brass are the dominant components in the φ2=45° ODF section and the Goss and Cube occur with relatively weaker intensities. After transformation to BCC products, the resulting texture is very similar both quantitatively and quantitatively to those measures experimentally. As discussed in the previous section, the Copper, Brass, and Goss components, resulting from finishing rolling of γ below Tnr, transformed to the so-called "deformation fiber" (or BCC beta fiber) (see Chapter II.4 for reference φ2=45° ODF section). This fiber is composed of the {114}<110>, {113}<110>, {112}<131>, {111}<132>, {111}<011>, {111}<123>, {554}<225>, {332}<113>, and {001}<110> components. The predicted and measured textures differ only as it relates to the presence of the rotated Goss component {110}<110>. Although predicted by the simulation, the {110}<110> component was not present in the measured samples. In addition, the rotated Goss component may have originated from Cube and Copper parent orientations [19]. The absence of

certain variants is known as the variant selection mechanism. *Butron-Guillen et al.* [20] attributed the absence of the rotated Goss{110}<110> orientation to the residual stresses remaining in the material. In their own words "*During transformation, the relaxation of this residual stress acts to favour certain possible Bain contraction axes over others and therefore to the derivation of a residual stress rule. The role of this rule is to reject some of the variants selected by both the planar growth and slip-based criteria; this applies to all of the {110}<110> and {100}<uvw> orientations otherwise chosen by the latter two criteria."*
The results presented in this section are further discussed in chapter VI.

V.2 Analysis of mechanical properties

V.2.1 Analysis of the mechanical behavior as a function of the chemical composition

The mechanical behavior of steels with different C-Nb compositions will be described in this section. Properties such as the YS, UTS, elongation, and ductile to brittle transition behavior of the TMCP laboratory processed steels, with constant reduction draught, High/Low FRT and ACC/Air cooling (see Table V.2-1), are described in relation to variations in the chemical composition (for details regarding the composition see section IV.1).

V.2.1.1 Reference material: Med. C – High Nb

The engineering stress-strain curves for the reference composition were measured in the transversal direction and are shown in *Figure V.2-1*. Three samples were tested for each material. In order to prevent overcrowding in the plots, *Figure V.2-1* only displays the representative curves for each material and the average values. Complete figures are shown in Table V.2-4. The YS, UTS, and elongation changed significantly with variations in the processing conditions. At low FRT, the YS increased irrespective of the cooling rate, whereas the UTS increased only after ACC. However, for the same FRT, the yield and ultimate tensile strengths both improved significantly with increased cooling rate.

All of the air-cooled samples exhibited larger elongations at fracture than their ACC counterparts; the elongation of the ACC samples exhibited low sensitivity to the FRT.

A plot of the energy absorbed during the Charpy V-Notch impact test as a function of temperature (Figure V.2-2) reveals that all of the plates have similar upper (of ~250 J) and comparable lower shelf energies, respectively. In addition, the samples produced under ACC, had approximately the same toughness and the ductile to brittle transition temperature (DBTT), irrespective of the FRT; however, the DBTT of the air-cooled samples decreased by ~30 °C with a reduction in the FRT.

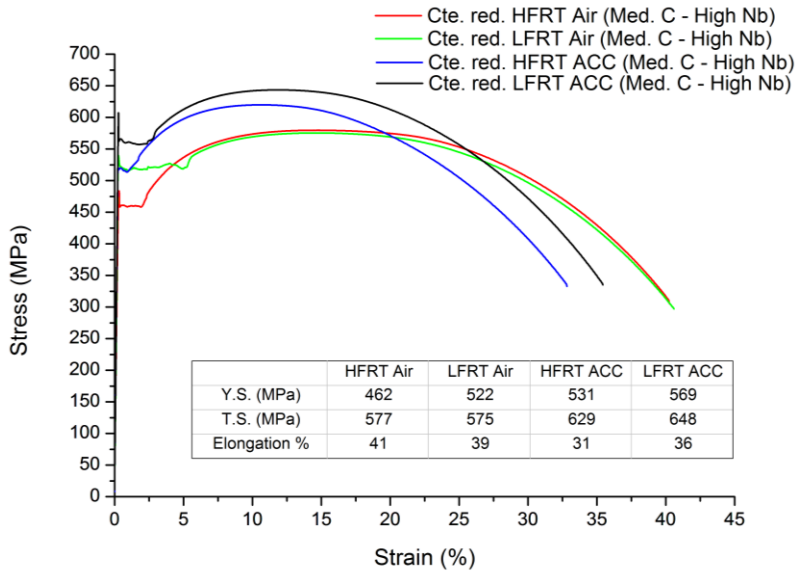

	HFRT Air	LFRT Air	HFRT ACC	LFRT ACC
Y.S. (MPa)	462	522	531	569
T.S. (MPa)	577	575	629	648
Elongation %	41	39	31	36

Figure V.2-1 *Stress-strain curves (uniaxial tensile test). Comparison of schedules with different TMCP parameters.*

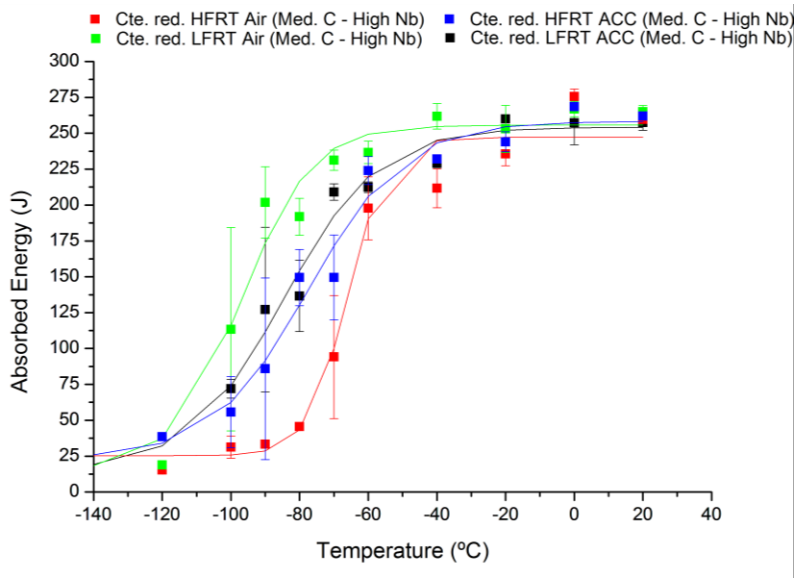

Figure V.2-2 *Energies absorbed during Charpy V-notch impact testing at various temperatures. Comparison of schedules with different TMCP parameters.*

V.2.1.2 Laboratory cast steels

Four HSLA steel grades were specially designed in order to investigate the effect of varying C and Nb content (c.f. Table V.2-2.) on the corresponding mechanical behavior.

V.2.1.2.1 Low C - Low Nb

The YS of this steel varied in a similar manner to that of its Med. C – High Nb counterpart. i.e., the yield strength increased with decreasing FRT for both high and low cooling rates. Moreover, for the same FRT, the YS and UTS both increased with increasing cooling (c.f. *Figure V.2-3*). Samples that were cooled in the same manner, by either air or ACC, had similar DBTT (c.f. *Figure V.2-4*). In addition, for the same cooling rate, the DBTTs of the plates rolled at high FRT are ~10 °C lower than those of their low FRT counterparts. The spread in the DBTT values corresponding to the different TMCP schedules was reduced, however, for temperatures ranging from -80 °C to -100 °C; this spread is half as large as that observed in the case of the Medium C – High Nb steel.

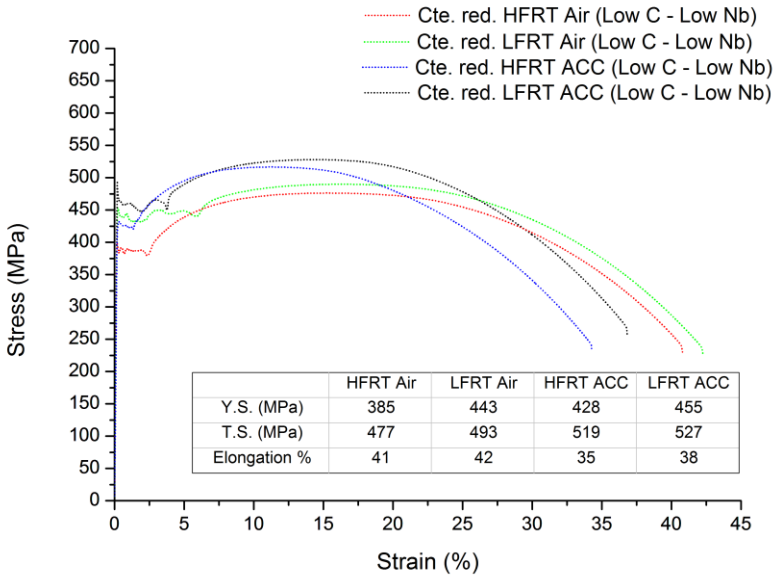

	HFRT Air	LFRT Air	HFRT ACC	LFRT ACC
Y.S. (MPa)	385	443	428	455
T.S. (MPa)	477	493	519	527
Elongation %	41	42	35	38

Figure V.2-3 *Stress-strain curves (uniaxial tensile test). Comparison of schedules with different TMCP parameters.*

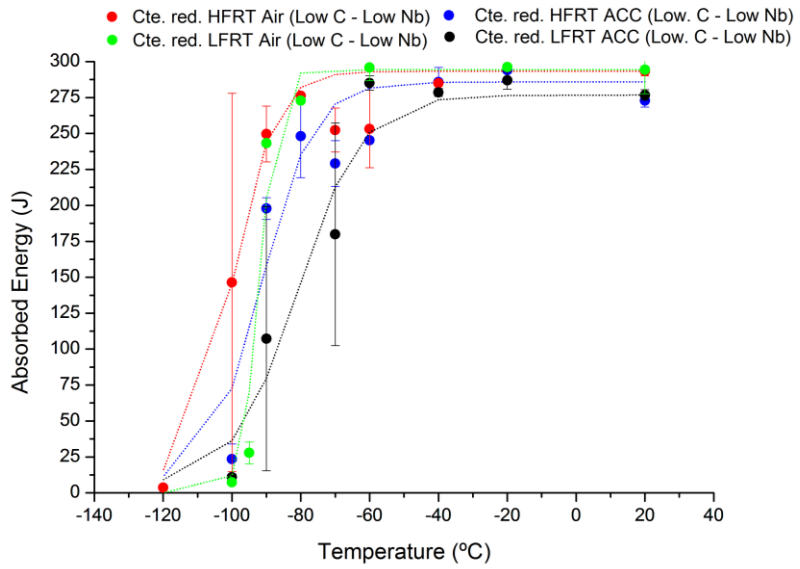

Figure V.2-4 *Energies absorbed during Charpy V-notch impact testing at various temperatures. Comparison of schedules with different TMCP parameters.*

V.2.1.2.2 Low C –Med. Nb

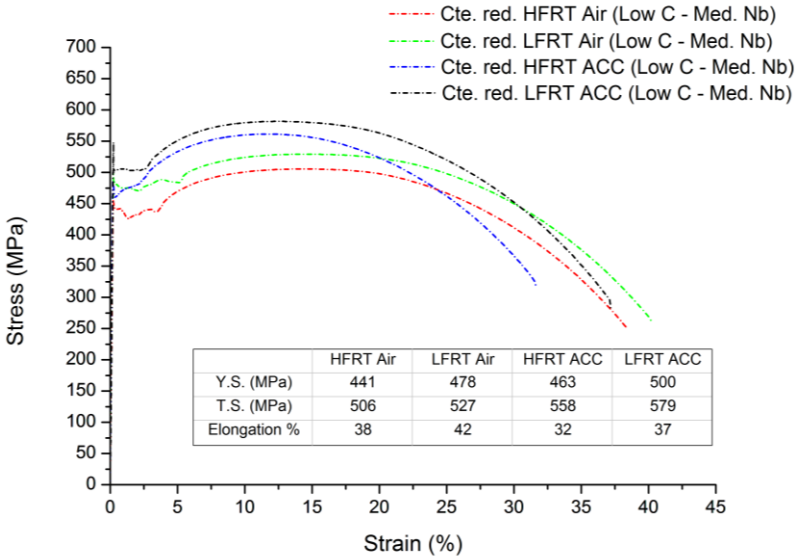

Figure V.2-5 *Stress-strain curves (uniaxial tensile test). Comparison of schedules with different TMCP parameters.*

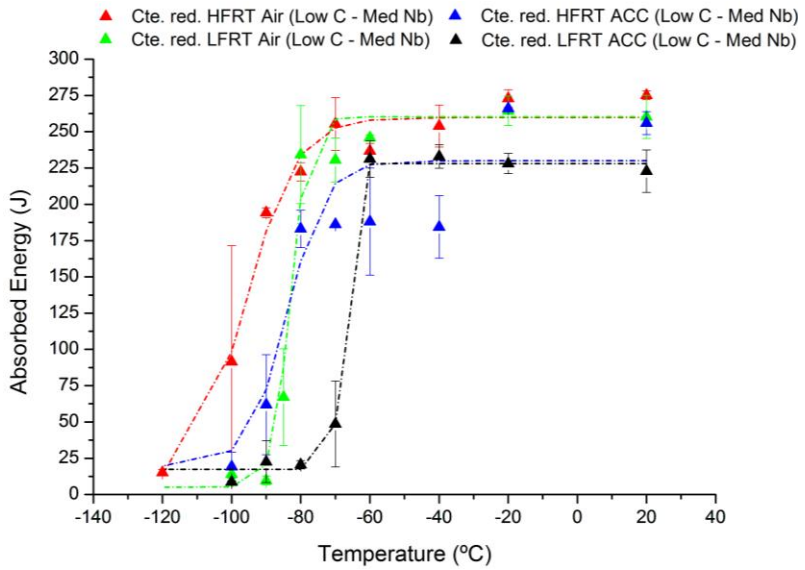

Figure V.2-6 *Energies absorbed during Charpy V-notch impact testing at various temperatures. Comparison of schedules with different TMCP parameters.*

Figure V.2-6 shows the DBTT curves of the low C- Med. Nb steel for different TMCP schedules. Low FRT followed by ACC route and high FRT followed by air cooling resulted in the highest and lowest DBTT, respectively. In contrast, high FRT followed by ACC and low FRT followed by air cooling resulted in similar mechanical response.

V.2.1.2.3 High C – Low Nb

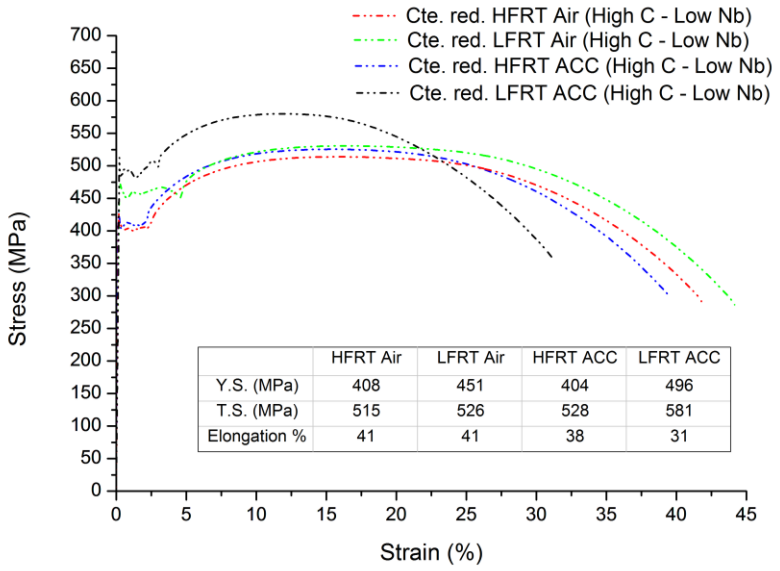

Figure V.2-7 *Stress-strain curves (uniaxial tensile test). Comparison of schedules with different TMCP parameters.*

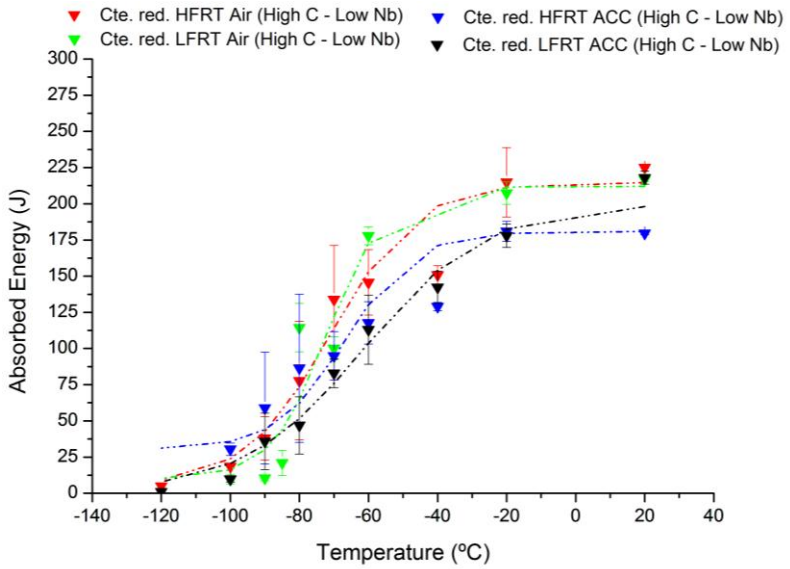

Figure V.2-8 *Energies absorbed during Charpy V-notch impact testing at various temperatures. Comparison of schedules with different TMCP parameters.*

High C- Low Nb steels exhibited similar behavior to that of their Med. C – High Nb counterparts; i.e., the YS increased with a decreasing of FRT irrespective of the cooling rate. However, the YS and UTS did not increase for the high FRT+ ACC route (see *Figure V.2-7*). The tensile properties of the High C – Low Nb composition are, therefore, insensitive to the cooling rate (in the context of our work) for finishing rolling performed at high temperatures. Furthermore, *Figure V.2-8*, shows that varying the TMCP route has little effect on the DBT behavior of these steels; the transition temperatures did not change significantly with TMCP route. Nevertheless, the ACC-processed samples had lower USE (approx. 25-30J) than their air-cooled counterparts.

V.2.1.2.4 High C – Med. Nb

The High C – Medium Nb steels exhibited identical stress-strain sensitivity to the various TMCP routes to those of the reference Medium C – High Nb (see V.2.1.1, *Figure V.2-1* and *Figure V.2-9*) steel. The High C – Medium Nb steel plates can be divided into two groups based on their ductile to brittle transition (DBT) behavior. On the one hand, the plates cooled via ACC had a DBTT of ~-50°C. On the other hand, the air-cooled plates had a DBTT of ~-75°C. The latter group exhibited somewhat sharper DBT behavior than that of the former.

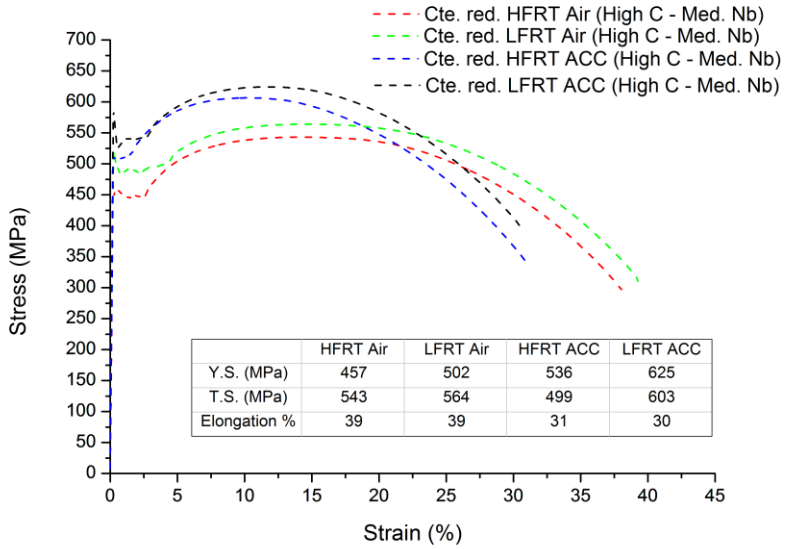

Figure V.2-9 *Stress-strain curves (uniaxial tensile test). Comparison of schedules with different TMCP parameters.*

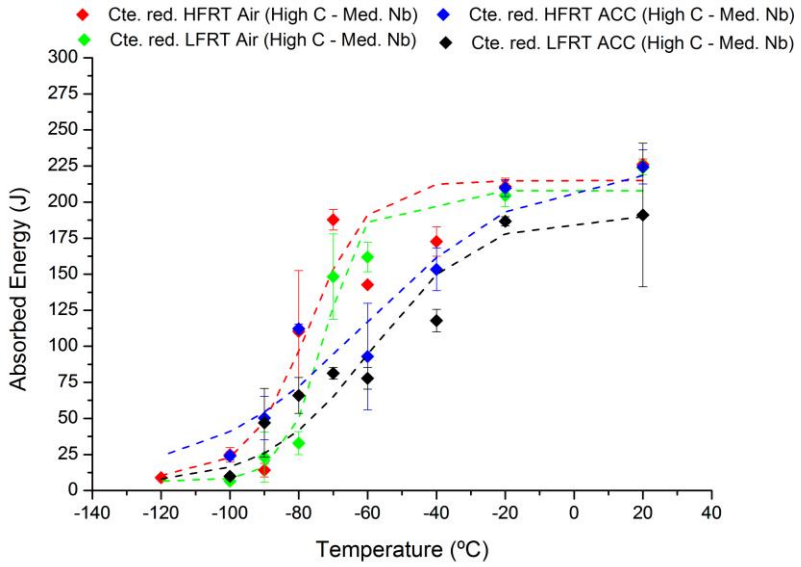

Figure V.2-10 *Energies absorbed during Charpy V-notch impact testing at various temperatures. Comparison of schedules with different TMCP parameters.*

V.2.2 Analysis of process parameters

V.2.2.1 Finishing rolling reduction draught

The variation of YS, UTS, elongation, and DBT behavior of the TMCP processed steels is analyzed as a function of the finish rolling reduction draft. To simplify the analysis, all further discussion in section V.2.2.1 will focus on the Med. C – High Nb composition.

V.2.2.1.1 Constant rolling reduction per pass

The variability of the mechanical properties as a function of different TMCP routes at constant reduction draught is discussed in section V.2.1.1 and shown in *Figure V.2-1* and *Figure V.2-2*.

V.2.2.1.2 Increasing rolling reduction per pass

For both cooling rates, the YS increases with increasing reduction per pass and decreasing FRT during the finish rolling. In contrast, the UTS did not change when the Air cooling route was followed. The UTS increased slightly with a decrease in FRT for the ACC condition (see *Figure V.2-11*). The figure clearly shows that an increase in the cooling rate at the same FRT leads to significant improvements of the YS and UTS. Furthermore, the total elongation was found to be quite sensitive to the FRT when ACC was employed. Plates rolled at Low FRT followed by the ACC route exhibited the lowest total elongation. As mentioned previously, in order to have a clear illustration of the trends, *Figure V.2-11* displays only the representative curves for each material and the corresponding average values. The complete data from the tensile test can be found in the annex.

The energies absorbed at various temperatures during Charpy V-notch impact testing are shown in *Figure V.2-12*. The figure shows that low FRT followed by the air cooling route resulted in an improved DBTT (i.e. decreases the DBTT) with respect to the other three TMCP routes.

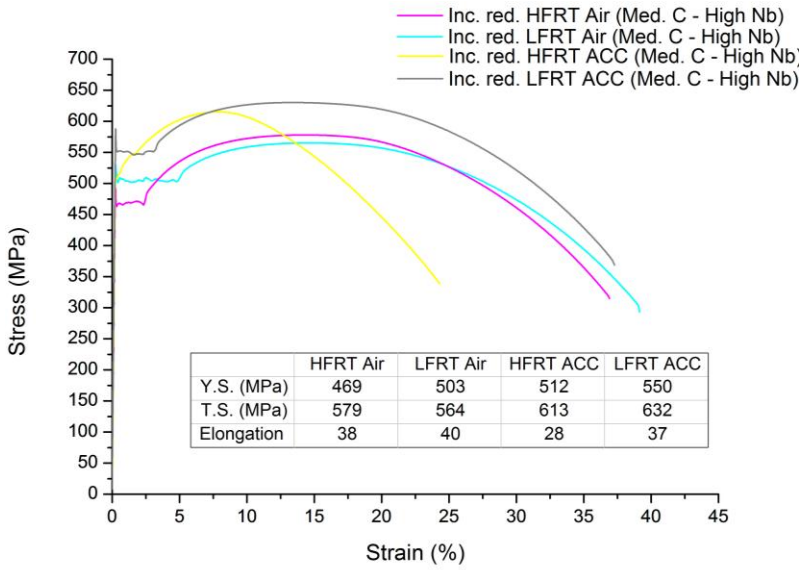

Figure V.2-11 *Stress-strain curves (uniaxial tensile test). Comparison of schedules with different TMCP parameters.*

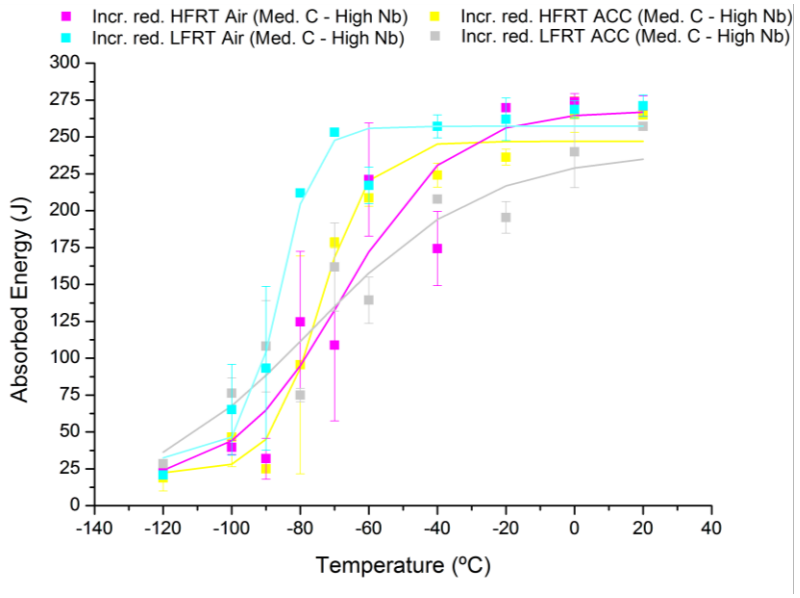

Figure V.2-12 *Energies absorbed during Charpy V-notch impact testing at various temperatures. Comparison of schedules with different TMCP parameters.*

V.2.2.1.3 Decreasing rolling reduction per pass

The sensitivity of the mechanical properties to variations in the FRT and cooling condition can be considered from the viewpoint of the reduction draught during finishing rolling. Comparing *Figure V.2-1* and *Figure V.2-13*, and *Figure V.2-2*. and *Figure V.2-14* reveals similar behavior of

the materials during tensile and Charpy V-notch testing for both constant and reducing reduction draught.

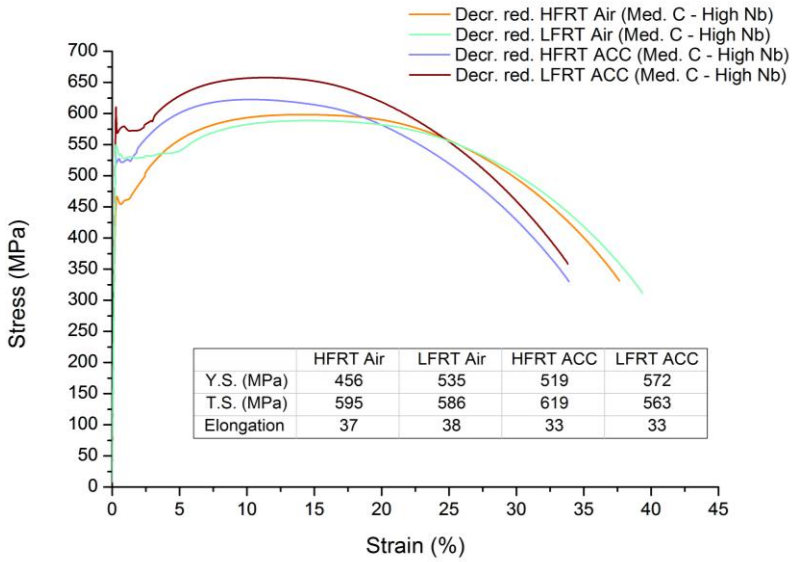

Figure V.2-13 *Stress-strain curves (uniaxial tensile test). Comparison of schedules with different TMCP parameters.*

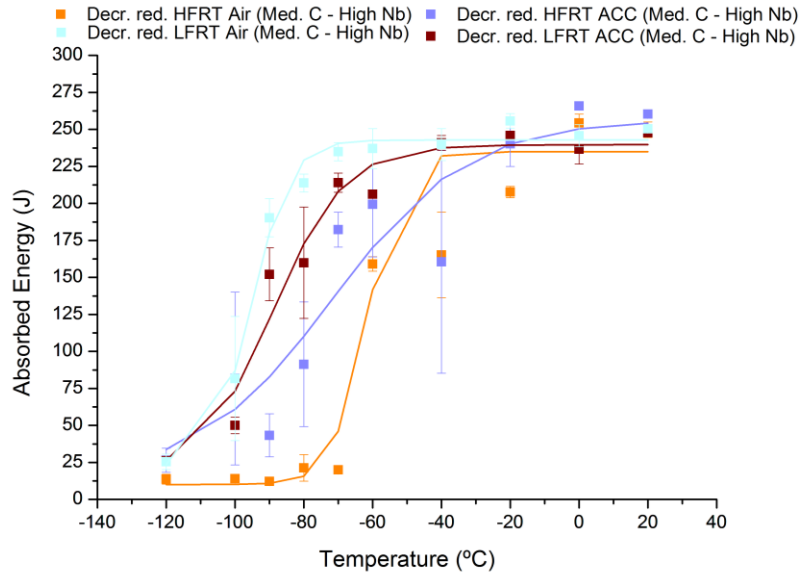

Figure V.2-14 *Energies absorbed during Charpy V-notch impact testing at various temperatures. Comparison of schedules with different TMCP parameters.*

The combined effect of deformation path, finishing temperature, and cooling condition on the average YS is presented in *Figure V.2-15*. It is clear from the figure that the three reduction

draughts responded similarly to changes in the FRT and cooling condition. The YS values vary, in general, with the different reduction draughts, except in the case of the high FRT&Air route (where the three reduction draughts show very similar values). Comparing constant and decreasing reduction draughts seems to indicate that increasing reduction draught had, in general, a negative effect on the YS. It is obvious that, in absolute numbers, the low FRT&ACC route resulted in the highest YS, particularly when decreasing or constant reduction draughts were applied.

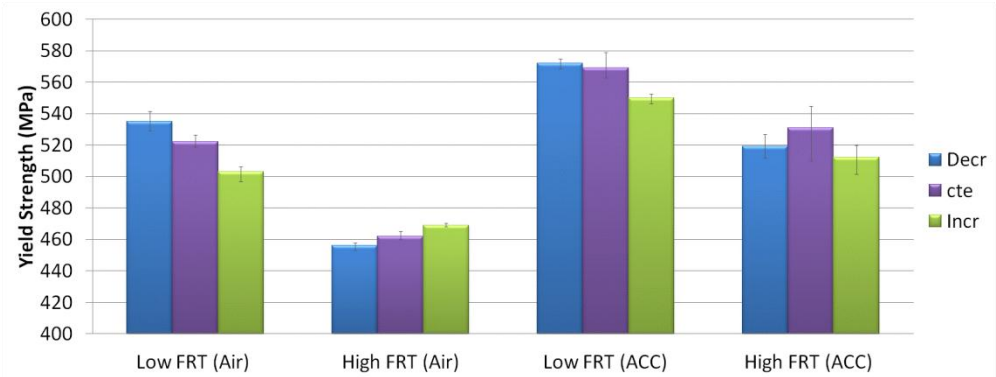

Figure V.2-15 *Comparison of the combined effect of FRT-cooling condition-reduction draught on the YS of Med. C – High Nb steel.*

Figure V.2-16 illustrates the combined effect of finishing rolling temperature and cooling condition on the average UTS. Again, the three reduction draughts exhibited similar response to the conjoining changes in FRT and cooling condition. Nevertheless, for all the conditions, there was a significant gap (in MP) between the decreasing and increasing draughts, except for high FRT and ACC. Decreasing reduction draught results in the highest values of the UTS in most of the studied schedules.

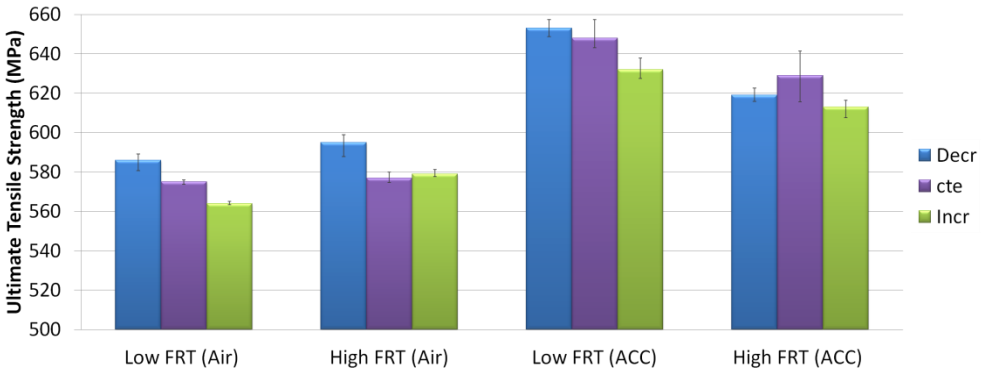

Figure V.2-16 *Comparison of the combined effect of FRT-cooling condition-reduction draught on the UTS of the material.*

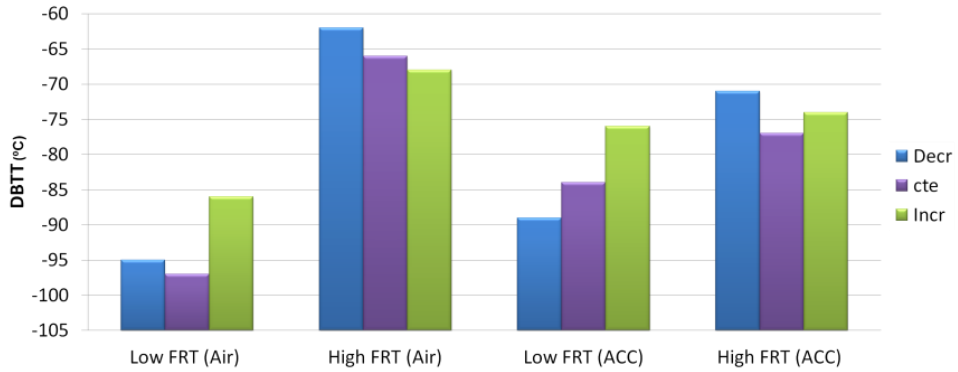

Figure V.2-17 *Comparison of the combined effect of FRT-cooling condition-reduction draught on the DBTT of the material.*

Figure V.2-17 compares the combined effect of finishing temperature and cooling condition on the DBTT for the three reduction draughts. Comparing reduction draughts reveals that the largest differences in the DBTT appear at low FRT. In this condition, increasing reduction draught resulted in the worst DBTT. High FRT conditions did not result in any significant differences in the DBTT.

V.2.2.2 Cooling conditions

Figure V.2-15, *Figure V.2-16*, and *Figure V.2-17* provide valuable information about the effect of cooling on the YS, UTS, and DBTT respectively. It is apparent from these figures that the YS and UTS increase when the cooling rate is increased after the same FRT. It is interesting to note that the DBTT of the air-cooled plates showed higher sensitivity to FRT than their ACC counterparts, particularly for increasing and constant reduction draughts. In the case of ACC, the decreasing reduction draught was the only scheduled that displayed sensitivity to changes in the FRT. These differences in sensitivity may be attributed to the microstructures which develop after each cooling condition. With air cooling (cooling rate of approx. 0.5°C/s) the microstructure consists primarily of α_p, α_q, and P_L. On the other hand, ACC (cooling rate higher than 10°C/s) resulted in a microstructure consisting mainly of α_B.

These results are consistent with those of other studies [21] on steels of similar chemical composition.

Table V.2-3 compares, for the different chemical compositions, the impact of variations in an individual TMCP parameter on the YS and UTS. The average increase in the YS and UTS when

the FRT decreases before ACC was found to be 9% and 3.5%, respectively. The most striking improvement of both the YS and UTS occurs in the High C - Low Nb composition steel. On the contrary, there were only minor enhancements of the YS and UTS when the Low C - Low Nb composition steel was processed.

V.2.2.2.1 Air cooling

In the case of air cooling, the YS and UTS and increased and decreased by an average of 10.2% and 2.4%, respectively with decreasing FRT (see *Table V.2-3*). Interestingly, Low C - Low Nb and Med. C - High Nb compositions exhibited the largest increases in the YS.

V.2.2.3 General comparison - Discussion

In order to have a complete picture of the materials under investigation, the variations in yield strength (YS), and ultimate tensile strength (UTS), as a function of the chemical composition (mainly variations of C and Nb contents) and TMCP routes are shown in *Figure V.2-18* and *Figure V.2-19*, respectively.

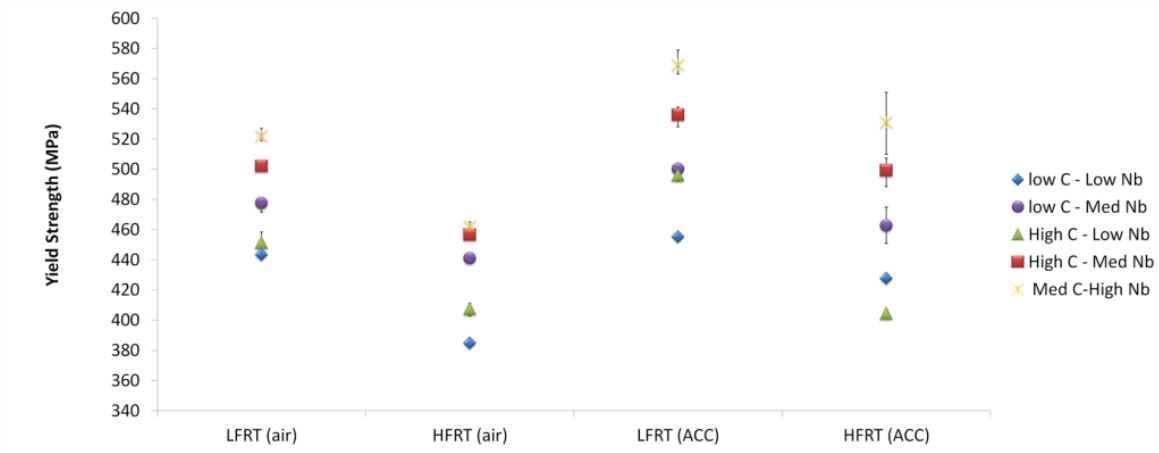

Figure V.2-18 *Comparison of the combined effect of FRT and cooling condition on the YS of HSLA pipeline steels with different compositions.*

Figure V.2-18 shows that the steels with high Nb content have the highest values of yield strength irrespective of the TMCP schedule; steels with low and medium Nb contents have, correspondingly, lower yield strengths for all the schedules considered. This can be explained by the fact that precipitation strengthening was enhanced in the steels which have high Nb contents.

In addition, for the same Nb content, the steels with higher amounts of C have slightly higher yield strengths than those with lower C contents.

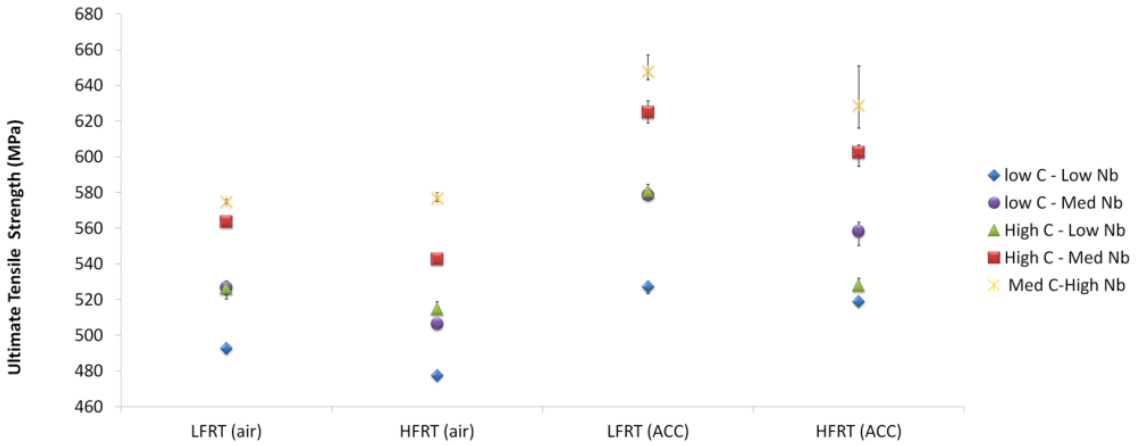

Figure V.2-19 *Comparison of the combined effect of FRT and cooling condition on the UTS of HSLA pipeline steels with different compositions.*

The plates rolled at low FRT show better yield strengths in comparison to the ones rolled at high FRT, because (as discussed in sections II.2.2 and II.5.4) the austenite pancaking at the former provides a higher number of potential ferrite nucleation sites and hence, more favorable conditions for ferrite (bainite) grain refinement than at the latter. The yield strength has maximum and maximum values of about 570MPa and 380MPa at low FRT&ACC and at high FRT followed by air cooling in the Med. C – High Nb and Low C - Low Nb steels, respectively.

Table V.2-3 summarizes the changes in the yield and ultimate tensile strengths. For example, at low and high FRT the yield strength increased an average 6% and 7%, respectively, with increasing cooling rate; the ultimate tensile strength also increased with increasing cooling rate. Low FRT combined with (especially) air cooling resulted in the largest increase (10%) of the yield strength but had minimal effect on the ultimate tensile strength. Furthermore, of all the steels considered, medium- or high-C steels exhibited the greatest variations in yield strength with increasing cooling rate after low FRT; however, the effect of increased cooling rate after high FRT on the yield strength, seemed to have no correlation with the chemical composition. In other words, the yield strength of the Low C - Low Nb and Medium C - High Nb steels increased

by 10% and 13%, respectively when ACC was used instead of air cooling. High FRT proceeded by ACC had no effect on the yield strength of the High C - Low Nb steel. In fact, in all of the steels considered, low FRT + air cooling resulted in larger increases in the yield strength than those resulting from low FRT + ACC.

Chemical composition	*Impact of increased cooling rate at LFRT*		*Impact of increased cooling rate at HFRT*		*Impact of decreased FRT before air cooling*		*Impact of decreased FRT before ACC cooling*	
	YS (%)	UTS (%)	YS (%)	UTS (%)	YS (%)	UTS (%)	YS (%)	UTS (%)
Low C - Low Nb	2.64	6.45	10.05	8.09	13.09	3.25	5.93	1.52
Low C - Med. Nb	4.40	8.98	4.75	9.32	7.74	3.98	7.40	3.63
High C - Low Nb	9.07	9.47	-0.99	2.46	9.53	2.09	18.55	9.12
High C – Med. Nb	6.34	9.76	8.42	9.12	8.96	2.84	6.90	3.52
Med. C -High Nb	8.26	11.27	12.99	8.27	11.49	-0.35	6.68	2.93
Average	6.14	9.18	7.04	7.45	10.17	2.36	9.09	4.14

Table V.2-3 *Quantitative impact of the variation of a TMCP parameter on strength, for various chemical compositions.*

Compared to the effect on the YS, low FRT + air cooling affected the ultimate tensile strength only slightly. This is worth mentioning owing to the importance of low YS/UTS ratios on pipeline steels [22]. A low ratio in steels, which exhibit work hardening behavior, ensures their ability to withstand plastic deformation. *Table V.2-4* shows the relatively low strain hardening of the Low C - Low Nb steels, which were rolled at low FRT and then air-cooled; a similar response was observed for all five steels. *Morrison* [23] identified the effect of grain size on the stress-strain relationships in low carbon steel which have microstructures consisting of ferrite and pearlite. More recently, other authors [24, 25] extended this correlation, between the work hardening coefficient and the grain size, to other steels and other microstructures. *Antoine* et al. [25], have, however, attributed the change in *n* to microstructural features other than grain size. Nevertheless, *Morrison's* equation [23] (see equation V.2-1), though simple, aptly describes the correlation between the work hardening behavior and the grain size.

Chemical composition	Engineering stress-strain curves
Low C - Low Nb	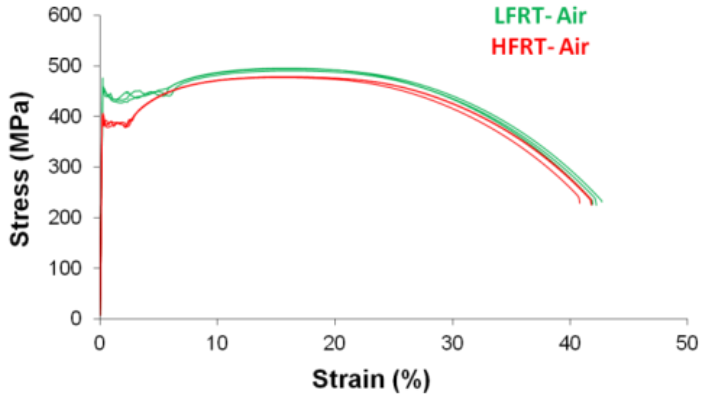
Low C - Med. Nb	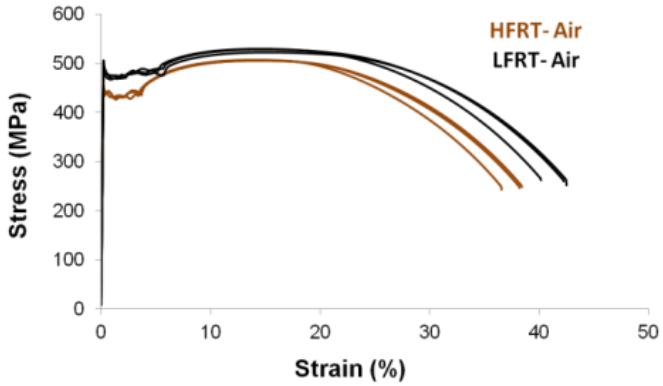
High C - Low Nb	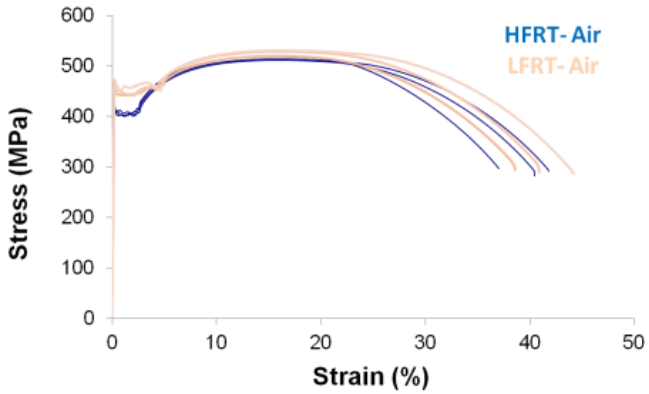

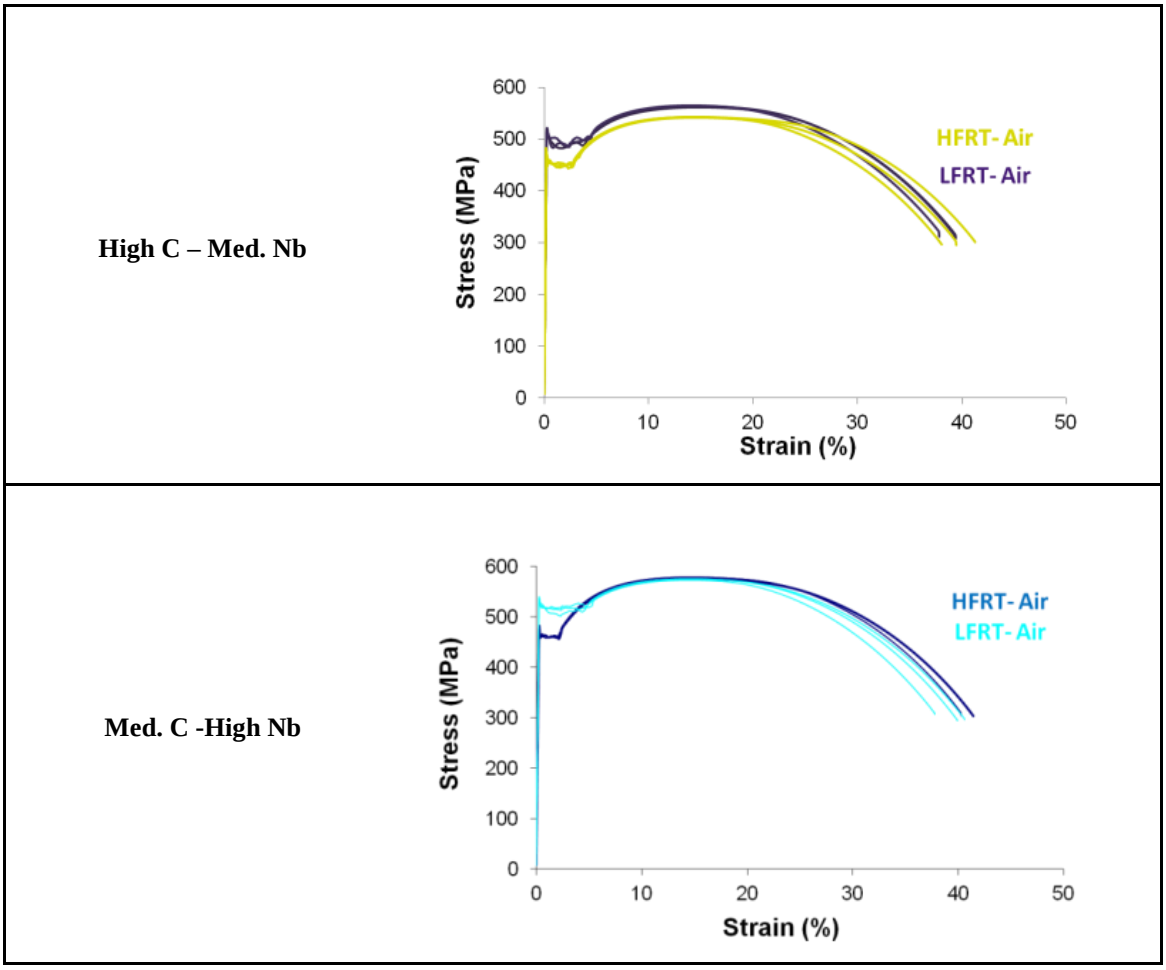

Table V.2-4 *Comparison of engineering stress-strain curves of TMCP schedules with low/high FRT and air cooling.*

Figure V.2-20 compares the results of previous works to those obtained in the present study. The data in *Table V.2-4* and *Figure V.2-20*, reveal that the different work hardening behaviors exhibited by steels processed at low and high FRT, and then air-cooled, is explained by the refinement of the average grain size. This has important consequences for the yield strength to ultimate tensile strength ratio, since the improvement in the yield strength, owing to the reduced average grain size of the α_p and α_{qp} microstructures, is not accompanied by an increase in the ultimate tensile strength. The lack of corresponding increase in the ultimate tensile strength results in an increased (deteriorated) ratio of the yield and ultimate tensile strengths ratio which is lower than unity.

$$n = \frac{5}{10 + D^{-\frac{1}{2}}} \qquad \textbf{V.2-2}$$

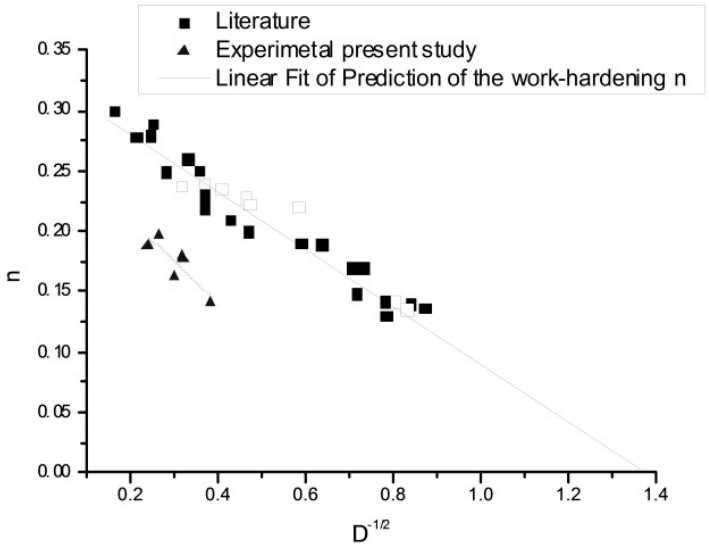

Figure V.2-20 *Correlation between the work hardening coefficient and the average grain size of ferritic microstructures* [24, 26].

The hyperbolic tangent function (see Chapter IV.3.2.2) was fitted to the plot of the absorbed energy versus temperature in order to determine the DBTT. The DBTT was defined using the so-called T_{50} criterion, which assumes that the DBTT is the temperature at which the impact energy is equal to half of the USE. *Figure V.2-21* c compares the DBTT of steels with different compositions after various TMCP schedules. As the figure shows, high- and low-C steels have (in general) high and low DBTTs, respectively. It is well-established that increasing C content results decreased toughness [27]. Nevertheless, it is worth noting that the addition of Nb to the high-C steels had only a slight impact on the DBTT. The four Low C - Low Nb have lower DBTT than that of their Low C – Medium Nb counterpart. However, of all the steels considered, the Medium C - High Nb steel exhibits the highest sensitivity to changes in the TMCP parameters (see *Figure V.2-21*).

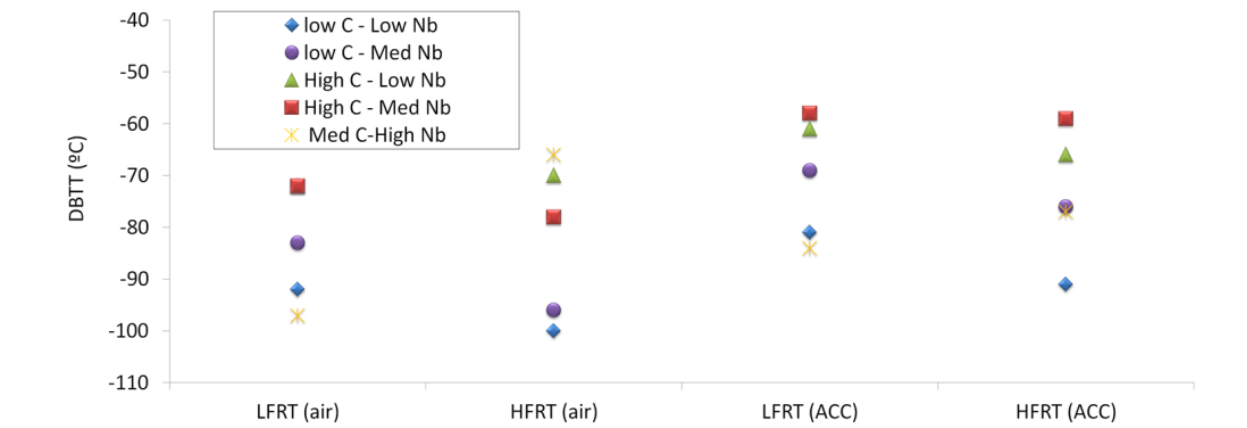

Figure V.2-21 *Comparison of the combined effect of FRT and cooling condition on the DBTT of HSLA pipeline steels with different compositions.*

V.2.3 Microstructural analysis

Representative optical, scanning electron, and transmission electron micrographs of the steels processed at different FRT and cooling conditions are presented in the figures in annex I. It is clear that the cooling conditions define, up to a certain level, the morphology of the microstructure. The main microstructural constituents at low cooling rates (air cooling) were α_p and α_{qp} with P_L and P_D. P_D was distributed in two types of arrangements, depending of the C content. C content has been found to define the fraction and distribution of second phases (especially pearlite). Pearlite islands were homogeneously distributed but appeared in banded arrays in the microstructures of steels with low and high C contents, respectively.

After ACC, the microstructures consist of $\alpha_{B(G)}$ with small amounts of P_L and P_D. Moreover, cementite particles were frequently observed at the grain boundaries.

The variations of the processing conditions (i.e. FRT, cooling condition, and strain path) resulted in differences in the average grain size. In *Figure V.2-22*, all the steels containing the reference Med. C - High Nb composition are separated and shown in different colors based on the strain path during the finish rolling. The schedule with decreasing reduction per pass showed the largest variation in the average grain sizes when the FRT and cooling condition are changed. Furthermore, compared to other schedules, a lowered FRT combined with air cooling resulted in greater amounts of grain refinement, particularly for decreasing strain path. The results from constant reductions per pass schedules bear a resemblance to the response displayed by

decreasing reduction path. A direct implication of this fact can be observed in *Figure V.2-15*, where similar YS values are observed, when decreasing and constant rolling paths are compared.

The path of increasing strain per pass resulted in a different response of the microstructure to variations of the FRT and cooling condition. The sensitivity was lowest for changes in the FRT or ACC. Varying the FRT and then air cooling resulted in no significant difference in the response of the microstructure. Moreover, the YS values changed significantly with the rolling schedules although there were only small differences in the average grain size.

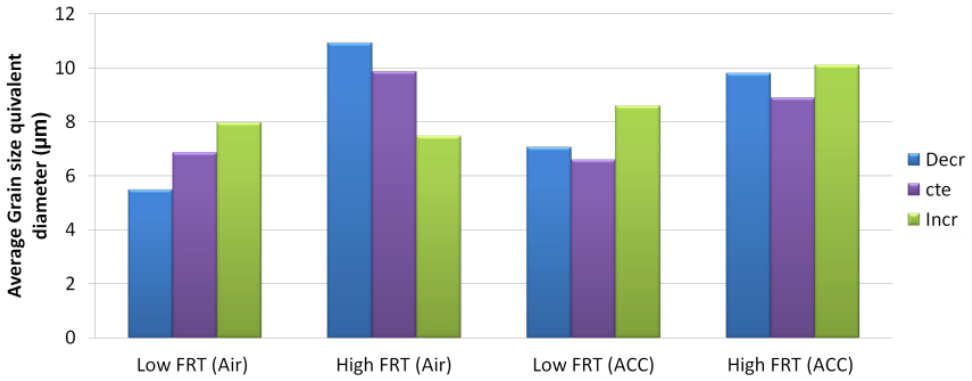

Figure V.2-22 *Comparison of the combined effect of FRT-cooling condition-reduction draught on the average grain size.*

All the chemical compositions under investigation were considered at constant reduction per pass. *Figure V.2-23* and V.2-24, show the effect of varying FRT and cooling condition on the average grain size; high and low angle grain boundaries (HAGBs and LAGBs) are defined by 15° and 5° misorientation criteria, respectively. As the figures show, lowering the FRT resulted in a decrease in the average grain size, irrespective of the cooling condition. As it relates to the impact of chemical composition, the Medium C – High Nb is relatively insensitive to the FRT and cooling condition. However, the effect of other compositions can be divided into two groups, especially in the case of air cooling. The low- and medium-Nb steels exhibit the highest and intermediate sensitivity, respectively, to variations in the FRT before air cooling, which indicates that Nb weakens the effect of varying FRT. This ability is especially highlighted in the case of air cooling. Furthermore, the materials processed at low FRT (Low C - Low Nb, Low C - Medium Nb, High C - Low Nb, High C - Medium Nb) had similar average grain size. As can be seen in *Figure V.2-15*, similar average grain sizes (i.e. at low FRT followed by air cooling) do not,

however, guarantee parity of the mechanical properties, and more specifically, of the YS. Hence, it is proposed here, that the grain size distribution and the potential clustering of certain microstructural elements be considered in addition to the average grain size. *Figure V.2-25* and *Figure V.2-26* show the grain size distribution maps obtained after processing the EBSD data of the ACC and air-cooled samples, respectively. Here, the reader can recognize the area fraction occupied by grains smaller than a pre-defined size. As can be seen from Figure V.2 25, the combination of low FRT with ACC and increasing draught gave rise to, in general, a fine-grained microstructure. In general, the cumulative fractions of ACC processed samples were smaller than those of air cooling. No significant differences were found between the ACC & constant reduction draught and the ACC & decreasing reduction draught when both low and high FRTs were considered.

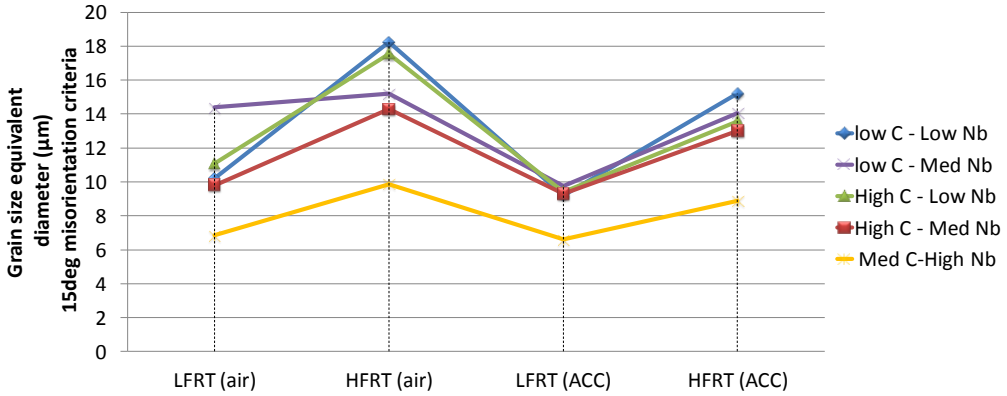

Figure V.2-23 *Comparison of the combined effect of FRT and cooling condition on the average grain size (15° misorientation criteria) of HSLA pipeline steels with different compositions.*

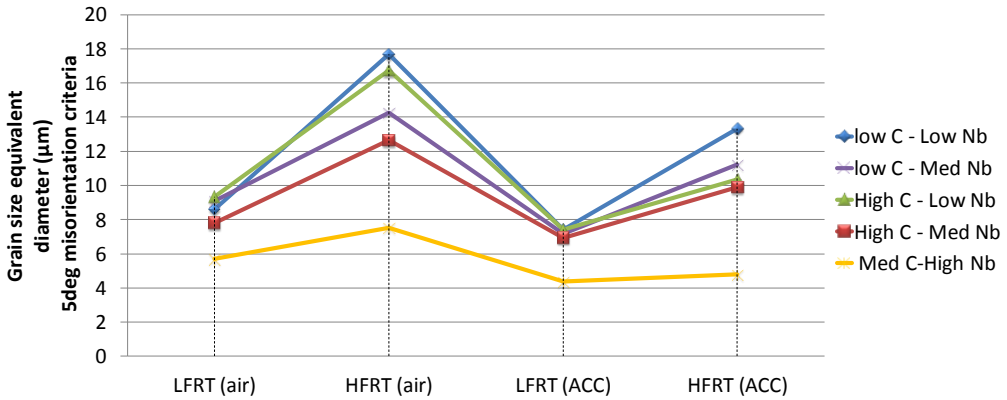

Figure V.2-24 *Comparison of the combined effect of FRT and cooling condition on the average grain size (5° misorientation criteria) of HSLA pipeline steels with different compositions.*

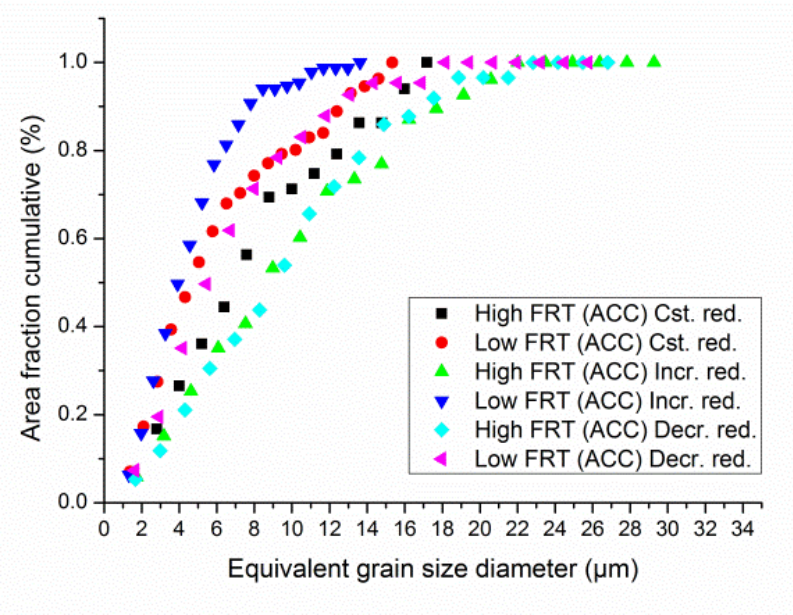

Figure V.2-25 *Comparison of the grain sizes obtained after ACC routes (15° misorientation criteria).*

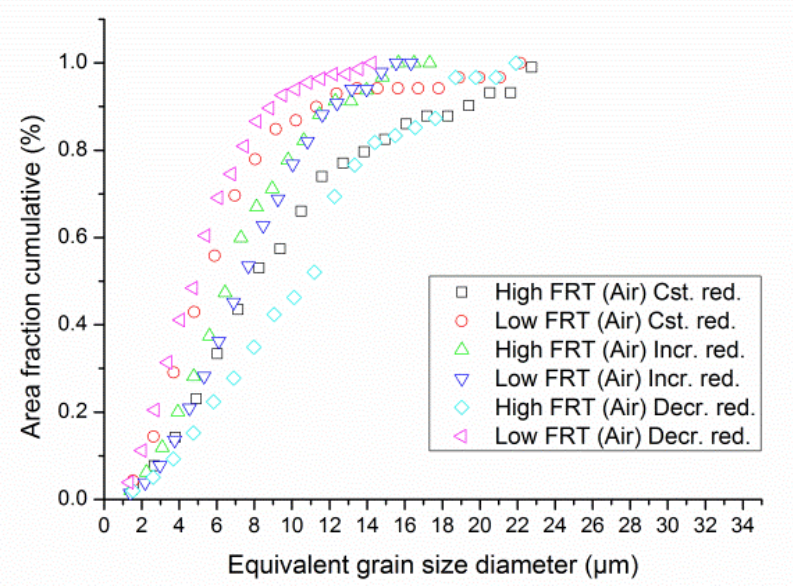

Figure V.2-26. *Comparison of the grain sizes obtained after air cooling routes (15° misorientation criteria).*

For the case of air cooling, the cumulative distributions indicate that, at low FRT, constant and decreasing reduction paths produced more refined microstructures than at high FRT. When the two FRTs were compared, there was, surprisingly, no significant difference in the size distributions of the samples which followed increasing reduction paths.

	ACC		
	↗ Increasing reduction per pass	Constant reduction per pass	↘Decreasing reduction per pass
	10%-21%-32%-35%	25%-25%-25%-25%	35%-32%-21%-10%
High FRT	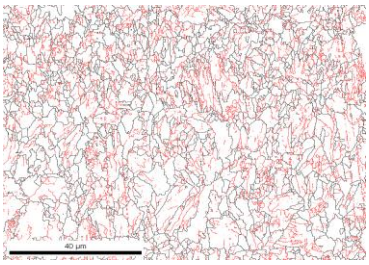	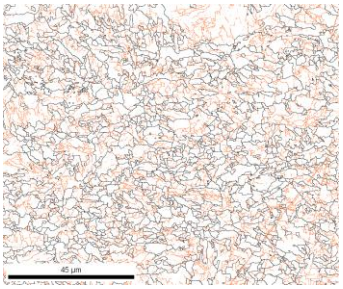	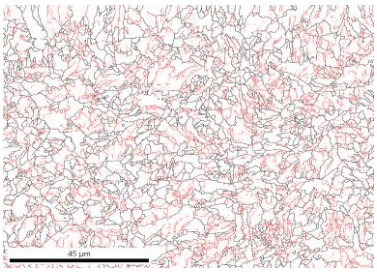
Low FRT	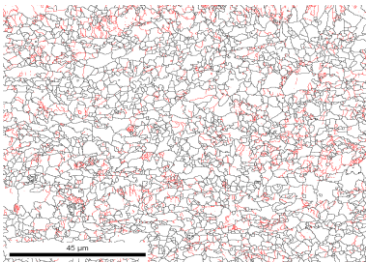	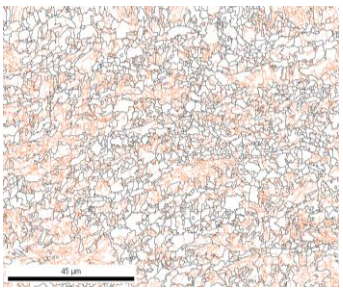	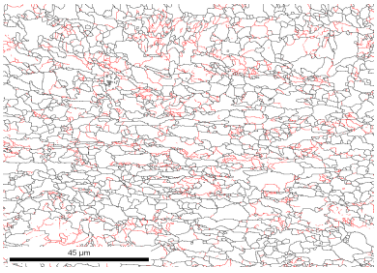

Figure V.2-27 *Grain boundary maps of various TMCP schedules with ACC showing HAGB >15° misorientation (black) and LAGB >2- 15° (red).*

	Air		
	↗ Increasing reduction per pass	Constant reduction per pass	↘Decreasing reduction per pass
	10%-21%-32%-35%	25%-25%-25%-25%	35%-32%-21%-10%
High FRT	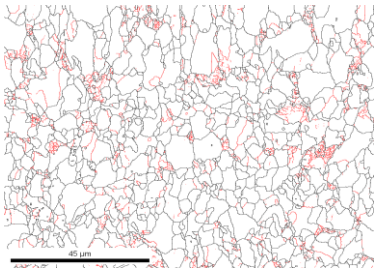	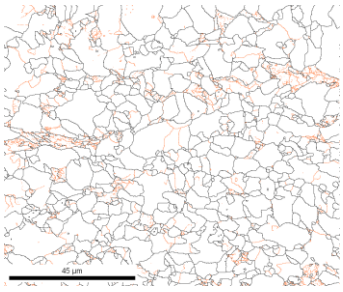	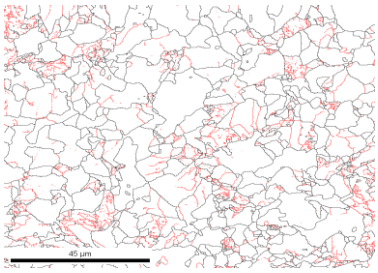
Low FRT	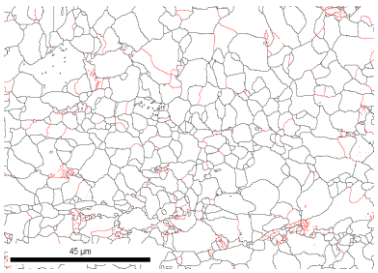	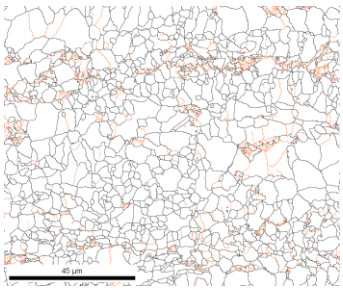	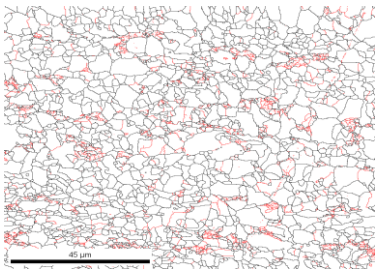

Figure V.2-28 *Grain boundary maps of various TMCP schedules with air cooling showing HAGB >15° misorientation (black) and LAGB >2- 15° (red).*

Two types of maps were used in order to assess the microstructure developed after each particular processing route. The traditional average values offer a quite broad description of the grain size. New maps are presented here, which visualize and identify the heterogeneities between the various grain size colonies (i.e. presence of larger grain size clusters). *Figure V.2-27* (ACC) and *Figure V.2-28* (air cooling) distinguish the distribution of high and low angle grain boundaries (HAGB and LAGB).

Compared to the simulation made with air cooling, ACC combined with simulated coiling was found to result in the formation of microstructures with more well-developed LAGB. The LAGB map confirmed that the main microstructural component present in all ACC steels is granular bainitic ferrite, but some small fractions of quasi-polygonal ferrite and dispersed islands of pearlite are also present.

Figure V.2-29 and *Figure V.2-30* show the grain size distribution maps obtained after post-processing of the EBSD data. These maps are useful for visualizing and identifying the microstructural heterogeneities (i.e. the presence of larger grain size clusters) and reveal that high FRT resulted, in general, in the prevalence of large grain size clusters. There were no significant differences in the grain size distributions for increasing or decreasing rolling reduction/per pass at high temperature combined with ACC. However, increasing draught at high FRT combined with air cooling resulted in a clear reduction in the number of large grain size clusters. Low FRT combined with both increasing reduction per pass and ACC, and constant reduction per pass and ACC, gave rise to a fine-grained microstructure in which large grain islands are homogeneously distributed.

These data aid in the interpretation of *Figure V.2-25* and *Figure V.2-26* and, compared to the average grain size value, provide a better explanation of the impact of TMCP parameters on the mechanical properties (see chapter VI.5).

	ACC		
	↗ Increasing reduction per pass	Constant reduction per pass	↘Decreasing reduction per pass
	10%-21%-32%-35%	25%-25%-25%-25%	35%-32%-21%-10%
High FRT	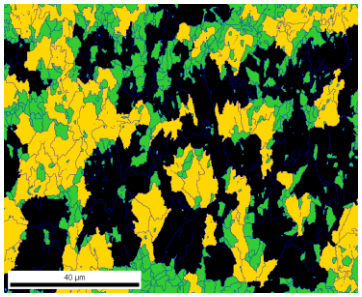	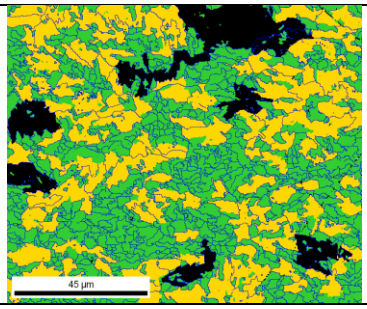	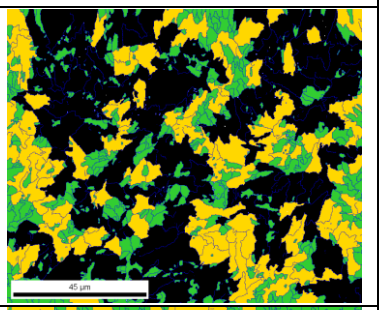
Low FRT	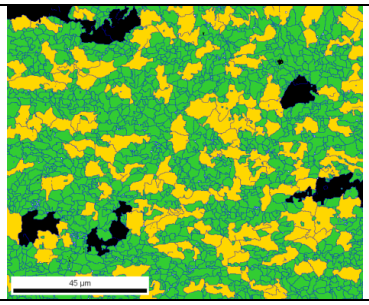	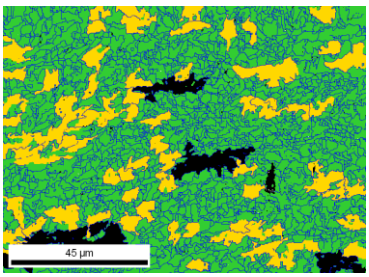	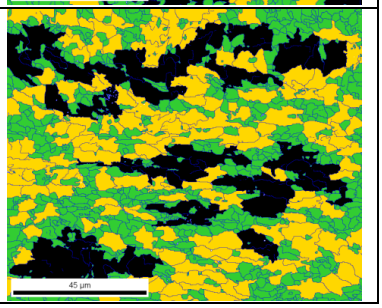

Figure V.2-29 *Grain size areas/cluster distribution maps of TMCP schedules following ACC and showing regions with grain size average diameter between: 1-5 µm (green), 5-10 µm (orange), 10-50 µm (black).*

	Air		
	↗ Increasing reduction per pass	Constant reduction per pass	↘Decreasing reduction per pass
	10%-21%-32%-35%	25%-25%-25%-25%	35%-32%-21%-10%
High FRT	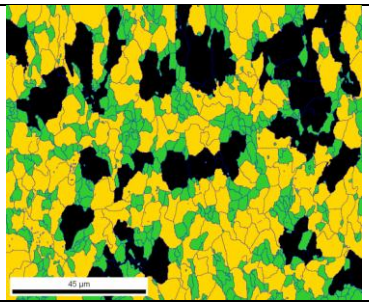	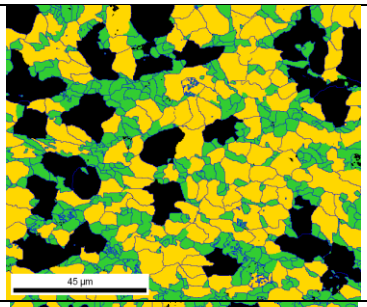	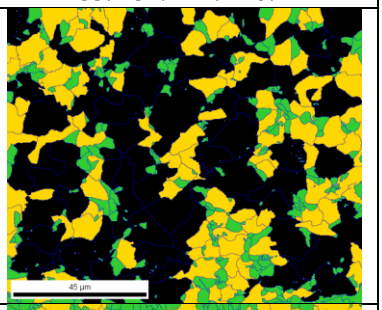
Low FRT	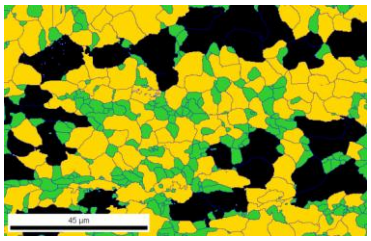	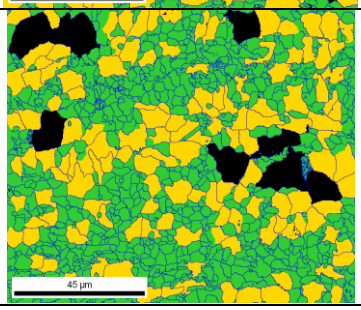	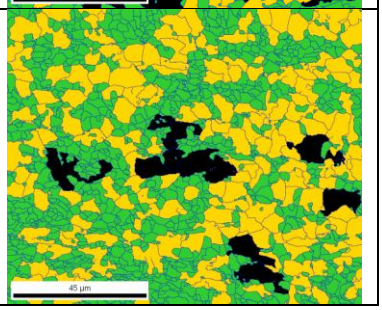

Figure V.2-30 *Grain size areas/cluster distribution maps of TMCP schedules following air cooling and showing regions with grain size average diameter between: 1-5µm (green), 5-10 µm (orange), 10-50 µm (black).*

V.2.4 Precipitation

Figure V.2-31 shows the dependence of %Nb precipitated on the variation of FRT, cooling condition, and deformation path. It is apparent from the data that the variation of the deformation schedule during finishing has little effect on the %Nb precipitated when low FRT and air cooling condition is applied. However, the other combinations of FRT and cooling condition resulted in some differences among the three deformation paths. Variations of ± 5% are considered to be within the observational error. Therefore, in the cases of ACC, decreasing and increasing reductions per pass have a similar effect on the precipitation kinetics whereas constant reduction resulted in a significantly lower % of Nb precipitated. This difference may possibly be explained by the fact that, at least one of the rolling reductions for either the decreasing or increasing reduction draught, was larger than the value applied for constant reductions. In addition, prior deformation is known to accelerate the onset of recrystallization [28, 29]. Strain-induced precipitation phenomena, generated in the "heavy reduction passes" of the decreasing and increasing reduction per pass, are, therefore, responsible for the large % of Nb precipitated at increasing/decreasing + ACC schedules when compared with constant reduction per pass. This precipitation behavior is of a particular interest in the case of ACC, since the onset of recrystallization plays a major role, and the progress of precipitation will be incomplete compared to that of their air-cooled counterparts. As Figure V.2-31 shows, there was a significant difference in Nb precipitated between the two cooling condition groups, especially when the same FRT is used. In the case of decreasing reduction per pass, compared to the case of ACC, approximately 20% more Nb was precipitated if air cooling followed the finishing rolling at both FRTs. When an increasing reduction path was applied, an enhancement of roughly 30% of Nb precipitated was achieved after air cooling. If the constant reduction draught is used, the amount of precipitated Nb increases to nearly 40%. These results suggest that, compared to increasing/decreasing reduction paths, variations in the FRT have a stronger impact on the fraction of precipitated Nb in the final rolling schedules executed with a constant reduction per pass.

Figure V.2-32 compares the % of Nb precipitated in the pipeline steels, which were subjected to constant reduction. In general, low FRT resulted in a higher % of precipitation and ACC resulted in a lower % of Nb precipitated. The Medium C - High Nb steel had the highest total amount of

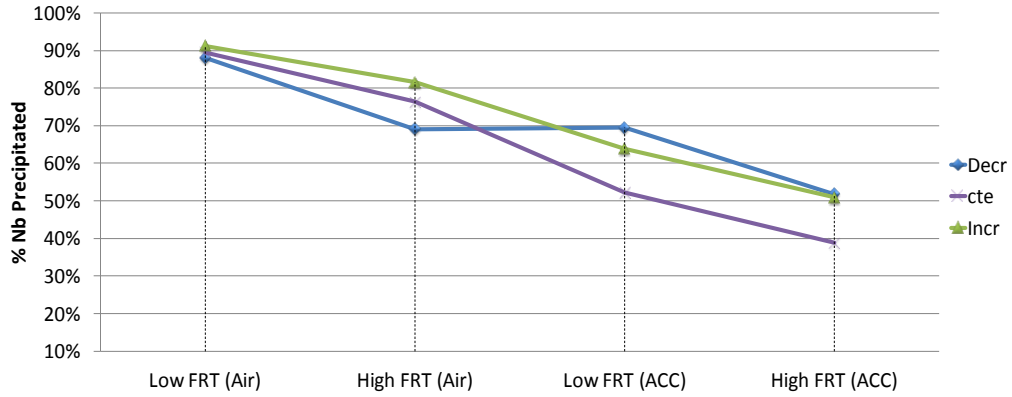

Figure V.2-31 *Comparison of the combined effect of FRT-cooling condition-reduction draught on the % of Nb precipitated.*

precipitated Nb. However, the fraction of Nb precipitated in the Medium C - High Nb, High C - Medium Nb, Low C - Medium Nb, and Low C - Low Nb steels varied by up to 50% with the TMCP route. The fraction of Nb precipitated in the High C - Low Nb steel varied, however, by only 25% with the TMCP route. This difference may be attributed to the difference in the Nb/C ratios (see *Table V.2-5*). The results from this study showed that, in general, after air-cooling, the higher the Nb/C ratio, the larger the % of total Nb precipitated. It can be seen from the data in *Table V.2-5* that Med C - High Nb and High C - Low Nb have the highest and lowest ratios, respectively. It is apparent that ACC did not result in significant differences except in the case of Med. C - High Nb. However, these data must be interpreted with caution because the ratio values do not show a wide enough spectra.

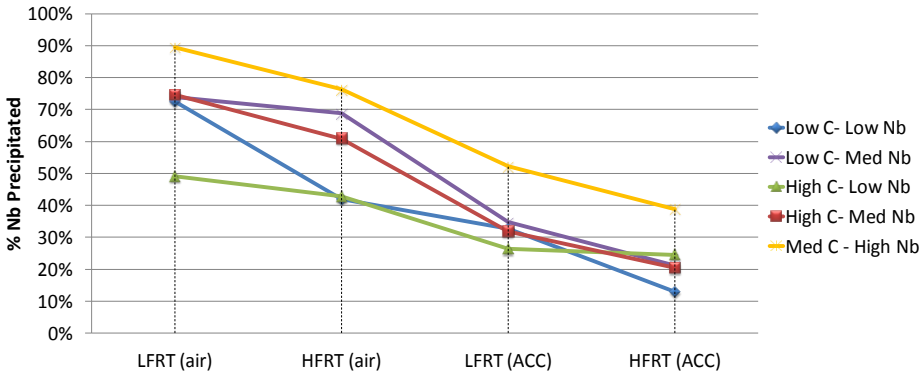

Figure V.2-32 *Comparison of the combined effect of FRT and cooling condition on the %Nb precipitated of various HSLA pipeline steel compositions.*

Composition	Nb/C
Low C - Low Nb	0,56
Low C - Med. Nb	0,95
High C - Low Nb	0,29
High C - Med. Nb	0,56
Med. C - High Nb	1,17

Table V.2-5 *Niobium-carbon ratio of the steels in this study.*

V.2.5 Texture

Figure V.2-33 shows the φ_2=45° ODF section that was determined from XRD measurements at the $\frac{1}{2}$ thickness of the plates, which were subjected to equal reduction per pass. All of the steels exhibited, in general, similar textures after a particular TMCP schedule. However, compared to those of other textures, the rotated cube component {001}⟨110⟩ (see *Table V.2-6*) occurred with higher intensities in the textures of the samples rolled at high FRT. The samples rolled at low FRT, in contrast, exhibited a shift of the maximum intensities along the RD fiber towards the {113}⟨110⟩ and {112}⟨110⟩ components. The increased intensity of the {001}⟨110⟩ rotated cube in the high FRT samples can be attributed to its occurrence as a transformation product of both the Brass component, from the strained and non-recrystallized austenite, and of recrystallized austenite that has the {100}⟨001⟩ cube orientation. This result indicates that static recrystallization possibly occurred during either finish rolling at high temperatures with inter-pass times of 10s, or during the transfer between the rolling mill and the cooling bed. In addition, the ACC and air-cooled samples had similar texture intensity distributions although they consist mainly of bainite-ferrite and α_p with banded P_L microstructures, respectively. This result suggests that textures developed independently of the cooling route for rolling performed at high FRT.

In the case of low FRT, the intensities of the textures of the ACC and air-cooled samples differed only slightly; the air-cooled plates exhibited weaker textures, except in the case of the High C - Medium Nb composition steel. The current results concur with previous findings [30] that the {001}⟨110⟩ constitutes the major texture component after finish rolling at high temperature.. *Ray et al.* [30] also reported that the {332}⟨113⟩ texture component strengthens after fast cooling, whereas the {113}⟨110⟩ is less sensitive to the cooling rate. The findings of the present study suggest that, at high FRT, the {332}⟨113⟩ and the {113}⟨110⟩ texture components have, in general, similar intensities regardless of the cooling rate. These results are consistent previous investigations (Baczynski et al. [31]), which obtained similar textures for finishing rolling performed within the austenite non-recrystallization range.

Composition	LFRT (air)	HFRT (air)	LFRT (ACC)	HFRT (ACC)
Low C Low Nb	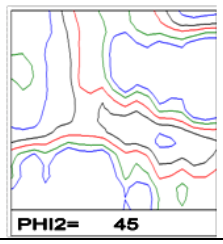	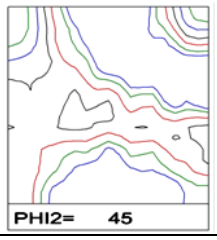	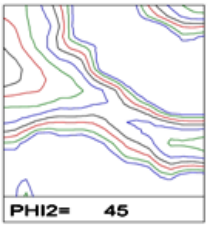	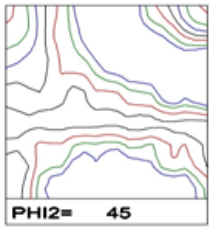
Low C Med. Nb	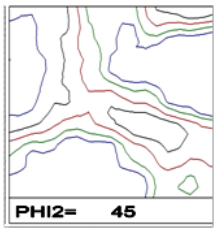	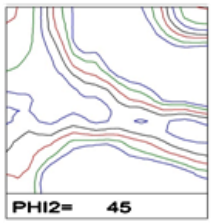	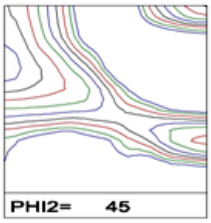	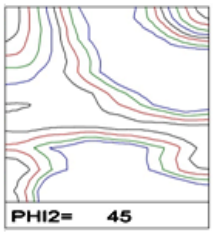
High C Low Nb	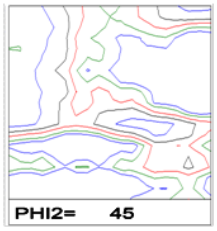	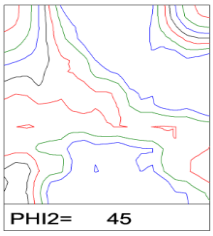	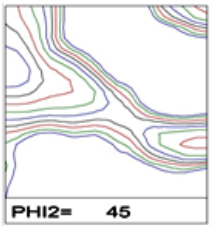	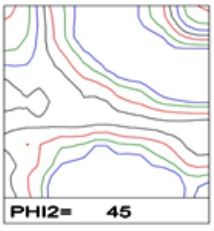
High C Med. Nb	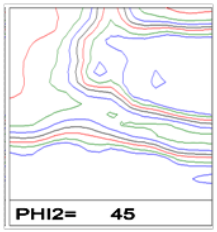	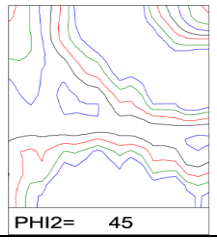	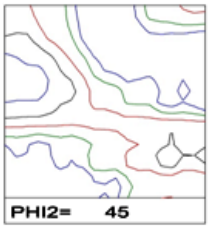	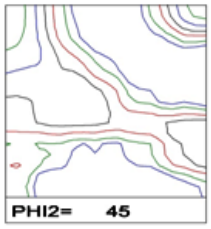
Med. C High Nb	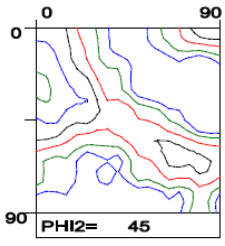	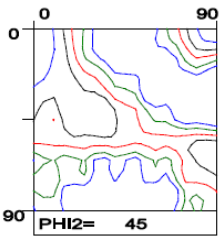	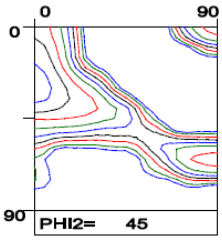	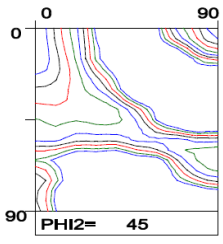

.80 1.00 1.30 1.60 2.00 2.50 3.20 4.00 5.00 6.40

Figure V.2-33 Texture at ½ thickness plotted in φ2 = 45° ODF sections. Iso-intensity lines: 0.8x -1x -1.3x -1.6x -2x -2.5x -3.2x -5x -6.4 x random.

Composition and TMCP route	*Dominant Texture component*	*Intensity ½ thickness*
Low C - Low Nb; LFRT Air	(113)[1$\bar{1}$0]	2.6
Low C - Low Nb; HFRT Air	(001)[1$\bar{1}$0]	3.1
Low C - Low Nb; LFRT ACC	(113)[1$\bar{1}$0]	4.6
Low C - Low Nb; HFRT ACC	(001)[1$\bar{1}$0]	3.4
Low C - Med. Nb; LFRT Air	(113)[1$\bar{1}$0]	2.5
Low C - Med. Nb; HFRT Air	(001)[1$\bar{1}$0]	3.2
Low C - Med. Nb; LFRT ACC	(113)[1$\bar{1}$0]	5.6
Low C - Med. Nb; HFRT ACC	(001)[1$\bar{1}$0]	4.7
High C - Low Nb; LFRT Air	(113)[1$\bar{1}$0]	2.5
High C - Low Nb; HFRT Air	(001)[1$\bar{1}$0]	3.5
High C - Low Nb; LFRT ACC	(113)[1$\bar{1}$0]	6
High C - Low Nb; HFRT ACC	(001)[1$\bar{1}$0]	3.4
High C - Med. Nb; LFRT Air	(113)[1$\bar{1}$0] (001)[1$\bar{1}$0]	3.8
High C - Med. Nb; HFRT Air	(001)[1$\bar{1}$0]	3.4
High C - Med. Nb; LFRT ACC	(113)[1$\bar{1}$0]	2.3
High C - Med. Nb; HFRT ACC	(001)[1$\bar{1}$0]	3
Med. C - High. Nb; LFRT Air	(113)[1$\bar{1}$0]	2.6
Med. C - High. Nb; HFRT Air	(001)[1$\bar{1}$0]	2.4
Med C - High. Nb; LFRT ACC	(113)[1$\bar{1}$0]	5.7
Med C - High. Nb; HFRT ACC	(001)[1$\bar{1}$0]	5.9

Table V.2-6 *Comparison of the combined effect of FRT and cooling condition on the main crystallographic texture components of various HSLA pipeline steel compositions.*

Figure V.2-34 illustrates the texture variations in the plate with Med. C - High Nb composition (represented by the φ2 = 45° ODF section) for all processing conditions combined with ACC. In all cases, high FRT results in higher intensities of the rotated cube component {001}⟨110⟩. Low FRT, in contrast, results in higher intensities of the {113}⟨110⟩ and {112}⟨110⟩ components. These results also match those observed in *Figure V.2-33*, where the textures associated with various chemical compositions are compared after rolling with constant reduction per pass. The followed reduction route has, in general, no influence on the presence of texture components. Similar texture intensity distributions were found when only the impact of increasing or decreasing rolling reduction per pass at high or low FRT was compared. Surprisingly, constant reduction per pass resulted in the largest intensities for both FRTs. The textures obtained after rolling with increasing reduction per pass showed the lowest intensities, even at low FRT. These results were unexpected since imparting the largest reductions at the end of finishing rolling should have enhanced the strength of the deformed austenite texture.

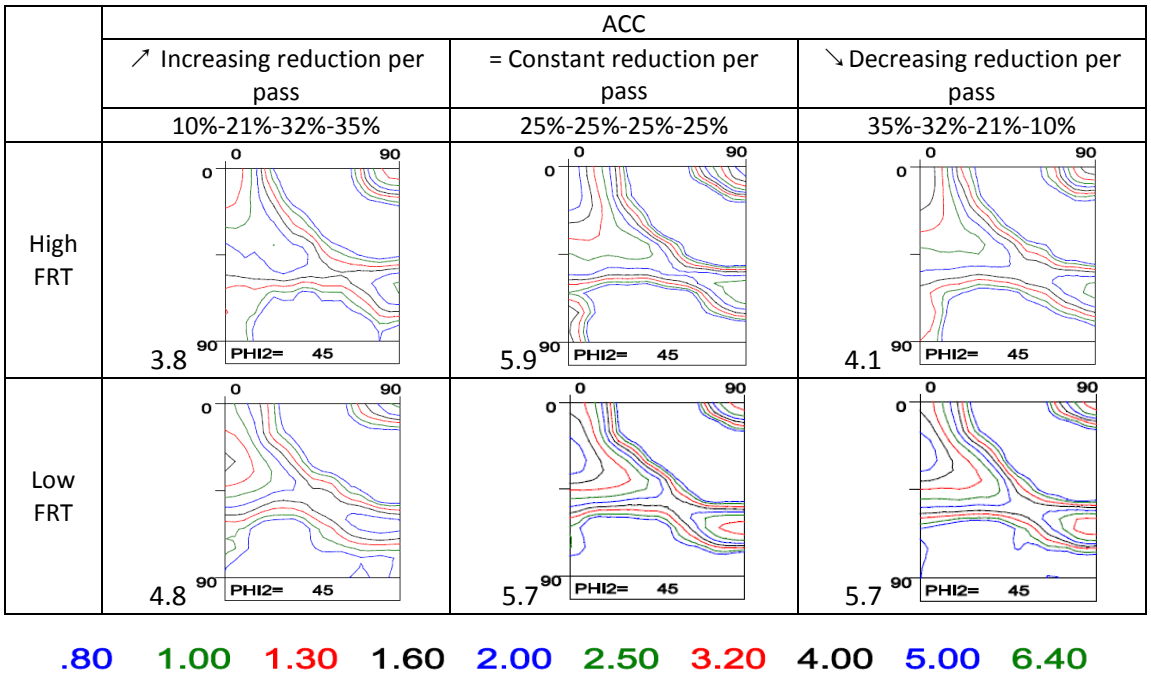

Figure V.2-34 Texture at ½ thickness plotted in the φ2 = 45° ODF section. Iso-intensity lines: 0.8x -1x -1.3x -1.6x -2x -2.5x -3.2x -5x -6.4x random.

Figure V.2-34 and *Figure V.2-35* also provide evidence of the weakening effect of air cooling on the texture intensities. The effects of strain path followed by air cooling (*Figure V.2-35*) and ACC were compared. It was found that unlike ACC, air cooling combined with increasing and decreasing reductions per pass resulted in stronger textures than the ones formed after constant reduction per pass. Moreover, as *Figure V.2-35* shows, there is no significant difference between the texture intensities of plates rolled at high or low FRT after air cooling. Based on these observations, it is hypothesized that the phenomenon responsible for the weakening of the texture during air cooling had larger impact after constant reduction per pass than after decreasing or increasing reductions.

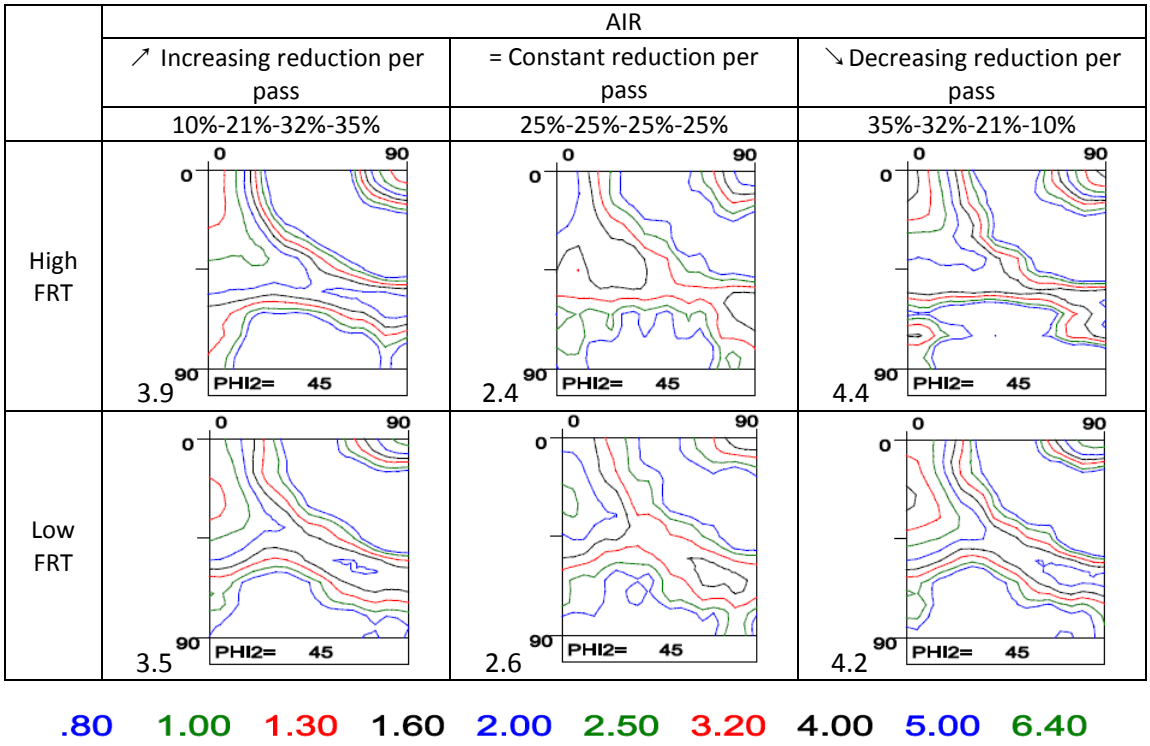

Figure V.2-35 Texture at ½ thickness plotted in the φ2 = 45° ODF section. Iso-intensity lines: 0.8x -1x -1.3x -1.6x -2x -2.5x -3.2x -5x -6.4x random.

The dominant texture components, together with the intensities measured at ¼ and ½ thickness of the plates after different processing conditions, are shown in *Table V.2*-7. There is some difference between the maximum intensities at ¼ and ½ thickness. This divergence in intensities at two thickness locations may be indicative of the through-thickness texture inhomogeneity. As stated previously, schedules following high FRT, result in higher intensities of the rotated cube

{001}⟨110⟩ texture component. In addition, all the schedules with low FRT, resulted in higher intensities of the {113}⟨110⟩ and {112}⟨110⟩ components. *Table V.2-7* shows, however, that after ACC a significantly stronger texture developed at ½ of the thickness, especially at low FRT. At constant reduction draught, the texture strength increased to 139%. Furthermore, the texture between the quarter and middle thickness sharpens by more than 220% with an increase or decrease of the reduction draughts. For TMCP routes with air cooling, the results indicate that constant reduction per pass results in a somewhat homogeneous texture between ¼ and ½ thickness. On the other hand, increasing/decreasing reduction per pass resulted in 40% to 60% stronger textures in the center of the specimen.

Material (Med. C High Nb)	*Dominant Texture component*	*Intensity ¼ thickness*	*Intensity ½ thickness*	*Relative difference (%)* $= \frac{(Int._{\frac{1}{2}} - Int._{\frac{1}{4}})}{Int._{\frac{1}{4}}}$
Cte. Red. HFRT Air	(001) [1$\bar{1}$0]	2.9	2.4	-18
Cte. Red. LFRT Air	(113) [1$\bar{1}$0]	2.3	2.6	11
Cte. Red. HFRT ACC	(001) [1$\bar{1}$0]	3.2	5.9	89
Cte. Red. LFRT ACC	(113) [1$\bar{1}$0]	2.4	5.7	139
Incr. Red. HFRT Air	(001) [1$\bar{1}$0]	2.9	3.9	36
Incr. Red. LFRT Air	(113) [1$\bar{1}$0]	2.2	3.5	61
Incr. Red. HFRT ACC	(001) [1$\bar{1}$0]	3.4	3.8	11
Incr. Red. LFRT ACC	(113) [1$\bar{1}$0]	1.6	5.2	225
Decr. Red. HFRT Air	(001) [1$\bar{1}$0]	2.9	4.4	47
Decr. Red. LFRT Air	(113) [1$\bar{1}$0]	2.6	4.2	65
Decr. Red. HFRT ACC	(001) [1$\bar{1}$0]	2.8	4.5	70
Decr. Red. LFRT ACC	(113) [1$\bar{1}$0]	2.2	7.1	227

Table V.2-7 *Maximum intensities of the dominant texture component at ¼ and ½ thickness and its relative difference in %.*

V.3 Microstructure control of fracture toughness

Crack arrestability can be approached in two ways [32], by either focusing on fracture initiation or by designing steel microstructures which are resistant to crack propagation. The prevention of fracture initiation, through pre-service inspection or in-service surveillance, is necessary. However, pipeline steels are not exempt from "flaws" (i.e. precipitates (TiN), non-metallic inclusions, phase interfaces) inherent to the production methods or material constituents and, as such, fracture initiation (in microscopic terms) is highly possible.

SEM and TEM analysis were performed with the aim of identifying martensite-austenite (M.A.) constituents or MnS inclusions which are known to have an influence on the toughness of hot rolled steel [33]. They were, however, not found in a significant amount. Figure (annex I) shows an example of the MA constituent present in one of the final TMCP steel microstructures. MnS inclusions were practically non-existent owing to the high cleanness of the lab-cast steel.

Based on these observations, M.A. constituents and MnS inclusions should not have any significant influence on the toughness of these materials. Four other factors which possibly control the toughness could be defined as follows: *(i)* precipitates (titanium nitrides or niobium-titanium carbo-nitrides), *(ii)* presence and distribution of second phases, *(iii)* grain size and/or morphology (shape, clustering distribution), and *(iv)* crystallographic texture.

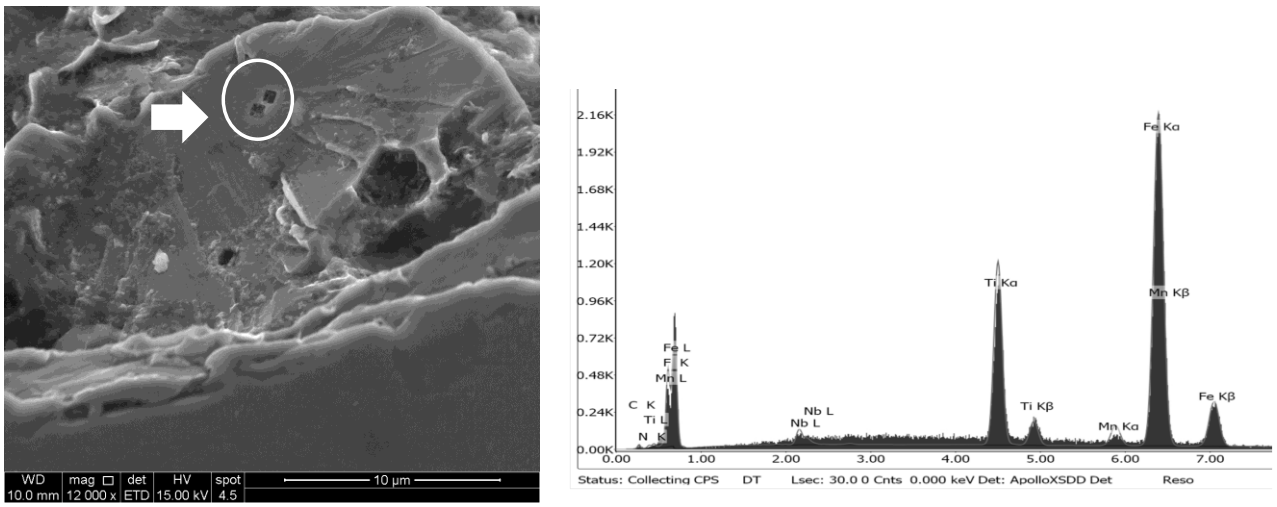

Figure V.3-1 *(a) Fractography of an impact-Charpy-tested sample showing the onset of a cleavage fracture in the vicinity on two Ti rich precipitates, (b) EDX spectra of one of the precipitates***.**

It was observed (see Figure V.3-1) that TiN plays a role in the fracture cleavage onset, as previously reported by *Echeverria et al.*[34] who reported that fracture begins with cracking of the Ti rich particles. The findings from the present study (see ***Figure V.3-2***) mirror those of *Echeverria et al.*[34]. Moreover, *Ghosh et al.*[35] reported that, compared to TiN particles, higher stress is required to fracture grain boundary carbides. Like *Chakrabarti et al.* [36], interpretations of the current work indicate that the presence of Ti(C,N) or Nb(C, N) may initiate fracture, but cannot control the propagation.

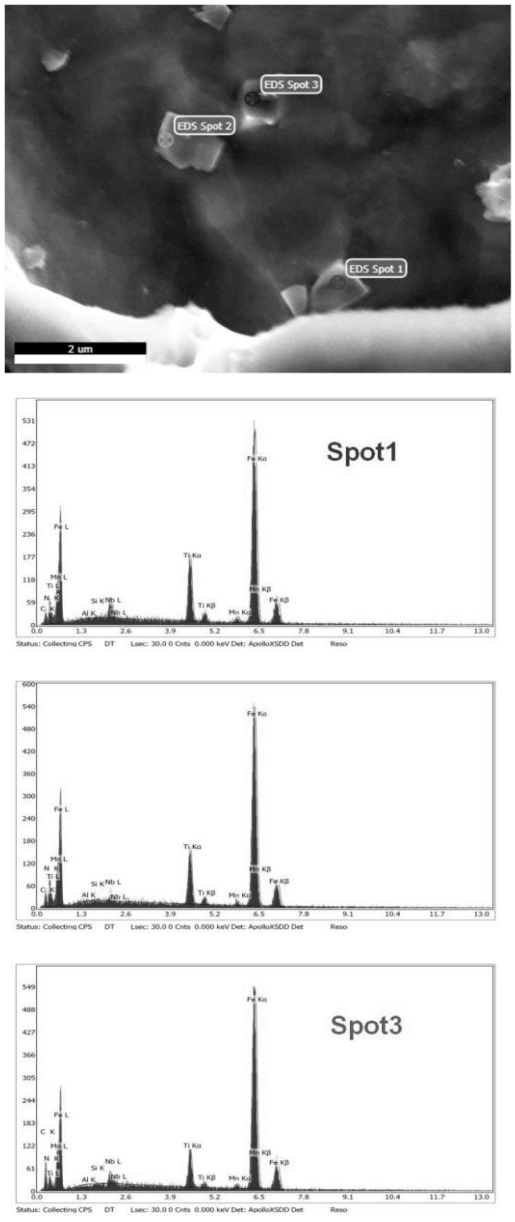

Figure V.3-2 *EDX analysis of precipitates.*

This fact is illustrated in *Figure V.3-3*, where a crack seems to nucleate at the interface of the precipitate and the matrix, but did not grow afterwards.

As mentioned in the literature review, the classical Charpy V-notch impact energy, CVN, contains the energies required for both crack initiation and propagation. These two contributions to the overall energy consumed during the test can be separated (detailed information can be found in Chapter II) by means of an Instrumented Charpy V-notch test.

$$E_f = E_i + E_p \qquad \text{V.3- 1}$$

The fracture energy can be expressed as the sum of the energies absorbed during crack initiation (E_i) and propagation (E_p). The energy absorbed during crack propagation should be controlled through microstructural steel design and, therefore, E_p is the focus of the current research.

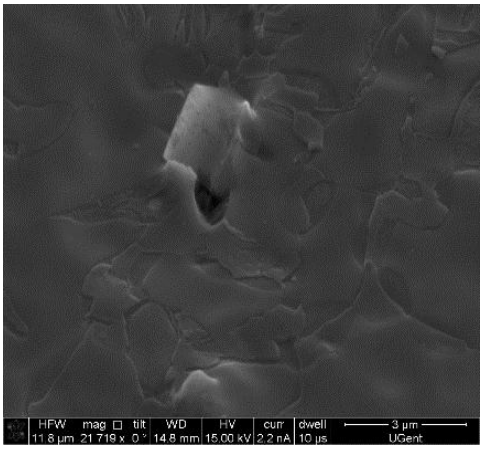

Figure V.3-3 *Illustration of crack initiation next to a precipitate.*

Figure V.3-4 shows various microstructures and the corresponding load-displacement curves measured during V-notch Charpy impact testing at -40°C (temperature at which samples still behave in a ductile manner). As the examples in *Figure V.3-4* show, there are various microstructural features which might influence the load-displacement response. A homogeneous ferrite-pearlite microstructure exhibited a load-displacement curve that is characteristic of ductile behavior (Figure V.3-4 (a)); a banded pearlite distribution presented a curve with brittle instability which occurred after a certain range of ductile propagation (Figure V.3-4 (b)).

Microstructure	Load – Displacement curve
Reference load – displacement curve	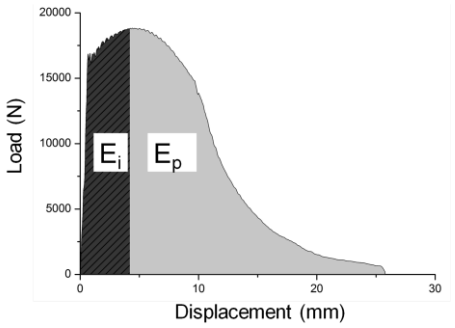
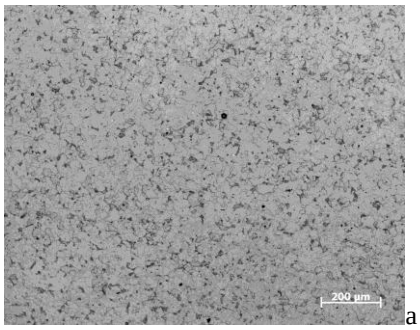 a	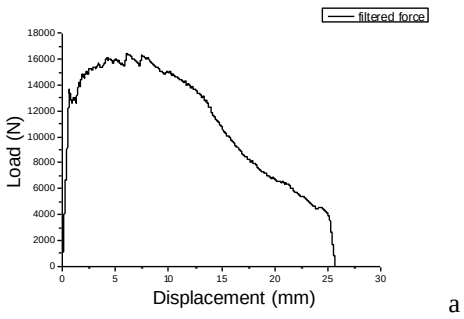 a

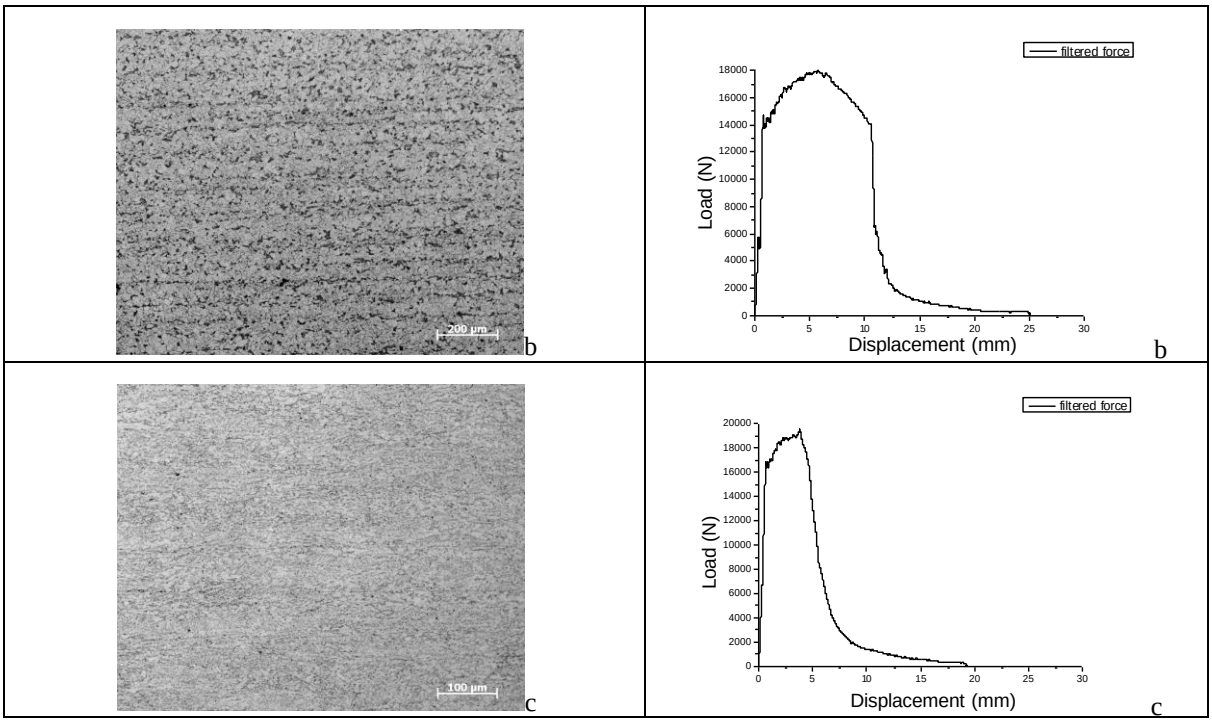

Figure V.3-4 *Load-displacement curves (at -40ºC) of various steels (variation of composition and process parameters) and their corresponding microstructures. Area under the curve represents the energy absorbed during fracture. (a) Homogeneous ferrite-pearlite distribution; (b) banded ferrite –pearlite structure; (c) homogeneous ferrite-bainite structure.*

The optical micrograph in Figure V.3-4 (c) shows a homogeneous microstructure of ferrite and bainite. However, this "apparently fine microstructure" did not absorb large amounts of energy during crack propagation in the transition region. In the present study, the area corresponding to the region E_p (absorbed energy during crack propagation) was calculated for each tested material in the range of the ductile to ductile-brittle transition region.

For all materials, a scatter diagram (see *Figure V.3-5*), and Pearson's correlation and ANOVA analyses (see *Table V.3-1*) were used to determine the relationship between the absorbed energy during crack propagation at the upper shelf region of the transition curve and at the DBTT. The DBTT range was determined through the T_{50} criteria by fitting the data to a hyperbolic tangent function. The data revealed that the DBTT is strongly correlated to E_p. Hence, the former can be thought of as an indirect representation of the latter.

Image J® software was used to measure the area fraction of pearlite from optical micrographs in order to understand its role in crack propagation. *Figure V.3-6* shows the

optical micrographs of Low C - Low Nb, Low C – Med. Nb, High C - Low Nb, and High C - Med. Nb steels which were processed using high and low FRT followed by air cooling. The volume fraction of pearlite located in dispersed islands (a, b, e, f) and banded patterns (c, d, g, h) was evaluated.

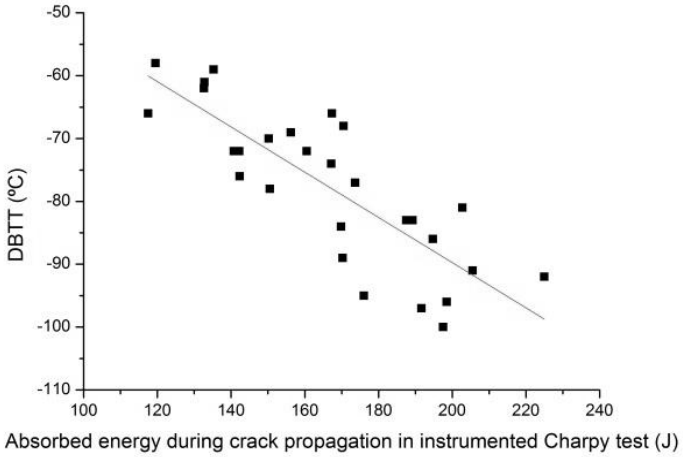

Figure V.3-5 *Correlation between the DBTT and the energy absorbed during crack propagation in an impact V-notch Charpy test.*

	DBTT - Energy absorbed during crack propagation
Pearson Correlation	0.82
Adj. R-Square	0.66
Prob. null hypothesis	$8.6 * 10^{-7}$

Table V.3-1 *Summary of the ANOVA analysis concerning the data in Figure V.3-5***.**

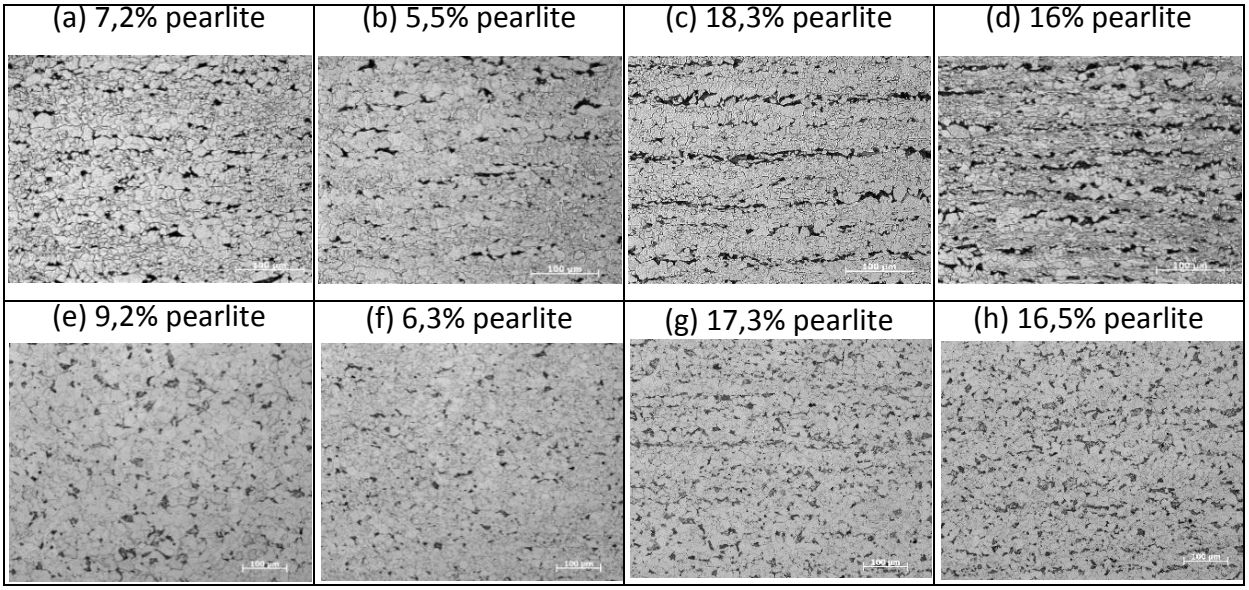

Figure V.3-6 *Optical micrographs of the eight steels showing a variety of ferrite-pearlite microstructures and the corresponding measured pearlite volume fraction: in dispersed pearlite islands (a, b, e, f) and banded patterns (c, d, g, h).*

A correspondence between fraction of pearlite and energy absorbed during the crack propagation was found (see Figure V.3-7). Samples with low pearlite content absorbed more energy during crack propagation. Moreover, increasing volume fractions resulted in increased banding of the pearlite. This banded pattern facilitates crack propagation either within the second constituent or at the interface. Prior studies, which had considered the role of microstructure on impact toughness [37-39], described *(i)* ferrite grain size, *(ii)* pearlite colony size (at constant inter-lamellar spacing), and *(iii)* lamellar pearlite versus non-lamellar pearlite, as toughness controlling factors. The findings of the current study complement with quantitative data, those which were previously cited. Many papers have addressed the issue of banding phenomena in steels. Most of these studies (many reviewed by *Verhoeven* [40]*)* reveal that the banded microstructures arise owing to micro-segregation of alloying elements, with two possible origins of segregation [41]: *(i)* pre-segregation (dendritic solidification) or *(ii)* trans-segregation (transformation from austenite to ferrite plus pearlite). Banded microstructures also form after slow cooling and the critical rate required to eliminate bands is a function of both the chemical composition and processing history of the steel [40]. The present results are consistent with this knowledge, since the banded morphology is observed in the steels with higher contents of micro-alloying elements and which were air-cooled. An ANOVA analysis was performed in order to quantitatively assess the relevance of pearlite fraction on fracture propagation. The adjusted R-square=0.77 and a probability of null hypothesis F<0.002, confirms the importance of pearlite in fracture propagation.

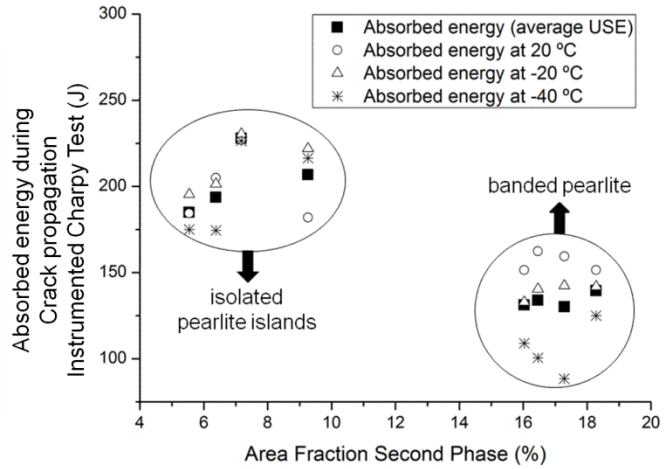

Figure V.3-7 *Energy absorbed during crack propagation in the instrumented Charpy test versus fraction of second phase (pearlite).*

As explained in sections II.1.2, II.6, and II.7.1, grain refinement has been reported [42] to enhance both the yield strength and toughness. This statement must, however, be expounded upon. In the past, the grain size was often measured on the basis of optical microscope quantification of the grain boundaries revealed after etching. However, many studies [42-47] have shown that two adjacent measured grains may be misoriented from each other by only a few degrees and, therefore, cleavage cracks can propagate easily. This is the case of bainitic-ferritic microstructures which include packet regions with low misorientation within the bainitic colony. In the 1970s, *Naylor* [42] described the difference between "classical theories of the grain size" and the concept of effective grain size. *Naylor* pointed to the way in which the DBTT is controlled by the deviation of the crack between high angle grain boundaries or packet boundaries. Inside a bainitic colony/packet, a brittle crack normally trails a straight fracture direction by following a particular group of planes (the preferred {001} planes in BCC materials). At the HAGB, the crack has to deviate until a new fracture propagation plane and direction are found, and this event, according to Naylor, "*imposes an energy requirement for the crack to undergo HAGB*" [42]. Similarly, *Song et al.* [47] stated "*If an intragranular cleavage crack moves across a HAGBs, the crack front usually branches according to the change of the preferred fracture plane. Such branching results in additional fracture work. In contrast, when a crack meets a low-angle grain boundary, the crack can typically penetrate such an interface without a substantial change in the propagation direction and without branching*". Nowadays, the EBSD technique allows users to establish the criteria for selecting the misorientation angle threshold. *Figure V.3-8* compares the results obtained when misorientation thresholds of 5° or 15° are used to define the regions belonging to a grain, and hence the grain boundaries.

The decrease in the average grain size (equivalent diameter) was found to be positively correlated to the reduction in the ductile to brittle transition temperature (DBTT) for a number of steels which have the same chemical composition but were processed in different ways. A linear fit analysis complemented by an ANOVA F-test was performed in order to compare the effect of misorientation angle on the DBTT. *Table V.3-2* shows the summary data of the regression analysis.

The comparison of the two results reveals that 15° misorientation criteria better correlates with the decrease in DBTT when the average grain size (equivalent diameter) is reduced.

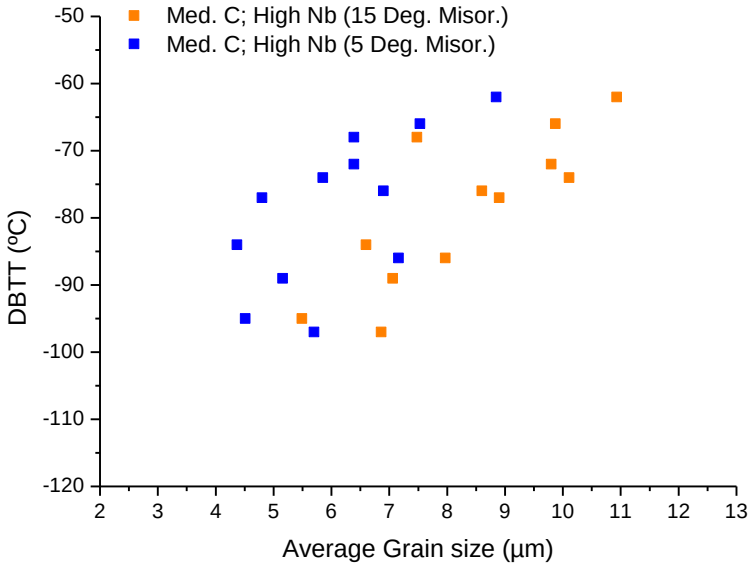

Misorientation criteria	5°	15°
Adj. R-Square	0.39	0.65
Prob. null hypothesis	0.02	0.0009

Figure V.3-8 *Comparison between the variation of DBTT as a function of the average grain size for: 5° and 15° misorientation criteria.*

Table V.3-2 *Summary of the ANOVA analysis of the data in Figure V.3-8.*

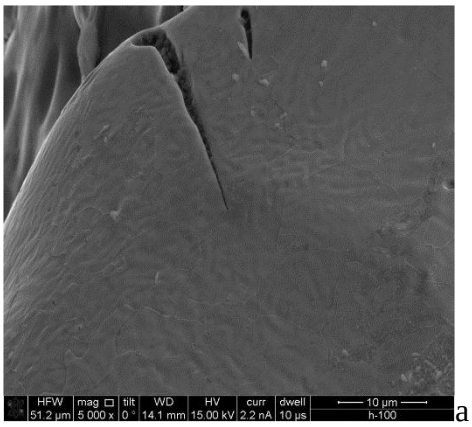
a

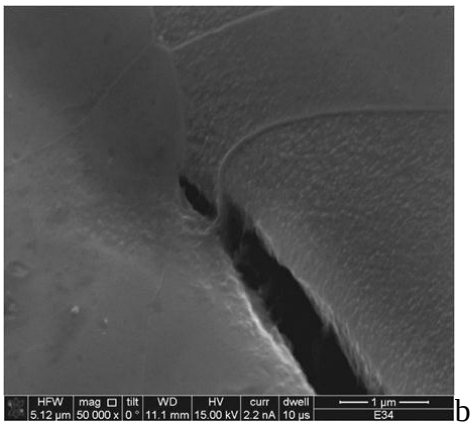
b

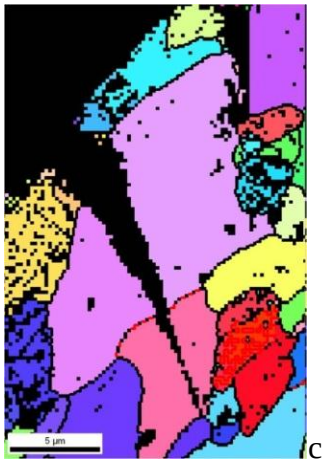
c

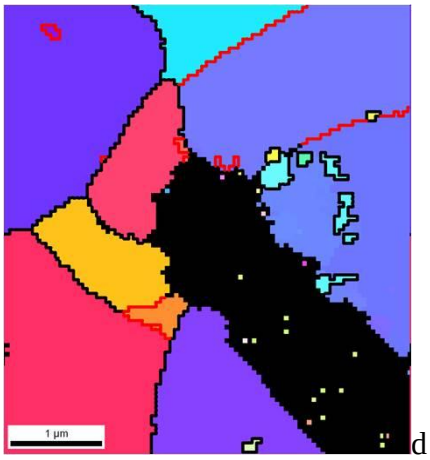
d

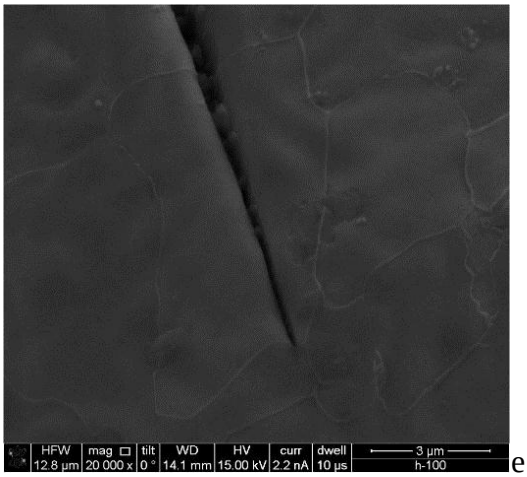

e

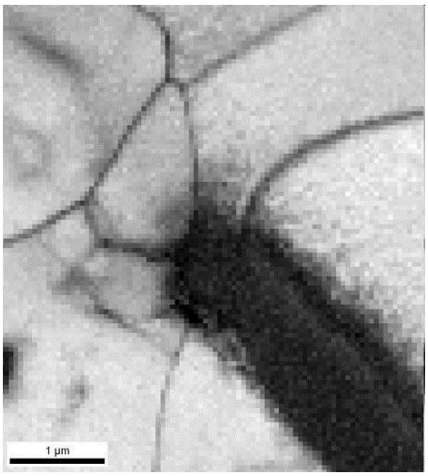

f

Figure V.3-9 *a), b),e) SEM images near the fracture plane of two different Charpy-tested sample. c), d), IPF maps (not cleaned) together with colour boundary maps (GB<15 deg. in red; GB≥15 deg. in black). f), Image quality map of the secondary crack arrest zone.*

This study produced quantitative and statistically significant results which corroborate the hypothesis of a number of previous works (i.e. [42, 48]) in the field considering HAGB (usually 15°) as "effective grain size" barriers to crack propagation during fracture. Figure V.3-9 illustrates these results with two examples. It can be seen that a secondary crack in an instrumented Charpy-tested sample was arrested by a HAGB; previously, the same crack travelled through a LAGB without being arrested.

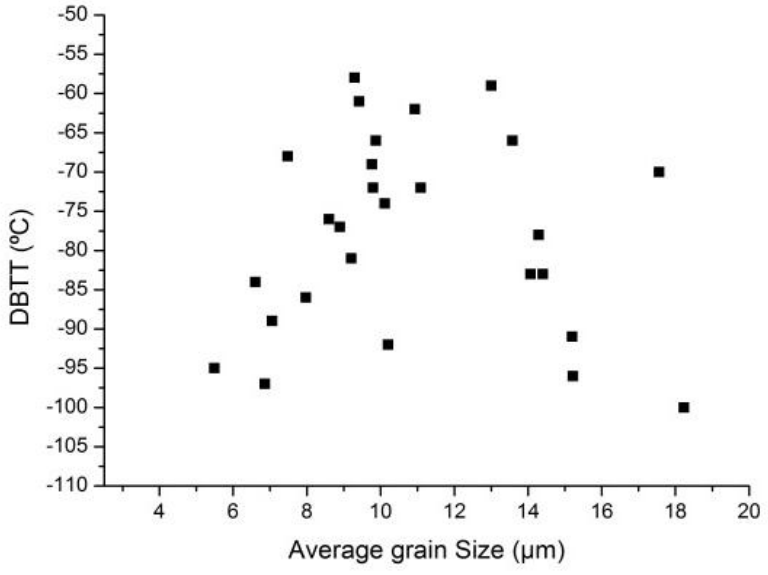

Figure V.3-10 *Correlation of the DBTT and the average grain size (all materials).*

It was somewhat surprising that no correlation was found between the DBTT and the average grain size when all the TMCP processed materials were considered (see *Figure V.3-10*). This observation provides important insights into the importance of other factors which affect the toughness. It seems quite possible that these results stem from the

heterogeneity of microstructures considered in present study. In other words, attributing the toughness behavior to a single factor/microstructural feature, fails to resolve the correlation between the crack propagation response and the microstructure. It is apparent from *Figure V.3-8* and *Table V.3-2*, that the grain size is probably the governing parameter with respect to impact toughness control in steels with Med. C - High Nb composition. The other chemical compositions might, however, be comprised of a feature which plays a major role in controlling the impact toughness. The suggested hypothesis is that the mentioned feature was somehow limited or restrained only in the TMCP processed Med. C - High Nb steels. Further discussion on the suggested hypothesis is given in Chapter VI.

The influence of the crystallographic texture on the toughness was analyzed by measuring the contribution of the b.c.c. cleavage planes to the fracture. It has been shown conclusively that brittle fracture in b.c.c. metals takes place along {100} cleavage planes [49, 50]. As previously mentioned in Chapter IV.3.2.2, the volume fraction of {001} planes parallel to the fracture surface was measured in order to understand the influence of crystallographic texture on the toughness. It is apparent from *Figure V.3-11* that the DBTT is correlated with the volume fraction of {001} planes parallel to the fracture surface.

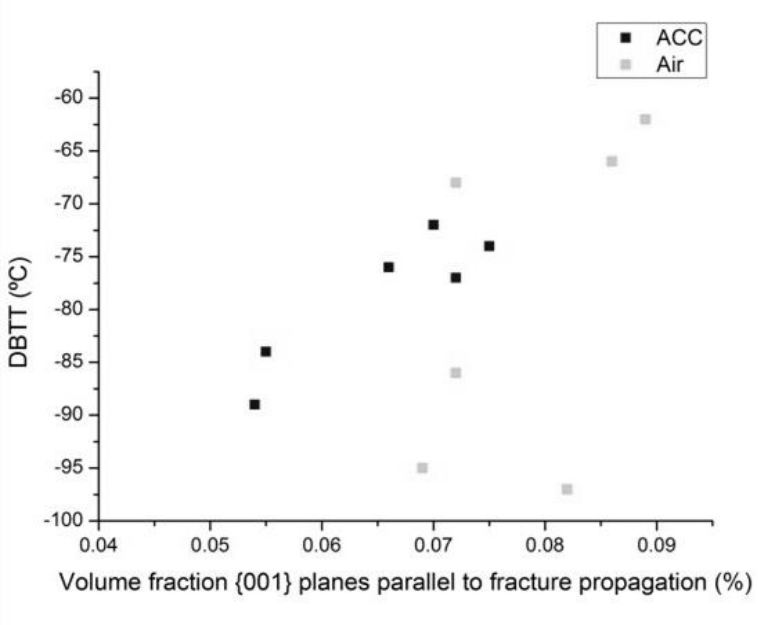

Figure V.3-11 *Variation of the DBTT as a function of the volume fraction of {001} planes parallel to the Charpy fracture plane.*

These data correspond to different TMCP steels whose chemical composition was designated as Med. C - High Nb. ACC samples displayed a particularly strong tendency towards decreasing DBTT with reduced fractions of {001} planes parallel to the fracture surface. When only ACC processed samples were considered, the ANOVA analysis revealed that more than 75% of the change in the DBTT can be explained by the variation in the

volume fraction of the {001} planes. On the other hand, the remaining chemical compositions did not exhibit noteworthy correlations. This suggests, as stated before, that there might be another factor which governs their toughness response.

Taken together, these results suggest that there are a number of microstructural features which influence the toughness response, but their individual impact on the DBTT is applicable only when the excesses of another relevant feature have been limited. It will be shown in Chapter VI that the synergies of various microstructural features determine the final response.

V.4 Determination of the strengthening mechanism under different rolling parameters

In this section, the various strengthening mechanisms in the HSLA pipeline steels produced under different TMCP parameters are quantitatively analyzed. Quantitative relationships between the structure and properties were used to provide a complete description of the processing conditions and their influence on the balance of the various contributions to the strength. The strengthening methods considered here, were already briefly introduced in chapter II.7. The common characteristic of the cited strengthening mechanisms is their role in reducing dislocation mobility and their capacity to increase the stress necessary to move a dislocation through a certain distance within the material. The principal strengthening mechanisms considered in this work were: *(i)* Grain size refinement, *(ii)* solid solution strengthening, *(iii)* precipitation strengthening, and *(iv)* dislocation strengthening.

As for experimental quantification, the yield stress of a material with a homogeneous microstructure can be described as a function of the grain size through the Hall-Petch relationship:

$$\sigma_Y = \sigma_0 + K_Y d^{-0.5} \qquad \textbf{V.4-1}$$

Where σ_0 is the intrinsic lattice friction stress, K_Y is a constant "grain boundary unlocking term", and d is the mean grain size in [m]. Values of K=17.4N mm $^{-3/2}$ and σ_0 =54MPa for similar steels were taken from references [51-55].

Conversely, the yield strength of polycrystalline materials, in particular the HSLA steels, results from a combination of various strengthening contributions: solid solution strengthening, grain

size strengthening, precipitation strengthening, dislocation strengthening, and texture strengthening [53].

Carbides in the TEM foils and carbon replica STEM samples exhibited mainly single spherical (primarily Nb carbides) and cuboidal (associated with spherical Ti-N carbides) morphologies. Since the precipitates are very hard, the bypass, rather than the cutting, mechanism (see Figure V.4-1) should be the major contributor to precipitation strengthening. Thus, the smaller precipitates found in the rolled plate are assumed to be responsible for the precipitation hardening [56]. The mechanism, known as Orowan type [57], was extended by Ashby [58] for a random arrangement of particles. Precipitation strengthening σ_p was quantified using a modified form of the Ashby-Orowan equation [59].

$$\sigma_p = \frac{0.3Gbf^{0.5}}{\bar{x}} ln\frac{\bar{x}}{2b} \qquad \textbf{V.4-2}$$

Where G [GPa] is the shear modulus, b [nm] is the Burgers vector, f is the volume fraction of particles and, x [mm] is the average particle size. Precipitates with sizes of up to 10nm were thought to contribute to precipitation hardening. The volume fraction, f, of the precipitates, was calculated as a function of the Nb content, which was measured using the ICP-MS technique.

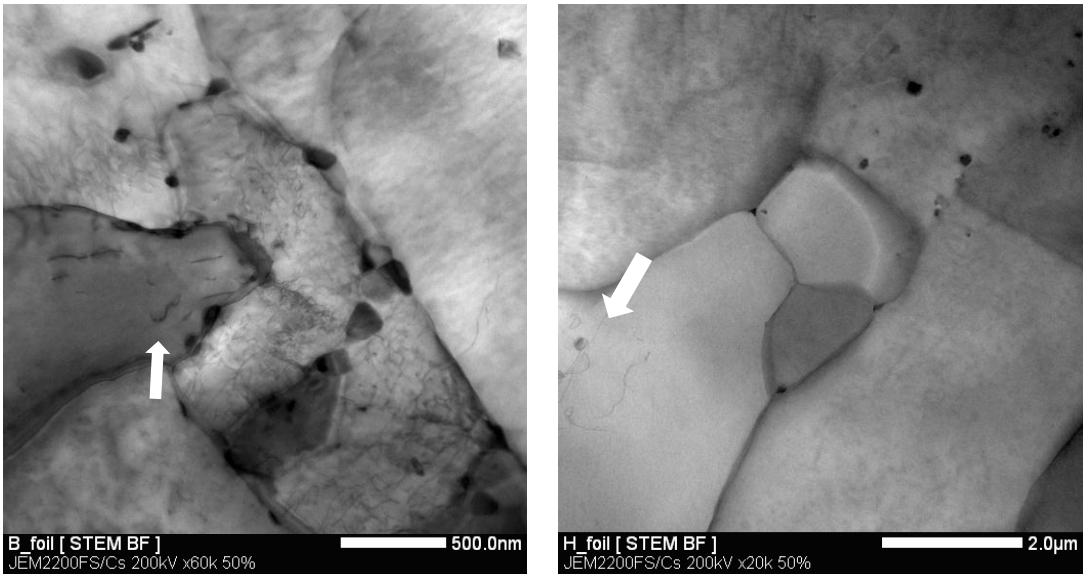

Figure V.4-1 *STEM micrographs showing a clear example of the role of dislocations in strengthening; bowing of dislocation as described by Orowan [57].*

The solid solution hardening contribution was quantified by using the analytical relationship developed for plain carbon steels [55].

$$\sigma_{ss} = 32.34w[Mn] + 83.16w[Si] + 354.2\,w[N] \qquad \textbf{V.4-3}$$

Likewise, the strengthening contribution due to dislocations was quantified using the Taylor [60] equation (V.4-4).

$$\sigma_d = \alpha M G b\sqrt{\rho} \qquad \textbf{V.4-4}$$

Where α is a constant, M is the average Taylor factor, G is the shear modulus, b is the Burgers vector, and ρ is the dislocation density. Values of α=0.13, M=2.73, G=64GPa, and b=0.25nm were used based on previously reported data for similar steel grades [56, 59, 61].

Despite the complete work presented in [52], one weakness in this and other studies is the lack of experimental results for the "dislocation density". Therefore, in this study, significant effort was expended in collecting experimental data which elucidate the contribution of dislocations to strengthening after a particular TMCP route. In the following section the method used for dislocation quantification will be described in detail, in order to facilitate correct reproduction of the results.

V.4.1 Dislocation density measurements

Dislocations of the four reference TMCP schedules were observed using bright field STEM imaging in order to minimize diffraction contrast in the background, i.e. bend and extinction contours [62]. A double tilt sample holder was used to achieve the prerequisite two-beam diffraction conditions required for correct measurement of the sample thickness at the desired location. At two-beam conditions, a CBED pattern consists of one of the most intense diffraction disks, which is composed of a series of contrast oscillation details (see example in Figure V.4-2) known as a *Kossel-Möllenstedt* fringes [63].

Thickness measurements were done following *Kelly's* [64] method, and the rocking curves which were perpendicular to the fringes of the CBED were treated using Digital Micrograph™ software.

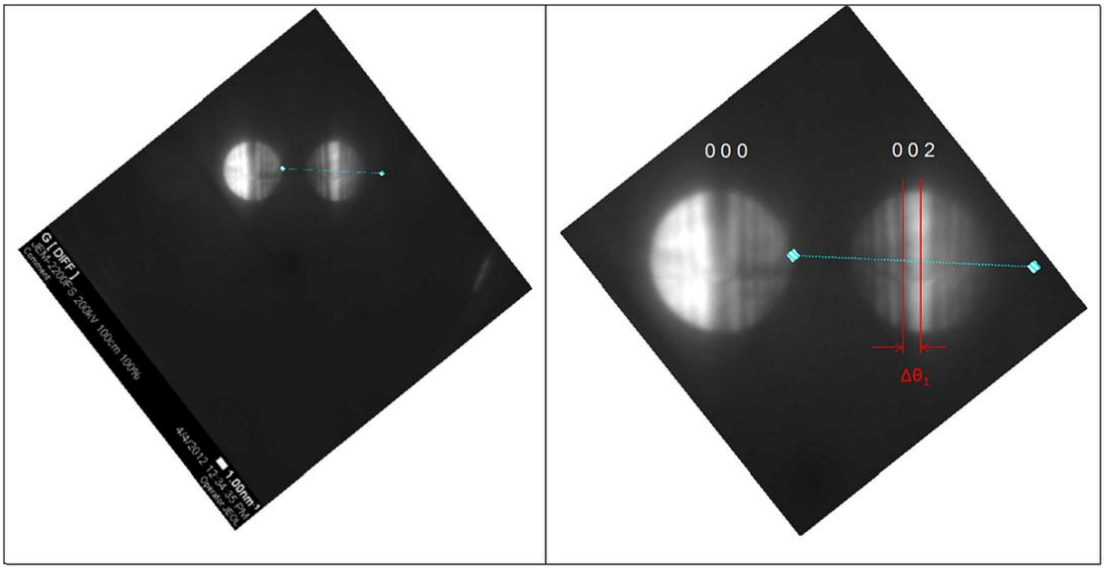

Figure V.4-2 *CBED pattern in two-beam conditions, with (002) reflection excited (a); and detail of the Kossel-Möllenstedt fringes under two beam conditions, showing the first spacing corresponding to Δθ1 necessary to calculate the deviation s1 from the exact Bragg condition.*

According to dynamic theory [65], the intensities of the direct and diffracted disks depend on a factor-denominated extinction distance (further details can be found below in the foil thickness measurement). Both experimental and theoretical extinction values were determined in this manner. The exact lattice parameter value was obtained by extrapolating various atomic scattering amplitudes which were measured by XRD.

Specimen	Reflection {h k l}	ξ_g theory (nm)	ξ_g experimental (nm)	Thickness (nm)
I	(0 1 1)	37.2	40	118
II	(0 1 1)	37.2	33	97.5
III	(2 0 0)	53.7	60	154
IV	(2 0 0)	53.7	52.6	180.7

Table V.4-1 *calculated and experimental extinction distance for the different rolling schedules and their corresponding experimental determined thickness.*

STEM BF micrographs of dislocations were subsequently taken from regions neighboring the CBEDs. To maximize the visibility of the dislocations, the specimen was tilted away from

dislocation line minimum contrast diffraction conditions $\bar{g} \cdot \bar{b} = 0$, where $\bar{g}$ *i*s the diffraction vector and $\bar{b}$ is the Burgers vector. The dislocation density was determined by using equation (V.4-5) [66].

$$\rho_d = \frac{2N}{Lt} \qquad \textbf{V.4-5}$$

Where L is the length of a mesh drawn on the micrograph, N is the number of intersections between dislocations and the mesh (cf. *Figure V.4-3*), and t refers to the TEM foil thickness in the field of view.

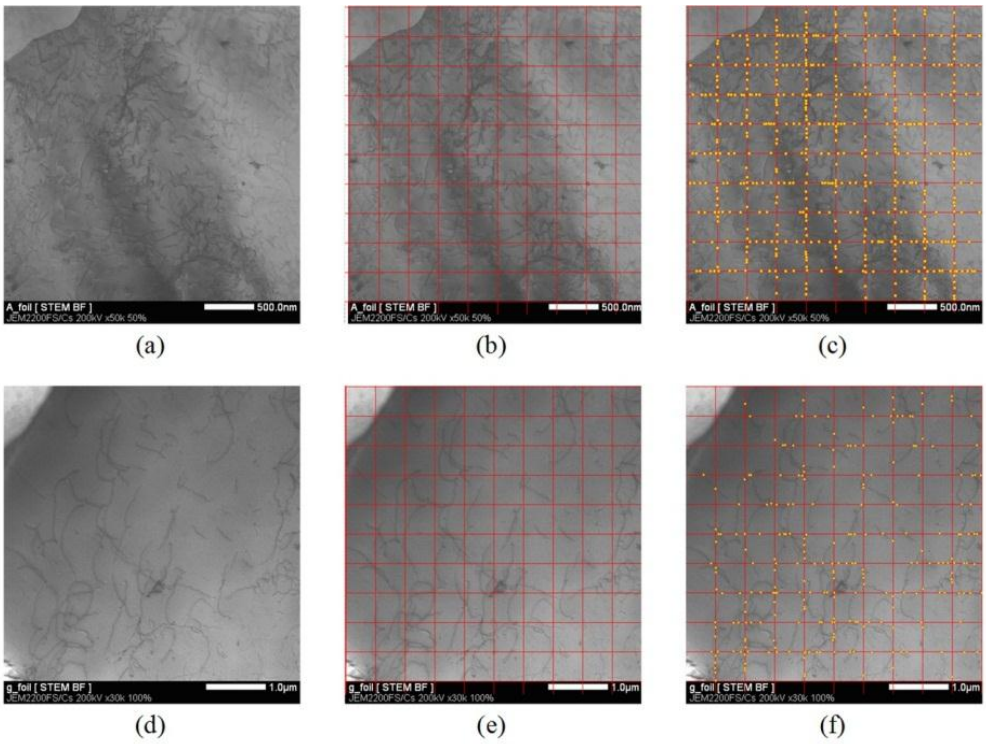

Figure V.4-3 *Example of samples with different dislocation density displaying the grain in position with maximum visibility of dislocations (a, d), superimposed quantification mesh (b, e);(c, f) same as (b, e) with highlighted interception point between the net and dislocations.*

Foil thickness measurement

Small variations in the thickness can lead to under or overestimation of the dislocation density. Foil thickness measurement is therefore one of the most important steps in TEM- based methods, which are used to determine the dislocation density. The combination of the CBED diffraction technique with Kelly's procedure is considered to be one of the most precise methods used to

extract the thickness from Kossel- Möllenstedt fringe patterns [67]. Although there are some possible sources of errors in TEM-based dislocation density measurements (see [68]), they are more reliable compared to indirect methods such as X-ray line broadening [69] or correlating dislocation measurement with micro-hardness measurements [70]. Only the technique which uses electron channeling contrast imaging in a scanning electron microscope [71] could be considered to have a comparable range of accuracy. There would always be, however, discussion over how statistically representative the TEM results are.

According to the dynamic theory [65], when the exact Bragg condition is satisfied, a dynamic diffraction effect takes place in which the intensities of the diffracted and transmitted waves oscillate periodically with a period equal to the extinction distance. When tilting to two-beam conditions, the Kossel-Möllenstedt fringes become parallel intensity oscillations which increase or decrease in number as a function of the thickness. *Table V.4-1* compares the theoretical and experimental values of extinction distances for the studied regions. The extinction distance can be determined [65] as a function of the Bragg angle θ_B, the structural factor $F(\theta_B)$ of a particular reflection, the volume of the unit cell V_c, and the wavelength of the incident electrons λ; that is:

$$\xi_g = \frac{\pi V cos\,\theta_B}{\lambda F_g} \qquad \textbf{V.4-6}$$

Kelly et al. [64] developed a graphical method that relates the minima of intensity oscillations to the foil thickness through the equation:

$$\frac{s_i^2}{n_K^2} + \frac{1}{\xi_g^2 n_K^2} = \frac{1}{t^2} \qquad \textbf{V.4-7}$$

The central bright fringe is at the exact Bragg condition, s_i is the deviation of the i^{th} minimum from the exact Bragg position, n is an integer, and ξg is the extinction distance. By analyzing the diffracted disk with the Digital Micrograph™ software, it was possible to accurately measure the distance between the central bright fringe and each of the dark fringes, which reflects the i^{th} deviation from exact the Bragg condition. The plot of $\frac{s_i^2}{n_k^2}$ versus $\frac{1}{n_k^2}$ gives a straight line that intersects the Y-axis at$\frac{1}{t^2}$; the slope of the aforementioned line is the inverse of the square of the extinction distance (see example in *Figure V.4-4*).

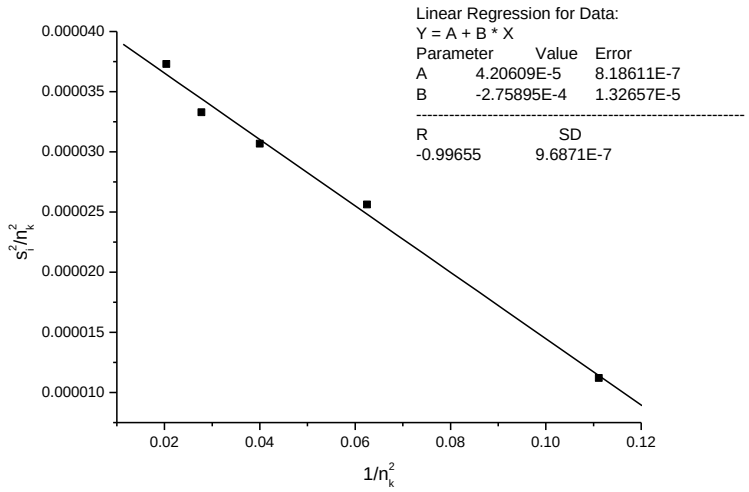

Figure V.4-4 *$\frac{s_i^2}{n_k^2}$ plotted as a function of $\frac{1}{n_k^2}$. The regression fitting of the data gives a straight line whose intersection with the Y-axis determines $\frac{1}{t^2}$ (the inverse square of the thickness). The slope of the mentioned line is the inverse of the square of the extinction distance.*

Samples produced under the four reference TMCP schedules (combination of constant reduction per pass with high/low FRT and Air/ACC), were analyzed according to the described technique. The bar chart in *Figure V.4-5* illustrates that steels rolled at low FRT after either ACC or air cooling, have higher dislocation densities than those rolled at high FRT. A high cooling rate, as is the case of ACC, clearly leads to an increased dislocation density in the material.

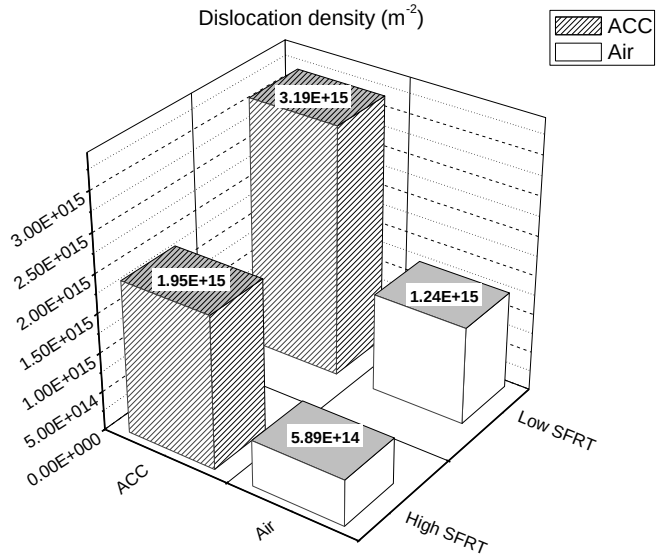

Figure V.4-5 *Dislocation density measured in samples processed under different TMCP schedules.*

Figure V.4-6 is an indication that the strength of HSLA steels is also affected by the dislocation density, that creates effective barriers to slip, and the former is positively correlated to the latter. As described previously, decreasing the FRT results in grain size refinement and increased dislocation density, irrespective of the cooling route. Air cooling leads to a polygonal ferritic-pearlitic microstructure and a relatively low dislocation density. Conversely, ACC results in a bainitic ferrite–quasi-polygonal ferritic microstructure with a characteristically higher density of dislocations. This is not surprising, since the partially displacive transformation (leading to a bainitic microstructure) involves plastic strain, which should be accommodated by the generation of dislocations.

The findings of the current study are consistent with those of *Irvine and Baker* [59], who (for a similar steel grade) found that the dislocation density increases from $5*10^9$ cm^{-2} to $8*10^9$ cm^{-2} if the finish rolling temperature decreases from 800ºC to 700ºC. These values seem to be slightly lower than the ones measured in this work. However, the dislocation density is also correlated to the solutionizing (reheating) temperature. Less Nb is dissolved at lower reheating temperatures, and therefore, at the end of TMCP, a reduced volume fraction of NbC is present in a fine precipitated form. This, in turn, results in less pinning and hence, in retention of dislocations. In the cited reference [59], the reheating temperatures were 1120ºC and 1050ºC but was 1250ºC in the case of the present study.

Despite the different methods used to establish the dislocation density, and the over- or under-estimation of the measurements "intrinsic" to each method, there are similarities between the dislocation density values measured in this work and those described by [72] and [73]. This work also supports the results reported by *Takahashi et al.* [72], who proposed an empirical relation to calculate the dislocation density in ferrite as a function of the transformation temperature. Although the distinct cooling rates in ACC and air lead to different transformation temperatures, the measured values for both cases approach those estimated in the denoted study [72]. The current work contributes experimental data in terms of dislocation measurements, but more saliently, broadens our understanding of the role of dislocation strengthening in materials which were processed under different TMCP parameters. Dislocation density quantification is important not only to the yield strength. *Gladman et al.* [74] introduced the contribution of random and forest dislocations in an equation used to predict the transition temperature of bainitic steels.

Therefore, the obtained data could also be used in predictive models for the transition temperatures of pipeline steels.

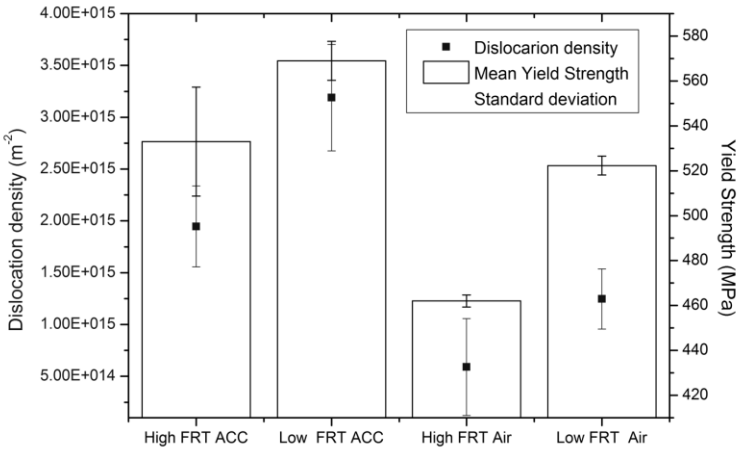

Figure V.4-6 *Measured values of the yield strength and correlation to the final dislocation density for different TMCP rolling schedules.*

Figure V.4-7 plots the strengths calculated from equations (2-5). It is apparent from this comparison that the contribution of dislocation strengthening to YS is considerably larger in schedules with ACC. On the other hand, precipitation strengthening provides a greater impact in air cooling schedules. Moreover, at low FRT the grain size strengthening contribution is higher than at high FRT irrespective of the cooling condition.

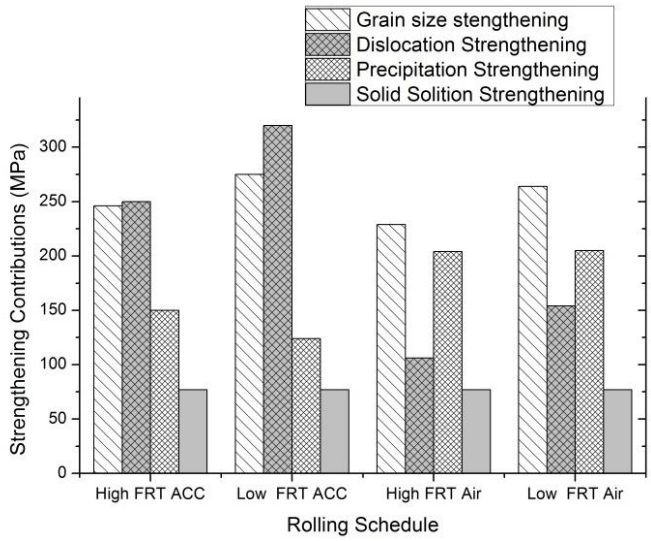

Figure V.4-7 *Comparison of the strengthening mechanisms for schedules I, II, III, and IV with different FRT and cooling calculated according to equations (4-6-7-8).*

References

[1] B. Sum-Met, *The Science Behind Material Preparation*, 2004.

[2] A. Perlade, D. Grandemange, D. Huin, A. Couturier, and K. Oostsuka, "A model to predict the austenite evolution during hot strip rolling of conventional and Nb microalloyed steels," *Revue de Métallurgie,* vol. 105, pp. 443-451, 2008.

[3] S. Roy, D. Chakrabarti, and G. K. Dey, "Austenite Grain Structures in Ti- and Nb-Containing High-Strength Low-Alloy Steel During Slab Reheating," *Metallurgical and Materials Transactions A,* vol. 44, pp. 717-728, 2013/02/01 2013.

[4] S. G. Hong, H. J. Jun, K. B. Kang, and C. G. Park, "Evolution of precipitates in the Nb–Ti–V microalloyed HSLA steels during reheating," *Scripta Materialia,* vol. 48, pp. 1201-1206, 4/14/ 2003.

[5] R. G. Baker and J. Nutting, "Precipitation Processes in Steels," *Iron and Steel Institute,* pp. 1-21, 1959.

[6] H.-J. Kestenbach and E. V. Morales, "Transmission Electron Microscopy of Carbonitride Precipitation in Microalloyed Steels," *Acta Microscopica,* vol. 7, pp. 22-33, 1998.

[7] J. L. Verger-Gaugry, G. Ocampo, and J. D. Embury, "Microanalysis of TiNb carbonitrides in HSLA steels," *Metallography,* vol. 18, pp. 381-393, 11// 1985.

[8] G. K. Tirumalasetty, M. A. van Huis, C. M. Fang, Q. Xu, F. D. Tichelaar, D. N. Hanlon, *et al.*, "Characterization of NbC and (Nb,Ti)N nanoprecipitates in TRIP assisted multiphase steels," *Acta Materialia,* vol. 59, pp. 7406-7415, 2011.

[9] J. J. Jonas, "Transformation Textures Associated with Steel Processing," in *Microstructure and Texture in Steels*, Springer, Ed., ed, 2009.

[10] R. K. Ray and J. J. Jonas, "Transformation textures in steels," *International Materials Reviews,* vol. 35, pp. 1-36, 1990.

[11] N. Wittridge and J. Jonas, "The austenite-to-martensite transformation in Fe–30% Ni after deformation by simple shear," *Acta Materialia,* vol. 48, pp. 2737-2749, 2000.

[12] W. Z., *Fundamentals of rolling*. Oxford, 1969.

[13] M. Suehiro, K. Sato, Y. Tsukano, H. Yada, T. Senuma, and Y. Matsumura, "Computer modeling of microstructural change and strength of low carbon steel in hot strip rolling," *Transactions of the Iron and Steel Institute of Japan,* vol. 27, pp. 439-445, 1987.

[14] J. H. Beynon and C. M. Sellars, "Modelling Microstructure and Its Effects during Multipass Hot Rolling," *ISIJ International,* vol. 32, pp. 359-367, 1992.

[15] J. J. Sidor, R. H. Petrov, and L. A. I. Kestens, "Modeling the crystallographic texture changes in aluminum alloys during recrystallization," *Acta Materialia,* vol. 59, pp. 5735-5748, 8// 2011.

[16] L. Kestens and J. J. Jonas, "Modeling texture change during the static recrystallization of interstitial free steels," *Metallurgical and Materials Transactions A,* vol. 27, pp. 155-164, 1996/01/01 1996.

[17] P. Van Houtte, S. Li, M. Seefeldt, and L. Delannay, "Deformation texture prediction: from the Taylor model to the advanced Lamel model," *International Journal of Plasticity,* vol. 21, pp. 589-624, 3// 2005.

[18] Q. Xie, P. Eyckens, H. Vegter, J. Moerman, A. Van Bael, and P. Van Houtte, "Polycrystal plasticity models based on crystallographic and morphologic texture: Evaluation of predictions of plastic anisotropy and deformation texture," *Materials Science and Engineering: A,* vol. 581, pp. 66-72, 10/1/ 2013.

[19] M. P. Butron-Guillen, "Transformation textures in hot rolled steels," Ph.D. Thesis, McGill University, Montreal, Canada, 1995.

[20] M. P. Butrón-Guillén, C. S. Costa Viana, and J. J. Jonas, "A variant selection model for predicting the transformation texture of deformed austenite," *Metallurgical and Materials Transactions A,* vol. 28, pp. 1755-1768, 1997/09/01 1997.

[21] S. Shanmugam, N. K. Ramisetti, R. D. K. Misra, T. Mannering, D. Panda, and S. Jansto, "Effect of cooling rate on the microstructure and mechanical properties of Nb-microalloyed steels," *Materials Science and Engineering: A,* vol. 460–461, pp. 335-343, 7/15/ 2007.

[22] A. International, "Standard Test Methods for Tension Testing of Metallic Materials," ed. United States: ASTM International, 2004.

[23] W. B. Morrison, "The effect of grain size on the stress-strain relationship in low carbon steel," *Trans. ASM,* vol. 59, pp. 824-46, 1966.

[24] H. Qiu, L. N. Wang, T. Hanamura, and S. Torizuka, "Prediction of the work-hardening exponent for ultrafine-grained steels," *Materials Science and Engineering: A,* vol. 536, pp. 269-272, 2/28/ 2012.

[25] P. Antoine, S. Vandeputte, and J. B. Vogt, "Empirical model predicting the value of the strain-hardening exponent of a Ti-IF steel grade," *Materials Science and Engineering: A,* vol. 433, pp. 55-63, 10/15/ 2006.

[26] R. Song, D. Ponge, and D. Raabe, "Improvement of the work hardening rate of ultrafine grained steels through second phase particles," *Scripta Materialia,* vol. 52, pp. 1075-1080, 6// 2005.

[27] I. Tamura, C. Ouchi, T. Tanaka, and H. Senike, *Thermomechanical Processing of High Strength Low Alloy Steels*. London: Butterworth, 1988.

[28] B. Dutta and C. M. Sellars, "Effect of composition and process variables on Nb(C, N) precipitation in niobium microalloyed austenite," *Materials Science and Technology,* vol. 3, pp. 197-206, 1987/03/01 1987.

[29] A. Pandit, A. Murugaiyan, A. S. Podder, A. Haldar, D. Bhattacharjee, S. Chandra, *et al.*, "Strain induced precipitation of complex carbonitrides in Nb–V and Ti–V microalloyed steels," *Scripta Materialia,* vol. 53, pp. 1309-1314, 12// 2005.

[30] R. K. Ray, J. J. Jonas, M. P. Butron-Guillen, and J. Savoie, "transformation textures in steels," *ISIJ International,* vol. 34, pp. 927-942, 1994.

[31] G. J. Baczynski, J. J. Jonas, and A. E. Collins, "The Influence of Rolling Practice on Notch Toughness and Texture Development in High-Strength Linepipe," *Metallurgical and Materials Transactions A,* vol. 30A, pp. 3045- 3054, 1999.

[32] G. D. Fearnehough, "Fracture propagation control in gas pipelines: A survey of relevant studies," *International Journal of Pressure Vessels and Piping,* vol. 2, pp. 257-282, 10// 1974.

[33] W. A. Spitzig, "Effect of Sulfides and Sulfide Morphology on Anisotropy of Tensile Ductility and Toughness of Hot-Rolled C-Mn Steels," *Metallurgical Transactions A,* vol. 14, pp. 471-484, 1983/02/01 1983.

[34] A. Echeverria and J. M. Rodriguez-Ibabe, "Cleavage micromechanisms on microalloyed steels. Evolution with temperature of some critical parameters," *Scripta Materialia,* vol. 50, pp. 307-312, 1// 2004.

[35] A. Ghosh, A. Ray, D. Chakrabarti, and C. L. Davis, "Cleavage initiation in steel Competition between large grains and large particles," *Materials Science and Engineering A,* vol. 561, pp. 126-135, 2013.

[36] D. Chakrabarti, M. Strangwood, and C. Davis, "Effect of Bimodal Grain Size Distribution on Scatter in Toughness," *Metallurgical and Materials Transactions A,* vol. 40, pp. 780-795, 2009/04/01 2009.

[37] R. Anumolu, B. R. Kumar, R. D. K. Misra, T. Mannering, D. Panda, and S. G. Jansto, "On the determining role of microstructure of niobium-microalloyed steels with differences in impact toughness," *Materials Science and Engineering: A,* vol. 491, pp. 55-61, 9/15/ 2008.

[38] I. Gutiérrez, "Effect of microstructure on the impact toughness of Nb-microalloyed steel: Generalisation of existing relations from ferrite–pearlite to high strength microstructures," *Materials Science and Engineering: A,* vol. 571, pp. 57-67, 6/1/ 2013.

[39] B. Garbarz and F. B. Pickering, "Effect of pearlite morphology on impact toughness of eutectoid steel containing vanadium," *Materials Science and Technology,* vol. 4, pp. 328-334, // 1988.

[40] J. Verhoeven, "A review of microsegregation induced banding phenomena in steels," *Journal of Materials Engineering and Performance,* vol. 9, pp. 286-296, 2000/06/01 2000.

[41] J. S. Kirkaldy, J. von Destinon-Forstmann, and R. J. Brigham, "Simulation of Banding in Steels," *Canadian Metallurgical Quarterly,* vol. 1, pp. 59-81, // 1962.

[42] J. P. Naylor, "The influence of the lath morphology on the yield stress and transition temperature of martensitic- bainitic steels," *Metallurgical Transactions A,* vol. 10, pp. 861-873, 1979/07/01 1979.

[43] A. F. Gourgues, H. M. Flower, and T. C. Lindley, "Electron backscattering diffraction study of acicular ferrite, bainite, and martensite steel microstructures," *Materials Science and Technology,* vol. 16, pp. 26-40, // 2000.

[44] M. P. Aarnts, R. A. Rijkenberg, F. A. Twisk, D. Wilcox, M. J. Zuijderwijk, A. Arlazarov, *et al.*, "Microstructural quantification of multi phase steels (Micro-quant)," European commission2011.

[45] A. Iza-Mendia and I. Gutiérrez, "Generalization of the existing relations between microstructure and yield stress from ferrite–pearlite to high strength steels," *Materials Science and Engineering: A,* vol. 561, pp. 40-51, 1/20/ 2013.

[46] S. Y. Shin, B. Hwang, S. Lee, N. J. Kim, and S. S. Ahn, "Correlation of microstructure and charpy impact properties in API X70 and X80 line-pipe steels," *Materials Science and Engineering: A,* vol. 458, pp. 281-289, 6/15/ 2007.

[47] R. Song, D. Ponge, D. Raabe, and R. Kaspar, "Microstructure and crystallographic texture of an ultrafine grained C–Mn steel and their evolution during warm deformation and annealing," *Acta Materialia,* vol. 53, pp. 845-858, 2// 2005.

[48] V. Carretero Olalla, R. H. Petrov, P. Thibaux, M. Liebeherr, P. Gurla, and L. A. I. Kestens, "Influence of Rolling Temperature and Cooling Rate on Microstructure and Properties of Pipeline Steel Grades," *Materials Science Forum,* vol. 706-709, pp. 2710-2715, 2012.

[49] R. Ayres and D. F. Stein, "A dislocation dynamics approach to prediction of cleavage planes in b.c.c. metals," *Acta Metallurgica,* vol. 19, pp. 789-794, 8// 1971.

[50] V. S. Ivanova and V. M. Plastinin, "Analysis of cleavage in bcc single crystals from the positions of physics and fracture mechanics," *Strength of Materials,* vol. 12, pp. 163-166, 1980/02/01 1980.

[51] K. J. Irvine, "Keynote Speech PHYSICAL METALLURGY OF STEEL," *Phil. Trans. R. Soc. Lond. A,* vol. 282, pp. 339-346, 1976.

[52] J. Majta, J. G. Lenard, and M. Pietrzyk, "A study of the effect of the thermomechanical history on the mechanical properties of a high niobium steel," *Materials Science and Engineering,* vol. A208, pp. 249-259, 1996.

[53] W. B. Morrison and J. A. Chapman, "Controlled Rolling," *Phil. Trans. R. Soc. Lond. A,* vol. 282, pp. 289-303, 1976.

[54] Y. Hai-Iong, D. Lin-xiu, W. Guo-dong, and L. Xiang-hua, "Development of Nb-V-Ti Hot-Rolled High Strength Steel With Fine Ferrite and Precipitation Strengthening," *Journal of Iron ans Steel Research International,* vol. 16, pp. 72-77, 2009.

[55] C. M. José, E. Guillermo, and P. T. Estela, "Characterisation of microalloy precipitates in the austenitic range of high strength low alloy steels," *Steel Research,* vol. 73, pp. 340-346, 2002.

[56] M. Charleux, W. J. Poole, M. Militzer, and A. Deschamps, "Precipitation behavior and its effect on strengthening of an HSLA-Nb Ti Steel," *Metallurgical and Materials Transactions A,* vol. 32A, pp. 1635-1647, 2001.

[57] E. Orowan, "The Theory of yield without particle shear," in *Symposium on Internal Stresses in Metals and Alloys,* London - United Kingdom, 1948, pp. 451-453.

[58] M. F. Ashby, "The Theory of the Critical Shear Stress and Work Hardening of Dispersion-Hardened Crystals," in *Metallurgical Society Conference Oxide Dispersion Strenghening,* New York - USA, 1966, pp. 143-205.

[59] J. Irvine and T. N. Baker, "The influence of rolling variables on the strengthening mechanisms operating in niobium steels," *Materials Science and Engineering,* vol. 64, pp. 123-134, 1984.

[60] G. I. Taylor, "The Mechanism of plastic deformation of crystals," *Proceedings of the Royal Society of London. Series A,* vol. 145, pp. 362-388, 1934.

[61] P. Gilormini, B. Bacroix, and J. J. Jonas, "Theoretical analyses of 111 pencil glide in B.C.C. crystals," *Acta metall. ,* vol. 36, pp. 231-256, 1988.

[62] Y. Miyajima, M. Mitsuhara, S. Hata, H. Nakashima, and N. Tsuji, "Quantification of internal dislocation density using scanning transmission electron microscopy in ultrafine grained pure aluminium fabricated by severe plastic deformation," *Materials Science and Engineering: A,* vol. 528, pp. 776-779, 2010.

[63] W. Kossel and G. Möllenstedt, "Elektroneninterferenzen im konvergenten Bündel. Ann. Phys.," *Ann. der Phys.,* vol. 428, pp. 113-140, 1939.

[64] P. M. Kelly, A. Jostsons, R. G. Blake, and J. G. Napier, "The determination of foil thickness by scanning transmission electron microscopy," *Phys. Stat. Sol. (A),* vol. 31, pp. 771-780, 1975.

[65] P. B. Hirsh, A. Howie, R. B. Nicholson, D. W. Pasley, and M. J. Whelan, *Electron microscopy of thin crystals* London: Butterwoths, 1965.

[66] R. K. Ham, "The determination of dislocation densities in thin films," *Philosophical Magazine,* vol. 6, pp. 1183-1184, 1961.

[67] D. B. Williams and C. B. Carter, *Transmision Electron Microscopy* vol. Difraction II: KLUWER ACADEMIC / PLENUM PUBLISHERS, 1996.

[68] D. M. Norfleet, D. M. Dimiduk, S. J. Polasik, M. D. Uchic, and M. J. Mills, "Dislocation structures and their relationship to strength in deformed nickel microcrystals," *Acta Materialia,* vol. 56, pp. 2988-3001, 2008.

[69] I. C. Dragomir, D. S. Li, G. A. Castello-Branco, H. Garmestani, R. L. Snyder, G. Ribarik, *et al.,* "Evolution of dislocation density and character in hot rolled titanium determined by X-ray diffraction," *Materials Characterization,* vol. 55, pp. 66-74, 2005.

[70] S. Graça, R. Colaço, P. A. Carvalho, and R. Vilar, "Determination of dislocation density from hardness measurements in metals," *Materials Letters,* vol. 62, pp. 3812-3814, 2008.

[71] I. Gutierrez-Urrutia and D. Raabe, "Dislocation density measurement by electron channeling contrast imaging in a scaning electron microscope," *Scripta Materialia,* vol. 66, pp. 343-346, 2012.

[72] M. Takahashi and H. K. D. H. Bhadeshia, "Model for transition from upper to lower bainite " *Materials Science and Technology,* vol. 6, pp. 592-603, 1990.

[73] C. Garcia-Mateo, F. G. Caballero, C. Capdevila, and C. G. d. Andres, "Estimation of dislocation density in bainitic microstructures using high-resolution dilatometry," *Scripta Materialia,* vol. 61, pp. 855-858, 2009.

[74] T. Gladman, D. Dulieu, and R. M. Ivo, in *Microalloying 75, International Symposium on HSLA Steel*, NY, 1975, p. 32.

"Intuition and concepts constitute... the elements of all our knowledge, so that neither concepts without an intuition in some way corresponding to them, nor intuition without concepts, can yield knowledge".

"All our knowledge begins with the senses, proceeds then to the understanding, and ends with reason. There is nothing higher than reason."

Immanuel Kant (1724-1804) Selections from: The Critique of Pure Reason

CHAPTER VI

General discussion

VI.1 Correlation: Processing parameters – Microstructure – Properties

Historically, materials for engineering applications were developed and selected on a trial and error basis. Nowadays, with the help of available technologies, material scientists are tasked with building an understanding of the correlation between processing conditions, microstructure, and the final properties which will determine the performance of the material. In the present chapter, a number of explanations will be given to clarify the variability of the mechanical properties presented in Chapter V.

Inspired by Kant, we followed our intuition, and played with the concepts, with the aim of increasing our knowledge. What follows, therefore, is a description linking "Processing parameters – Microstructure – and Properties". The first part is presented from the viewpoint of possible strategies that can be implemented in order to increase the strength of a reference TMCP HSLA pipeline steel. Within the frame of this project, these strategies were limited to changes in the: *(i)* FRT, *(ii)* cooling rate, and *(iii)* C and Nb composition. *Figure VI.1-1* summarizes the analyzed strategies.

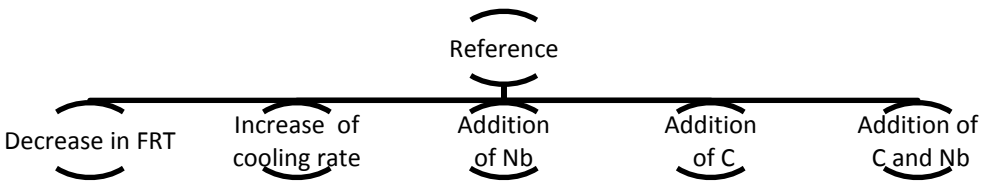

Figure VI.1-1 *Schematic view of the TMCP strategies analyzed in order to determine their effect on the mechanical properties.*

It is worth mentioning that for this particular analysis the reference material corresponds to the Low C - Low Nb composition.

A series of tables are presented in order to easily assess the improvement of the YS and the corresponding impact on the DBTT. *Table VI.1-1* compares quantitatively, the impact of each strategy on the DBTT as well as the YS, UTS. *Table VI.1-3, Table VI.1-4, Table VI.1-5, Table VI.1-6,* and *Table VI.1-7* list, the microstructural parameters, which will aid in explaining the trends summarized in *Table VI.1-1*.

	Decrease in FRT	Increase cooling rate	Addition of Nb	Addition of C	Addition of C and Nb
Variation in YS	+58MPa	+43MPa	+56MPa	+23MPa	+72MPa
Variation in UTS	+16MPa	+42MPa	+29MPa	+38MPa	+66MPa
Variation in DBTT	+8°C	+9°C	+4°C	+30°C	+22°C

Table VI.1-1 *Impact of adopted strategy on the mechanical properties with respect to the reference TMCP material.*

The material produced by decreasing only the FRT while keeping the other TMCP parameters constant had a 58 MPa higher yield strength than the reference material. This increase is attributed to the refinement of the microstructure (see *Table VI.1-3*). which is apparent from both the Grain Clustering Maps (GCM) and the average grain size obtained when grains are partitioned on the basis of their surrounding boundaries; i.e., on the basis of being surrounded by HAGB or LAGB. The GCM provide additional information about the homogeneity of the microstructure. For the present case, the GCM indicate that the entire microstructure was homogeneously refined. These results concur with the well-established Hall-Petch relationship (*Hall* [1] and *Petch* [2]) that describes the dependence of the YS on the grain size. Statistical analyses were also performed in order to determine the influence of HAGB and LAGB on the yield strength. *Figure VI.1-2* plots the experimentally-measured YS (average of 3 samples per material) as a function of the average grain size determined from EBSD measurements of the 28 materials investigated in this project. The blue and orange markers correspond to grain boundaries defined by 5° and 15° misorientation criteria, respectively. Furthermore, *Table VI.1-2* summarizes the statistical analysis performed in order to determine whether the variation in the YS can be explained by changes in the grain size. This analysis is

quite revealing in two ways. First, a strong correlation was obtained when a significant number of samples with different microstructures were evaluated. Second, compared to the 15° criterion, a slightly higher dependency of the YS on the average grain size was found when the boundaries were defined by a misorientation of 5°.

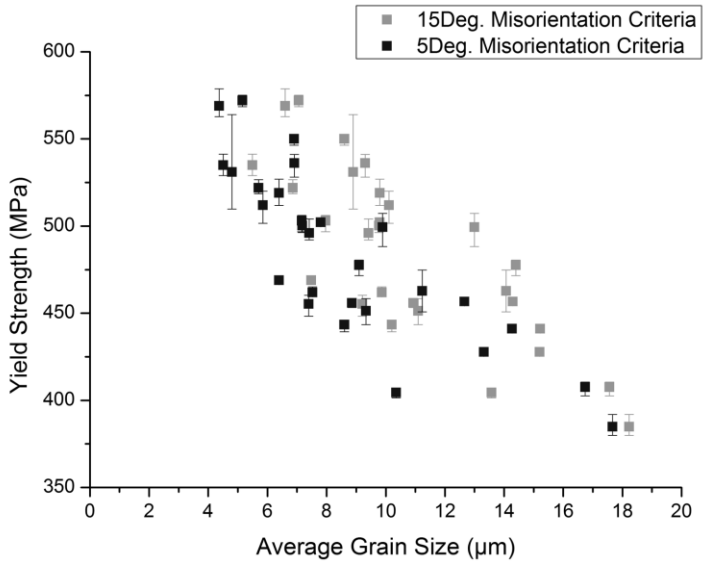

Figure VI.1-2 *YS as a function of average grain size, as defined by two misorientation criteria.*

Criteria	15° Miso.	5° Miso.
Pearson's Cor.	-0.79	-0.83
Adj. R-Square	0.62	0.67
Prob.Null Hyp.	< 4.6E-7	< 5.1E-8

Table VI.1-2 *Summary of the ANOVA analysis for the data in Figure VI.1-2.*

In addition, the remaining variables in *Table VI.1-3* are compared in the form of KAM or misorientation angle distribution maps (which can be used to discern the different morphological phases present in the material), it becomes evident that increases in the YS are governed by decreases in the grain size. Increased precipitation (e.g. +31%) of Nb, via precipitation strengthening, may have also had an impact on the yield strength. Since the chemical composition of the materials remained unchanged, the additional precipitation of Nb may have resulted from strain-induced precipitation (SIP), which occurs more readily at low temperatures than at high temperatures.

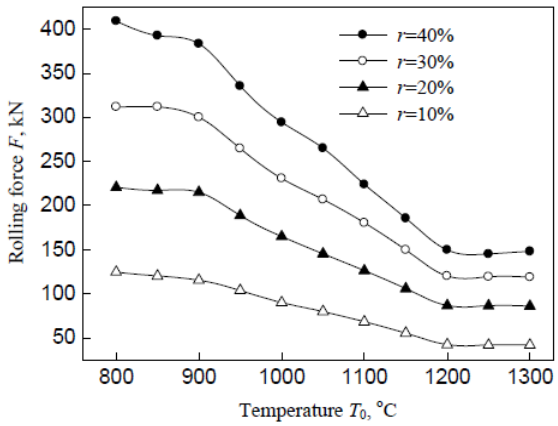

Figure VI.1-3 *Effect of temperature and rolling reduction on the rolling forces for steel [3].*

One of the disadvantages or limitations of reducing the FRT is the accompanying increase in the rolling forces at low temperatures. *Figure VI.1-3* [3] illustrates the influence of

temperature on the rolling force for different reductions. The results shown in the figure suggest that the decreasing FRT strategy might be constrained by the limitations of the rolling mill.

	Reference	**Decrease FRT**
Grain cluster map	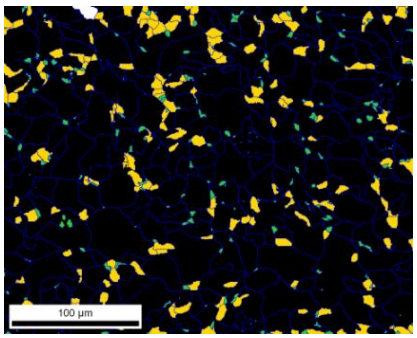	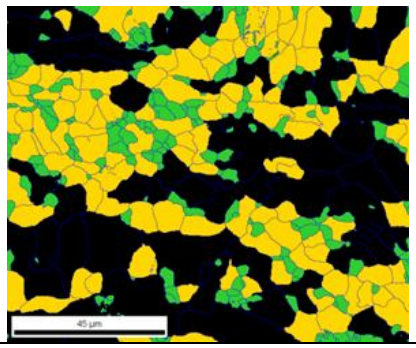
Average grain size (µm) Criteria: 15° and >1µm	18.2	10.2
Average grain size (µm) Criteria: 5° and >1µm	17.7	8.6
Difference in % Nb precipitated	Ref.	+31%
HAGB fraction	0.82	0.78
LAGB fraction	0.18	0.22
Kernel average misorientation (KAM) map	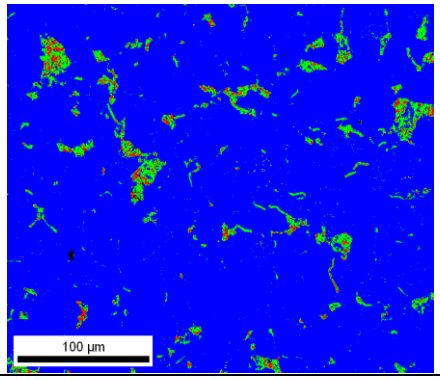	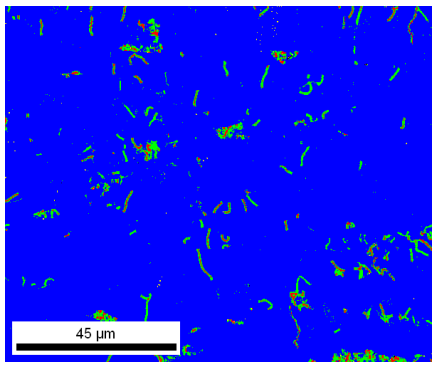
Misorientation angle distribution	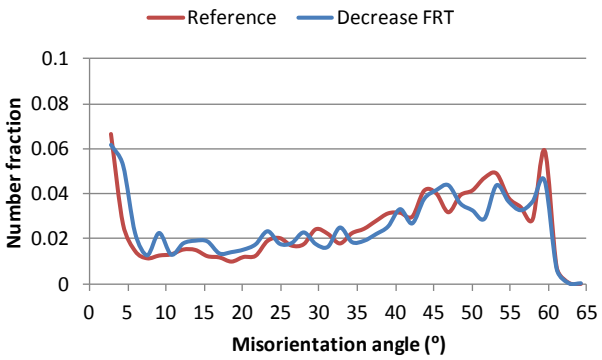	

Table VI.1-3 *Comparison between the reference material and the decrease FRT strategy. Summary of the relevant microstructural parameters.*

In addition, the microstructure resulting from the increasing cooling rate strategy has a significantly higher fraction of (i.e., approximately twice many) LAGB than that of the reference material.

	Reference	**Increase cooling rate**
Grain cluster map	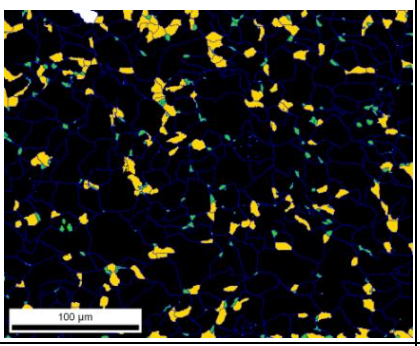	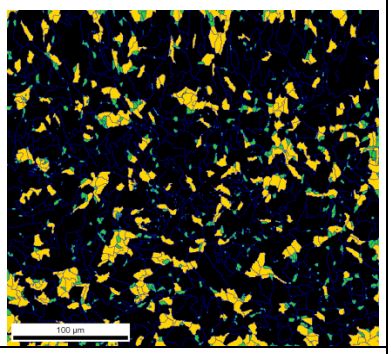
Average grain size (µm) Criteria: 15° and >1µm	18.2	15.2
Average grain size (µm) Criteria: 5° and >1µm	17.7	13.3
Difference in % Nb precipitated	Ref.	-29%
HAGB fraction	0.82	0.61
LAGB fraction	0.18	0.39
Kernel average misorientation (KAM) map	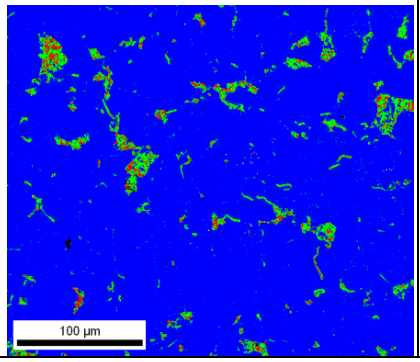	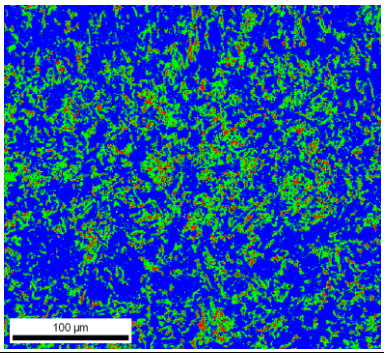
Misorientation angle distribution	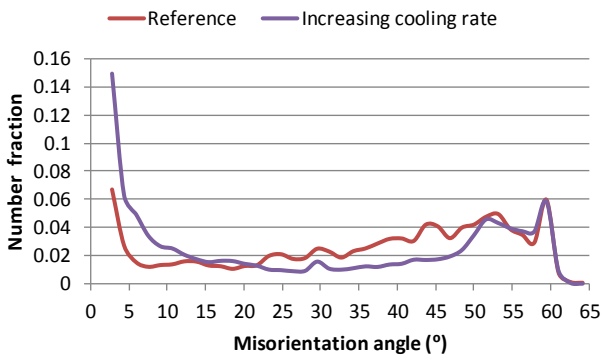	

Table VI.1-4 *Comparison between the reference material and the increasing cooling rate strategy. Summary of the relevant microstructural parameters. The micron bar in each of the KAM maps reads 100µm.*

Grain refinement is also less pronounced, and a lower fraction of Nb precipitates is obtained than that resulting from the strategy of decreasing FRT. These facts are reflected in the somewhat minor enhancement of the yield strength. On the other hand, the ultimate tensile strength increased significantly in the case of the cooling rate strategy. As *Figure VI.1-4* shows the samples processed according to the ACC strategy have a higher work hardening capacity than that of the reference material. This result can be attributed to the strain hardening capacity of the bainitic-ferritic microstructure.

Another important finding was that the addition of Nb strategy yielded similar results to those obtained from decreasing the FRT, see *Table VI.1-1*. Grain refinement is, however, less pronounced in samples resulting from the former compared to those from the latter. Conversely, as expected, the amount of Nb precipitated is an order of magnitude higher than in the decreasing FRT strategy, see *Table VI.1-3* and *Table VI.1-5*.

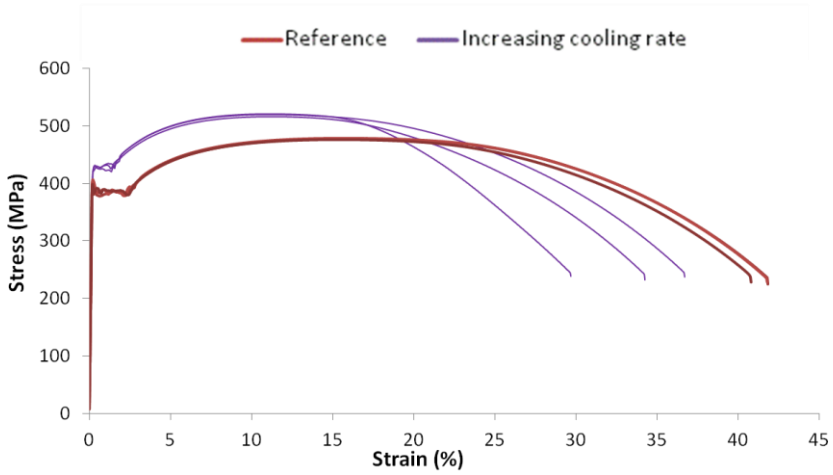

Figure VI.1-4 *Comparison of the stress-strain curves for the reference material and materials processed via the increasing cooling rate strategy.*

This result implies that the enhancement of the YS occurs primarily through precipitation hardening and secondarily via grain refinement.

Grain refinement did not occur in the case of the increased C content strategy (see *Table VI.1-6*); the YS is enhanced owing to the increased fraction of pearlite. KAM and misorientation angle distribution maps (see *Table VI.1-6*) confirm the increase of pearlitic regions, which correspond to highly misoriented neighboring points in the former, and an increase in the fraction of LAGB in the latter. Furthermore, despite the hardening effect of cementite, the ferrite-cementite and ferrite-pearlite interfaces provide an excellent path for the nucleation and growth of cracks. The addition of C strategy results, therefore, in a decrease in the fracture toughness, which, leads to a significant increase (30°C) in the DBTT.

	Reference	**Addition of Nb**
Grain cluster map	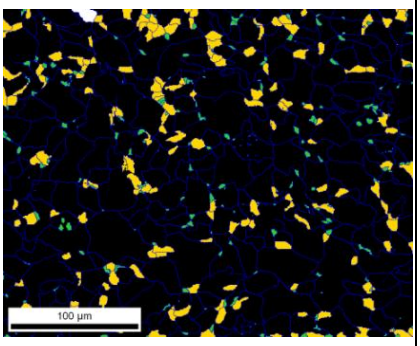	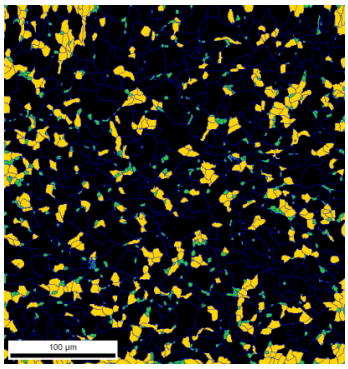
Average grain size (µm) Criteria: 15° and >1µm	18.2	15.2
Average grain size (µm) Criteria: 5° and >1µm	17.7	14.3
Difference in % Nb precipitated	Ref.	+328%
HAGB fraction	0.82	0.84
LAGB fraction	0.18	0.16
Kernel average misorientation (KAM) map	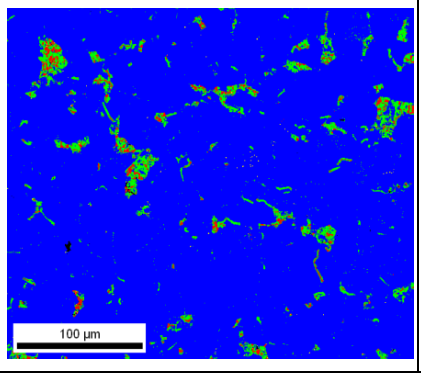	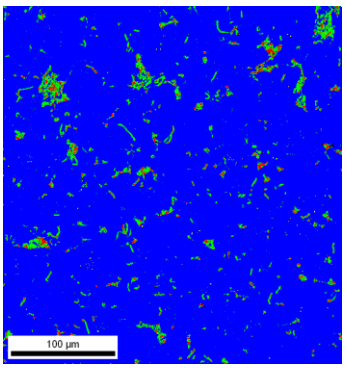
Misorientation angle distribution	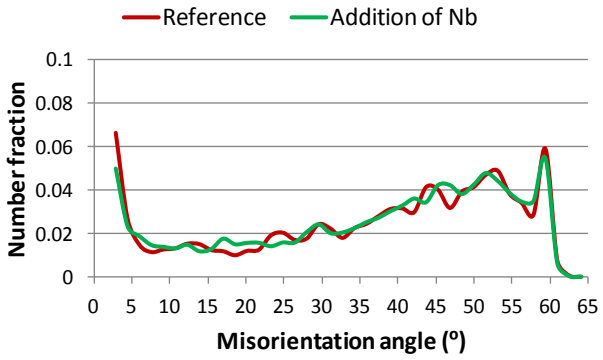	

Table VI.1-5 *Comparison between the reference material and the addition of Nb strategy. Summary of the relevant microstructural parameters. The micron bar in each of the KAM maps reads 100µm.*

	Reference	**Addition of C**
Grain cluster map	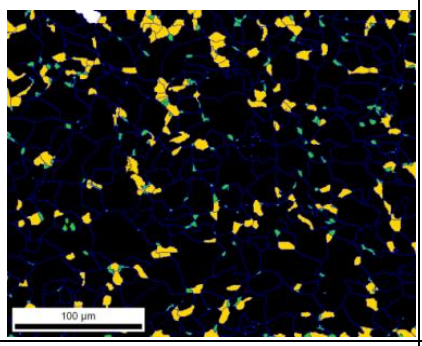	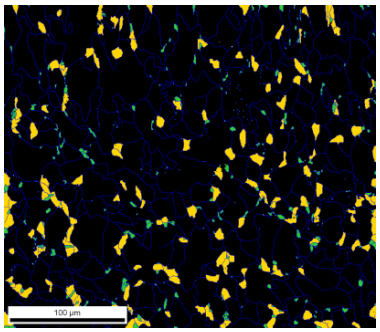
Average grain size (µm) Criteria: 15° and >1µm	18.2	17.6
Average grain size (µm) Criteria: 5° and >1µm	17.7	16.7
Difference in % Nb precipitated	Ref.	+1%
HAGB fraction	0.82	0.76
LAGB fraction	0.18	0.24
Kernel average misorientation (KAM) map	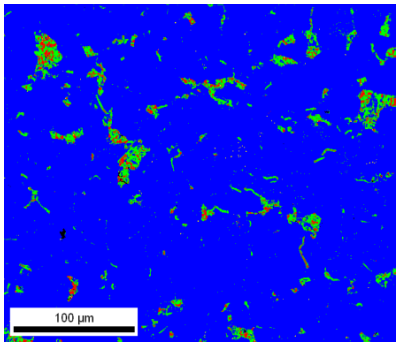	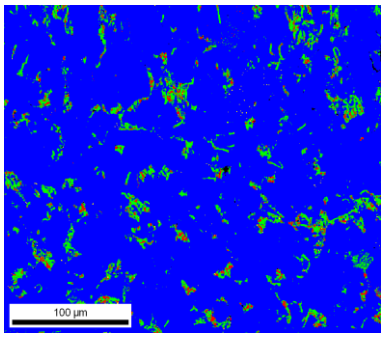
Misorientation angle distribution	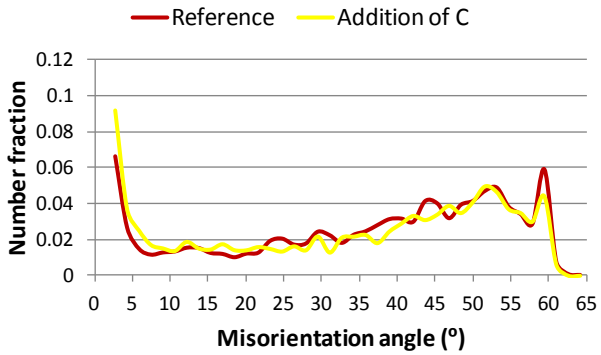	

Table VI.1-6 *Comparison between the reference material and the material with increased C content (C addition strategy). Summary of the relevant microstructural parameters. The micron bar in each of the KAM maps reads 100µm.*

It is interesting to note that the enhancement of the YS achieved with the addition of C and Nb strategy, equals the total attained when the Nb and C addition strategies are considered separately (see *Table VI.1-1*.) Comparing the degree of grain refinement achieved with these

	Reference	Addition of C and Nb
Grain cluster map	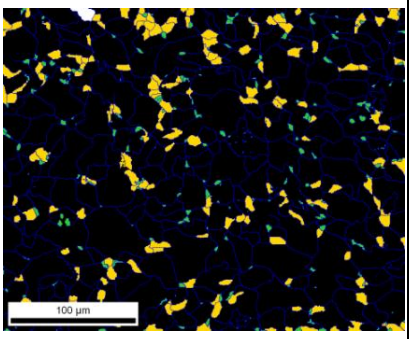	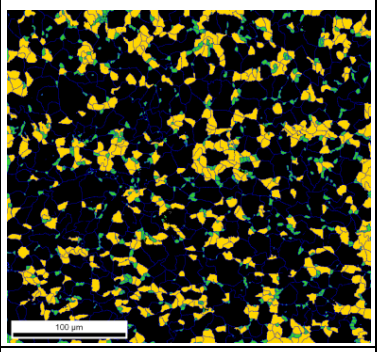
Average grain size (µm) Criteria: 15° and >1µm	18.2	14.3
Average grain size (µm) Criteria: 5° and >1µm	17.7	12.7
Difference in % Nb precipitated	Ref.	+284%
HAGB fraction	0.82	0.81
LAGB fraction	0.18	0.19
Kernel average misorientation (KAM) map	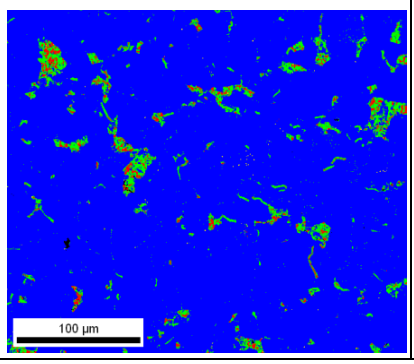	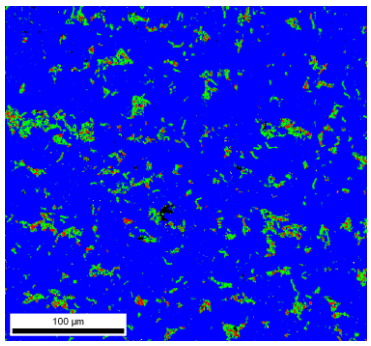
Misorientation angle distribution	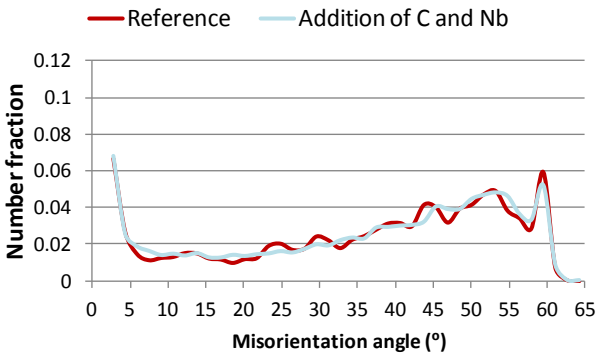	

Table VI.1-7 *Comparison between the reference material and the addition of C +Nb strategy. Summary of the relevant microstructural parameters. The micron bar in each of the KAM maps reads 100µm.*

three strategies reveals an increase in the amount of Nb precipitated, and a difference in the fraction of LAGB relative to that of the reference material (see *Table VI.1-5, Table VI.1-6,*

and *Table VI.1-7*). Therefore, the grain refinement achieved with the C + Nb strategy can be considered as an additional refinement to that achieved with the separate C and Nb addition strategies.

In general, the effects produced independently by the C and the Nb addition strategies, represent a coupling of the effect of adding the C and Nb simultaneously (so-called C+Nb strategy). The similarities in the fractions of LAGB and between the KAM maps (see *Table VI.1-7*) of the C+Nb strategy and the reference material indicate that the excess C exists in the form of NbC rather than as pearlite.

VI.1.1 Varying process parameters (temperature and deformation schedule)

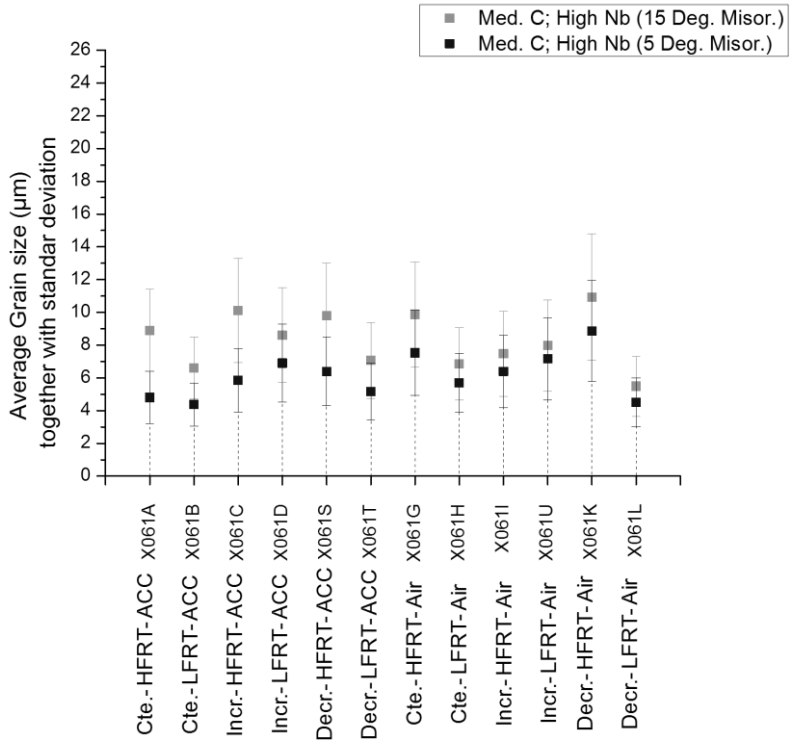

Figure VI.1-5 *Average grain size as a function of the processing condition.*

The influence of the changes in the finishing rolling reduction draught and cooling condition on the microstructure and properties will now be discussed with reference to the composition referred to as Med. C - High Nb. *Figure VI.1-5*, *Figure VI.**1-6***, and *Figure VI.1-7* perfectly illustrate the potential of TMCP for microstructure property control. These figures (*Figure VI.1-5* and *Figure VI.**1-6***) can be seen as examples of the microstructural response (average grain size/microstructure homogeneity) to variations in the TMCP parameters. *Figure VI.1-7* is an illustration of how the mechanical properties are linked to the entire set of TMCP parameters.

Figure VI.1-5 shows a number of findings. For example, when the FRT is decreased, the average grain size is consistently reduced for all reduction draughts and cooling conditions,

except for the combination "increasing reduction per pass-air cooling" which does not show a significant difference. Strain accumulation during the last pass of the increasing reduction draught was possibly high enough to activate grain boundary migration (of certain orientations as will be discussed in section VI.1.9) at low FRT instead of only at high FRT. In other words, the austenite grain size, before the γ–to-α transformation, might be similar after both schedules (high FRT + increasing reduction per pass + air cooling, and low FRT + increasing reduction per pass + air cooling) since increasing deformation draught combined with air cooling counteracts the differences between finishing rolling at high and low temperatures. The mechanical properties after these TMCP schedules are, however, disparate (*Figure VI.1-7*). This implies that the strength and toughness are influenced by a combination of various strengthening mechanisms and multiple other factors. In addition, there was no significant difference in the average grain sizes, and the corresponding standard deviations, of the steels processed by constant and decreasing reduction draughts.

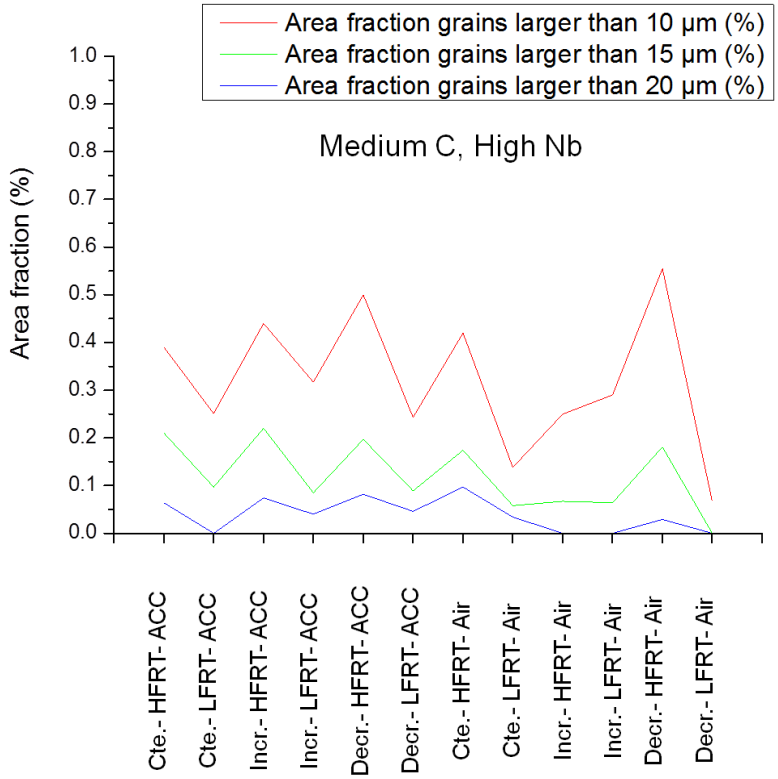

Figure VI.1-6 *Influence of the TMCP schedule on microstructural homogeneity.*

The literature contains very little information about the quantification of microstructural heterogeneity, when process parameters are changed. *Figure VI.1-6* offers a direct and quantifiable way through which the microstructural heterogeneity of the TMCP materials can be analyzed. The results, in *Figure VI.1-6*, are significant in at least two major respects: *(i)* Med. C – High Nb composition exhibited, in general, rather homogeneous microstructures irrespective of the TMCP schedule. For example, grains larger than 20µm constitute, in terms of area fractions, <10% of these microstructures. This fact is corroborated by examining

Figure VI.1-10 and *Figure VI.1-11*. *(ii)* Low FRT followed by air cooling at either constant or decreasing reduction draught results in significant homogenization of the grain size distribution.

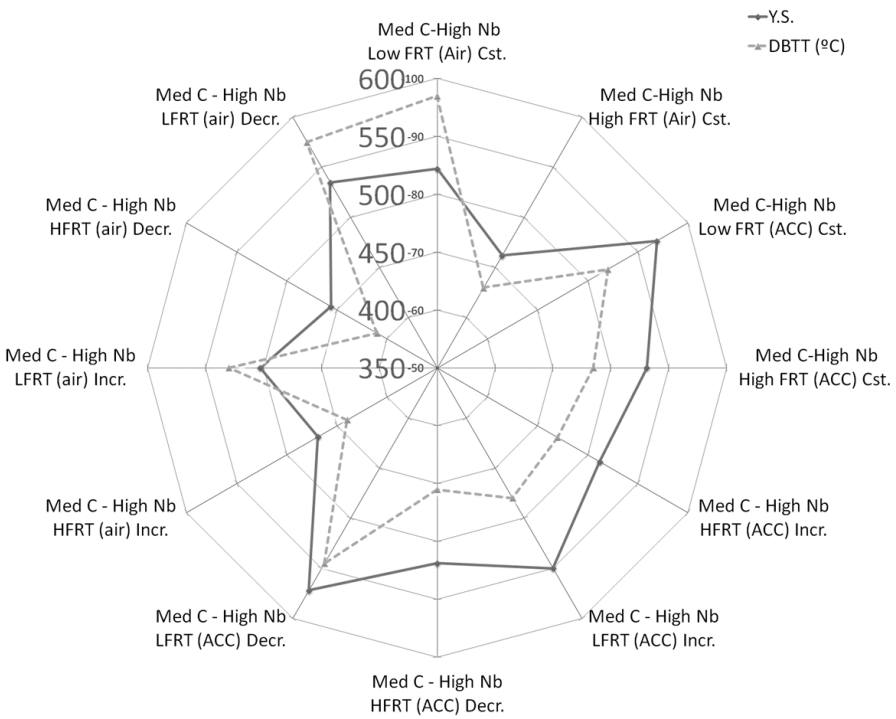

Figure VI.1-7 *Radar plot showing the combination of YS and DBTT as a function of TMCP schedule.*

Figure VI.1-7 illustrates the impact of the processing route on the strength and toughness of HSLA steels. The scales are arranged in such a way that the more external the markers, the better is the mechanical property under consideration. Hence, in the case of the optimal material both markers will lie close to the external perimeter of the radar plot. In other words, it is the steel which balances strength and toughness. The single most direct observation to emerge from the data comparison in *Figure VI.1-7* is the variability of mechanical properties with the TMCP schedule. Consequently, the wide spread in toughness and strength, by itself, provides valuable information about the product-processing capabilities. Interestingly, the best DBTT was observed in the case of low FRT and air cooling for both constant and decreasing reduction draughts. In contrast, the more balanced steel, in terms of the DBTT and YS, was processed by low FRT, decreasing reduction per pass and accelerated cooling (ACC). Steels following low FRT, constant draught and ACC, also have a good combination of strength and toughness. The worst combination of properties was found in the steels processed with a combination of high FRT and air cooling, irrespective of the reduction draught.

VI.1.2 Varying Nb-C content

During the 1950s, the concept of Nb micro-alloyed steel, was developed at Sheffield University, and industrially realized thanks to Great Lakes Steel [5]. Since then, Nb has been used increasingly to improve the properties of plain carbon steel, and micro-alloyed steels currently represent 75% of the Nb consumption [6]. *Figure VI.1-8* [4] plots the evolution of niobium and carbon contents as a function of time and the corresponding increases in strength. Large quantities of Nb micro-alloyed steels have been used for various applications. However, a detailed, systematic, and quantitative study of the effects of varying Nb and C content on the final properties, has not been performed; i.e., a complete understanding of the respective correlations between the mechanical properties and chemical composition and the microstructure, remains elusive. Therefore, one of the goals of this thesis is to contribute and cultivate new quantitative data and "concepts", respectively in order to further improve the understanding of the aforementioned correlation.

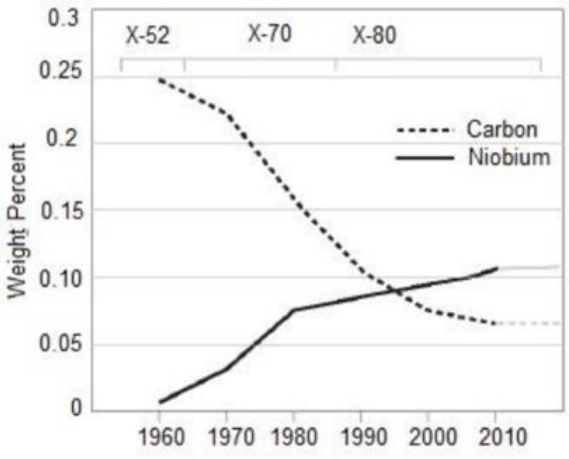

Figure VI.1-8 *Changes in maximum niobium and carbon contents with time (and strength increase) for pipeline steels (courtesy of J. Malcolm Gray [4]).*

It is clear from *Figure VI.1-9* that the grain size determined with the 5 and 15° misorientation criteria vary similarly with the TMCP schedule. Different chemical compositions vary not only in absolute values of the average grain size, but also in their sensitivity to changes in the TMCP schedule (see *Figure VI.1-10*). The present results are significant from various viewpoints. For example, the lower the Nb content, the higher the scatter of the average grain size with changes in TMCP (FRT and cooling rate). This fact is made clear in *Figure VI.1-11*, where, for all rolling schedules, the area fraction of larger (10-20µm in size) grains increases with decreasing Nb content. This finding has important implications for developing homogeneous microstructures in HSLA pipeline steels, whose fracture toughness values are intimately linked to the homogeneity of the microstructure (see Chapter V.3 and VI. 6).

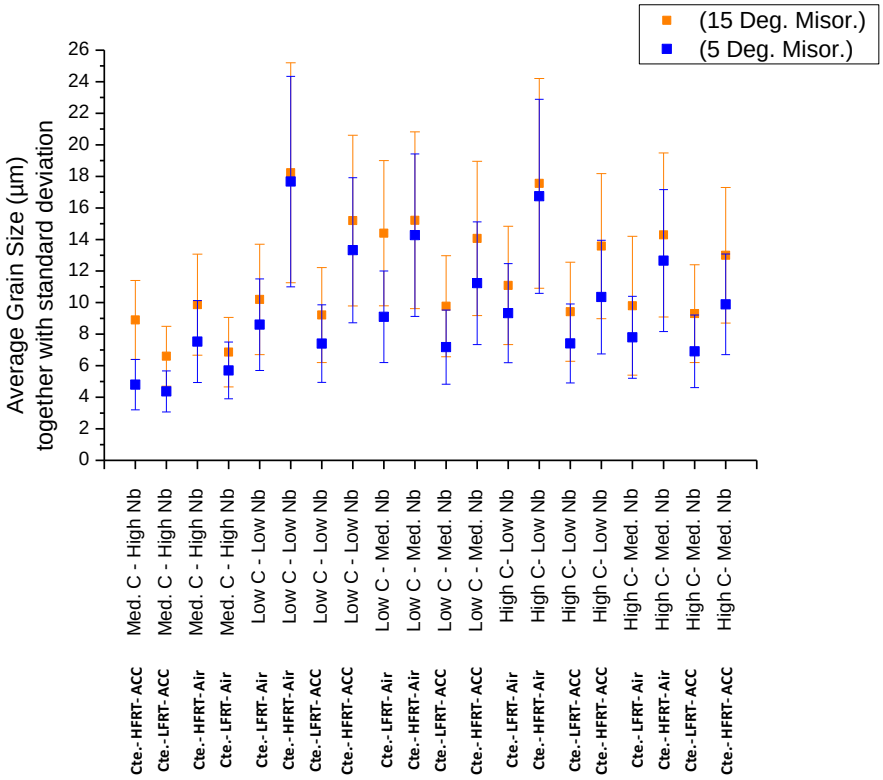

Figure VI.1-10 *Average grain size as a function of the processing condition and the chemical composition.*

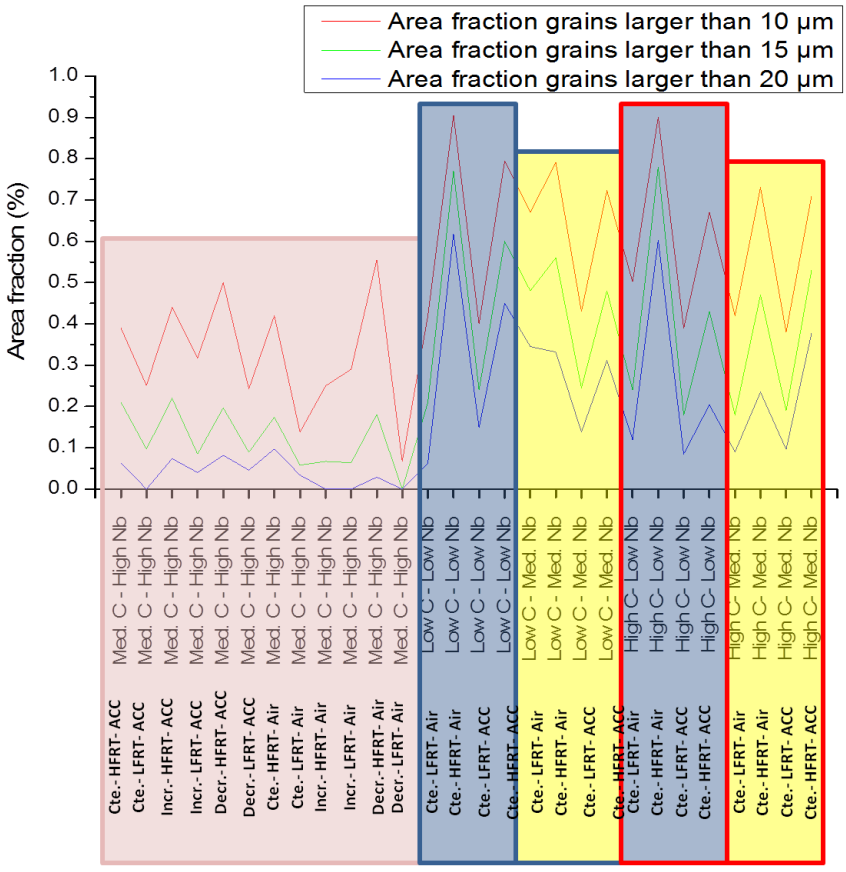

Figure VI.1-11 *Influence of the TMCP schedule and the chemical composition on the homogeneity of the microstructure.*

Med. C – High Nb steels have, in general, more homogeneous microstructures than those of other compositions. This result concurs with earlier observations made in this work. Moreover, these findings provide further support for the premise that Nb, as a micro-alloying element, is not only quite effective as a microstructure refining instrument, but furthermore, it acts as a microstructure homogenizer agent.

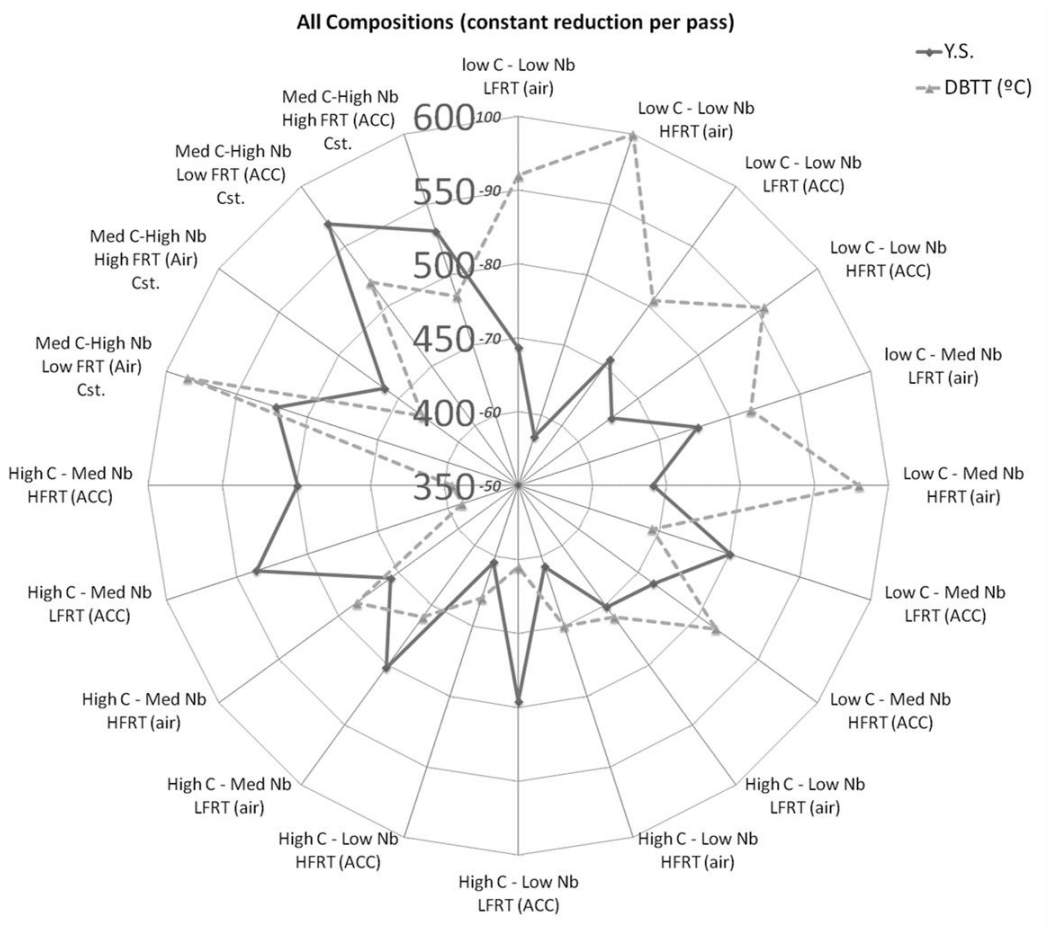

Figure VI.1-12 *Radar plot showing the combination of YS and DBTT as a function of the TMCP schedule.*

The radar plot may be divided into three main sectors: the first one (covering the upper and central right sides) corresponds to steels with low C content and characterized by significantly low DBTTs. The second sector, located in the lower central region, is characterized by high DBTTs; the steels present in this sector have high C content. Finally, the third sector (central/upper left) displays no clear tendency with regards to toughness. This indicates that the toughness of the Med. C - High Nb composition is quite sensitive to the changes in the TMCP schedule compared to that of the other compositions. Some of the details emerging from this finding relate specifically to the degree of mechanical property optimization that can be achieved with each composition.

It appears that all the compositions can offer improvements in the strength and toughness by tuning the TMCP parameters. However, Med. C - High Nb steel exhibits, undoubtedly, the largest sensitivity to variations in the TMCP parameters. This steel should, therefore, benefit from the tuning of the TMCP but, at the same time, may suffer from a scatter in properties if certain parameters (at FRT or cooling rate) are not perfectly controlled.

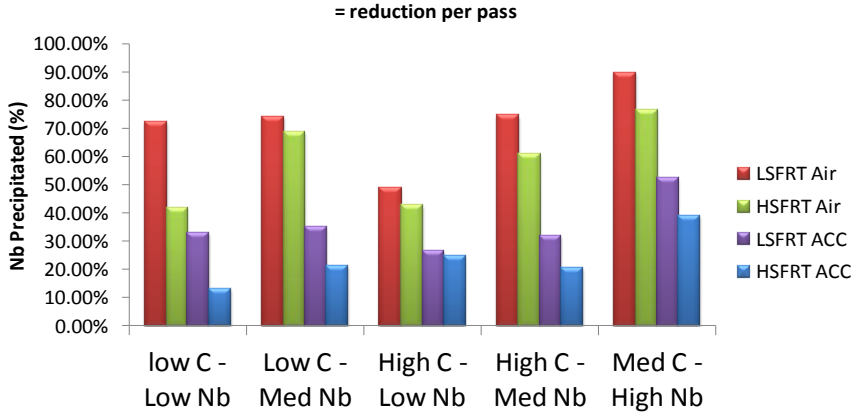

Figure VI.1-13 *Comparison of Nb precipitated as a function of the TMCP schedule and the chemical composition.*

Figure VI.1-12 shows that the best combination of DBTT and YS is obtained for the Med. C-High Nb composition after rolling at low FRT and ACC. The results presented in Chapter V and the findings discussed here suggest that there are two main reasons which account for the capacity of the Med. C – High Nb composition to offer a good balance between the strength and toughness when appropriate TMCP is followed. These are:

(I) The ability to develop a relatively homogeneous microstructure in all the studied TMCP scenarios, which (in the author's opinion) represents the first step in controlling the fracture toughness (assuming that the inclusion content has been previously strictly controlled). as is discussed in Chapters V.3, VI.5, and VI.6.

- A relatively homogeneous microstructure develops, at least in part, owing to the larger fraction of Nb precipitates (see *Figure VI.1-13*) present in this steel compared to those of the other steels. Some of these precipitates prevent the growth of γ grains prior to the γ to α transformation. For the same TMCP schedule, the same relative fraction of Nb should precipitate during finishing rolling (see Chapter V.1 for details) irrespective of the composition. In other words, the measured evolution of precipitates in one steel should be a valid reference for the steels of other compositions.

(II) The high yield strengths obtained at low FRT are correlated with the enhanced precipitation hardening achieved in the low FRT + ACC and low FRT + air cooling TMCP routes (see comparison of % Nb precipitated in the steels with different compositions, *Figure VI.1-13*).

VI.2 Recrystallization – Precipitation interaction

A detailed review of the interactions among deformation, recovery, recrystallization, and precipitation can be found in the doctoral thesis of *Vervynckt [7]*. *Figure VI.2-1* summarizes the effects related to the occurrence (green mark) or non-occurrence of the aforementioned events. The particular implications of recrystallization-precipitation interactions on the TMCP schedules used in the current thesis will also be discussed.

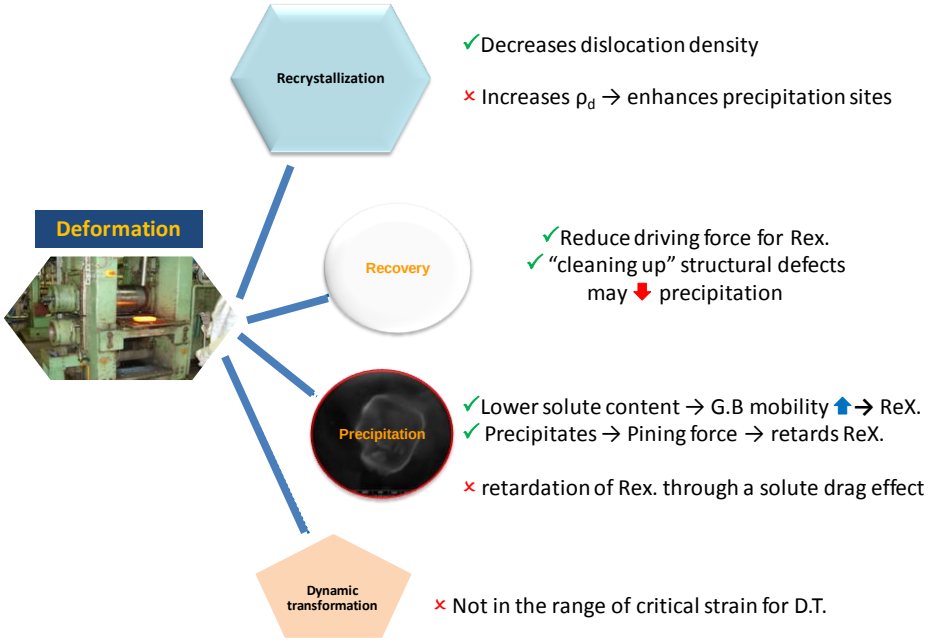

Figure VI.2-1 *Schematic summary of the effects related to the occurrence or non-occurrence of recrystallization, recovery, and precipitation.*

Some important differences are observed when the transformed quenched texture at Q3 (c.f. *Figures V.1-1* and *V.1-21*) is compared with that resulting at the end of a complete TMCP schedule performed with high FRT (i.e. *Figure V.2-33*).

Table VI.2-1 shows a comparison of the φ_2=45° ODF sections along various TMCP routes. From these data, one can see that routes with high FRT combined with either ACC or air cooling, resulted in the highest relative intensity of the {100} ⟨011⟩ component at the final production stage. In contrast, {113}⟨110⟩ and {112}⟨110⟩ transformation components occur

Route	**Q1 at 1180ºC**	**Q3 at 980ºC**	**Final**
high FRT-ACC	**After Roughing**	**After finishing**	**After ACC + coiling**
Nb Precipitated(%)	15	33	39
ODF section at φ_2 = 45°	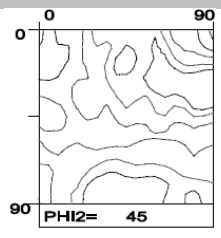	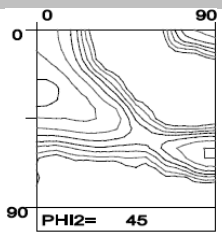	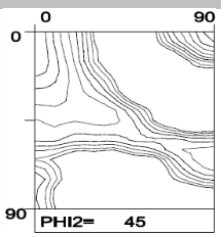
Route	**Q1 at 1180ºC**	**Q4 at 800ºC**	**Final**
low FRT - ACC	**After Roughing**	**After finishing**	**After ACC + coiling**
Nb Precipitated (%)	15	40	52
ODF section at φ_2 = 45°	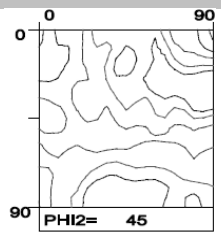	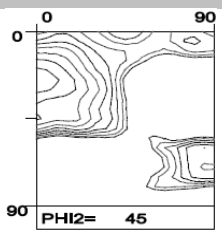	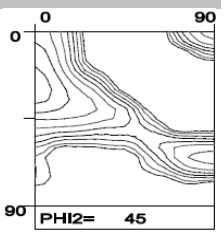
Route	**Q1 at 1180ºC**	**Q3 at 980ºC**	**Final**
high FRT - Air	**After Roughing**	**After finishing**	**After Air Cooling**
Nb Precipitated(%)	15	33	76
ODF section at φ_2 = 45°	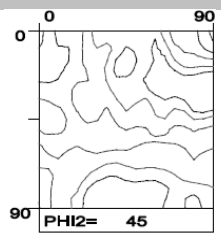	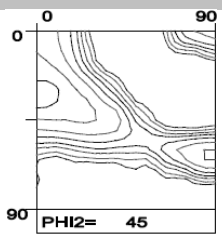	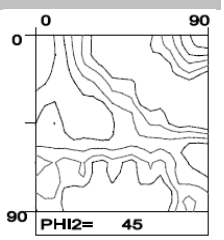
Route	**Q1 at 1180ºC**	**Q4 at 800ºC**	**Final**
low FRT - Air	**After Roughing**	**After finishing**	**After Air cooling**
Nb Precipitated(%)	15	40	90
ODF section at φ_2 = 45°	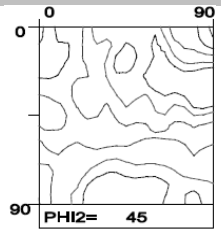	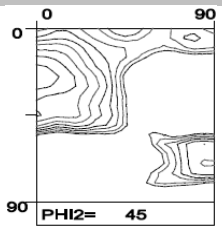	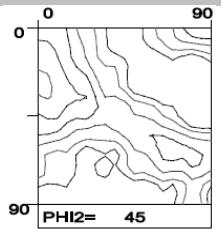

Table VI.2-1 *Nb precipitated at different stages of the TMCP and the corresponding textures in the φ2 = 45° ODF sections. Iso-intensity lines: 0.8x -1x -1.3x -1.6x -2x -2.5x -3.2x -5x -6.4x random.*

with maximum intensities after the routes of low FRT followed by either ACC or air cooling. In addition, compared to final processing routes with low FRT, the intensities of the {113}⟨110⟩ and {112}⟨110⟩ components did not change significantly after Q4. Samples rolled at high FRT (either ACC or air cooling) display, however, a shift of the maximum intensities along the RD fiber towards the {001}<110> rotated cube component.

A possible explanation for this might be that a decrease in the FRT allows a larger amount of niobium to precipitate (see *Table VI.2-1* and *V.1-2*) owing to the expansion of the time-temperature window as lower temperatures are approached. On the other hand, the increase of strain-induced Nb precipitation is also enhanced owing to higher dislocation densities at low rolling temperatures of austenite [8]. The Nb precipitates retard, or even suppress, the recrystallization of austenite, which results in a pancake-type microstructure that consists of a large number of ferrite nucleation sites.

The above observation is confirmed by the strengthening of the so-called deformation fiber that extends from {111}⟨112⟩, {554}<225>, {332}<113>, along {112}<131> to a maximum intensity at the {113}⟨110⟩ and {112}⟨110⟩ transformation components. A number of conclusions can be drawn if *Table VI.2-2* is compared with *Figure VI.1-1*. *Figure VI.1-1* is used as a reference $\varphi 2=45°$ ODF section with border color codes. This figure illustrates, schematically, the well-established understanding [9] for linking the parent γ and product α transformation textures (red border: recrystallized γ; pink border: deformed γ; combined red-pink represents the contribution of both recrystallized and deformed γ).

According to the aforementioned mechanism, the {001}<110 > rotated cube component might be a BCC product orientation that resulted from the parent γ Brass and/or γ Cube components. In other words, the presence of rotated cube might result from two γ states namely, recrystallized and deformed γ.

Furthermore, based on the microstructural observations and on the fractions of Nb precipitated (c.f. *Table VI.2-1*), it appears that in the schedules with low FRT, the presence of {001}<110> rotated cube is mainly a contribution of the parent Brass component. In the case of high FRT, the shift of the maximum intensities along the RD fiber, from {113}⟨110⟩ and {112}⟨110⟩ toward the {001}<110> rotated cube, results possibly from various metallurgical events. Various scenarios, representing these events, were contemplated including recrystallization after finishing rolling at high temperature and recrystallization of certain

components. These scenarios were studied by modeling the texture development for each case (for more details see V.1.4.1 and [10] [11]).

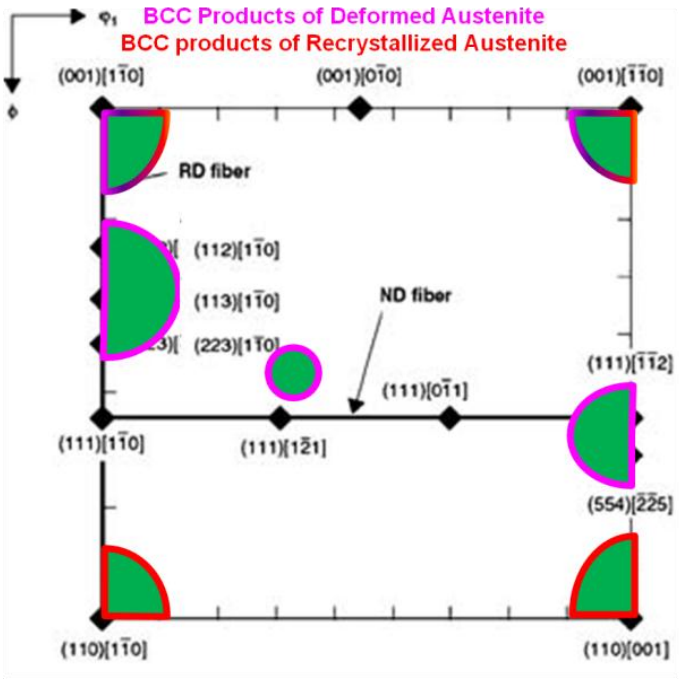

Figure VI.2-2 *Reference φ2=45° ODF section illustrating the parent origin of the transformed textures, adapted from [9].*

Figure VI.2-3 shows the predicted textures at different stages of finishing rolling. The parent austenite was transformed according to the Kurdjumov-Sachs (K-S) transformation pattern and growth of the recrystallized austenite grains was assumed. The initial texture of austenite was assumed to consist mainly of recrystallization texture components (cube) and minor fractions of retained deformation texture components (brass and copper). This assumption appears realistic in light of the measured textures obtained after Q1 where reheated samples were quenched following rough rolling (cf. *Figure V.1-2*). The K-S transformation pattern was simulated by a ±90° crystal rotation of the parent orientations along <112> axes. The grain growth of recrystallized austenite was introduced into the model by assigning higher mobility to those orientations that fulfill the <111> 40° orientation relationship with the deformed matrix [10]. The φ_2=45° ODF section reveals that the measured and predicted textures are reasonably similar although the texture is stronger in the former than in the latter. It is important to bear in mind the occurrence of variant selection in the measured texture, which, in this case, is manifested in the noticeable absence of the Goss component.

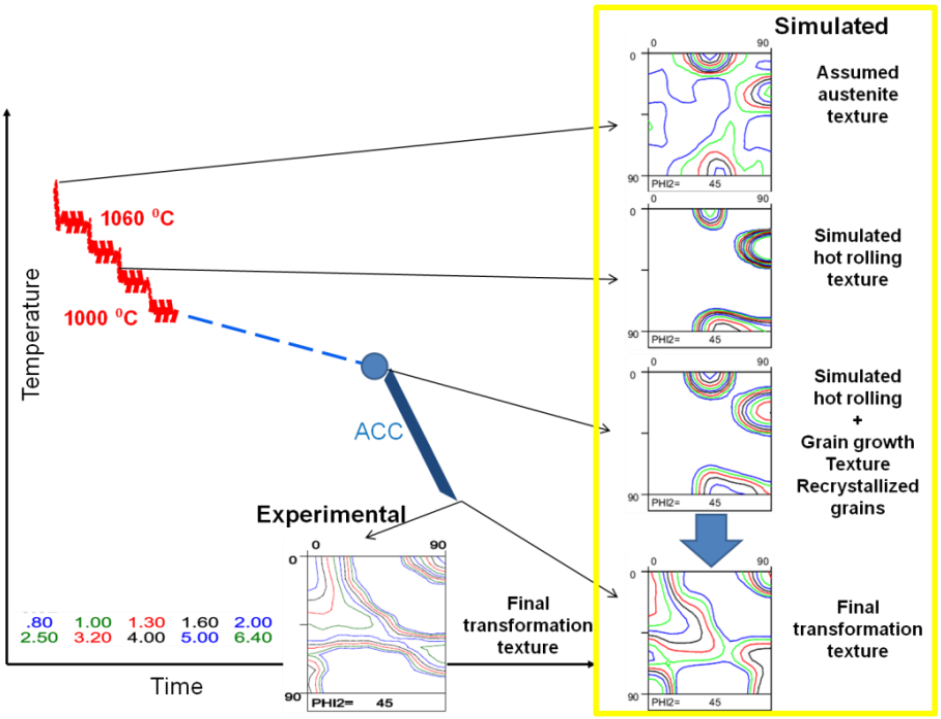

Figure VI.2-3 *Illustration of the calculated textures at various stages of TMCP (high FRT), and comparison between the experimentally measured and calculated transformed textures.*

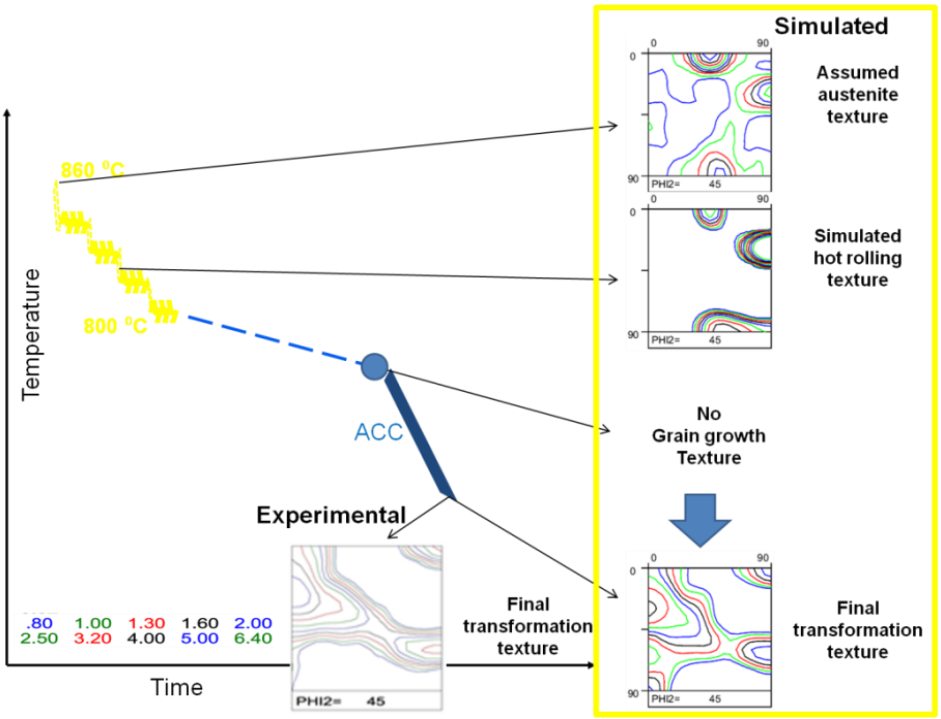

Figure VI.2-4 *Calculated textures at various stages of TMCP (low FRT), and comparison between the experimentally-measured and calculated transformed textures.*

Hutchinson et al. [12] and *Butron-Guillen et al.* [13] investigated the possible reasons for the occurrence of variant selection during the γ to α transformation. The absence of Goss when cube-oriented γ transforms to α has, however, still not been clearly explained. On the other hand, it is interesting to note that the aforementioned shift of maximum intensities along RD has been perfectly reproduced in the predicted texture without any other change in the texture. This result validates, to some extent, the assumed hypothesis. The textures at various stages of finishing rolling at low FRT were also predicted without considering grain growth (*Figure VI.2-44*) and a remarkable resemblance among the measured and simulated textures is observed.

To validate these findings, EBSD scans were made at Q3 and Q4 (c.f. *Figure V.1-1*), and for samples after the completion of TMCP schedules under both high and low FRT conditions. Quantitative analysis of the EBSD data showed that the rotated cube component accounts for 2-2.5% (area fraction) of the grains in the transformation texture at either Q3 or Q4. Furthermore, the fraction of grains which have the rotated cube orientation increased to 11% and approximately 6.5% after completion of the TMCP schedule with high and low FRT, respectively. This result implies that the rotated cube grains grow between the end of finishing rolling and the onset of the γ to α transformation, and, in addition, validates the hypothesis developed using the texture model. The analysis regarding the evolution of Nb precipitated (discussed previously, and included in *Table VI.2-1*) also concurs with these findings.

It must be said that the rest of the evaluated hypotheses presented both qualitative, in terms of the resulting final texture components, and quantitative differences between the modeled and calculated textures.

VI.2.1 Analysis of the recrystallization behavior of γ for Low C – Med. Nb and High C – Low Nb compositions.

Low C – Med. Nb and High C – Low Nb compositions exhibited, albeit unexpectedly, similar texture strengths when the steels were processed following low FRT & ACC; the measured results are shown in *Figure VI.2-5*.

Double deformation tests were also conducted on these steels using a Bähr® DIL 805 plastodilatometer in order to study the γ softening and recrystallization behavior at high temperatures. Details of the experimental method are described in Chapter IV.3.1.6. Owing to

unclear technical limitations (quality of the pushing rods) the "safe" strain rate used to compare hot γ austenite behavior was lowered to $0.05s^{-1}$ and the "safe" minimum temperature at which the double deformation test was carried out was 950°C. Nevertheless, in order to evaluate the extrapolation of the results (see *Figure VI.2-6*), analysis of the strain rate dependence was carried out by calculating the time for 50% recrystallization, using the equation developed by Abad *et al*. [14].

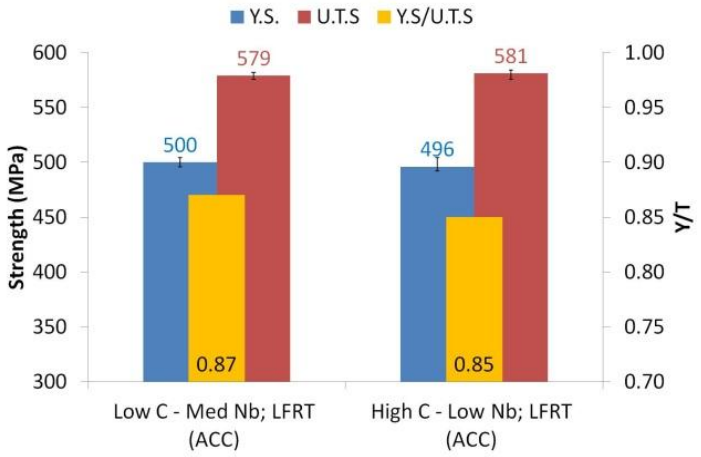

Figure VI.2-5 *Comparison of the texture strengths of Low C – Med. Nb and High C – Low Nb steels processed following low FRT & ACC.*

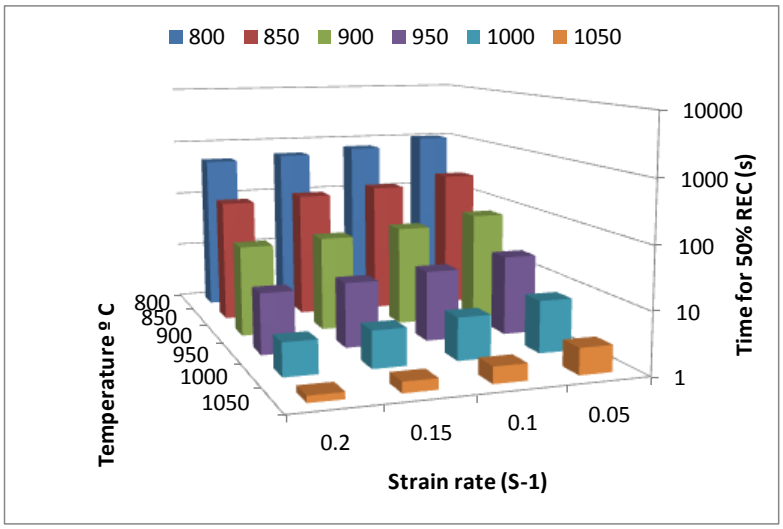

Figure VI.2-6 *Time for 50% recrystallization as a function of temperature and strain rate.*

Figure VI.2-7 shows the representative flow curves obtained during double deformation testing of the Low C – Med. Nb steel at 950°C. At this temperature, softening occurs in about 5000s, owing, possibly, to the small strain rate., Higher strain rates are, as shown in *Figure VI.2-6*, expected to result in shorter times to reach 50% softening. Notwithstanding the absolute values cannot be compared with those of the TMCP, the analysis is still valid

because the double hit test experiments were aimed at comparing the relative behavior of the two compositions.

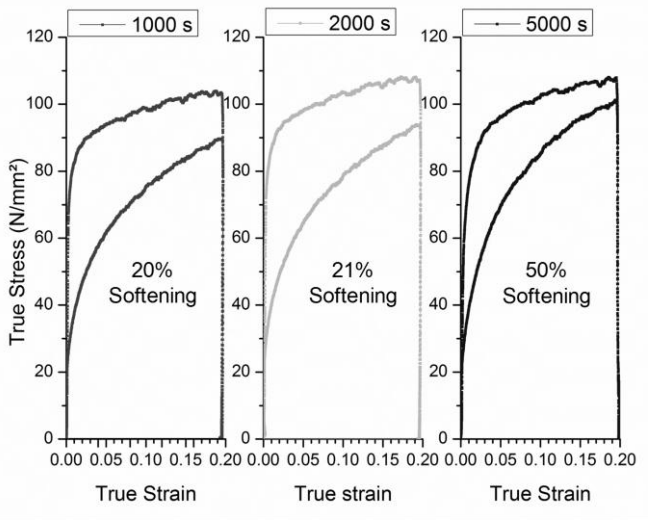

Figure VI.2-7 *Double deformation test flow curves at 950°C with various inter-pass times. Fractional softening, calculated according to the 2% offset method.*

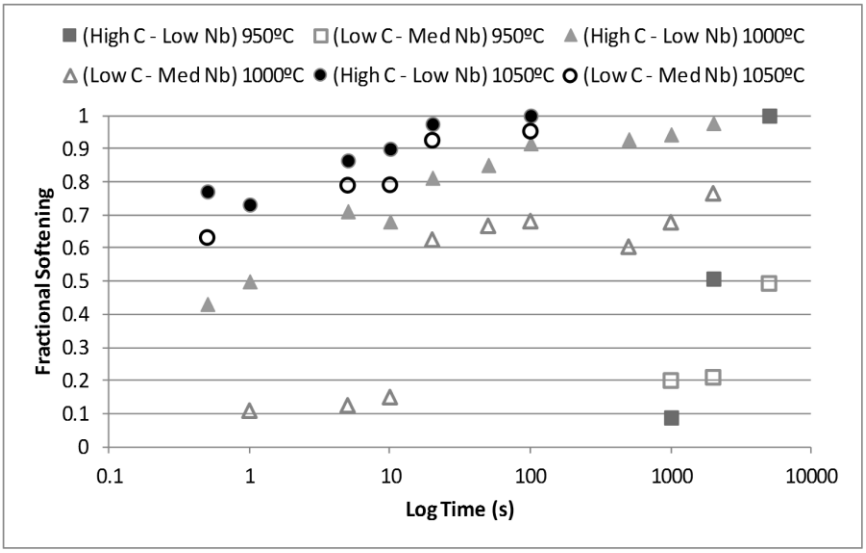

Figure VI.2-8 *Comparison of the fractional softening of the Low C – Med. Nb and High C – Low Nb steels as a function of temperature and inter-pass time.*

Figure VI.2-8 compares the fractional softening for the aforementioned compositions. It is interesting to note that at 1050°C, the softening behavior is identical for the considered materials. Furthermore, at 1000°C, the behavior after 10s is quite similar. This can be explained by the fact that the resulting microstructures (see *Table VI.2-3*) are similar from a quantitative viewpoint. For example, the average grain size was the same (see *Table VI.2-4*) and the KAM map also indicated some similarities in the granular ferritic-bainite

microstructures. All these findings are consistent with the equality in strength of these two steels.

Material	Grain cluster map	KAM map	A. Grain size (5°) (µm)	A. Grain size (15°) (µm)
Low C – Med. Nb Low FRT&ACC	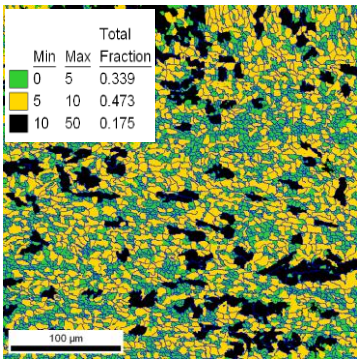	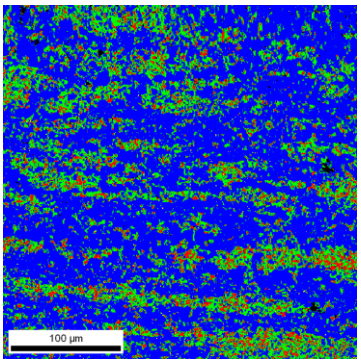	7.2	9.8
High C – Low Nb Low FRT&ACC	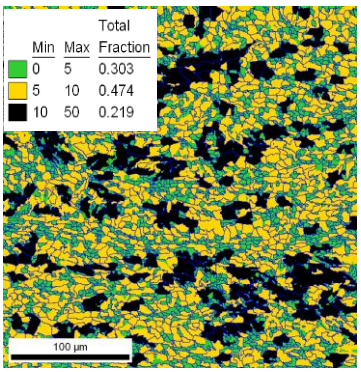	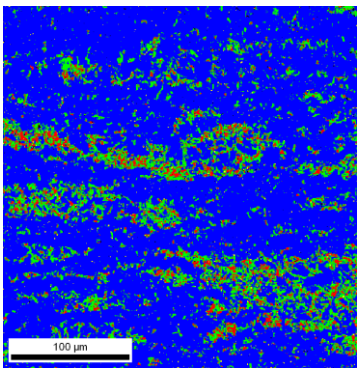	7.4	9.4

Table VI.2-5 *Comparison of the microstructural features in Low FRT&ACC Low C – Med. Nb and High C – Low Nb steels processed with the same TMCP schedule.*

VI.3 Combined effect of deformation temperature and cooling rate

This section of the thesis assesses the analysis of the microstructures that resulted from the combined effect of deformation temperature during finishing rolling and the cooling rate of the TMCP. Firstly, a summarized examination of representative results reported in the literature is presented and secondly, a structured synthesis of the results obtained in the present work is given.

Table VI.3-1 lists the compositions of various HSLA steels; *Table VI.3-2* lists the TMCP parameters (FRT, and cooling conditions), resulting microstructures, and the mechanical properties of the aforementioned steels, which are comparable to those investigated in the present work. These previous studies have reported a variety of microstructures and strengths. The results of the current study are consistent with those studies in which the microstructures

ranged from acicular ferrite + bainitic ferrite + quasi polygonal ferrite to polygonal ferrite + pearlite which resulted from high and low cooling rates, respectively. Moreover, in the case of mixed bainite-ferrite microstructures, the YS alternates between ≈490 and ≈590MPa. In the present study, the YS values of granular bainitic-ferritic steels range from ≈400 to 570MPa.

Steel	C	Si	Mn	Nb+V+Ti	Reference
1	0.075	0.26	1.54	0.095-0.105	[15]
2	0.046	0.26	1.53	0.095-0.105	[15]
3	0.038	0.27	1.77	0.11	[16]
4	0.1	0.01	0.91	0.075	[17]

Table VI.3-1 *Chemical compositions of steels which underwent similar TMCP schedules.*

Steel	FRT (°C)	Finish cooling temperature (°C)	Cooling rate (°C/s)	Microstructure	YS (MPa)	UTS (MPa)	Ref.
1	840	580	12	$\alpha_A + \alpha_{qp}$	540	706	[15]
1	840	480	14	$\alpha_A + \alpha_{qp}$	568	694	[15]
1	840	430	9	$\alpha_A + \alpha_{qp}$	526	733	[15]
1	840	340	16	$\alpha_A + \alpha_B\ \alpha_{qp}$	533	747	[15]
1	840	200	19	$\alpha_A + \alpha_B\ \alpha_{qp}$	527	745	[15]
1	840	100	16	$\alpha_A + \alpha_B\ \alpha_{qp}$	519	757	[15]
2	840	580	8	α_{qp}, $\alpha_p + \alpha_A$	495	650	[15]
2	840	480	10	α_{qp}, $\alpha_p + \alpha_A$	515	644	[15]
2	840	430	10	$\alpha_A + \alpha_{qp}$	486	658	[15]
2	840	100	12	$\alpha_A + \alpha_{qp}$	493	681	[15]
3	777	580	13	$\alpha_{qp} + \alpha_A$	580	725	[16]
4	860		0.5	PF+P			[17]

Table VI.3-2 *Summary of the literature review of representative TMCP parameters and the resulting properties/microstructures.*

The description of the microstructures based on optical and scanning electron microscopy can be supplemented with a more accurate evaluation. It was pointed out by *Gourgues et al.* [18] and *Zajac et al.* [19] that the misorientation angle distribution histograms are a powerful tool by which microstructures can be examined. *Figure VI.3-1* summarizes some of the outcomes of their study. In that study, the morphology of the observed microstructures could be identified by the use of theoretical and experimental misorientation histograms.

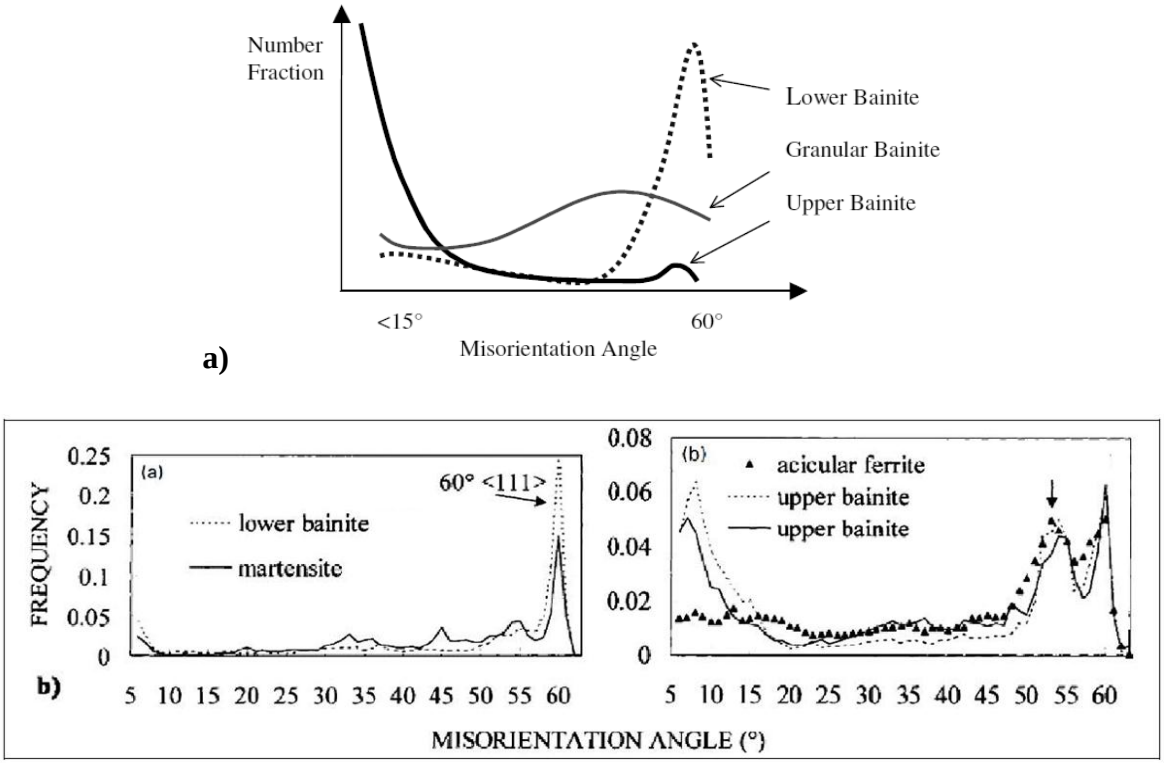

Figure VI.3-1 *a) Definition of bainite based on distribution of misorientation angles [19]; b) Histograms of experimental angle distributions and their correspondence with a particular type of microstructure [18].*

The approach proposed by *Gourgues et al.* [18] was used in the European project "Microstructural quantification of multi-phase steels (Micro-quant)"[20]. In an attempt to identify the microstructures developed after certain TMCP schedules, the above-mentioned approach was also employed in the present work. *Figure VI.3-2* compares the experimentally-determined misorientation angle distributions grouped according to the TMCP schedule. It is apparent from *Figure VI.3-2*, that materials which underwent the same TMCP have, in general, similar histograms. Furthermore, to a certain extent, one could identify the TMCP employed just by looking at the misorientation histogram.

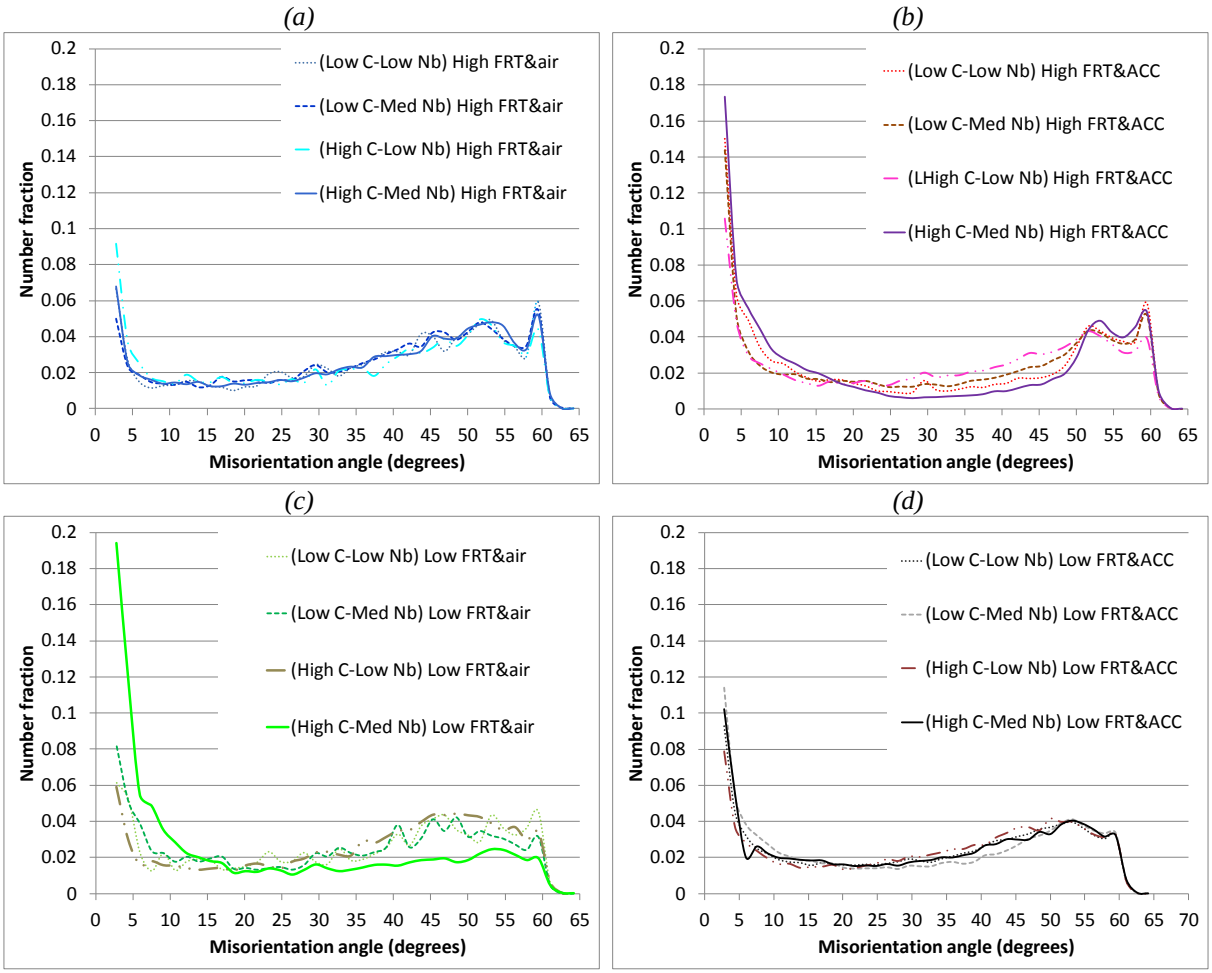

Figure VI.3-2 *Experimentally-determined misorientation angle distributions grouped according to the followed TMCP route.*

Numerous low misorientation angles were found in schedules with ACC (charts on the right). Their presence was particularly noticeable at high FRT & ACC schedules, but, with number fractions lower than 0.08, occur far less frequently in most of the air-cooled steels (see *Figure VI.3-2*(a), (c)). The single deviation observed was that of the High C- Med. Nb composition with low FRT & air cooling TMCP schedule; no clear reason was found to explain this behaviour. Interestingly, high FRT schedules exhibited a marked peak for misorientation angles lying between 59° and 60°. A less marked peak between 48° and 53° was also characteristic of the high FRT schedules. The histograms of the low FRTs exhibited, in contrast, a rather broad plateau of high misorientation angles between 47° and 60° instead of significantly sharp peaks. If the current results are compared with those of *Gourgues et al.* [18] and *Zajac et al.* [19], then the misorientation histograms after ACC match those identified for upper bainite and granular bainite. This finding corroborates our earlier observations (OM, SEM, TEM) of granular bainitic-ferrite microstructures in the samples processed with ACC.

In summary, it has been shown that combinations of deformation, temperature, and cooling rate introduce a range of microstructures, which could be identified by misorientation histograms. Although common TMCP schedules resulted in different mechanical properties when various compositions were compared, it has been shown that the nature of the corresponding microstructures remain the same and can be identified by the aforementioned misorientation histograms.

VI.4 Interpretation of the synergies between different strengthening mechanisms

The strengthening mechanisms which lead to an increase in the resistance to plastic deformation, by means of blocking dislocation motion, were reviewed in Chapter II.7.

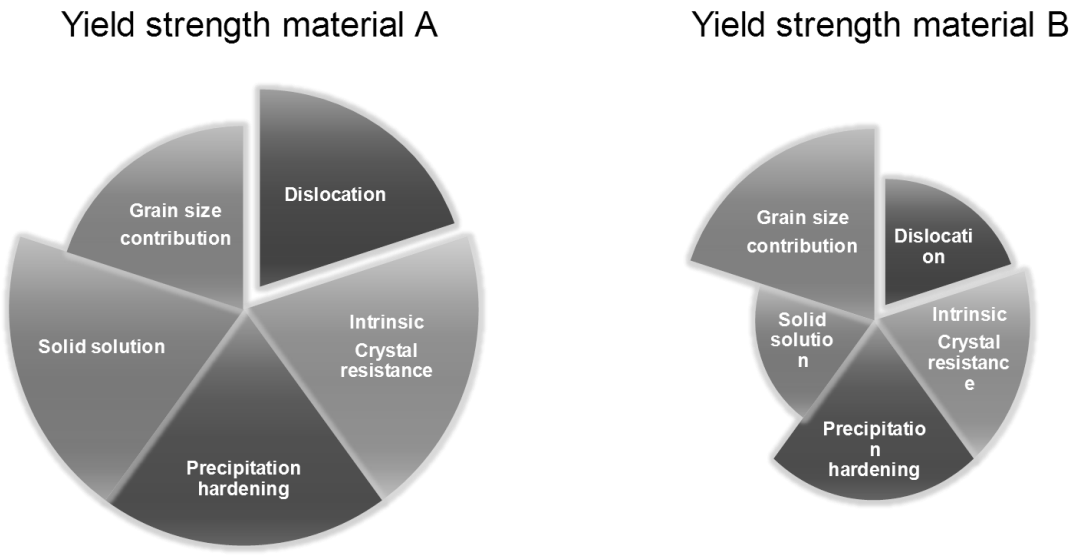

Figure VI.4-1 *Schematic illustration of the contribution of possible strengthening mechanisms to the YS.*

Similarly, various strengthening mechanisms in HSLA pipeline steels, produced under different TMCP parameters, were quantitatively analyzed in Chapter V.4. So far, this work has contributed to the existing knowledge by providing an understanding of the qualitative relationships between strength and microstructure. This was achieved by determining the contribution of each strengthening mechanism to the global yield strength (see *Figure VI.4-1*), for a given material "A" (produced under a known TMCP schedule) and comparing these contributions to those of material "B" that was produced under an alternative TMCP route.

To complete the work, predicted yield strengths, based on microstructural features, will be discussed and compared with the experimentally-determined values of the TMCP HSLA processed steels. As *Gray and Siciliano* [21] stated, from the early 70s onwards, our understanding of the strengthening mechanisms operating in micro-alloyed steel has increased. The work presented here represents one more step toward understanding the individual contributions to the total strength.

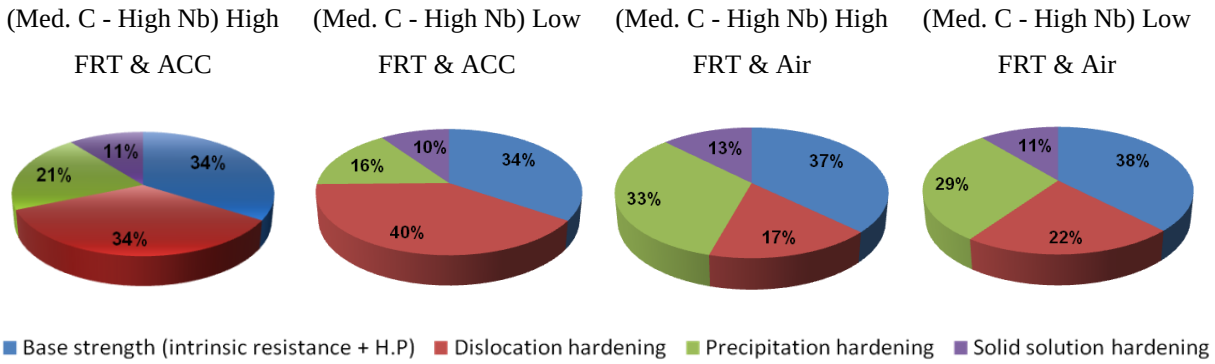

Table VI.4-1 *Contribution to the total strength of the following strengthening mechanisms: (blue) base strength (intrinsic resistance + Hall -Petch contribution); (red) dislocation hardening; (green) precipitation hardening; (purple) solid solution hardening.*

Table VI.4-1 illustrates the contribution of each strengthening mechanism as a function of the TMCP schedule. The studied TPCPs followed equal reduction per pass. Details about the quantification are included in Chapter V.4. *Table VI.4-1* reveals that, for both high and low FRTs, the contribution of dislocation hardening to the yield strength in the steels which underwent ACC is almost twice that of their air-cooled counterparts. This is consistent with the fact that compared to air cooling, ACC resulted in lower transformation temperature products (granular bainitic ferrite) which contain a high density of dislocations. In addition, the contribution of precipitation hardening to the total YS was limited to 20% and 30% in the steels which underwent ACC and air cooling, respectively. Interestingly, there was no significant difference between the schedules, as it relates to the contribution of grain size strengthening, which was about 34% for ACC and around 38% of the total YS when air cooling was applied.

Several authors [22, 23] posit a simple summation law of the strengthening contributions. However, Koppenaal [24] and then Irvine, Kocks, and Majta [25-27] obtained a better agreement between the calculated and experimental results by using a root mean square (r.m.s) summation. The r.m.s is preferred to simple summation since it results in a lower quantification error when two microstructural obstacles of the same order of magnitude are

measured. A thorough explanation of the theory of obstacle-controlled yield strength can be found in [27].

The aforementioned works express the yield stress as the sum of two terms. In [28], the first term groups together matrix (solid solution, precipitation, intrinsic lattice friction) and grain boundary strengthening and the second term considers only dislocation strengthening. *Charleux et al.* [29] proposed other types and numbers of arrangements. The current study follows the approach described in [28] where the dislocation density accounts for a larger contribution to strengthening, compared to precipitation hardening. When the density of precipitates is higher than that of dislocations, the second term of the r.m.s is modified to account only for precipitation strengthening. The volume fraction of second phase constituents is too low to significantly contribute to the strength. Consequently, the yield strength of the steel plate can be expressed as:

$$\sigma_T = \sqrt{\left(\sigma_Y + \sigma_p + \sigma_{ss}\right)^2 + {\sigma_d}^2} \qquad \textbf{VI.4-1}$$

where σ_y, σ_p, σ_{ss}, and σ_d are the strengthening contributions associated with the grain size, precipitation, solid solution, and dislocations, respectively.

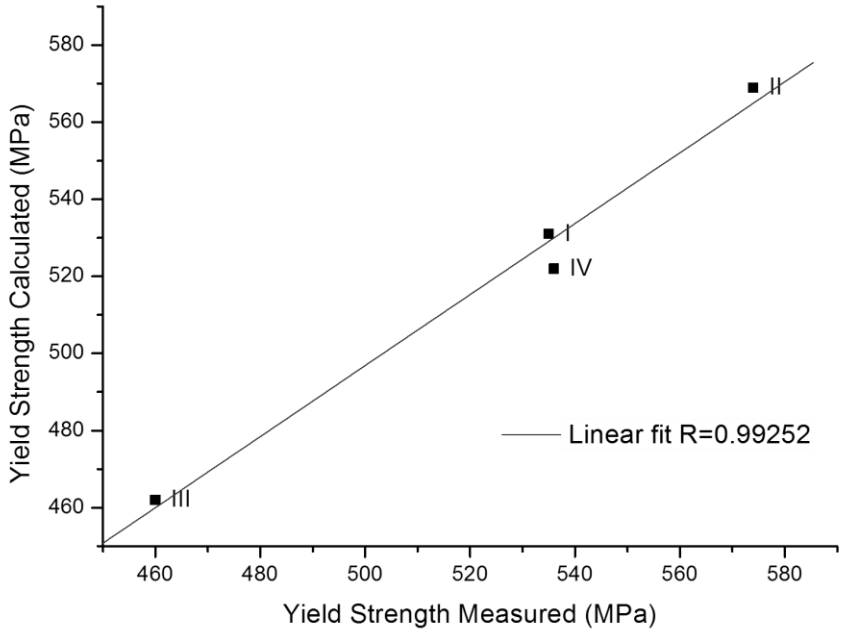

Figure VI.4-2 *Comparison of the calculated and measured YS of the reference schedules with different FRT and cooling condition.*

Samples produced under the four reference schedules were fully characterized in order to measure the contributions of grain size, precipitation, solid solution, and dislocations to the YS. Therefore, the strengthening mechanisms were neither taken from the literature nor calculated as the difference between the experimentally- measured YS and the addition of other strengthening contributions. The calculated and measured values (*Figure VI.4-2*) show respectable agreement.

The model was validated by analyzing four new compositions (see Chapter IV.1) that were processed with constant reduction draught and varying FRT and cooling conditions. A total of 16 new materials were characterized. However, owing to time constraints, the dislocation density in these new materials could not be measured and, therefore, the reference values, which were measured after each TMCP schedule (see *Figure V.4-5*), were used instead. Compared to conventional practice of assuming a fixed dislocation density, these values should better represent the real dislocation density of the various materials.

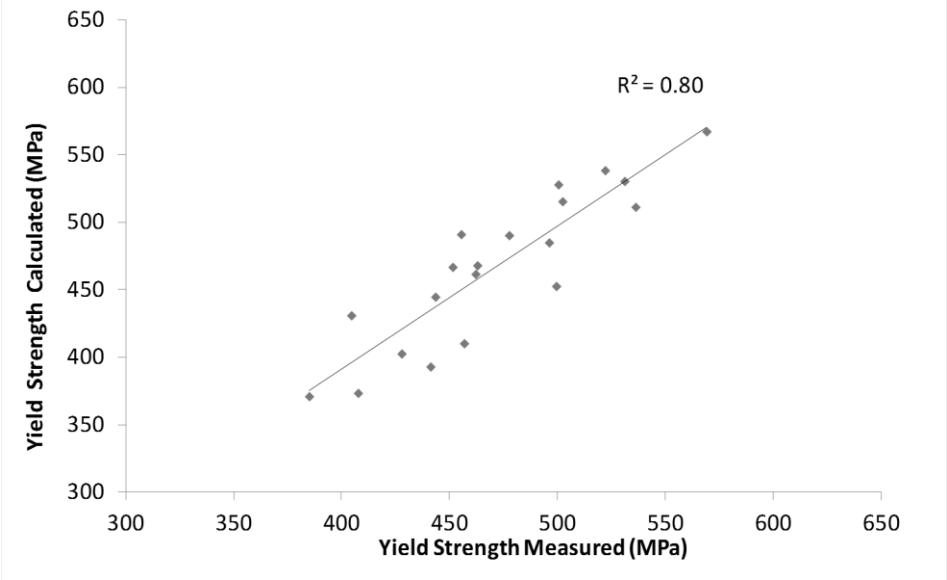

Figure VI.4-3 *Comparison of the calculated and measured YS values when TMCP parameters are changed (five chemical compositions were studied).*

Figure VI.4-3 plots the calculated YS values as a function of their experimentally-measured counterparts. The results are significant in at least two major respects. Firstly, the values predicted by the individual strengthening models and the r.m.s approach match those measured experimentally. Secondly, having the ability to predict the YS of HSLA steels, which have various chemical compositions and different types of microstructures (i.e. bainitic ferrite and polygonal ferrite-pearlite microstructures), is invaluable. It was previously reported

[30] that the FRT has a strong impact on the strength of HSLA steels, but the detailed understanding of the preferred strengthening mechanisms, garnered by varying the FRT or cooling route, provides comprehensive and interesting insight into the industrial processing of pipeline steels.

VI.5 Description of the new proposed variables (combination of: large grain size cluster distribution, low aspect ratio, rotated cube-textured grains) governing fracture resistance in HSLA pipeline steels.

As explained in Chapter II, in the field of the pipeline infrastructures, an increased efficiency could be obtained by using high strength long distance steel line pipes with good weldability, excellent corrosion resistance and without compromising toughness [8, 31-33]. Maintaining suitable toughness values, with the simultaneous improvement of other properties, is one of the major concerns among pipeline energy operators and steel makers, that was emphasized during the last Pipeline Technology Conference (held in 2013) hosted in Ostend. The control of ductile fracture propagation has also been a major area of concern.

Commercialization of pipes made from the X80, X100, and X120 grades (based on ISO3183

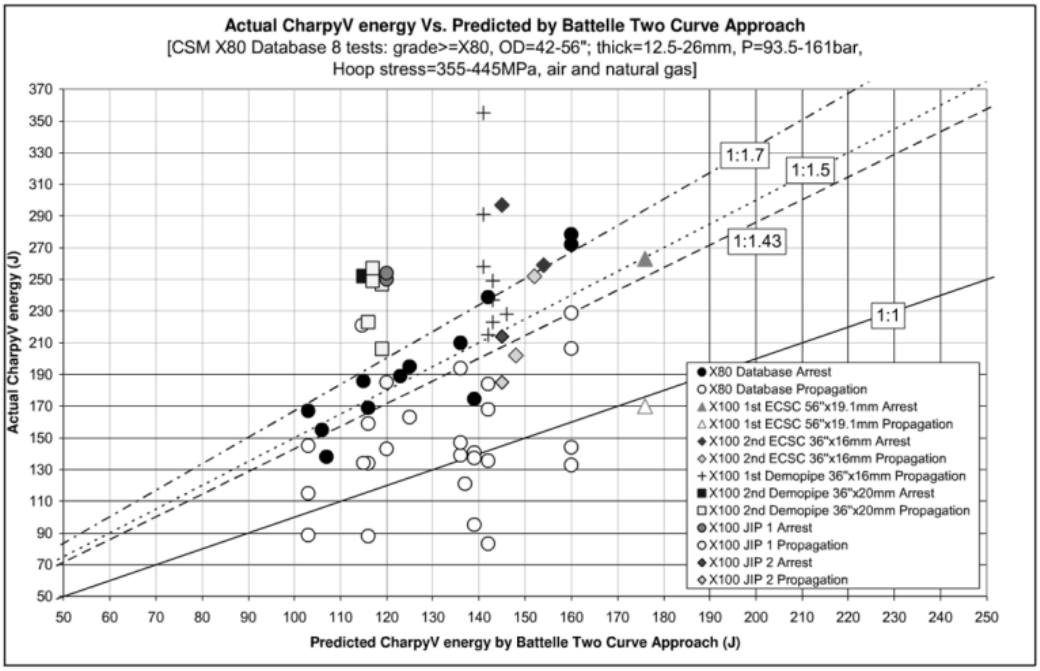

Figure VI.5-1 *Actual vs. predicted CVN energies by BTCM for X-80 and X-100 HSLA grades [34].*

and API 5L specifications) has begun as a result of the need for increasing flow rates. However, when new steel grades are tested, the existing methods which are used to predict the arrest of a running ductile fracture (i.e. Battelle two curve method (BTCM)) fail to resolve [34-36] the correlation between the toughness expressed by the Charpy absorbed energy and the full scale burst test. Recent work (see *Figure VI.5-1* [34]) has repeatedly shown that there is a discrepancy between the predicted values for crack arrest and the experimental results of the full scale burst test. As *Figure VI.5-1* shows, the toughness of materials with absorbed energies higher than 100 J are incorrectly predicted by the BTCM and the successive correction factors. Moreover, full-scale experiments on X-80 and X-100 grades, revealed a non-linear relationship between the Charpy USE and the ductile propagation resistance. These facts reveal the need for a complete (from the "old" to the "new" pipeline steel grades) metallurgical understanding of the features which control ductile crack propagation, since other approaches (such as correction factors to the prevailing analytical equations) are nothing but patches for each particular steel grade. Therefore, a methodology was developed in order to assess the understanding of the microstructural features which govern fracture resistance in general, and separation or splitting behavior in particular. This methodology can be described by defining two parameters, namely the Morphology Clustering (MC) and the Cleavage Morphology Clustering (CMC) parameters. These parameters are defined in a series of steps which are explained below.

Full scale burst tests were performed with several pipeline steels within the framework of a collaboration with the Russian Research Institute for the Tube and Pipe Industries [37]. Splitting or separation of the fracture surface was observed in the steels that failed during testing. *Figure VI.5-2* shows an area adjacent to a split (colored green) and the surrounding microstructure. Rotated cube, {001}<110> crystallographic orientation, grains are colored red.

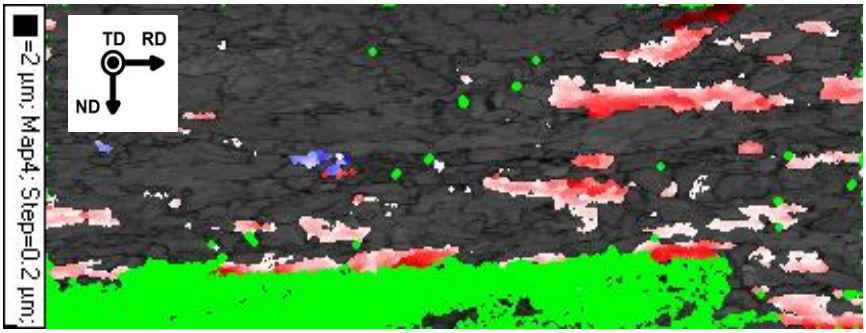

Figure VI.5-2 *Picture showing an area adjacent to a split (colored green). Rotated cube {001}<110> crystallographic orientations are colored red.*

The figure is quite revealing in several ways. First, the split seems to develop along elongated

grains. Second, many of the elongated grains which neighbor or pass through the split have a rotated cube orientation. The objective of the current research was to determine whether the aforementioned microstructural features play a role in fracture propagation.

The initial step in defining the MC or CMC parameters consisted of quantifying the fraction of large grains present in previously constructed grain size cluster maps (see Chapter V.2.2.3). Grain cluster maps are colored plots which show areas with different grain size ranges. For example, *Figure VI.5-3* displays a portion of the through-thickness microstructure of one of the processed steels. Here, green, orange, and black grains have equivalent diameters of up to 5µm, between 5 and 10 µm, and larger than 10µm, respectively.

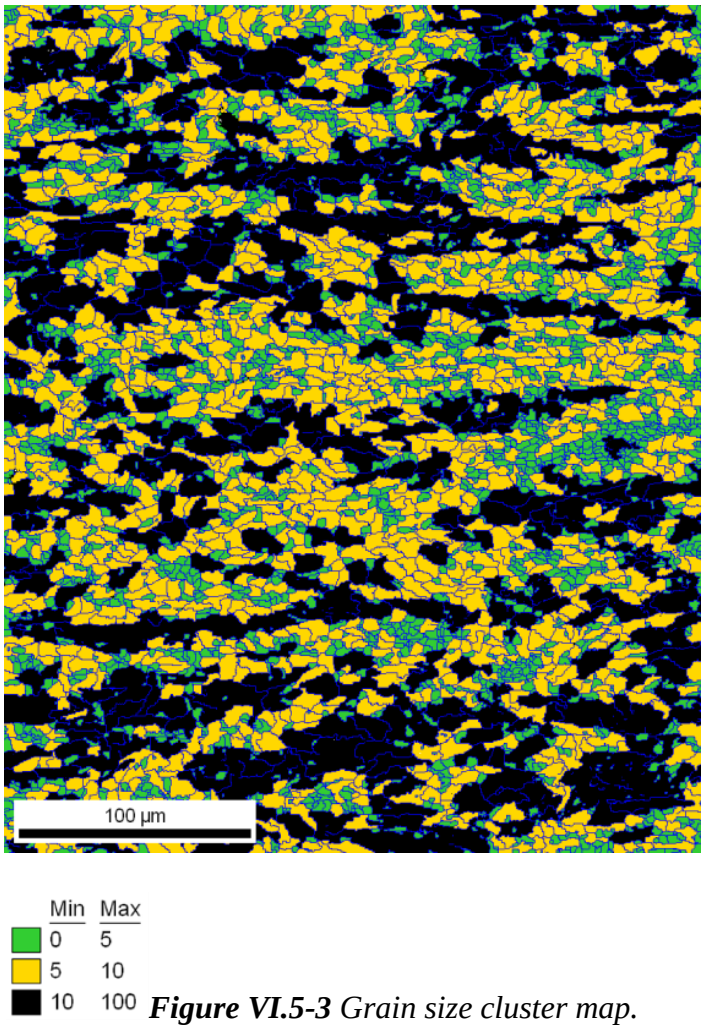

Figure VI.5-3 *Grain size cluster map.*

The criteria defining the cutoff value of large equivalent diameter grain sizes were based on statistical analysis. *Figure VI.5-4* plots the DBTT as a function of the area fraction of grains which fall into certain size classes (each steel is represented three times in the chart, same DBTT but various area fractions). *Table VI.5-1* shows the summary of the statistical regression analysis performed for each case. The adjusted R square value is ~0.7 (i.e. 70%) for grains larger than 10µm. This means that the change in the DBTT can be attributed mainly to the variation in the area fraction of grains with sizes larger than 10µm. Moreover, as the table shows, with a probability of <0.0007, the random occurrence of such a correlation is highly unlikely.

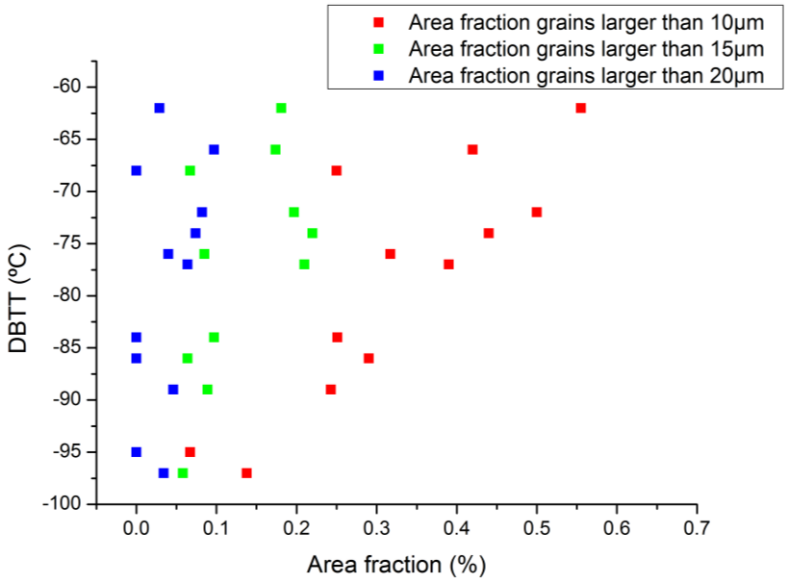

Figure VI.5-4 *Correlation between the DBTT and the cut-off criteria for larger grain sizes.*

Criteria	Adj. R^2	Prob. Null Hypoth.
Grains larger than 10µm	0.67	<0.0007
Grains larger than 15µm	0.40	<0.01
Grains larger than 20µm	0.09	<0.18

Table VI.5-1 *Summary of the statistical regression analysis considering the correlation between the DBTT and the area fraction of grains larger than a given value.*

Figure VI.5-5(a) shows a partition of *Figure VI.5-3* that contains only grains which are larger than 10µm. The succeeding analysis will only take into account those grains shown in *Figure VI.5-5*. Interestingly, a large number of the elongated grains contains a significant population of LAGB (shown as red lines in *Figure VI.5-5*(b)). These grains were identified as granular bainitic regions.

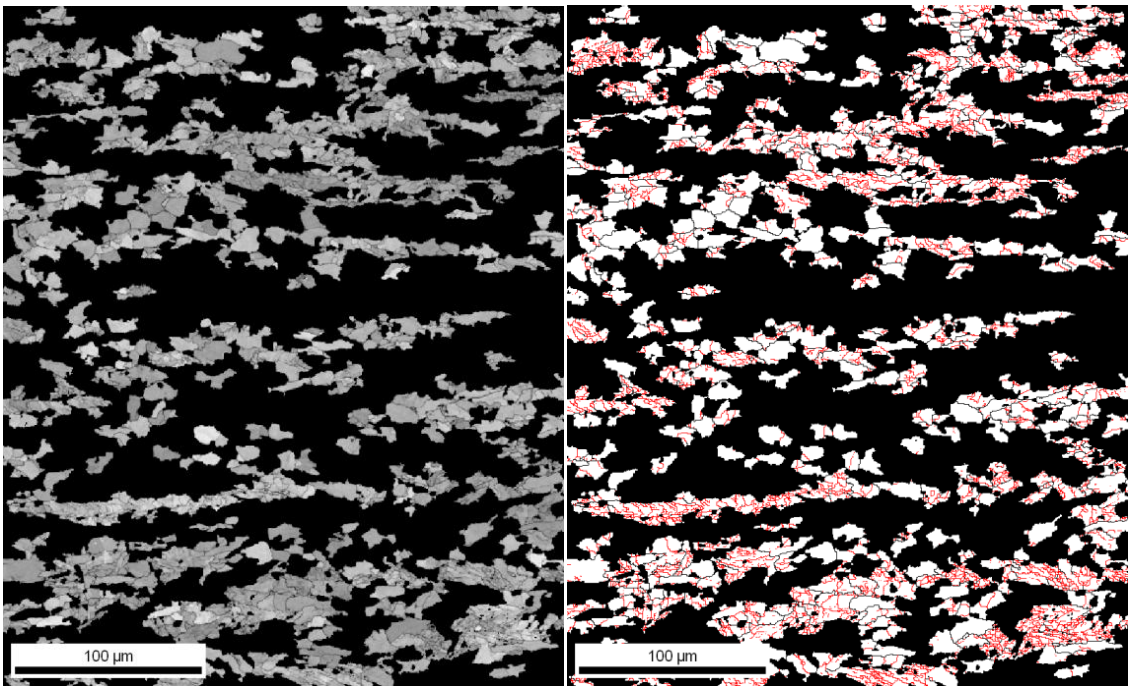

Figure VI.5-5 *(a) IQ map of the partition with grains larger than 10µm. (b) Grain boundary map of the aforementioned partition.*

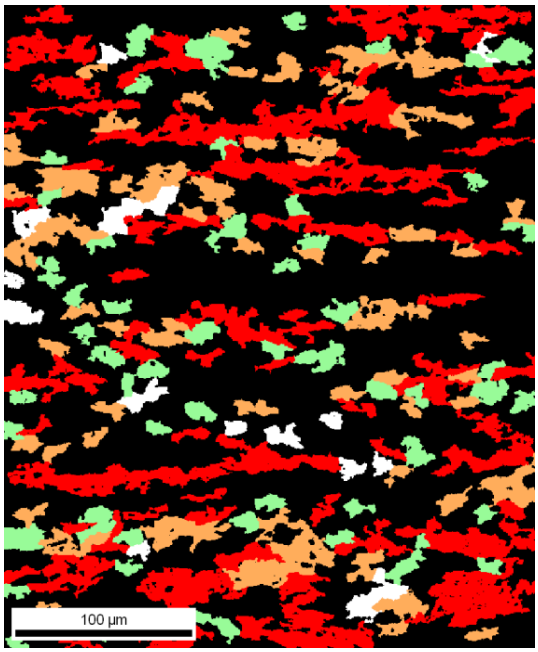

Figure VI.5-6 *Grain size aspect ratio map of the partition containing grains larger than 10µm.*

The final step in defining the MC parameter consists of quantifying the area fraction of grains with low aspect ratios; i.e., grains with a very elongated shape. *Figure VI.5-6* shows the large grains, previously presented in *Figure VI.5-5*, colored according to their respective aspect ratios. Four aspect ratio ranges are displayed, in white: grains with an ellipse axis ratio between 0.5 and 1, in red: heavily elongated grains with a ratio lower than 0.3, and in orange and green: regions comprised of intermediate (between heavily elongated and almost circumferential) grain shapes. The area fractions of grains with aspect ratio below 0.3 were determined for use in the MC and CMC analysis.

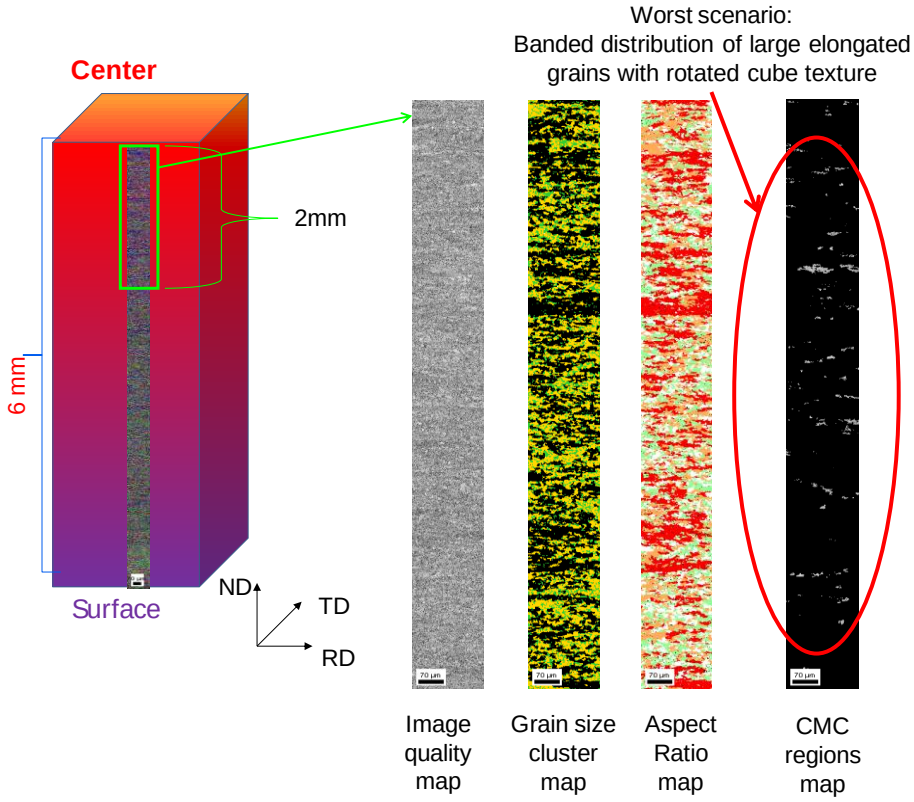

Figure VI.5-7 *Illustration of the steps needed to identify the CMC parameter.*

The CMC parameter was fully defined with the completion of an additional step, which consists of quantifying the fraction of heavily elongated rotated cube grains. Although the scanned areas were very large, at least by the standards of EBSD, post-processing of the data revealed that the covered regions for the regular scans, measured with the FEI Nova 600 Nanolab Dual-Beam equipment, were too small [38] to perform a statistically significant analysis of the texture. Nevertheless, a few materials were characterized by means of through-thickness scans, which, as shown in *Figure VI.5-7*, provide clear insight into the CMC parameter. This figure summarizes the concept of the CMC parameter, that accounts for the fraction of the grain size clusters that is composed of heavily elongated, rotated cube grains. This parameter also accounts for the relative distribution of these grains. CMC regions which consist of spatially banded rotated cube grains (as marked in *Figure VI.5-12*), offer a potentially easy path for the propagation of cracks.

An attempt was made to establish a qualitative relationship between metallurgical-microstructural features and the crack arrest behavior in pipeline steels. This was done by examining the crack propagation primarily in the ductile to brittle transition region of two high strength low alloy pipeline steels (with identical chemical composition) after different TMCP. These steels, as shown in the optical micrographs in *Figure VI.5-8*, have similar bainitic ferrite microstructures. Furthermore, the corresponding average grain sizes were determined by means of EBSD.

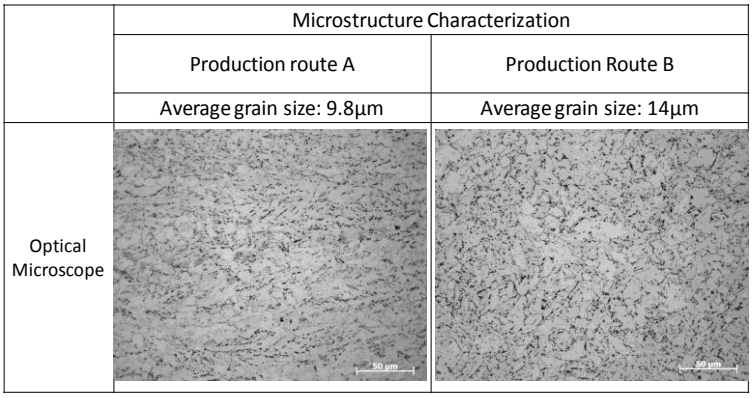

Figure VI.5-8 *Representative optical micrographs of the studied steels.*

A priori (c.f. *Figure VI.5-8*), there was no significant qualitative difference between the microstructures of the two steels. However, significant differences were found when the

impact fracture toughness was evaluated by means of the: *(i)* instrumented Charpy impact testing in the range of 20 to -100ºC and *(ii)* analysis of the fracture surface. In addition to the

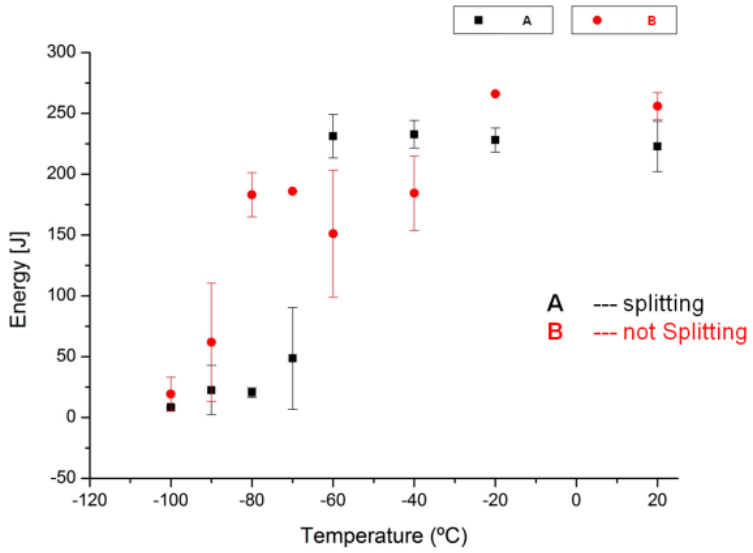

Figure VI.5-9 *Energy absorbed during Instrumented Charpy impact testing at different temperatures.*

differences in the DBTT, steel (A) developed splitting while the other (steel B) did not (see *Figure VI.5-10* and *Figure VI.5-11*). The results were correlated with microstructural characterization of the steel via the EBSD technique and the CMC approach (see the through thickness scans in *Figure VI.5-10*). Band-like clusters, predominately in the middle thickness of the sample, and homogeneously distributed clusters were observed in materials A and B, respectively. In addition, steel A consisted of a high density of elongated (low aspect ratio) grains, which comprised the banded microstructure. These grains were, however, not observed in steel B (see *Figure VI.5-11*).

Figure VI.5-12 compares the CMC regions (detail of the central region) for both materials. This figure illustrates, for both steels, the difference (in grey) in the energy absorbed during crack propagation.

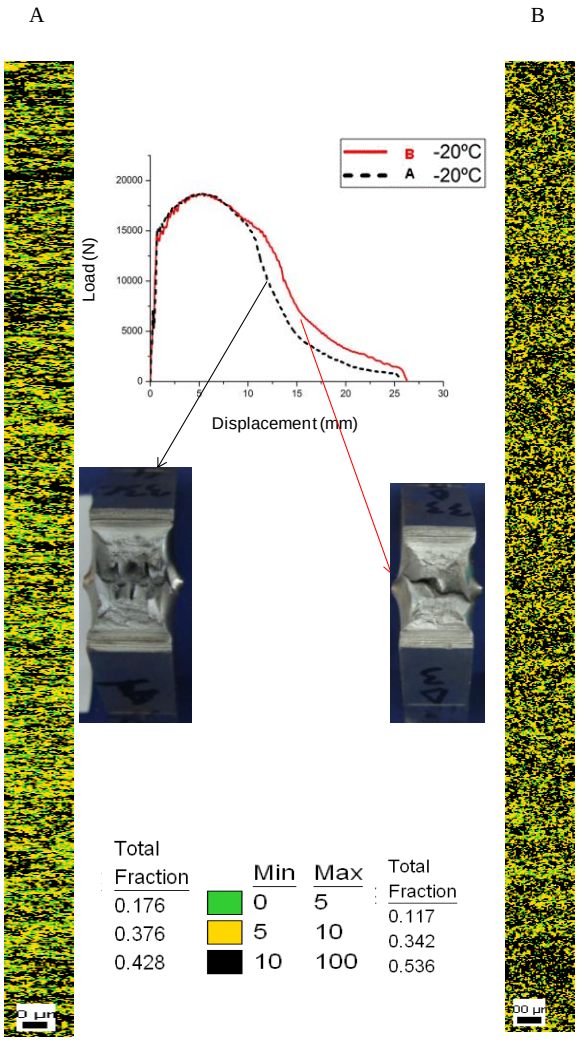

Figure VI.5-10 *Comparison of through-thickness grain size cluster map correlated with Charpy fracture appearance and load displacement curves at -20ºC. Scale bars for A and B read 70µm and 100µm, respectively.*

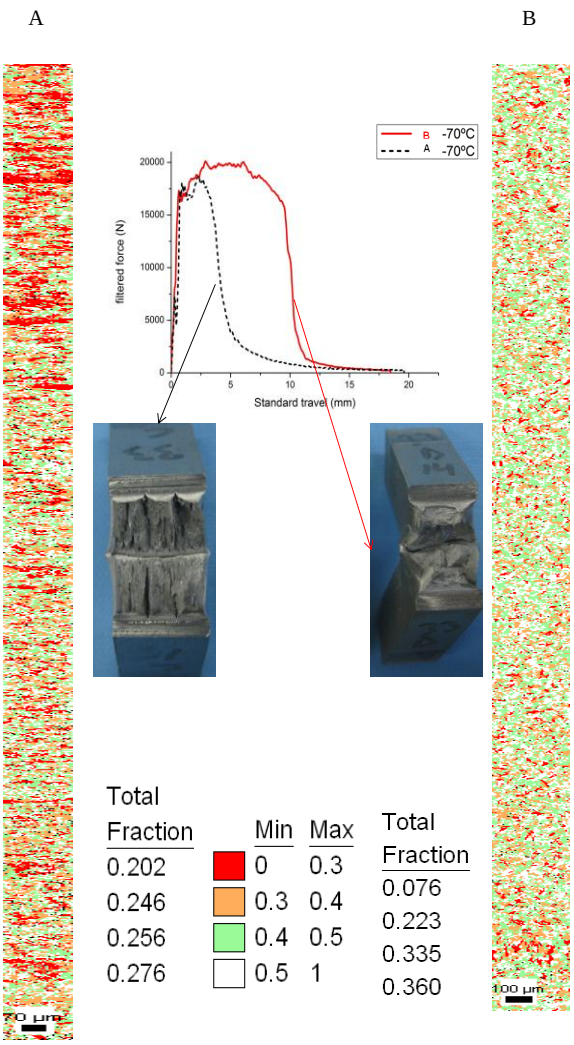

Figure VI.5-11 *Comparison of through-thickness aspect ratio map correlated with Charpy fracture appearance and load displacement curves at -70ºC.*

The load displacement curves are correlated to details (for e.g. partition IQ maps) of the central regions of the steels. These maps display the large grain size cluster distribution, low aspect ratio, and the rotated cube textured grains. High and low CMC clustering lead to lower and higher energy absorption during crack propagation in steels A and B, respectively. These results indicate that the occurrence of splitting, can be reasonably correlated with the Cleavage Morphology Clustering (CMC) parameter. Furthermore, these findings show excellent agreement with those reported for an industrial grade after full-scale burst tests [37]. *Figure VI.5-13* shows the microstructure of a steel that did not pass the full-scale burst tests. A large fraction of CMC regions is clearly visible in this microstructure (clusters of large and elongated {001}<110> rotated cube grains are colored in red).

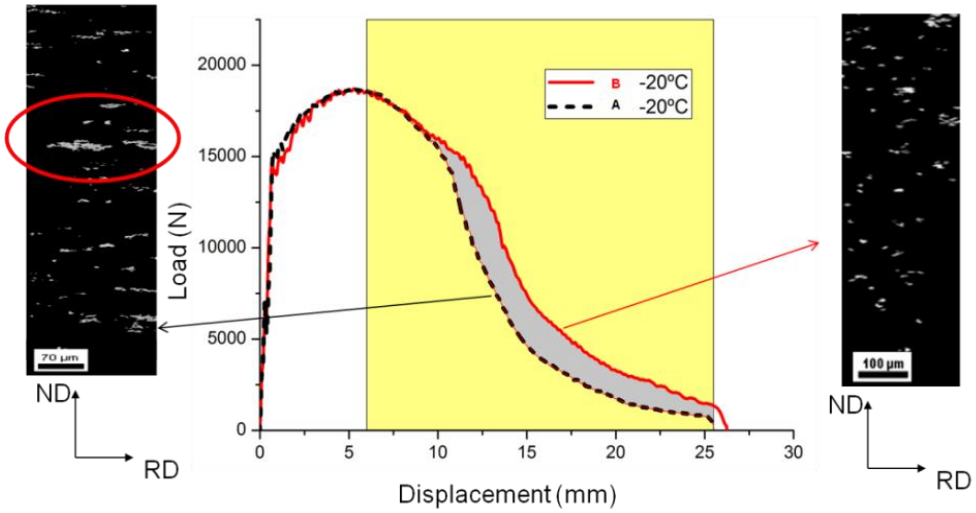

Figure VI.5-12 *Illustration of the difference in the energy absorbed during the crack propagation stage of steels A and B. The load displacement curves are correlated to the microstructural features which govern the crack propagation (e.g. fraction of CMC parameter).*

It was explained in Chapter II.8 that there are two main hypotheses which describe the origin and development of splitting. The present findings support the premise that the occurrence of delamination results from both texture and microstructure (distribution, shape, and size of the grains) anisotropy. The validity of the approach was verified by performing statistical analysis, with the help of the specialized software for Analysis Of Variance (ANOVA), on materials produced within the frame of the PhD project. Owing to area constraints, only the MC parameter was quantified in the remaining materials.

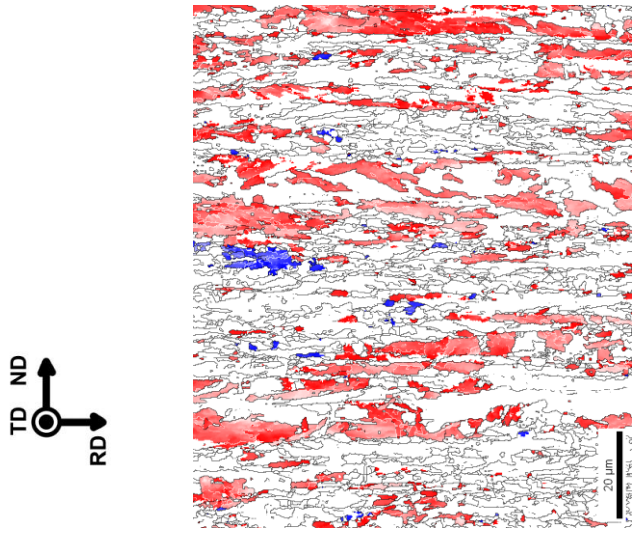

Figure VI.5-13 *Microstructure of a steel that did not pass the full-scale burst tests [37].*

The EBSD scans were from ¼ of the plate thickness, which exhibits less clear trends than those of the central region. However, there is a clear correlation between the fraction of the MC parameter and the DBTT (see *Figure VI.5-14*). A noticeable Pearson correlation is observed in the summary (*Table VI.5-2*) of the regression analysis data of both groups of steels. In addition, the adjusted R square parameter indicates that the DBTT varies as a function of the MC fraction.

Population	Number	Correlation		ANOVA-Linear fit			
		Pearson Corr.	Sig.	Adj. R-Square	Prob. Null Hypo	Intercept	Slope
High C	8	0.81	0.014	0.61	0.014	-83.9	48.8
Low C	8	0.73	0.039	0.46	0.04	-107.8	60.7

Table VI.5-2 *Summary of the statistical regression analysis considering the correlation between the DBTT and the fraction of the MC parameter.*

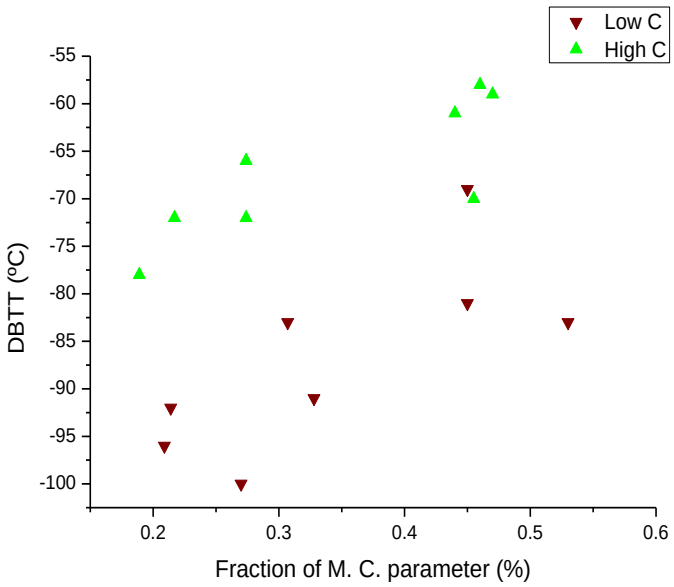

Figure VI.5-14 *Variation of the DBTT as a function of the MC parameter.*

VI.6 Origin and development of MC regions

The splitting observed in the impact test experiments can be reasonably correlated to the Cleavage Morphology Clustering (CMC) parameter. At the same time, the increase of the MC fraction seems to have a detrimental effect on the DBTT. This observation gives rise to questions regarding the origin of the MC regions and their development at specific stages of the TMCP.

The following analyses were carried out in order to answer these questions:

(I) Intermediated-quenched samples from different stages of the TMCP were analyzed in detail. In particular, samples from the Q3 and Q4 (see *Figure V.1-1*) stages were thoroughly examined. The impact of the Q3- and Q4-inherited microstructures on the final steel was also evaluated.

(II) The hypothesis was validated through texture modeling.

	Q3	Q4
Inverse pole figure map of the experimentally-measured transformation texture after quenching 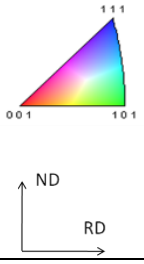	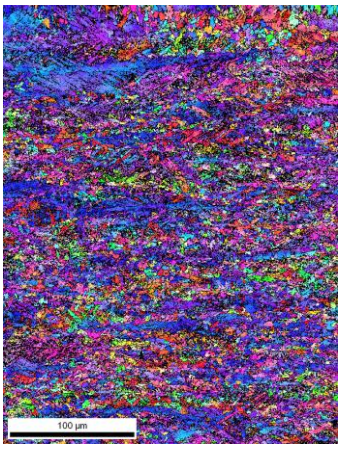	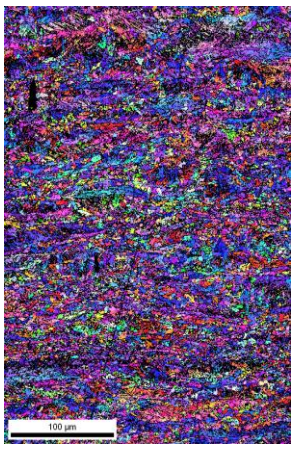
ODF φ2=45°	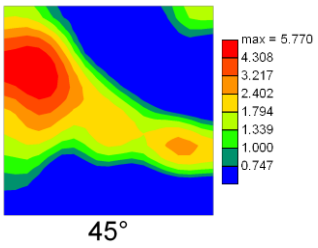	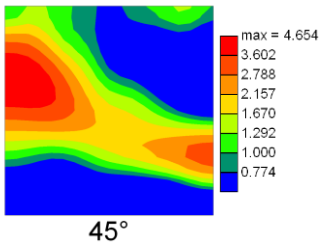
Partition showing only Gamma fiber orientations	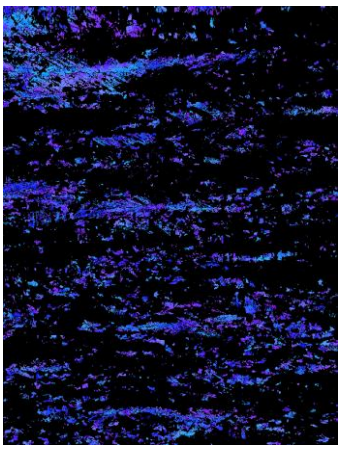	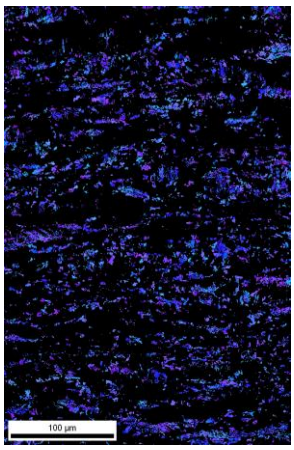
Partition showing only Gamma fiber + {001}<110> orientations	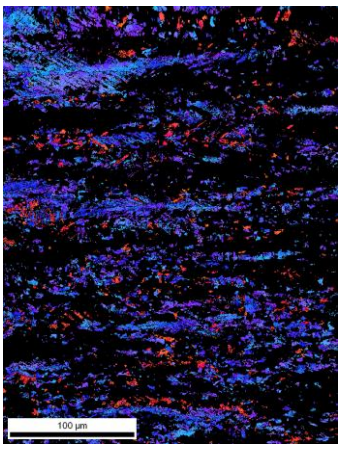	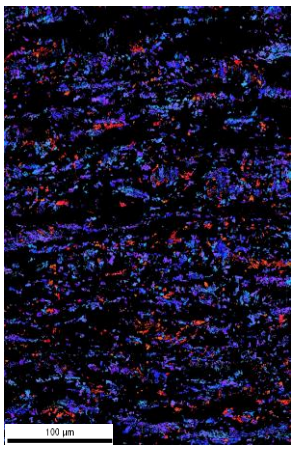

Figure VI.6-1 *(Rows 1 and 2) Representative IPF and ODFs at Q3 and Q4; (Row 3) Identification of the corresponding MC regions and cube components; tolerance of 15°.*

Figure VI.6-1 compares the microstructures, represented by ND IPF maps in row 1, and the textures (row 2) just after finish rolling at high and low FRTs. In addition, crystal orientation maps showing only grains with {111}<uvw> (gamma fiber) orientations, and a combination of those comprising the gamma fiber and {001}<110> (rotated cube) texture components are shown in rows 3 and 4, respectively. All texture components in the partition are plotted with a tolerance of 15° from the ideal orientation. The textures and microstructures at the Q3 and Q4 stages were similar, although at low FRT the pancaking seems to be somewhat more severe than at high FRT. Moreover, the gamma fiber partitions consisted of a high density of elongated grains, which seemed to develop along the pancaked austenite grain boundaries. The patterns of elongated grains with transformed gamma fiber orientation were present at both Q3 and Q4 stages. These findings support the idea that the MC regions are formed during finishing rolling below Tnr irrespective of the FRT. The MC regions may have formed possibly as a result of the preferential development/accommodation of certain orientations at the pancaked γ boundaries.

Furthermore, the rotated cube grains occur with volume fractions of 2.6% and 2.1% for high and low FRT, respectively and are fairly homogeneously distributed throughout both microstructures. It is interesting to note that the rotated cube grains neighbor, in many cases, the elongated, gamma fiber grains.

The maps from the Q3 and Q4 stages (*Figure VI.6-1* row 4) were compared to those obtained after complete TMCP (*Figure VI.6-2* row 2). After the high FRT schedule, elongated grains of orientations which transformed to the gamma fiber, were not observed in the steel that underwent complete TMCP. However, elongated grains, distributed in a somewhat banded pattern, and which form the MC regions, are still present in the microstructure of the plates after low FRT. So, why were these so-called MC regions “erased” from one material and not the other? The answers seem to be linked to the presence of the {001}<110> crystallographic orientation. The quantitative evidence points toward growth of the Cube orientation in the austenite phase during TMCP with high FRT, which in the end is reflected as growth of the rotated cube after transformation. The volume fraction of the rotated cube grains was, therefore, 11% and 6.6% at the end of the TMCP schedule with high and low FRT, respectively. Furthermore, the banded microstructure was consumed (*Figure VI.6-2*) as a result of this growth.

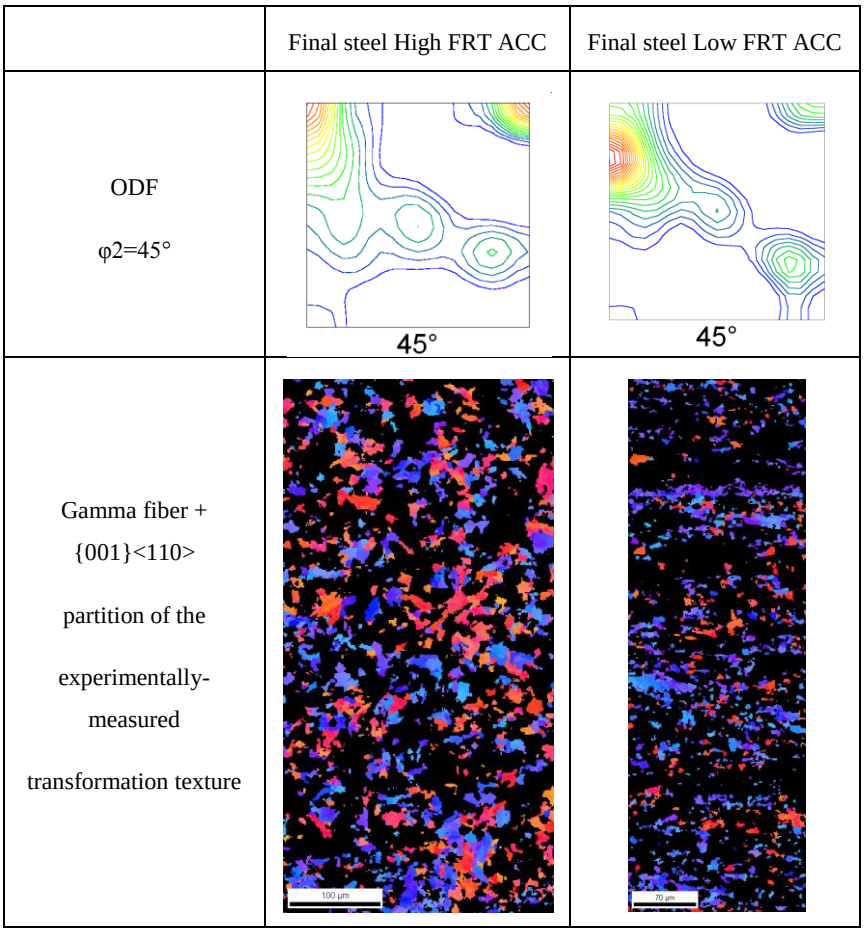

Figure VI.6-2 *(Row 1) Representative ODFs at the end of two TMCP schedules with high and low FRT respectively; (Row 2) Identification of the MC regions and cube components at the end of the mentioned TMCP schedules.*

Simulation of the texture evolution corroborates the discussed findings. The model is explained in section VI.2 of the present chapter. In short, modeling demonstrated that grain growth resulted from the high mobility of boundaries which fulfill the <111>40° orientation relation with the deformed matrix grains [10]. As explained in Chapter II.4.1, the {001}<110> component is possibly a product of the (parent) Cube orientation, which forms the aforementioned <111>40° orientation relation with the deformed matrix. Moreover, analysis of % Nb precipitated (Chapter VI.2) supports these observations. Compared to processing with high FRT, the larger amount of Nb precipitated during finish rolling in the route with low FRT contributes to grain-boundary pining, which, in turn, limits the mobility of the aforementioned boundaries.

VI.7 Synergies between features affecting the DBTT

This part of the thesis provides a brief overview of various findings which emerged from the previous analysis. The aim, here, is to emphasize the fact that the toughness varies with

several microstructural features (see *Figure VI.7-1*). In this figure, each radar plot compares two TMCPs, which have different FRTs but are otherwise identical. Four microstructural features are evaluated on the basis of their impact on the DBTT. These features are the: average grain size, area fraction of second constituent/phase (which corresponds with pearlite phase and/or cementite), volume fraction of cleavage planes parallel to the fracture propagation plane during instrumented Charpy impact testing, and fraction of M.C. parameter.

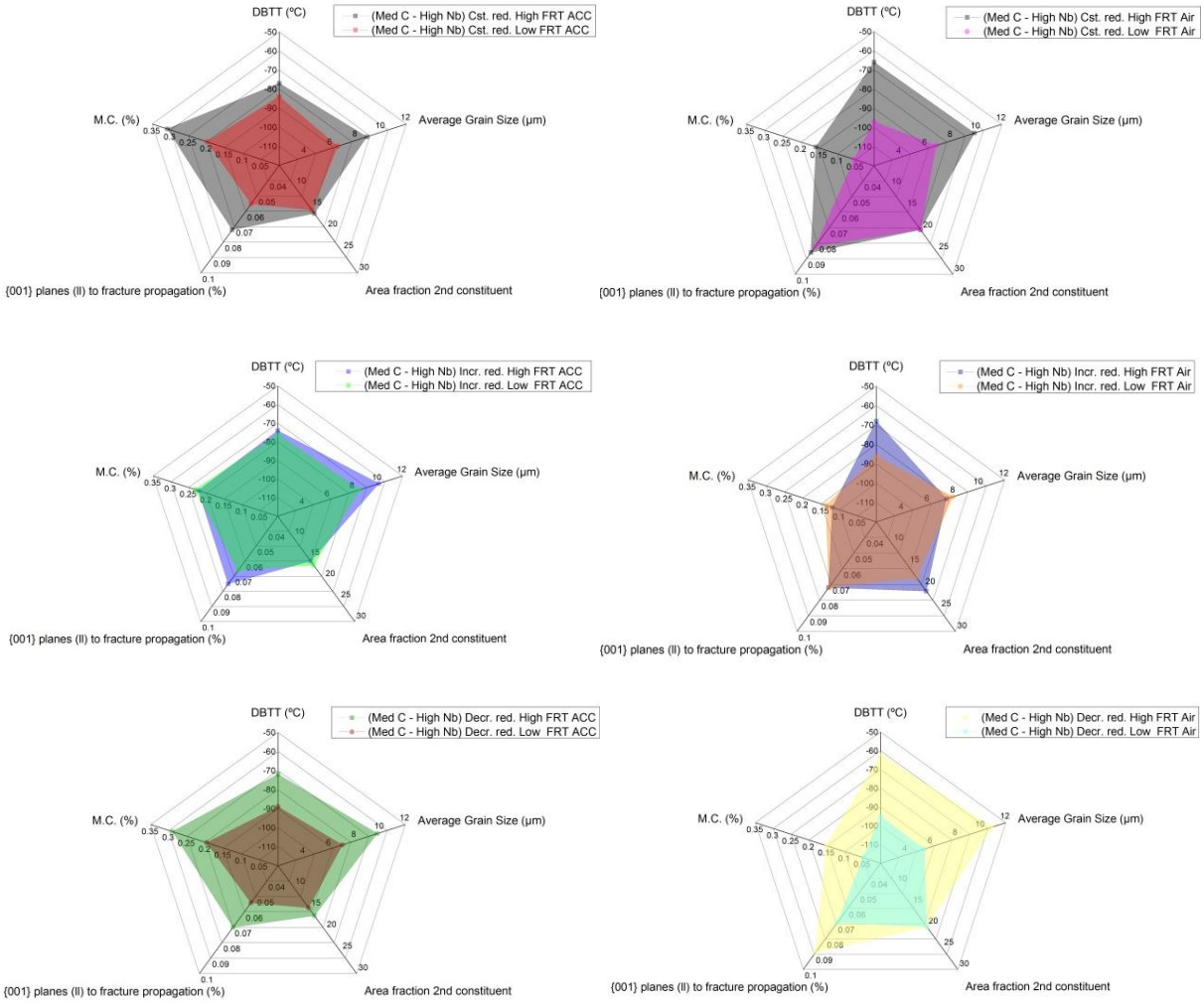

Figure VI.7-1 *Comparisons of the relationships between microstructural features and the DBTT for several TMCP schedules. Each radar plot compares the influence of FRT when the remaining TMCP is kept constant.*

Evaluating the radar plots situated in the top row, reveals that the DBTTs of low FRT schedules benefitted from a diminution of different microstructural features. In other words, the decrease in the DBTT seems to be correlated to a reduction in the proposed features. This

behavior is particularly evident at decreasing reduction draught (radar plots situated in the bottom row). It is also interesting to note that for the case of increasing reduction draught, the decrease in FRT did not result in significant variation in the DBTT. This result may be explained by the fact that no substantial differences were measured among the various microstructural factors.

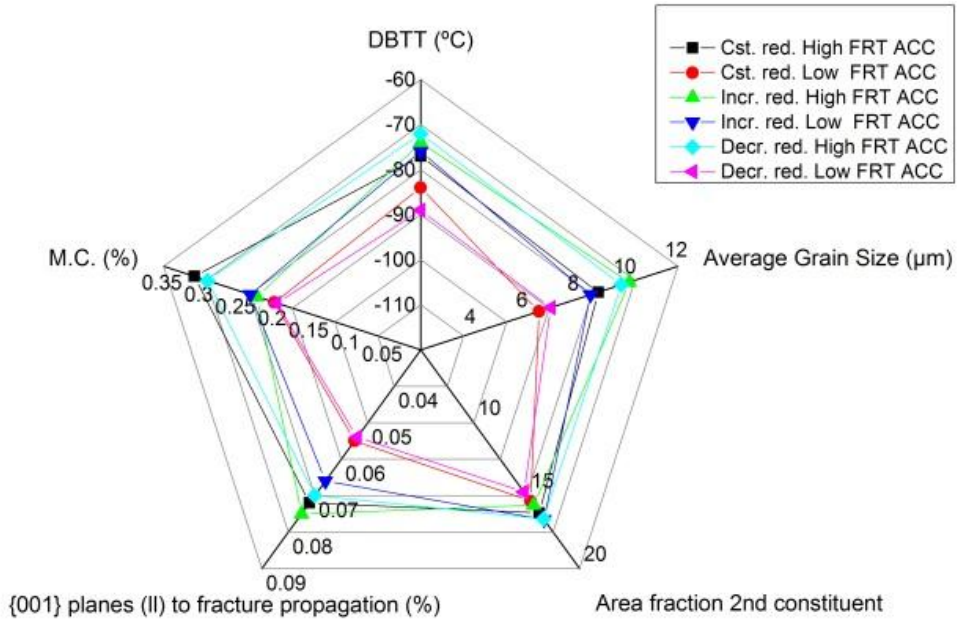

a

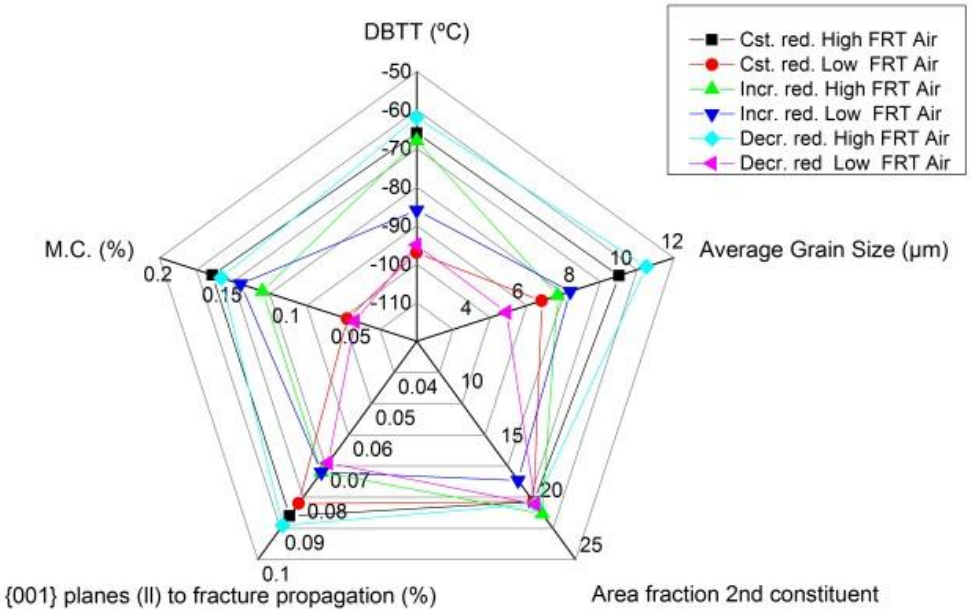

b

Figure VI.7-2 *Comparison of the relationships between microstructural features and the DBTT for several TMCP schedules when (a) ACC and (b) air cooling were used.*

Figure VI.7-2 presents a general overview when the TMCP schedules are grouped in terms of the cooling condition. This combination provides some support for the premise that the decrease in the DBTT, in steels processed with a TMCP including ACC, occurs largely as a result of grain refinement and the reduction in the volume fraction of cleavage planes parallel to the fracture propagation. Conversely, the DBTT depends mainly on the grain size and the fraction of M.C. parameter in steels processed with a TMCP with air cooling.

The ANOVA analysis further supported the stated hypothesis.

When the variations in TMCP parameters (reduction draught and FRT) were evaluated for the steels with ACC, the ≈75% change in the DBTT was attributed to a dependence on the grain size and the volume fraction of {001} planes parallel to the fracture crack propagation during Charpy impact testing.

The resulting equation that fits the described behavior is:

$$DBTT = -118.3 + 2.4 * D + 292 * Cp \qquad \textbf{VI.7-1}$$

Where D is the average grain size in μm and Cp is the volume fraction of regions with {001} planes parallel to the facture propagation during Charpy impact testing.

When the variations in TMCP parameters (reduction draught and FRT) were evaluated for the steels with air cooling, the ≈60% change in the DBTT was attributed to a dependence on the grain size and the fraction of M.C. regions.

The resulting equation that fits the described behavior is:

$$DBTT = -120 + 2.67 * D + 178 * M.C. \qquad \textbf{VI.7-2}$$

Where D is the average grain size in μm and M.C. is the % of regions that have an M.C parameter.

One of the objectives of the present work was to contribute to the understanding of the impact of TMCP on the properties of HSLA pipeline steels. The results presented in this chapter emphasize the necessity of a multi-microstructural-factor approach in order to control the strength of the steel without having a detrimental effect on the fracture toughness.

References

[1] E. O. Hall, "The deformation and ageing of mild steel: III Discussion of results," *Proceedings of the Physical Society. Section B,* vol. 64, p. 747, 1951.

[2] N. J. Petch, "The cleavage strength of polycrystals," *Journal of the Iron and Steel Institute,* vol. 174, 1953.

[3] L. Yang, J. Ji, J. Hu, and A. Romagos, "Effect of process parameters on mechanical behavior in hot-slab rolling," *Mechanika,* vol. 17, pp. 474-479, 2011.

[4] J. M. Gray and P. R. Kirkwood, "Changes in maximun niobium and carbon contents with time for pipeline steel," ed. Charles Hatchett seminar, London, UK, 2013.

[5] G. L. S. Corporation, *Steel,* vol. 116, 1960.

[6] C. H. Award. Available: http://www.charles-hatchett.com/Niobium_6.aspx

[7] S. Vervynckt, "Control of the non-recrystallization temperature in high strength low alloy (HSLA) steels," Doctor in Materials Science, Department of Materials Science and Engineering, Ghent University Gent, 2010.

[8] T. Tanaka, "Controlled rolling of steel plate and strip," *International Metals Reviews,* vol. 26, pp. 185-212, 1981.

[9] J. J. Jonas, "Transformation textures associated with steel processing," in *Microstructure and Texture in Steels*, Springer, Ed., ed, 2009.

[10] J. J. Sidor, R. H. Petrov, and L. A. I. Kestens, "Modeling the crystallographic texture changes in aluminum alloys during recrystallization," *Acta Materialia,* vol. 59, pp. 5735-5748, 2011.

[11] L. Kestens and J. J. Jonas, "Modeling texture change during the static recrystallization of interstitial free steels," *Metallurgical and Materials Transactions A,* vol. 27, pp. 155-164, 1996.

[12] B. Hutchinson, L. Ryde, E. Lindh, and K. Tagashira, "Texture in hot rolled austenite and resulting transformation products," *Materials Science and Engineering: A,* vol. 257, pp. 9-17, 1998.

[13] M. P. Butrón-Guillén, C. S. Costa Viana, and J. J. Jonas, "A variant selection model for predicting the transformation texture of deformed austenite," *Metallurgical and Materials Transactions A,* vol. 28, pp. 1755-1768, 1997.

[14] R. Abad, A. I. Ferandez, B. Lopez, and J. M. Rodriguez-Ibabe, "Interaction between recrystallization and precipitation during multipass rolling in a low carbon niobium microalloyed steel," *ISIJ International,* vol. 41, pp. 1373-1382, 2001.

[15] B. Hwang, Y. Kim, S. Lee, N. Kim, and J. Yoo, "Effects of microstructure on inverse fracture occurring during drop-weight tear testing of high-toughness X70 pipeline steels," *Metallurgical and Materials Transactions A,* vol. 36, pp. 371-387, 2005.

[16] G. J. Baczynski, J. J. Jonas, and A. E. Collins, "The influence of rolling practice on notch toughness and texture development in hgh-strength linepipe," *Metallurgical and Materials Transactions A,* vol. 30A, pp. 3045-3054, 1999.

[17] J. Zrnik, T. Kvackaj, D. Sripinproach, and P. Sricharoenchai, "Influence of plastic deformation conditions on structure evolution in Nb–Ti microalloyed steel," *Journal of Materials Processing Technology,* vol. 133, pp. 236-242, 2003.

[18] A. F. Gourgues, H. M. Flower, and T. C. Lindley, "Electron backscattering diffraction study of acicular ferrite, bainite, and martensite steel microstructures," *Materials Science and Technology,* vol. 16, pp. 26-40, 2000.

[19] S. Zajac, V. Schwinn, and K. Tacke, "Characterisation and quantification of complex bainitic microstructures in high and ultra-high strength linepipe steels," in *Materials Science Forum,* pp. 387-394, 2005.

[20] M. P. Aarnts, R. A. Rijkenberg, F. A. Twisk, D. Wilcox, M. J. Zuijderwijk, A. Arlazarov, *et al.*, "Microstructural quantification of multi phase steels (Micro-quant)," European commission 2011.

[21] J. M. Gray and F. Siciliano, "High strength microalloyed linepipe: Half a century of evolution," presented at the 5th International Conference on Pipeline Technology, Ostend, Belgium, 2009.

[22] W. B. Morrison and J. A. Chapman, "Controlled rolling," *Philosophical Transactions of the Royal Society of London A,* vol. 282, pp. 289-303, 1976.

[23] Y. Hai-Iong, D. Lin-xiu, W. Guo-dong, and L. Xiang-hua, "Development of Nb-V-Ti hot-rolled high strength steel with fine ferrite and precipitation strengthening," *Journal of Iron and Steel Research International,* vol. 16, pp. 72-77, 2009.

[24] T. J. Koppenaal and D. KuhlmannWilsdorf, "The effect of prestressing on the strength of neutron irradiated copper single crystals," *Applied Physics Letters,* vol. 4, 1964.

[25] K. J. Irvine, "Keynote Speech Physical metallurgy of steel," *Philosophical Transactions of the Royal Society of London A,* vol. 282, pp. 339-346, 1976.

[26] J. Majta, J. G. Lenard, and M. Pietrzyk, "A study of the effect of the thermomechanical history on the mechanical properties of a high niobium steel," *Materials Science and Engineering,* vol. A208, pp. 249-259, 1996.

[27] U. F. Koks, "The theory of an obstacle-controlled yield strength," *Materials Science and Engineering,* vol. 27, pp. 291-298, 1977.

[28] J. Irvine and T. N. Baker, "The influence of rolling variables on the strengthening mechanisms operating in niobium steels," *Materials Science and Engineering,* vol. 64, pp. 123-134, 1984.

[29] M. Charleux, W. J. Poole, M. Militzer, and A. Deschamps, "Precipitation behavior and its effect on strengthening of an HSLA-Nb Ti steel," *Metallurgical and Materials Transactions A,* vol. 32A, pp. 1635-1647, 2001.

[30] V. Carretero Olalla, R. H. Petrov, P. Thibaux, M. Liebeherr, P. Gurla, and L. A. I. Kestens, "Influence of rolling temperature and cooling rate on microstructure and properties of pipeline steel grades," *Materials Science Forum,* vol. 706-709, pp. 2710-2715, 2012.

[31] Y. Nagahama and S. Yamamoto, "High performance steel pipes and tubes securing and exploiting the future demands," NKK Technical Review 2003.

[32] M. Y. Matrosov, L. I. Éfron, V. I. Il'inskii, I. Y. Severinets, Y. I. Lipunov, and K. Y. Éismondt, "Use of accelerated cooling to improve the mechanical and processing properties of rolled plates used to make large diameter gas-line pipe," *Metallurgist*, vol. 49, pp. 220-229, 2005.

[33] H.-G. Hillenbrand, C. Kalwa, J. Schröder, and C. Kassel, "Challenges to a pipe manufacter driven by worldwide pipe projects," presented at the 18th JTM, 16/19 May 2011, San Francisco, CA, 2011.

[34] G. Demofonti, G. Mannucci, and P. Roovers, "Existing methods for the evaluation of material fracture resistance for high grade steel pipes," in *PRCI-EPRG-APRA 16th Biennial Joint Technical Meeting on Pipeline Reseach*, Canberra Australia, 2007.

[35] R. Higuchi, H. Makino, and I. Takeuchi, "New concept and test method on running ductile fracture arrest for high pressure gas pipeline," presented at the 24th World gas conference, Buenos Aires (Argentina), 2009.

[36] X.-K. Zhu and B. N. Leis, "Ductile-fracture arrest methods for gas-transmission pipelines using Charpy impact energy or DWTT energy," *Journal of Pipeline Engineering*, vol. 12, pp. 259-272, 2013.

[37] I. Pyshmintsev, A. Gervasyev, R. H. Petrov, V. Carretero Olalla, and L. A. I. Kestens, "Crystallographic texture as a factor enabling ductile fracture arrest in high strength pipeline steel," *Materials Science Forum*, vol. 702-703, pp. 770-773, 2011.

[38] S. Wright and M. Nowell, "High-speed EBSD," *Advanced Materials & Processes*, vol. 166, pp. 29-31, 2008.

"The noblest pleasure is the joy of understanding"

Leonardo da Vinci (1452-1519)

CHAPTER VII

Conclusions

The purpose of the present study was to improve the understanding of the influence of the finishing TMCP condition on the microstructure and properties of HSLA pipeline steels. Several multi-factor investigations were conducted in order to fulfill this objective.

The following conclusions can be drawn based on the analysis of the findings:

The variation of TMCP parameters, such as FRT and cooling condition, had an important effect on the γ microstructure evolution, which, in turn, had strong implications on the final microstructure. Several γ main product phases, and γ secondary product constituents were found after the TMCP schedules. The main phases were: polygonal ferrite α_{p}, quasi polygonal ferrite α_{qp}, and granular bainitic ferrite $\alpha_{B(G)}$; the secondary constituents were: lamellar pearlite $P_{L,}$ degenerate pearlite P_{D}, martensite/ austenite constituents M/A, and cementite (located mainly at the grain boundaries). Steels which were air-cooled consisted primarily of $\alpha_{p,}$ $P_{L,}$ and, $P_{D.}$ The steels processed with ACC exhibited predominantly α_{qp}, and $\alpha_{B(G)}$ microstructures.

The evolution of various microstructural features at several stages of TMCP were investigated through intermediate-quenched samples. These microstructural features were: γ grain size/morphology, crystallographic texture, precipitation of Ti, Mn, and especially Nb.

Furthermore, γ evolved to a pancake-like morphology during finish rolling at either high or low FRT. The pancaking, which seemed to be more severe in the latter than in the former, was attributed to the lower driving force for recovery at low FRT, and to extra grain boundary pinning resulting from the larger amount of Nb precipitated.

The Ti content was measured as precipitates form, in all the quenched samples. On the other hand, the amount of Mn precipitated was quite low, indicating that most of the Mn remained in solid solution during the austenitic rolling stages of TMCP.

Although Nb did not precipitate during roughing, almost 10% was precipitated during finishing, when a high FRT route was followed. The total amount of Nb precipitated immediately after finishing rolling at low FRT was 7% larger than that of its high FRT counterpart. In addition, the Q4 stage immediately following low FRT resulted in a bi-modal distribution of precipitate sizes. The Q3 stage gave rise to a similar precipitate size distribution. However, the extended transfer time between roughing and finishing allowed the occurrence of additional precipitation before finishing rolling. During transfer (roughing-finishing), the microstructure of the material consisted of recrystallized austenite and, hence, precipitates were preferentially nucleated at the previously formed precipitates and at the grain boundaries. This resulted in a shift toward the formation of large precipitates.

The increased potential for strain-induced precipitation was measured at both high and low FRT. Moreover, at high and low FRT, the differences in both the % Nb precipitated during finishing rolling and the different strain-induced precipitation response, were found to be insensitive to the cooling condition for rates in the range of 1°C/s to 11°C/s.

Significant differences between the two cooling conditions were also observed. For example, the percentage of precipitates with equivalent radius larger than 100nm was clearly superior for air cooling. Moreover, for the same cooling condition, low FRT-processed materials consisted of a greater fraction of these large precipitates than their high FRT counterparts.

Reheating resulted in the formation of random textures. Subsequently, the FCC rolling fibers recrystallized after each pass of rough rolling carried out above the Tnr. Finishing rolling, at either high or low FRT, resulted in identical textures. These textures sharpened and evolved as follows: copper, brass, and Goss, which resulted from finishing rolling of γ below the Tnr, transformed to the {114}<110>, {113}<110>, {112}<131>, {111}<132>, {111}<011>, {111}<123>, {554}<225>, {332}<113>, and {001}<110> crystallographic texture components.

Experimental results (grain size and texture evolution) were compared with predictions from phenomenological/analytical models.

Various materials were also analyzed by means of EBSD through-thickness scans. A pronounced texture gradient developed for processing at both FRTs. This gradient was manifested as textures represented by components related to plane strain compression mode at the centre of the plate, shear textures at the sub-surface/surface, and weak transition textures at the ¼ thickness. The shear textures at high FRT differed significantly from their low FRT

counterparts. The reason for this difference is not clear and two possible explanations were discussed. Increasing deformation draughts resulted in only shear texture components (Goss, Brass, and Copper), while the decreasing draught triggers the development of slightly weaker textures where Brass, Goss "*beta*" fiber texture components are combined. This finding concurs with the fact that the friction coefficient increases with increasing reduction draught which, in turn, promotes the formation of shear texture components. The "weak transition texture" developed at the ¼ thickness in the increasing deformation draught was, however, quite unexpected.

The results of this study indicate that the finish rolling temperature influences the texture development in the plates whereas, the reduction draught has, in general, no impact on the austenite transformation textures. One consequence of the processing temperature is that well-defined patterns of particular texture gradients can be identified.

Effect of C and Nb on the strength and toughness

The present study was aimed at determining the effect of different C-Nb compositions on the strength and toughness when TMCP schedules, consisting of constant reduction draught - high/low FRT and ACC/air cooling, were applied.

Analysis of the mechanical behavior as a function of the chemical composition indicated that high Nb steels exhibit higher yield strength irrespective of the TMCP schedule, compared to their low Nb counterparts, which had lower strengths for all of the schedules. The yield strengths of the high Nb steels were attributed to *(i)* enhanced precipitation strengthening with large weight percent of Nb and *(ii)* excellent grain refinement during TMCP owing to the presence of Nb precipitates.

Increasing the cooling rate had, in general, a positive impact on the yield strength, which increased 6% and 7%, at low and high FRT, respectively; the ultimate tensile strength also improved with increasing cooling rate. On the other hand, the largest change (increase of 10%) in the yield strength occurred in the case of the low FRT + air cooling condition. The ultimate tensile strength did not, however, change significantly with a decrease in FRT before air cooling. Moreover, increasing the cooling rate at low FRT had a greater impact on the yield strengths of medium- or high-carbon steels compared to those of other compositions. Compared to steels of other compositions, low-C steels were less sensitive to changes in the rolling schedule.

An important observation to emerge from this study was: Low FRT on UTS before air cooling had only a slight impact on the ultimate tensile strength. In addition, the difference in the work hardening behaviors of steels processed via low FRT + air cooling and high FRT + air cooling, was attributed to grain size refinement; this refinement had a significant effect on the yield ratio, since the yield strength improved, owing to the reduced average grain size of the α_p and α_{qp} microstructures, without an accompanying increase in the UTS. This differing response to refinement of the average grain size resulted in a deterioration of the YS/UTS ratio.

High- and low-C steels had, in general, high and low DBTTs, respectively; Low C - Low Nb steels exhibited lower DBTT than their Low C – Med. Nb counterparts. It is well-established that the toughness decreases with increasing C content. However, the toughness changed only slightly when Nb was added to the high-C steels. The Med. C - High Nb steel exhibited the highest sensitivity to variations in the TMCP schedule.

Influence of TMCP on the microstructure

Reducing the FRT resulted, in general, in a decrease in the average grain size, irrespective of the cooling condition. When the impact on steels of different chemical compositions is compared, it is apparent that Med. C – High Nb steel is only slightly sensitive (in terms of microstructure changes) to the FRT and cooling condition. This finding highlighted the ability of Nb to act as a weakening agent toward variations in the FRT, especially when air cooling conditions were applied. Furthermore, there was only a small scatter in the grain size values of the different grades processed at low FRT.

Higher fractions of precipitates were obtained for rolling at low FRT compared to those resulting from high FRT. However, ACC subsequent to low FRT resulted in a lower fraction of Nb precipitates than those obtained after air cooling. In addition, the fraction of total Nb precipitated, which was highest in the Medium C - High Nb steel, is attributed to the Nb/C ratio; i.e., in the case of air cooling, the percentage of total Nb precipitated increased, in general, with increasing Nb/C ratio. ACC resulted in only slight differences in the precipitation conditions when steels of various chemical compositions were compared. The Medium C - High Nb steel was, however, an exception to this observation.

This project was undertaken to design different TMCP schedules and evaluate the effect of the finishing TMCP condition on the microstructure and, by extension, the properties of a fixed pipeline steel composition.

The variation of the processing conditions (e.g. FRT, cooling condition, and strain path) had a significant impact on the variability of the microstructure and precipitation. Schedules with decreasing reduction per pass showed the largest variation in the average grain sizes when the FRT and cooling condition were changed. Grain refinement, at low FRT, was more extensive for air cooling conditions than for ACC, especially in the case of decreasing strain path. The constant reduction per pass schedule bears a resemblance to the response displayed by the decreasing reduction path. Steels processed with an increasing strain path were insensitive to variations in the FRT and cooling condition.

Similarly, of all three draughts, the impact of variations in the FRT on the precipitation of Nb was largest in the case of constant reduction path rolling schedules.

Stain-induced precipitation phenomena, generated in the “heavy reduction passes” of the decreasing and increasing reduction draughts, gave rise to a large fraction of Nb precipitates for schedules with increasing or decreasing reduction per pass followed by ACC. These fractions were larger than those produced in the case of the constant reduction draught.

Microstructure - fracture control

Various significant findings emerged from this study regarding microstructure fracture control. Precipitates, particularly TiN, were found to play a role in the onset of fracture, but did not control the propagation.

Furthermore, this study has shown that there is a strong correlation between the energy absorbed during crack propagation at the upper shelf region of the transition curve and the DBTT. The DBTT, which was defined through the T_{50} criteria, was determined using the hyperbolic tangent function fitting.

The fraction of pearlite and energy absorbed during the crack propagation were also found to be correlated. For example, samples with lower pearlite content absorbed more energy during crack propagation than those with higher fractions. Further analysis revealed that the arrangement of pearlite into bands increased with corresponding increases in the volume fraction. Compared to a non-banded microstructure, this banded pattern provides an easier crack propagation path, either within the second phase or at the interface.

An important finding that emerged from the presented results is that, the attribution of toughness behaviour to a single factor/microstructural feature, fails to resolve the correlation between crack propagation response and microstructure.

Moreover, different chemical compositions differ not only in absolute values of average grain size but also in the way (microstructure heterogeneity) in which they display sensitivity to changes in the TMCP schedule. The current results are, therefore, significant in various respects.

The lower the Nb content, the higher the variability (scatter) of the average grain size with changes in the TMCP (FRT and cooling rate). In addition, the heterogeneity of the microstructure increases with decreasing Nb content. High Nb - Med. C steels having, in general, more homogeneous microstructures, than the steels of other compositions, also agrees with earlier observations made in this work. This combination of findings provides further support for the premise that Nb as a micro-alloying element is quite effective both as a microstructure refiner, but furthermore, a microstructure homogenizer agent.

In steels with Med. C - High Nb composition, the average grain size represents probably the best parameter through which the impact toughness can be controlled. However, the other chemical compositions might be composed of a feature (or features) which play(s) a major role in controlling the impact toughness.

The findings discussed in this work suggest that the capacity of the Med. C – High Nb composition to offer a good balance between the strength and toughness when appropriate TMCP was followed is attributable to two main reasons, namely:

(I) The ability to develop relatively homogeneous microstructures in all the studied TMCP scenarios. This is, in the author's opinion, the first stage in controlling the fracture toughness (taking into account that inclusion content has been previously controlled). To some extent, this occurs as a result of the greater % of Nb precipitated compared to that of the other compositions. These Nb precipitates prevent, at least partially, the coarsening of γ grains before the γ to α transformation.

(II) The high values of YS achieved at low FRT, by steels of said composition, show correlation with the enhanced precipitation hardening attained in TMCP routes with low FRT (both ACC and air cooling).

The presence of splitting observed in the impact test experiments was shown to be reasonably correlated with the Cleavage Morphology Clustering (CMC) parameter. The CMC characterizes large grain size clusters of heavily elongated, rotated cube grains. The results suggest that the crack arrest-ability in the ductile and ductile to brittle transition regions is mostly influenced by the volume fraction and relative distribution of large and elongated rotated cube grains. The correlation analysis also revealed that increasing fractions of the MC may have a detrimental effect on the DBTT.

After the role of the MC regions was determined, their origin and mode of development were also investigated. It was found that high density of elongated structures developed along the pancaked γ grain boundaries. The patterns of elongated grains with transformed gamma fiber orientations were present at both Q3 and Q4 stages. In other words, they developed during finishing rolling, below Tnr, at both high and low FRT. This microstructure was inherited by the final material after low FRT+ACC (but not after high FRT+ACC) owing to the growth of certain orientations at high FRT between the end of the finish rolling and the entry to the cooling bed. However, this grain growth was not significant in the case of low FRT. These facts were measured experimentally, and corroborated via texture modeling. Modeling demonstrated that this grain growth resulted from the high mobility of boundaries fulfilling the <111>40° orientation relation with the deformed matrix grains.

These results provide both an interesting insight into the industrial processing of HSLA steels and a clear methodology by which the failure of a steel, owing to so-called delimitation, can be predicted.

Concerning the Med. C – High Nb composition

In this investigation, quantitative and statistically significant results were obtained which corroborate the hypothesis of considering HAGB (usually 15° misorientation) as “effective grain size” barriers to crack propagation during fracture.

Moreover, the enhancement of the DBTT during Charpy impact testing benefitted from a diminution of one/more microstructural features, namely the average grain size, area fraction of second constituent, volume fraction of cleavage planes parallel to the fracture propagation, and fraction of the M.C. parameter. In particular, it has been found that in steels processed with a TMCP including ACC, the decrease in DBTT results, to a large extent, from the grain refinement and reduction in the volume fraction of cleavage planes parallel to the fracture

propagation. However, the DBTT of steels processed with a TMCP schedule including air cooling, depends mainly on the grain size and the fraction of M.C. parameter.

This thesis has evaluated a number of possible strategies that can be implemented to increase the strength of a reference TMCP HSLA pipeline steel. Within the frame of this project, these strategies were limited to changes in the: *i)* FRT, *ii)* cooling rate, and *iii)* C and Nb composition. In absolute terms, the addition of C+Nb strategy resulted in the best option of increasing the YS, but with an accompanying drastic decrease in toughness. The addition of Nb was found to be the optimal strategy which achieves an increase in strength without significantly compromising the toughness. However, if the YS/UTS ratio is kept in mind, then increasing the cooling rate represents a more balanced strategy than the other strategies. Moreover, the impacts of the aforementioned strategies were analyzed on the basis of determining the factor/s (of the microstructural features considered) which govern the change in mechanical properties.

In order to better assess the influence of a given process parameter on a particular microstructural feature, four HSLA steels were processed under different TMCP conditions in which the finish rolling temperatures and cooling routes were systematically varied. Strengthening mechanisms were quantified based on experimentally-measured data. The influence of a specific process parameter on a particular microstructural feature and, correspondingly, the yield strength has been elucidated.

Higher yield strengths were attained with a decrease in the FRT even in plates which underwent slow (for example, air) cooling. This result can be attributed to the increase of dislocation strengthening and grain size refinement.

Analysis of materials processed under the same cooling condition indicates the major role of precipitates in the air-cooled materials. Precipitates during air cooling promote higher strength than those formed during ACC.

Contributions to the strengthening arising from the various microstructural features like solid solution strengthening, grain size, dislocation density, and precipitation hardening, were analyzed using Taylor, Hall-Petch, and Ashby–Orowan approaches. The root of the sum of the squares method was applied to link the experimental with the model-predicted strength.

Results from experiments and modeling showed good correlation. The model indicates which microstructural features (dislocation density and precipitation) have the most impact on the strength and how they can be controlled via TMCP parameters. Validation of the model with 16 other steels displayed high correspondence between the model and experimental measures of the yield strength.

These conclusions provide a more complete and comprehensive insight into the TMCP of HSLA pipeline steels.

"Life is pretty simple: You do some stuff. Most fails. Some works. You do more of what works. If it works big, others quickly copy it. Then you do something else. The trick is the doing something else."

Leonardo da Vinci (1452-1519)

CHAPTER VIII

Suggestions

This research has raised various questions which should be taken into account in further investigations.

The findings of this study have an important implication for future practice regarding EBSD characterization of TMCP material. Through-thickness characterization of the rolled plates is strongly recommended in order to obtain a complete picture of the morphology-texture gradient of the steels. Middle thickness regions were found to contribute significantly to the macroscopically behavior of the material. Observations at the ¼ thickness are typically representative of the ½ thickness microstructure, and in many cases display the same tendency or pattern, and even provide good quantitative results. However, the author is convinced that through-thickness scans of all the studied materials would provide much clearer correlations between the microstructure and final properties. Time constraints for scan acquisitions limited the dimensions of the scanned areas, particularly, when the core of the experimental characterization was performed with the EBSD technique. Fortunately, the equipment which is currently available at the Department of Materials Science and Engineering (UGent) has overcome this issue. If possible, it would be interesting for future research to concentrate on the through-thickness investigation of all the processed materials.

A new approach should be used in order to better assess the microstructure developed after each production route. Unlike the traditional average grain size values, which offer a quite broad description of the grain size, a new type of map, which visualizes and identifies the heterogeneities between the various grain size colonies (i.e. presence of larger grain size

clusters), was introduced in this study. These maps aid in quantifying the microstructures on the basis of the average grain size. In addition, they complement the analysis of maps that quantify the homogeneity/heterogeneity of a microstructure.

Furthermore, based on the results drawn from this study, the following suggestions should be considered when composition and production strategies of HSLA pipeline steels are formulated.

The single most direct observation to emerge from the comparison of the produced steels was the variability of mechanical properties as a function of the TMCP schedule. Consequently, the wide spread in toughness and strength, and the corresponding link with the applied TMCP schedule constituted, by itself, valuable information regarding product-processing capabilities.

The best (lowest) DBTT was associated with low FRT and air cooling either for constant or decreasing reduction draft, whereas, the more balanced steel in terms of DBTT and YS was processed by the combination of low FRT, decreasing draft, and ACC.

Med. C- High Nb steels are more sensitive to variations in the TMCP parameters compared to those of other compositions. Therefore, said composition can exploit the benefits of tuning the TMCP parameters. However, these steels may suffer from a scatter in their properties if certain parameters (at FRT or cooling rate) are not perfectly controlled.

The mechanical properties of low C content grades were found to be less sensitive to changes in the TMCP schedule compared to those of other steels.

In general, a decrease in the FRT before air cooling, has the most positive impact on enhancing the YS; however, this lowered FRT does not result in an improvement of the UTS.

Nb is not only a powerful grain refinement “tool” during TMCP or a precipitation strengthening element. Increasing the Nb content has the ability to develop homogeneous microstructures. This, in the author’s opinion, is the first stage in controlling the fracture toughness (taking into account that the inclusion content has been previously controlled).

Low finishing temperature combined with ACC has a detrimental effect on the control of splitting (delamination) fracture.

The evaluation of the fraction of CMC regions provides valuable insight into the tendency of a HSLA pipeline steel to suffer ductile crack propagation (splitting/delamination mode). Alternatively, quantification of the MC regions is useful in assessing the (absolute/relative) toughness behavior of the steel.

In addition, the following investigation topics are recommended for further research:

The present study was designed to determine the effect of different C-Nb compositions on the strength and toughness when TMCP schedules, with constant reduction draft - high/Low FRT and ACC/air cooling, were applied. The author encourages to complete the study by varying the coiling conditions (temperature, time) together with the defined ACC schedules.

Given that impingement of austenite grain boundaries during rough rolling when successive static recrystallization cycles might develop a homogeneous microstructure before finishing rolling. It has been observed in this work that Nb preferentially precipitates in already existing Ti particles. Additional work evaluating the impingement impact of Nb precipitation above Tnr on the mechanism to enhance austenite homogeneity is needed. The combination of present work results and the quantitative impact of aforementioned mechanism on the final mechanical properties would provide a fruitful guideline to the manufactures of HSLA pipeline steels.

Reconstruction of the so called parent austenite microstructure is getting a popular research topic. There are recent advances in modeling theoretical parent-product relationships. Up to now, the parent recrystallized austenite which trsansforms into martensitic microstructure has been successfully reconstructed. Present work provides a quantitative and qualitative amount of experimental data ready to validate models, which are aimed to trace back, not only recrystallize austenite, but austenite in deformed stated (pancaked) prior transformation.

The Batelle two curve method has been effective predicting crack arrest in full scale burst test on basis of Charpy V notch absorbed energies. However, the method, due to its degree of empiricism, does not work for modern pipeline steel grades. Therefore, it would be useful to develop a model where the influence of microstructural features on the fracture toughness are considered.

The so called “gurus of innovation” suggest that one of the best ways of finding inspiration, to solve a technological challenge in a particular field, is by looking at the potential application

of a well-developed knowhow in an alternative field/sector. Perhaps, the outcomes of present work focused on pipeline steels could be useful in the manufacturing of steels for structural applications operating under similar arduous environments, i.e. the towers supporting offshore wind turbines.

One final reflection. This work has been somewhat of a paradox. While modern society is devoted to striving for perfection, metallurgists owe their existence to defects, since metallurgy is nothing but the art of dealing with defects in such a way that their contribution to final metal properties is controlled.

"What you get by achieving your goals is not as important as what you become by achieving your goals".

Henry David Thoreau (1817-1862)

IX Annexe: microstructures developed after different TMCP schedules

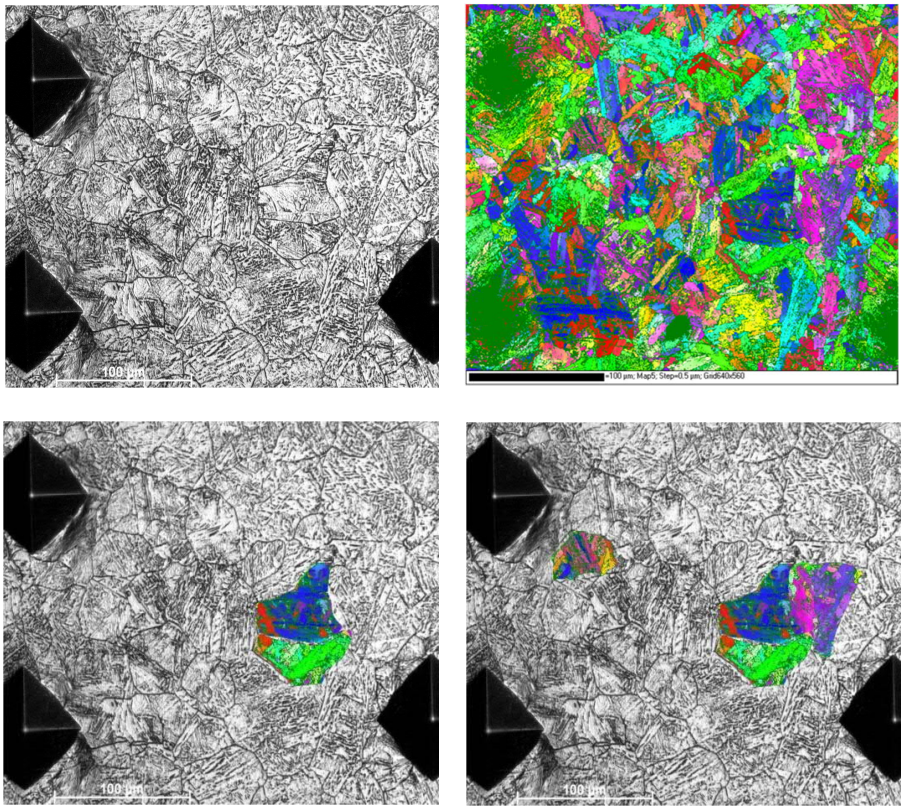

Figure IX-1 *(a) Former austenite microstructure (at Q1 stage) revealed with Bechet and Beaujard's etching. (b) IPF of the same region. (c) and (d) Examples of grouped martensite laths (austenite product orientations resulting from austenite common parent orientation) matching grains revealed with the etching.*

Representative optical micrographs of the steels after low/high FRT and ACC are shown in Figure IX-2. SEM images, of previously mentioned steels, are displayed in Figure IX-3 and TEM micrographs are exhibited in Figure IX-4. All the final microstructures as a result of ACC consists of an irregular lath-less dislocated substructure $\alpha_{B(G),}$ and some little regions of lath like bainitic ferrite $\alpha_{B,}$ also defined as degenerated upper bainite. Together with small islands of MA constituent. In the lower left side of the Figure IX-3 and Figure IX-4 examples of formation of upper degenerated bainite or α_B are shown. The α_B sheaf-like laths that have been nucleated from the prior austenite grain boundaries only extend for a few hundred on nm, due to the continuous ACC, the growth penetrating inside de grain is limited. Dispersion of cementite particles mainly precipitates at the grain boundaries are largely observed (see

Figure IX-4). An example of linear point EDS analysis of the cited cementite precipitates is presented in Figure IX-8.

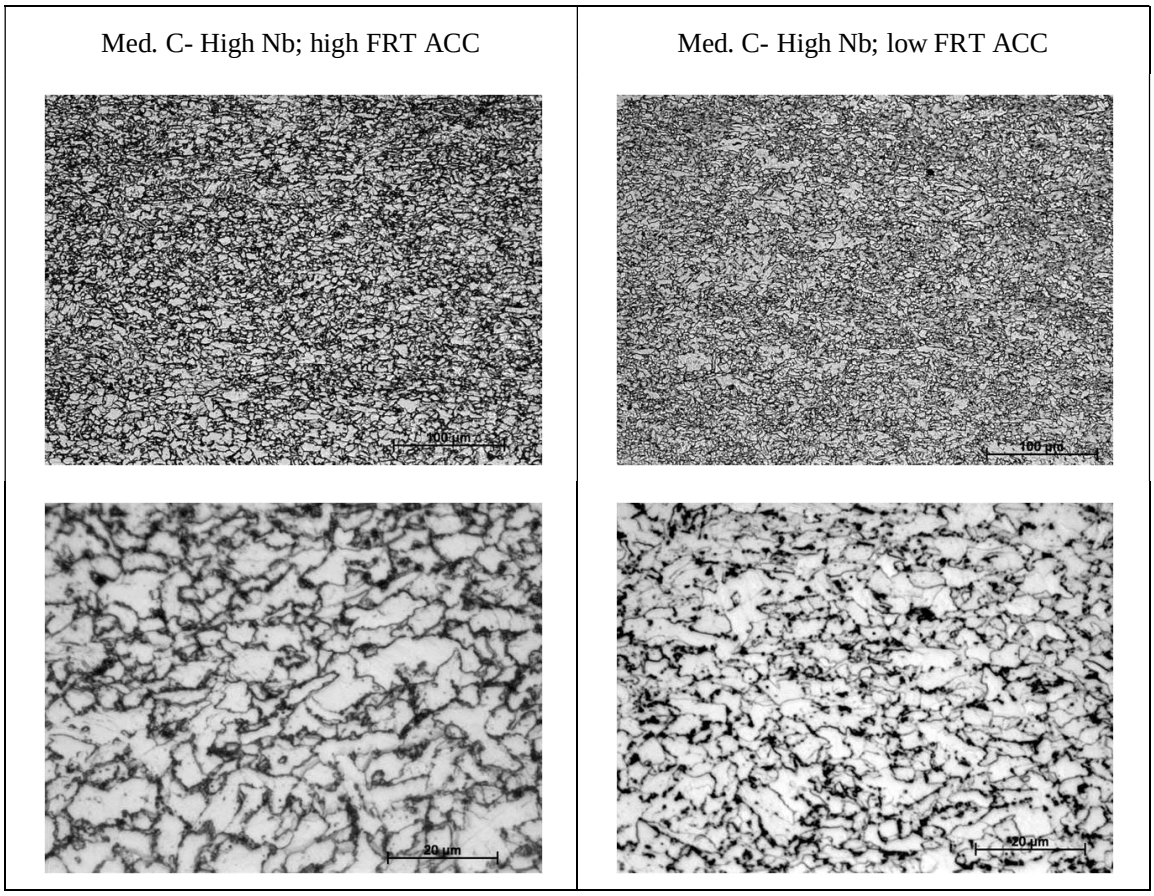

Figure IX-2 *Light micrographs showing ACC microstructures.*

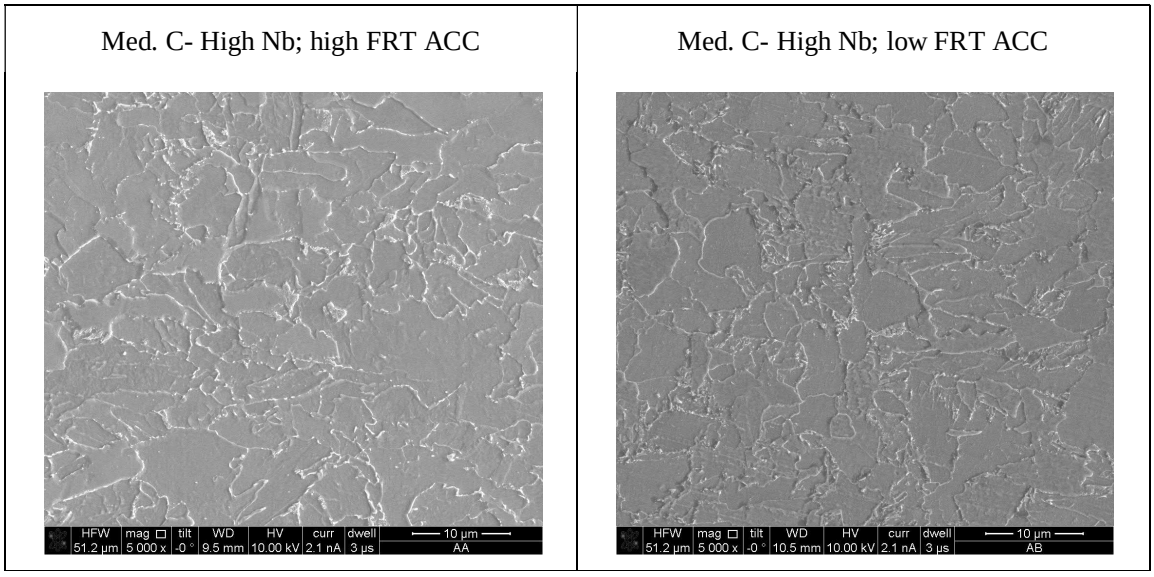

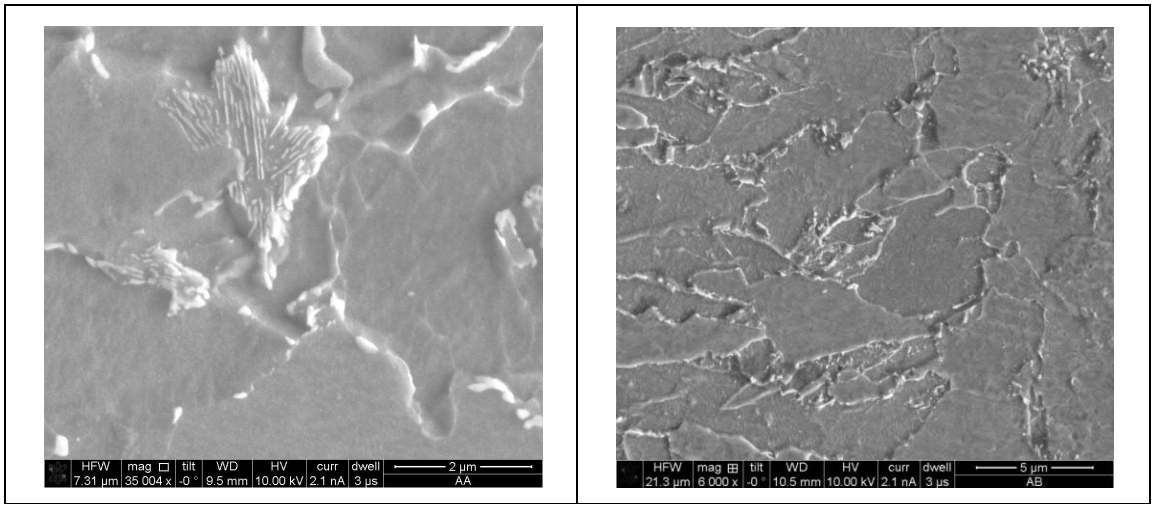

Figure IX-3 *SEM micrograph showing ACC microstructures.*

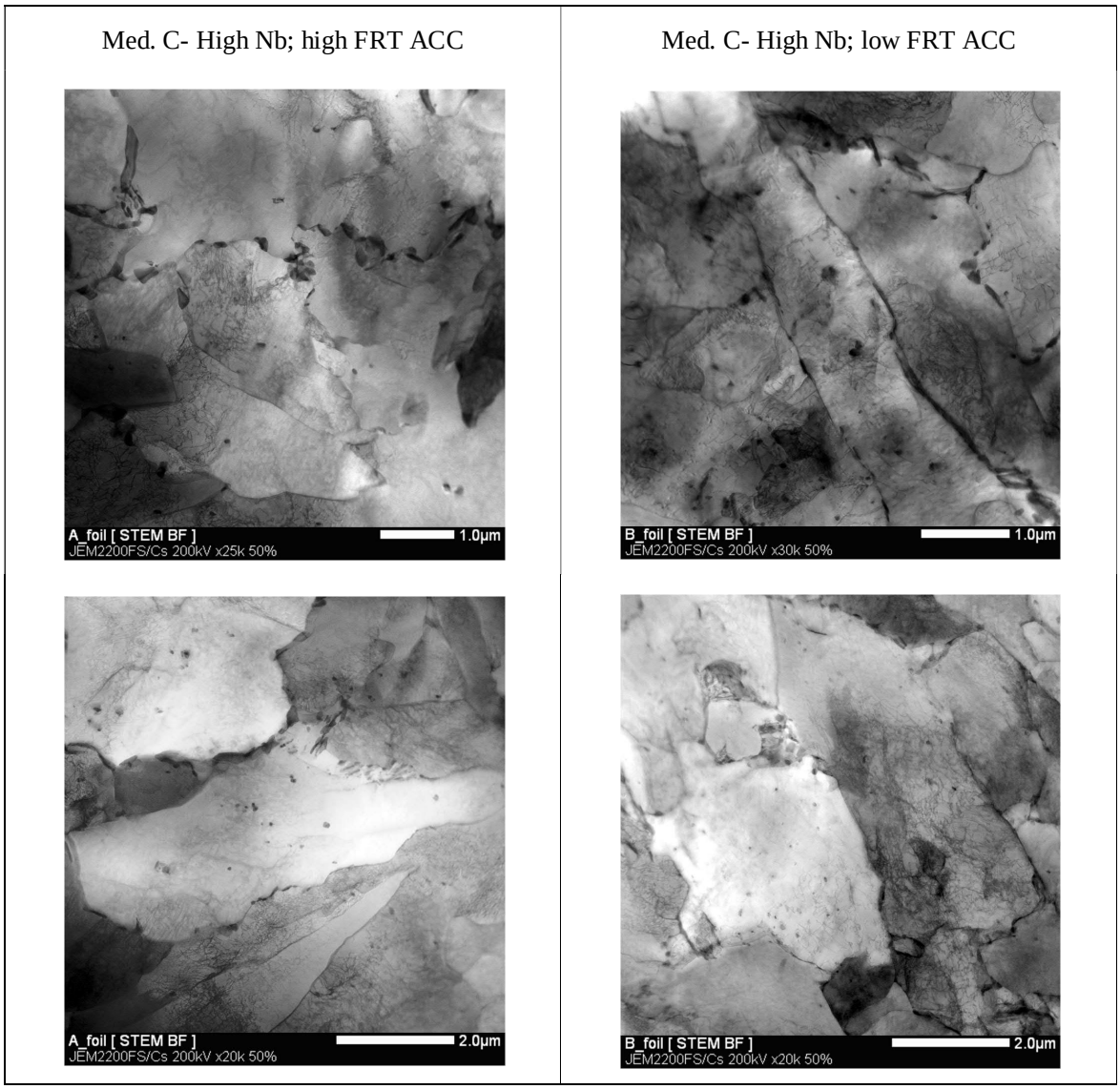

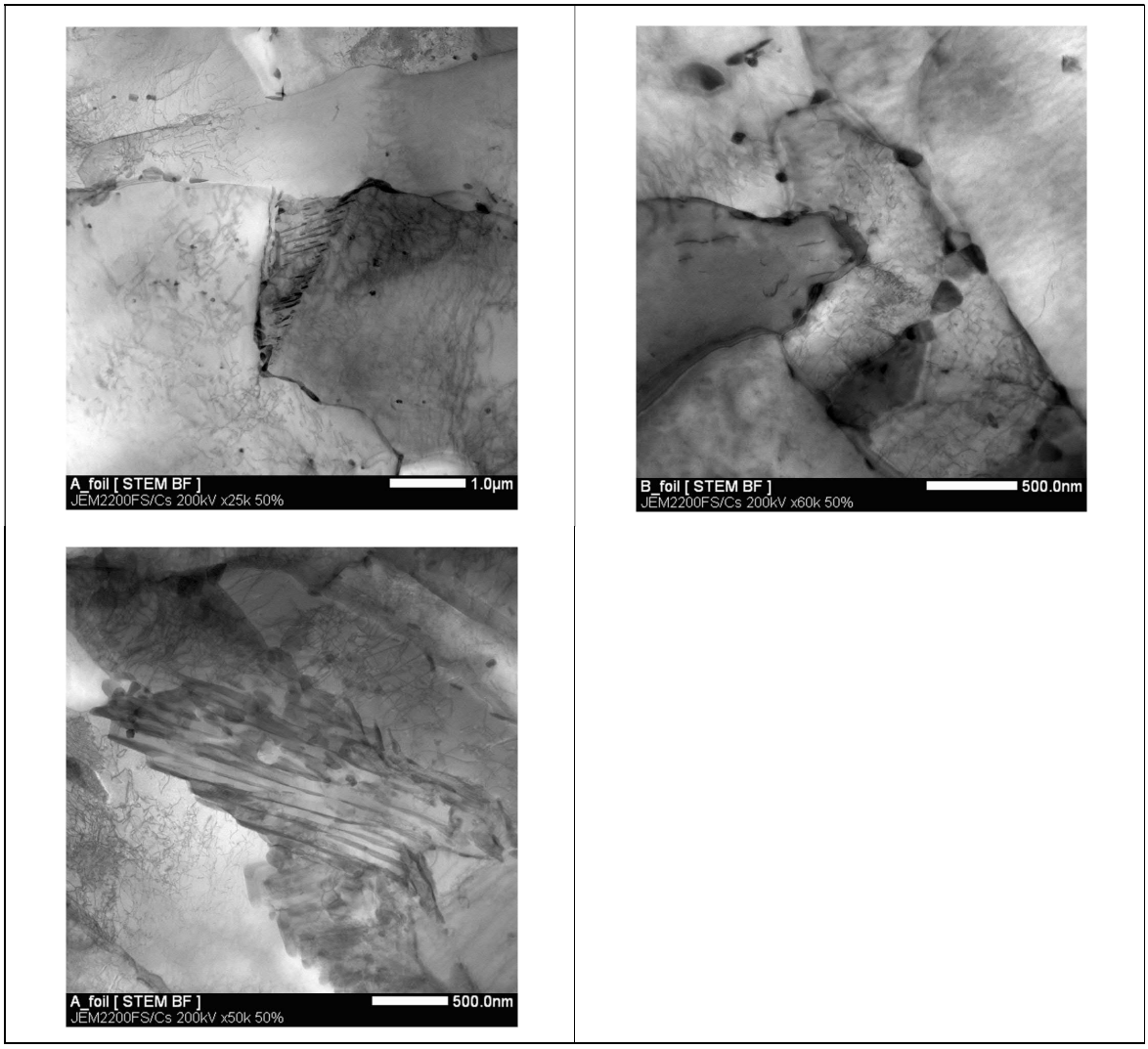

Figure IX-4 *STEM BF micrographs showing ACC microstructures.*

At a lower cooling rate (air cooling ≈0.5°C/.s) the microstructures (OM *Figure IX-5*, SEM Figure IX-6 and TEM Figure IX-7) of both high FRT and low FRT show polygonal ferrite α_p, Quasi-polygonal ferrite α_{qp} and P_L/ P_D. At the bottom Figure IX-7 presents the TEM BF micrographs of P_D (Incomplete lamellar growth of ferrite and Fe_3C) left side and P_L right side. Additionally in Figure IX-9 a line EDX analysis of a P_L island was included. The later clearly shows the C rich and C depleted regions.

Med. C- High Nb; high FRT Air	Med. C- High Nb; low FRT Air
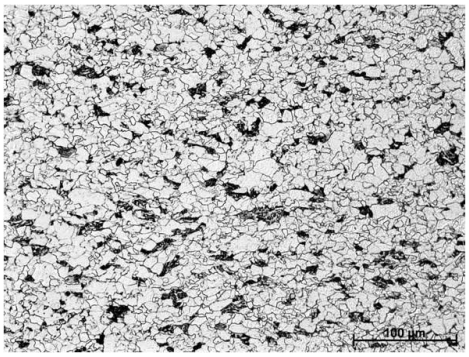	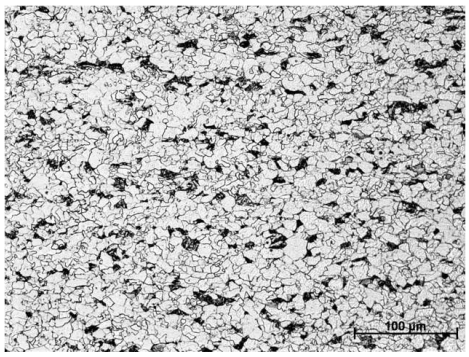
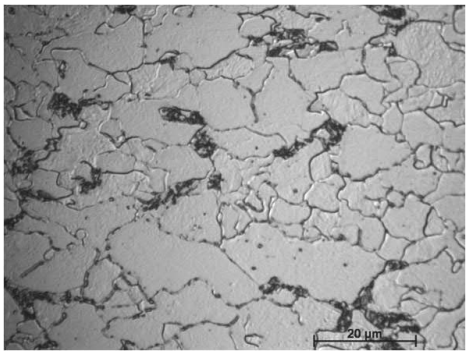	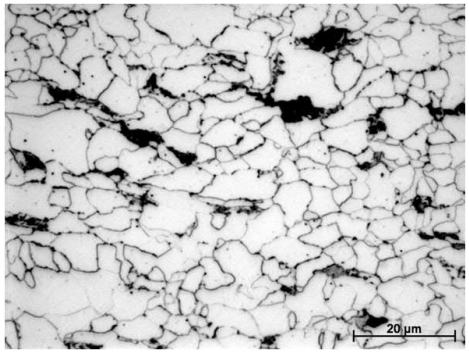

Figure IX-5 *Light micrographs showing Air cooled microstructures*

Med. C- High Nb; high FRT Air	Med. C- High Nb; low FRT Air
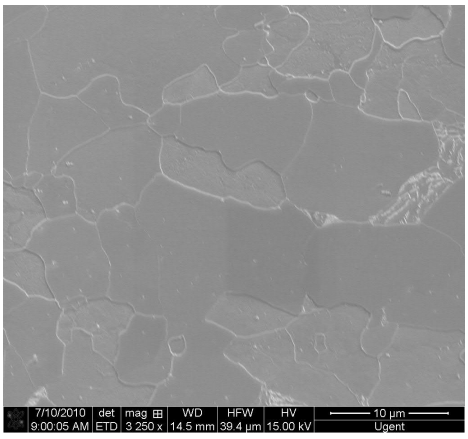	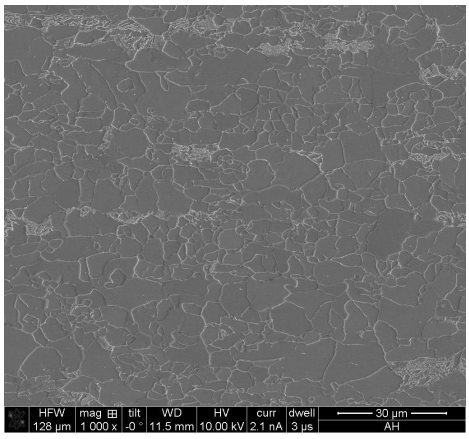

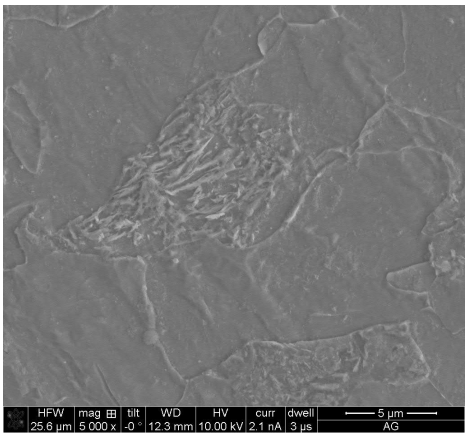

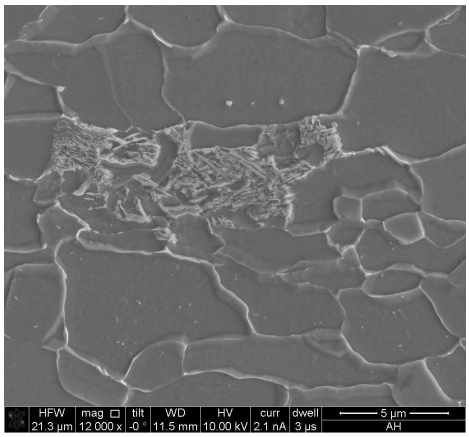

Figure IX-6 SEM *micrographs showing Air cooled microstructures.*

Med. C- High Nb; high FRT Air	Med. C- High Nb; low FRT Air
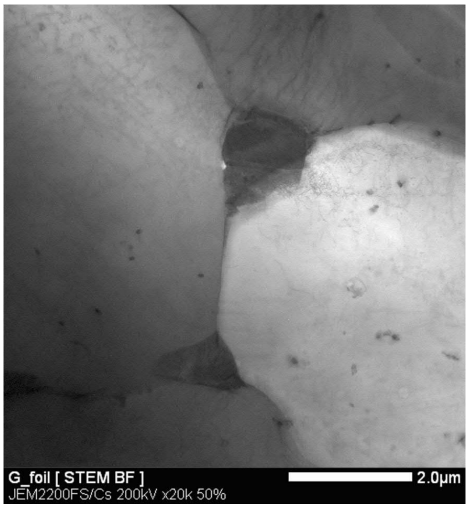	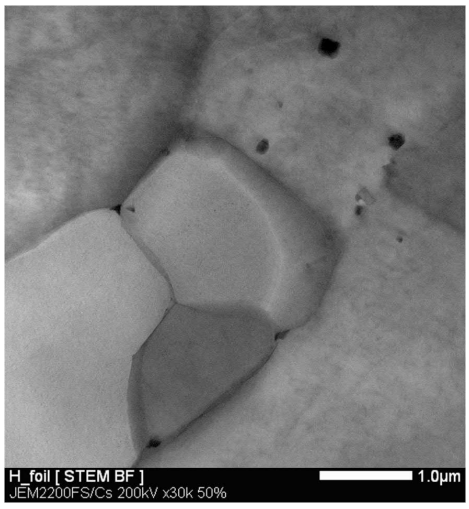
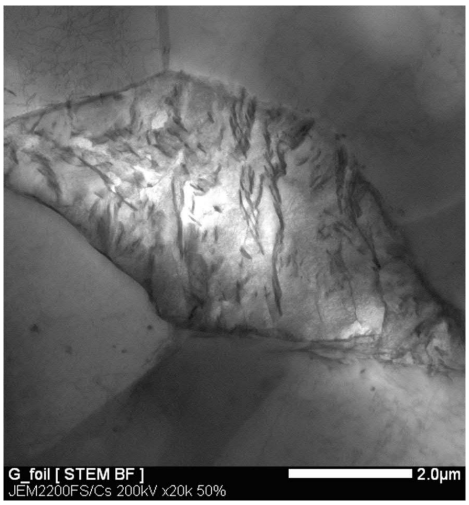	

Figure IX-7 *STEM BF micrograph of Air cooled microstructures.*

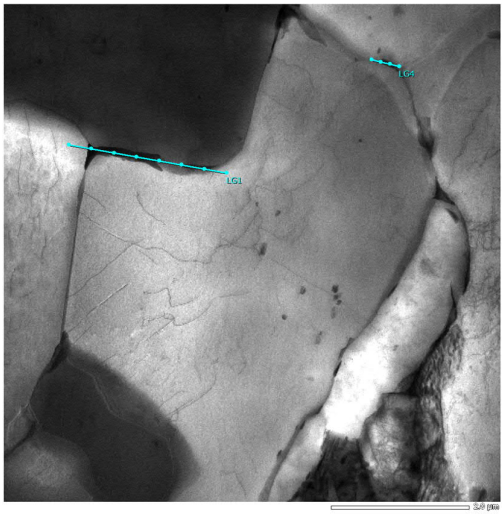

Memo	C	S	Ti	V	Mn	Fe	Nb	Mo	Total(Atom%)
LG40000 ; 0.000 µm	36.2	0	0	0	0.8	62.8	0.1	0	100
LG40001 ; 0.140 µm	34.8	0	0	0	1	64.2	0	0	100
LG40002 ; 0.280 µm	34.1	0.1	0	0	0.9	64.8	0.1	0	100
LG40003 ; 0.419 µm	34.2	0	0	0	1	64.8	0	0	100
LG10000 ; 0.000 µm	38.3	0	0	0	0.9	60.8	0	0	100
LG10001 ; 0.334 µm	32.9	0	0	0	1.8	65.3	0	0	100
LG10002 ; 0.669 µm	31.2	0.1	0	0	1.3	67.5	0.1	0	100

Figure IX-8 *STEM BF micrograph showingcarbide precipitates at grain boundaries.*

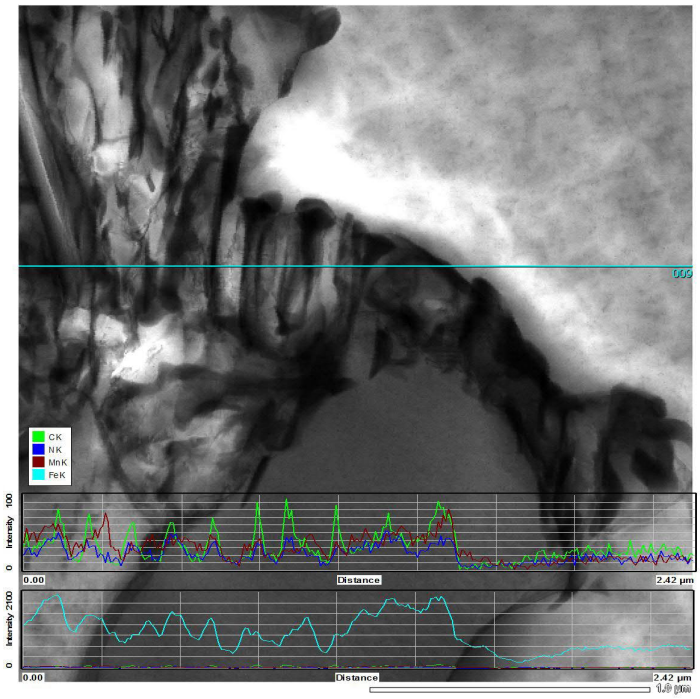

Figure IX-9 *STEM BF micrograph showing a colony of lamellar pearlite.*

Name	Symbol	Description	O.M.	SEM (EBSD-IQ)	T.E.M
Polygonal ferrite	α_p	Equiaxed-polyhedral recrystallized shaped grains, crossing over former γ grain boundaries. No sub structure low dislocation density	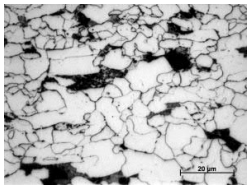	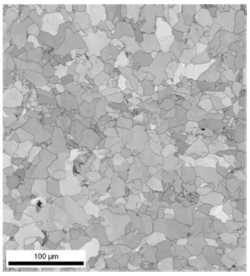	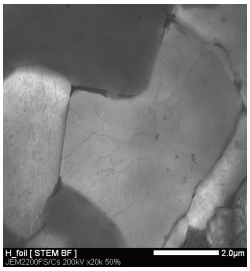
Quasi polygonal ferrite	α_{qp}	Irregular, varying shape, crossing over former γ grain boundaries mostly recovered	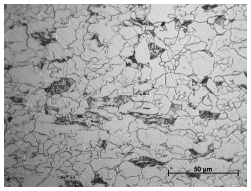	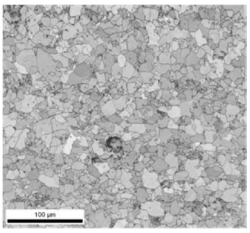	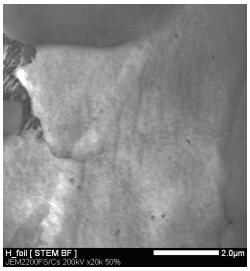
Granular bainitic ferrite	$\alpha_{B(G)}$	Lathless bainitic ferritic structure, partially dislocated-recovered	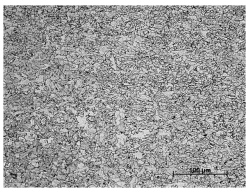	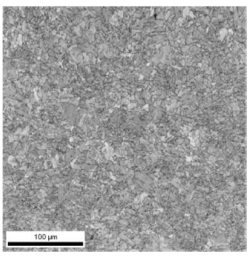	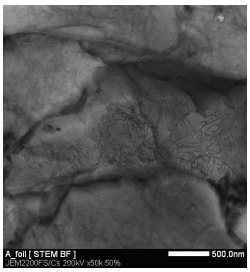
Bainitic ferrite	α_B	Sheaf-like, lath-like dislocated structure preserves prior γ grain boundaries	 [1]	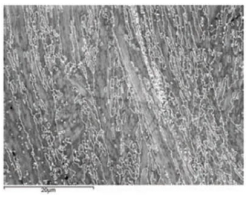 [2]	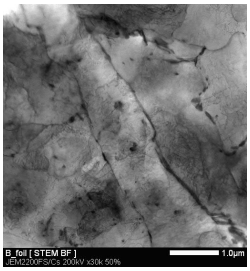
Widmanstaten ferrite	α_W	Lath/plate shape, no internal substructure, nucleates at γ grain boundaries	 [3]	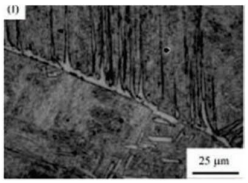 [4]	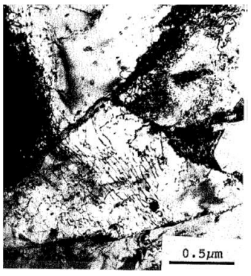 [3]

Acicular ferrite	α_A	Small feathery needles with low aspect ratio	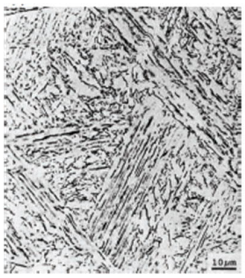 [3]	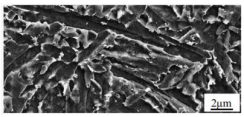 [5]	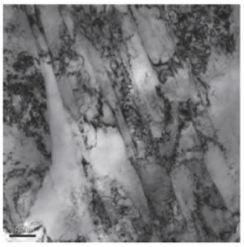 [5]
Lamellar pearlite	P_L	Lamellar growth of ferrite and Fe_3C	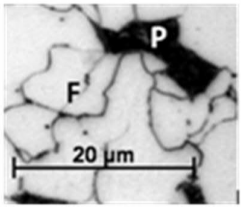	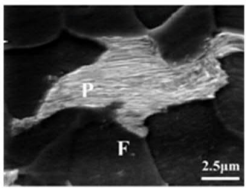 [6]	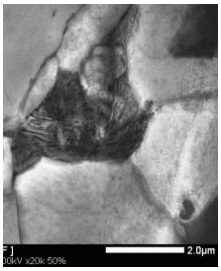
Degenerate pearlite	P_D	Incomplete lamellar growth of ferrite and Fe_3C	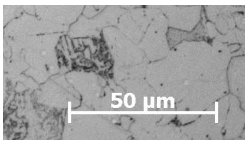	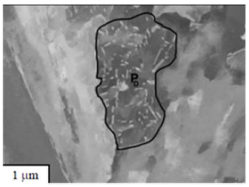 [2]	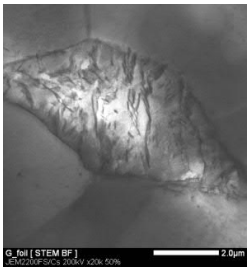
Upper bainite	B_U	Structure with intra-lath cementite	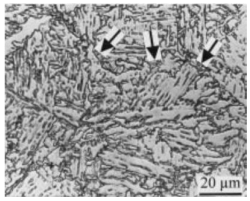 [7]	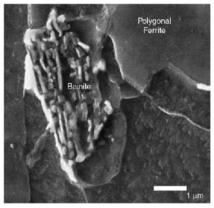 [8]	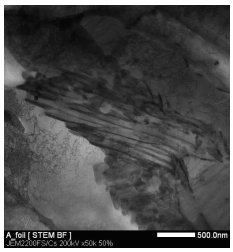
Lower bainite	B_L	Structure with intra and inter lath cementite	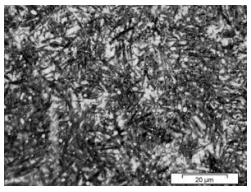 [9]	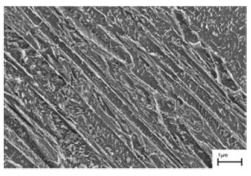 [10]	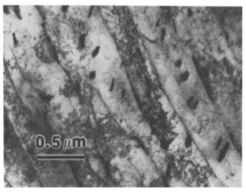 [11]

Martensite	α'_M	Lath/plate like highly dislocated structure preserves prior γ grain boundaries	 [1]	 [1]	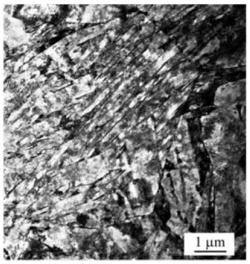 [12]
Martensite/ Austenite constituents	M/A	Minor, secondary constituent, highly dislocated, M and A phases coexist in a crystallographic relationship	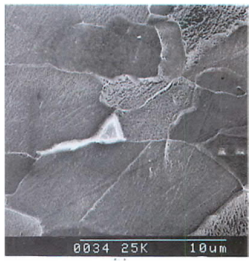 [3]		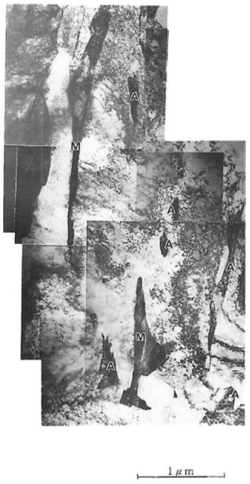 [3]

Table IX.1 Description, nomenclature and representative micrographs of the γ transformation products.

References

[1] B. R. Commitee, *Atlas for Bainitic Microstructures* vol. 1: Iron and Steel Institute of Japan 1992.

[2] M. P. Aarnts, R. A. Rijkenberg, F. A. Twisk, D. Wilcox, M. J. Zuijderwijk, A. Arlazarov, *et al.*, "Microstructural quantification of multi phase steels (Micro-quant)," European commission2011.

[3] G. Krauss and S. W. Thompson, "Ferritic Microstructures in Continuously Cooled Low- and Ultralow-carbon Steels," *ISIJ International,* vol. 35, pp. 937-945, 1995.

[4] A. Fadel, D. Glisic, N. Radovic, and D. Drobnjac, "Intragranular ferrite morphologies in medium carbon vanadium-microalloyed steel," *Journal of Mining and Metallurgy,* vol. 49, pp. 237-244, 2013.

[5] J. Hu, L.-X. Du, J.-J. Wang, H. Xie, C.-R. Gao, and R. D. K. Misra, "Structure–mechanical property relationship in low carbon microalloyed steel plate processed using controlled rolling and two-stage continuous cooling," *Materials Science and Engineering: A,* vol. 585, pp. 197-204, 11/15/ 2013.

[6] Y. LIU, F. ZHU, y. LI, and G. WANG, "Effect of TMCP Parameters on the Microstructure and Properties of an Nb-Ti Microalloyed Steel," *ISIJ International,* vol. 45, pp. 851-857, 2005.

[7] A. F. Gourgues, H. M. Flower, and T. C. Lindley, "Electron backscattering diffraction study of acicular ferrite, bainite, and martensite steel microstructures," *Materials Science and Technology,* vol. 16, pp. 26-40, // 2000.

[8] R. D. K. Misra, H. Nathani, J. E. Hartmann, and F. Siciliano, "Microstructural evolution in a new 770MPa hot rolled Nb–Ti microalloyed steel," *Materials Science and Engineering: A,* vol. 394, pp. 339-352, 2005.

[9] N. Luzginova. *Formation of Bainite*. Available: http://www.3me.tudelft.nl/en/about-the-faculty/departments/materials-science-and-engineering/research/microstructural-control-in-metals/research/formation-of-bainite/

[10] E. Keehan, L. Karlsson, M. Thuvander, and E. Bergquist, "Microstructural characterisation of as-deposited and reheated weld metal—High Strength Steel Weld Metals," *Welding in the World,* vol. 51, pp. 44-49, 2007.

[11] B. L. Bramfitt, "Structure/Property Relationships in Iron and Steels," in *Materials selection and design ,Volume 20 ASM Handbook*, A. International, Ed., ed, 1997.

[12] S. W. Thompson, "A Transmission Electron Microscopy Investigation of Reaustenitized-and-Cooled HSLA-100 Steel," *Metallography, Microstructure, and Analysis,* vol. 1, pp. 131-141, 2012/08/01 2012.